



UNIVERSITY OF
BIRMINGHAM

Manufacturing Optimisations for Micro-tubular Fuel Cells by Extrusion and Dip Coating Techniques

Qingbin Liu

**A thesis submitted to The University of Birmingham for the
degree of**

Doctor of Philosophy

School of Metallurgy and Materials,

University of Birmingham

September 2018

UNIVERSITY OF
BIRMINGHAM

University of Birmingham Research Archive

e-theses repository

This unpublished thesis/dissertation is copyright of the author and/or third parties. The intellectual property rights of the author or third parties in respect of this work are as defined by The Copyright Designs and Patents Act 1988 or as modified by any successor legislation.

Any use made of information contained in this thesis/dissertation must be in accordance with that legislation and must be properly acknowledged. Further distribution or reproduction in any format is prohibited without the permission of the copyright holder.

ACKNOWLEDGEMENTS

I would like to thank Prof. Tim Button firstly, my supervisor, for his supervision and guidance during the past few academic years.

I would like to thank Dr. Michaela Kendall, my co-supervisor, for patient support and suggestions.

Many thanks are given to my colleagues and friends in Functional Materials Group, for helping me get familiar with all the facilities in our labs. Carl Meggs, our technician, is always willing to give me timely assistance related to experimental issues.

Also, I am really grateful for all the backing electrical testing work from Centre for Hydrogen and Fuel Cell Research, Chemical Engineering, University of Birmingham.

Finally, I would like to express my thanks to my family for their kind support to build my motivation when accomplishing this thesis.

ABSTRACT

The optimisation of micro-tubular Solid Oxide Fuel Cells (mSOFCs) was studied, including anode extrusion, electrolyte dip coating and heat treatment of the resultant half-cells.

The study of NiO-YSZ anode extrusion started with an analysis of powder packing, followed by the determination of the optimum liquid content required to produce reliable roll milled viscous paste mixtures. Rheological tests were carried out using a simple die configuration to predict the extrusion pressure during the anode processing. The mechanisms, which lead to differences between the predicted and experimental extrusion pressures were explored. The pore former (corn starch) in the paste formulation was used as a microscopic indicator of phase maldistribution distribution. This redistribution gave a dense ceramic layer at the interface between the bulk paste and the die pin or mandrel. It was suggested that this redistribution was the major contributor to the varied extrusion pressure recordings as extrusion progressed. The phenomenon was thought to be a significant contributor to the experimentally measured pressure being three times of the predicted value.

Extrusions with a solid load of ~70 vol% were shown to exhibit stable pressures and produce homogeneous defect-free anode tubes.

A YSZ electrolyte coating method was developed, involving the determination of binder and dispersant fractions within the slurry to optimise performance, plus the control of coating thickness by adjusting processing parameters (solid weight fraction and withdrawal speed). Two-step heat treatments were employed to generate a dense electrolyte layer. Dip coated electrolyte layers with a dense sintered thickness

between 20 and 30 μm were obtained at a solid mass fraction of 50 wt% in the slurry and a withdrawal rate of 80 mm/min. The heat treatment to develop a dense electrolyte structure was determined as a pre-heating of the anode tube at 1100 °C followed by a re-heating of the electrolyte coated dual structure at 1350 °C.

After the addition of cathode ($\text{La}_{0.8}\text{Sr}_{0.2}\text{MnO}_3$, LSM) and current collection (silver) components by brush coating, the fabricated full cells are electrically characterised in terms of current-voltage polarization and electrochemical impedance spectroscopy (EIS). The open circuit voltage (OCV) and peak power density were 0.82 V and 0.11 W/cm^2 respectively.

Table of Contents

Chapter 1 Introduction	1
1.1. Power generation techniques	1
1.1.1. Fossil fuel power generation	2
1.1.2. Nuclear power generation	4
1.1.3. Renewable energy power generation	5
1.2. Types of fuel cells	12
1.2.1. Phosphoric Acid Fuel Cell (PAFC)	12
1.2.2. Molten Carbonate Fuel Cell (MCFC)	14
1.2.3. Proton Exchange Membrane Fuel Cell (PEMFC)	15
1.2.4. Alkaline Fuel Cell (AFC) and Alkaline Exchange Membrane Fuel Cell (AEMFC) ..	17
1.2.5. Solid Oxide Fuel Cell (SOFC)	20
1.3. Fuel types	21
1.3.1. Direct hydrogen	21
1.3.2. Methane and hydrocarbons	22
1.4. SOFC configurations	24
1.4.1. Planar Design	25
1.4.2. Tubular Design	25
1.4.3. Micro-tubular Design	26
1.5. SOFC cell components	26
1.5.1 Components for the electrochemical reaction	26
1.5.2 Interconnects	26
Chapter 2 Literature review	28
2.1. mSOFC Materials	28
2.2. Fabrication techniques	30
2.2.1 Extrusion – support layer	31
2.2.2. Deposition techniques	43
2.2.3. Impregnation technique	44
2.3 Development of fuel cell performance	44
2.4. Aims of the project	46
Chapter 3 Experimental techniques	47
3.1. As-received materials	47
3.2. Viscous plastic processing (VPP)	48
3.3. Extrusion die design	52

3.4. The Instron load frame	54
3.4.1. Powder packing behaviour	55
3.4.2 Paste rheology test.....	56
3.4.3 Dip coating	57
3.5. Sintering	58
3.6. Particle size analysis	58
3.7. Thermal gravity analysis (TGA)	59
3.8. Dilatometry	59
3.9. Viscosity test.....	60
3.10. BET surface area characterisation.....	62
3.11. Scanning electron microscopy (SEM)	62
3.12. Cell testing	63
3.12.1. Current-Voltage measurement.....	64
3.12.2. Electron Impedance Spectroscopy (EIS).....	66
Chapter 4 Powder characterisation and anode processing	71
4.1. Introduction	71
4.2. Results and discussion	71
4.2.1. As-received powder characterisation	71
4.2.2 The introduction of pore former	77
4.2.3 Powder packing study and initial extrusion trials	79
4.3. Conclusions	99
Chapter 5 Paste rheology analysis	101
5.1. Introduction	101
5.2. Results and discussion	101
5.2.1 Six-parameter Benbow-Bridgwater fit.....	101
5.2.2. Modifications to the Benbow-Bridgwater expression for the tubular anode extrusion die set.....	107
5.2.3. Study of the extrusion pressure variations.....	109
5.2.4 Local phase redistribution analysis	120
5.3. Conclusions and future work.....	134
Chapter 6 Dip coating of YSZ electrolyte.....	137
6.1. Introduction	137
6.2. Results and discussion	137
6.2.1 Coating slurry adjustment.....	137
6.2.2 Coating thickness control	144

6.3. Conclusions and Future work	152
Chapter 7 Sintering of dual-layer half cells.....	153
7.1. Introduction	153
7.2. Results and discussion	153
7.2.1. Co-sintering of dual-layer structure.....	153
7.2.2. Dilatometry analysis for anode/electrolyte compacts	163
7.2.3. Discussion of initiation of electrolyte cracking for one-step sintering.....	167
7.3. Conclusions and future work.....	170
Chapter 8 Cell performance testing	171
8.1. Introduction	171
8.2. Preparation for cell testing.....	171
8.3. Handling of gas tightness issue	173
8.3. Results and discussion	176
8.4. Conclusions	181
Chapter 9 Conclusions and future work.....	182
Chapter 10 References	186

List of Figures

Figure 1 Schematic Diagram of (a) an AC Generator and (b) its output electromotive force (image source: BYU [5])	2
Figure 2 Electricity generated by different types of energy across UK in 2015 (image source: DBEIS [7]).....	3
Figure 3 Schematic of HDR heat mining system [35]	7
Figure 4 Mechanism of PV effect showing the direction of electron flows [45]	10
Figure 5 Schematic of a small thermoelectric device [52]	11
Figure 6 Summary of the most common types of fuel cell, the fuel and oxidising agents required, typical operating temperatures and the electrolyte ion transfer type and direction [57].....	12
Figure 7 Schematic sketch of a phosphoric acid fuel cell [60].....	14
Figure 8 Operating process of a molten carbon fuel cell [61]	15
Figure 9 Essential components of a proton exchange membrane fuel cell [64]	17
Figure 10 Fundamental layout of an alkaline fuel cell [72]	18
Figure 11 Schematic of an alkaline fuel cell with an anion-exchange membrane electrolyte [74].....	20
Figure 12 Typical designs for (a) planar and (b) tubular SOFCs [91, 92]	24
Figure 13 Picturing of C-shaped plastic tube holders [124]	33
Figure 14 Single cell fabrication process by Suzuki et al.	34
Figure 15 Schematic ternary phase diagram of polymer/solvent/non-solvent during polymeric membrane formation from Point A to Point D [133].....	36
Figure 16 Schematic diagram of ram extrusion [138]	38
Figure 17 SEM images of the dual layer hollow fibres with increasing ethanol content from 5 wt. % to 20 wt. % [142]	40
Figure 18 Manufacturing route for the structure of anode/electrolyte.....	48
Figure 19 Twin roll Bridge milling machine with and without load of processed compound mixture	50
Figure 20 3-D schematic of assembling and disassembling views of the tailor made extrusion die set for this project.....	52
Figure 21 Simplified section view of core components for the die set with essential dimensional information and indications of two convergence regions (the plunger and the capping part are not shown here)	53
Figure 22 Extrusion process where a vertical load is exerted via an Instron load frame to force the extrudates out of the die	54
Figure 23 Photograph and schematic of the compaction die used for the powder packing study in this project	55
Figure 24 2-D drawing of the alternative dies with varying die lengths, used for paste rheology study.....	56
Figure 25 Layout of the dip coating holder installation	57
Figure 26 Photographs of some equipment used in the project, i.e. (a) particle size analyser, (b) dilatometer, (c) TGA and (d) rheometer.....	61
Figure 27 SEM samples for characterisations of (a1) as-received powders (a2) longitudinal cell fracture surface and (b) axial cell fracture surface	63

Figure 28 Schematic of the test rig for electrical cell performance [57].....	64
Figure 29 Typical polarisation plot of a fuel cell [204].....	66
Figure 30 Impedance Z plotted in the complex plane [208]	67
Figure 31 Nyquist plots for (a) a capacitor, (b) a capacitor in series with a resistor, (c) a capacitor in parallel with a resistor, and (d) a resistor in series with a parallel resistor-capacitor circuit [209].....	68
Figure 32 Equivalent circuit for a simple fuel cell [210].....	69
Figure 33 Particle size distribution for (a) NiO and (b) YSZ-A powders.....	73
Figure 34 Particle size distribution for YSZ-E powders	74
Figure 35 SEM imaging for (a) NiO and (b) YSZ-A powders.....	75
Figure 36 SEM imaging for YSZ-E powders	76
Figure 37 Particle size distribution for corn starch powders	78
Figure 38 SEM image of the corn starch powders	79
Figure 39 Continuous compaction curves for NiO powders (3 g) with (a) multiple reloads at fixed maximum load 5 kN and (b) single reload at raised maximum load from 5 kN to 15 kN.....	81
Figure 40 Continuous compaction curves for corn starch powders (1.5 g) with (a) multiple reloads at fixed maximum load, (b) multiple reloads with rising maximum loads and (c) single reload at the highest maximum load, 25 kN.....	83
Figure 41 Compressive Load vs Extension curves for extrusions without pore former.....	90
Figure 42 SEM imaging for sintered anode cross section without pore former.....	93
Figure 43 Typical load vs extension curve profiles for extrusions with 5 g pore former and 2.6 g solvent.....	97
Figure 44 (a) Tube drying in the oven, (b) green anode tube and (c) schematic of anode paste sticking onto the extrusion pin and flowing slower than the paste being extruded behind it causing the paste to thicken and pucker up rather than forming a continuous tube.....	99
Figure 45 Extrusion load data for rheology test on the anode paste in relatively high-speed range.....	103
Figure 46 Unreliable extrusion trial with $L/D=1$ exhibiting a higher plunger load at 0.1 mm/min, compared to the one with $L/D=4$	104
Figure 47 Original load vs extension curves for 3 separate extrusion trials with 2.6 g cyclohexanone and 5 g corn starch, with highlights of notable load points described in Table 18	110
Figure 48 Assumed liquid phase distribution in the barrel during extrusion	113
Figure 49 TGA of green anode sample.....	114
Figure 50 Dilatometry data showing dimensional change during heating of debound anode sample.....	115
Figure 51 Particle size distribution for ground (a) Extrudate 1 and (b) Extrudate 4	119
Figure 52 Fracture surface of an extrudate from Paste 2 heated at 1000 °C without pore former	121
Figure 53 Fracture surface of an extrudate heated at 1000 °C, with an instantaneous extrusion load of 10.5 kN and 2.6 g usage of solvent.....	123
Figure 54 Fracture surface of an extrudate heated at 1000 °C, with an instantaneous extrusion load of 8.5 kN and 2.6 g usage of solvent	128
Figure 55 Fracture surface for (a) Extrudate E and (b) Extrudate D heated at 1000 °C.....	130
Figure 56 Plotted load vs extension curves for tubes made with Batch 3 and Batch 2	131
Figure 57 Fracture surface for (a) Extrudate C and (b) Extrudate B heated at 1000 °C.....	133
Figure 58 Schematic of dense ceramic regions formed during extrusion.....	135 ••

Figure 59 Schematic of fluid shear rate during dip coating.....	140
Figure 60 Viscosity for different dispersant contents at a shear stress of ~0.4 Pa.....	141
Figure 61 A viscosity test cycle for coating slurry with 2% dispersant and 50% solid weight fraction	143
Figure 62 Cross section of coated green tubes at a withdraw speed of (a) 5 mm/min (b) 20 mm/min (c) 40 mm/min (d) 60 mm/min and (e) 100 mm/min.....	146
Figure 63 Cross section of coated green tubes at a solid weight fraction of (a) 40%, (b) 50%, (c) 60% and (d) 70%.....	148
Figure 64 Plotted curves for coating thickness vs (a) speed and (b) solids weight fraction, with YSZ-E slurries.....	149
Figure 65 Cross section of coated pre-sintered tubes at a withdraw speed of (a) 20 mm/min, (b) 60 mm/min and (c) 100 mm/min.....	151
Figure 66 Dilatometry profiles for debound anode/electrolyte compacts.....	156
Figure 67 Cross section of co-sintered Tube B.....	158
Figure 68 Cross section of co-sintered Tube C	159
Figure 69 Apperances of (a) sintered anode tube, (b) non-sintered coating on green anode, (c) non-sintered coating on sintered anode and (d) co-sintered half cell.....	159
Figure 70 Cross section of co-sintered Tube D	161
Figure 71 Cross section of co-sintered Tube E.....	162
Figure 72 Dilatometry plots for anode/electrolyte compacts in the temperature range between 600 °C and 1400 °C	164
Figure 73 Mismatch strains between anode and electrolyte layers of Tube A-B.....	165
Figure 74 Mismatch strains between anode and electrolyte layers of Tube C-E.....	166
Figure 75 Dilatometry profile of electrolyte compact sintered at 1400 °C including debinding process.....	169
Figure 76 Imaging of prepared cells ready for testing.....	173
Figure 77 Ceramic manifold used (a) before and (b) after the initial tests.....	174
Figure 78 Metallic manifold used for later tests	175
Figure 79 Current-Voltage curve at 750 °C with 50 ml/min H ₂ and 50 ml/min N ₂	177
Figure 80 Electrolyte characteristics of (a) Cell FMG and (b) Cell AMI [2]	179
Figure 81 Nyquist plot of EIS at 750 °C and 0.1 V below OCV, with 50 ml/min H ₂ and 50 ml/min N ₂	181 ••

List of Tables

Table 1 SOFC main components and their capabilities.....	27
Table 2 Most frequently used materials for mSOFC components [1].....	29
Table 3 Single cell parameters for recently developed mSOFCs by conventional or phase-inversion extrusions.....	41
Table 4 Statistical particle size data for as-received ceramic powders.....	72
Table 5 BET surface area data for basic ceramic powders.....	77
Table 6 Statistical particle size data for as-received corn starch powders.....	78
Table 7 Processing parameters for powder compaction.....	84
Table 8 Calculated packing density results.....	84
Table 9 Materials with fixed dosage for anode extrusion.....	87
Table 10 Paste formulations with different liquid content.....	88
Table 11 Paste processing descriptions with different liquid content.....	89
Table 12 Drying process for anode tubes.....	91
Table 13 Heating regime for anode tubes.....	91
Table 14 Paste formulations for extrusions with pore former (72.6 vol% solid).....	96
Table 15 Paste formulations for extrusions with pore former (69.6 vol% solid).....	98
Table 16 Pressure data taken for curve fit with different velocity & L/D combinations.....	105
Table 17 Determined paste parameters using Benbow-Bridgewater fit.....	106
Table 18 Characteristic extrusion load for 3 separate extrusion trails.....	111
Table 19 Weight change for extrudates of Paste 2 after drying and heating.....	117
Table 20 Mean particle size and surface area data for extrudates exhibiting different instantaneous extrusion pressure.....	118

Table 21 Weight loss for extrudates at different instantaneous extrusion loads, with the usage of 2.6 g solvent and 5 g pore former.....	124
Table 22 Selected characterised results for different extrudates.....	126
Table 23 Calculated R values between different extrudates.....	127
Table 24 Adhesion strength at different binder fractions.....	138
Table 25 Coating slurry formulation for thickness characterisation at different pulling-up speed.....	144
Table 26 Coating slurry formulations for thickness characterisation at different solids loadings.....	147
Table 27 Heat treatments for the first-batch of tubular anode/electrolyte samples.....	154
Table 28 Heat treatments for second-batch tubular samples.....	163
Table 29 Heating regime for the functional/structural cathode layer.....	172
Table 30 Comparisons between commercial cells [2] and lab made cells using the identical electrical test rig.....	178

List of Equations

Equation 1 Nuclear fission reaction for U-235.....	4
Equation 2 Boudouard reaction.....	23
Equation 3 Pyrolysis.....	23
Equation 4 Steam gasification.....	23
Equation 5 Water gas shift reaction.....	23
Equation 6 Steam reforming.....	23
Equation 7 Partial oxidation.....	23
Equation 8 Dry reforming.....	23
Equation 9 Six-parameter Benbow-Bridgwater Equation.....	37
Equation 10 Definition of area-specific resistance.....	44
Equation 11 Divisions of area-specific resistance.....	45
Equation 12 Extended expression for the Westman model.....	49
Equation 13 Definition of TEC.....	60
Equation 14 Definition of apparent viscosity.....	60
Equation 15 Gibbs free energy change.....	65
Equation 16 Electromotive force.....	65
Equation 17 Gibbs free energy change for the reaction between H ₂ and O ₂ at STP.....	65
Equation 18 Electromotive force for the reaction between H ₂ and O ₂ at STP.....	65
Equation 19 Nernst equation.....	65
Equation 20 Sinusoidal perturbation voltage during EIS.....	67
Equation 21 Response current during EIS.....	67

Equation 22 Definition of impedance.....	67
Equation 23 Alternative expression for impedance.....	67
Equation 24 Extended Westman powder packing expression for binary system.....	85
Equation 25 Extended Westman powder packing expression for ternary system.....	94
Equation 26 Modified six-parameter Benbow-Bridgewater equation.....	107
Equation 27 Load growth rate by solvent change.....	126
Equation 28 Shear rate for the coating slurry.....	139
Equation 29 Landau-Levich equation.....	145
Equation 30 Definition of mismatch strain.....	164

List of Abbreviations

AC	Alternating Current
AEMFC	Alkaline Exchange Membrane Fuel Cell
AFC	Alkaline Fuel Cell
ASR	Area Specific Resistance
BZCYYb	$\text{BaZr}_{0.1}\text{Ce}_{0.7}\text{Y}_{0.1}\text{Yb}_{0.1}\text{O}_{3-\delta}$
CGO	(See GDC)
DBP	Dibutyl phthalate
DC	Direct Current
DOP	Diethyl phthalate
EIS	Electrochemical Impedance Spectroscopy
ESEM	Environmental Scanning Electron Microscope
GDC	Gadolinium Doped Ceria
ID	Inside Diameter
LSCF	Lanthanum Strontium Cobalt Ferrite
LSM	Lanthanum Strontium Manganite
MCFC	Molten Carbonate Fuel Cell
MFC	Mass Flow Controller
mSOFC	micro-tubular Solid Oxide Fuel Cell
OCV	Open Cell Voltage
OD	Outside Diameter
PAFC	Phosphoric Acid Fuel Cell
PDMS	Polydimethylsiloxane

PEMFC	Proton Exchange Membrane Fuel Cell
PVA	Polyvinyl Alcohol
PVB	Polyvinyl Butaryl
ScSZ	Scandia Stabilized Zirconia
SEM	Scanning Electron Microscope
SDC	Samaria Doped Ceria
SOFC	Solid Oxide Fuel Cell
STP	Standard Temperature and Pressure
TEC	Thermal Expansion Coefficient
TGA	Thermal Gravity Analysis
TPB	Triple Phase Boundary
VPP	Viscous Plastic Processing
WPS	Wet Power Spray
YSZ	Yttria Stabilized Zirconia

Chapter 1 Introduction

1.1. Power generation techniques

Power generation techniques have been developed since Michael Faraday discovered the phenomenon of electromagnetic induction and presented his law of induction in the 1830s [3, 4]. Energy in various forms, including mechanical energy and chemical energy, for example, have been transformed to electricity via subsequently developed methods, as the so-called secondary energy could be retransformed and meet nearly all the application situations for daily human activities.

A schematic diagram of a typical generator is given in Figure 1a. A metallic loop, located in a uniformly distributed magnetic field, is rotated by exertion of an external force. Electricity is induced when the conductive loop cuts the lines of magnetic induction. As the cut angle between the circuit surface and induction lines is altering all the time during rotation, the generated current is consequently in a sinusoidal form, as shown in Figure 1b. Large-scale national power plants in the modern world are all supplying this type of alternating current (AC) for domestic usage. The source of external force could be any form of energy that could be transformed to mechanical energy.

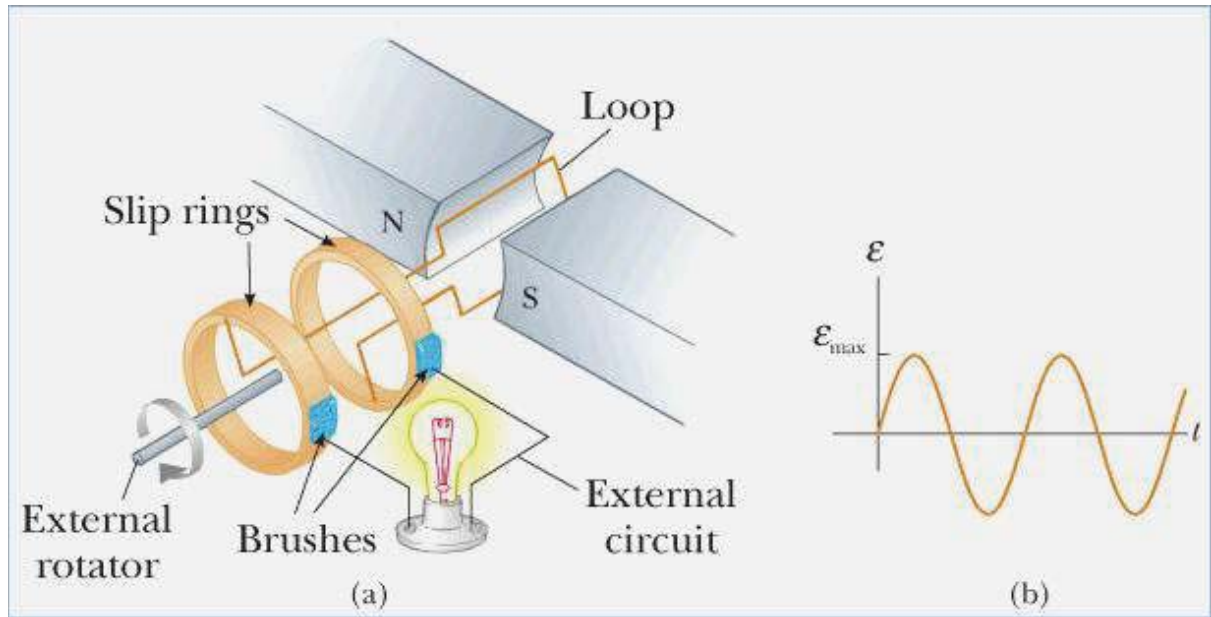


Figure 1 Schematic Diagram of (a) an AC Generator and (b) its output electromotive force (image source: BYU [5])

1.1.1. Fossil fuel power generation

In a fossil fuel power station, a fossil fuel (i.e. coal, petroleum or natural gas) is burnt for electricity generation [6]. Thermal energy is first acquired from the chemical energy of the fossil fuels via combustion. Usually, water is heated as a medium and transferred to steam via the fuel burning process. A turbine is driven by that steam to convert mechanical energy into electrical power by the electrochemical induction effect. In some cases, burning fuels could also activate a gas turbine or an internal combustion engine directly to perform the required mechanical work.

UK electricity generation, 2015

Source: DBEIS

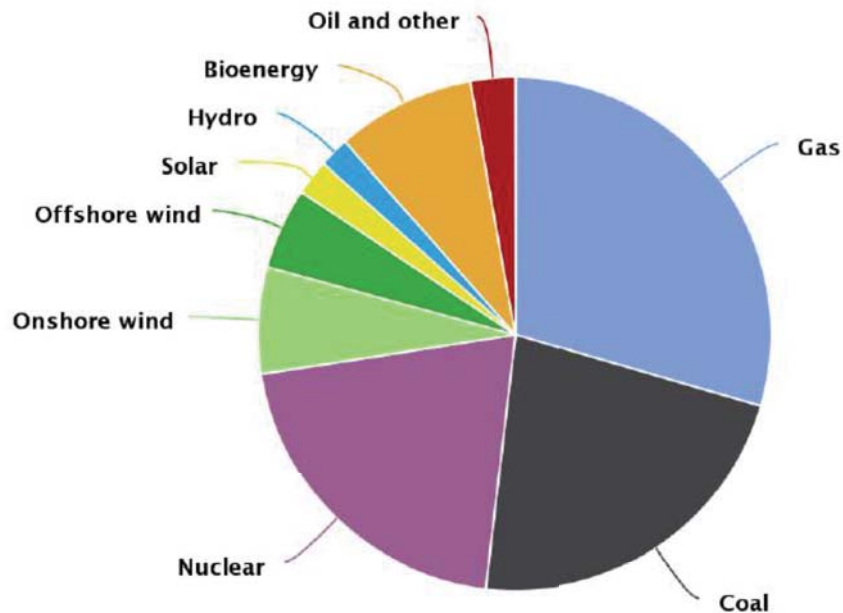


Figure 2 Electricity generated by different types of energy across UK in 2015 (image source: DBEIS [7])

Figure 2 gives the relative fractions of electricity generated by different energy sources across the UK in 2015. It can be seen that the contribution to total electricity generation by the burning of fossil fuels exceeded 50%. In the same year, on the global scale, this percentage was much higher. This indicates the heavy dependency of limited fossil fuel resources by current world energy consumption.

Besides the finite reserve of fossil fuels, the biggest problem of burning such types of energy is the emission of carbon dioxide, which is the major origin of the greenhouse effect and traditionally disposed by air dilution. The Royal Commission on Environmental Pollution (RCEP) published a report in 2000, suggesting that in UK,

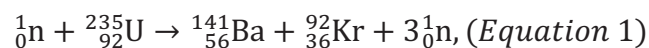
CO₂ emission by human activities must be reduced by 60% within the period between 1998 and 2050 [8]. This is an even tougher task compared to that agreed in the Kyoto protocol [9] in December 1997, but accepted by UK government to get involved in the inhibition of climate change and the continuing replacement of fossil fuels with renewable energy [10].

1.1.2. Nuclear power generation

Both fossil fuel and nuclear power generation can be categorised as thermal power generation, since thermal energy acts as an intermediate product for energy transformation. The difference of the latter is, a nuclear fission or fusion reactor is the heat source.

Generally, a nuclear reaction involves the fission of uranium-235, as the reaction itself could generate enormous amount of thermal energy (the energy released by 1kg U-235 is equal to that of 2700 t burnt coal [11]). During the fission process, the U-235 nucleus is struck by a neutron and absorbs its energy before vibrating and dividing into two smaller nucleus and 2-3 neutrons. The newly-created neutrons would strike adjacent U-235 nuclei to continue the fission chain reaction.

Considerable energy is created accordingly. A typical nuclear fission reaction for U-235 is given in Equation 1. For safety control, the nuclear reactors are inspected by self-cut-off systems to suspend the chain reaction when an emergency occurs [12], while being governed in terms of reaction violence at the same time, by adjusting the quantity of neutron to continue the fission reactions [13].



1.1.3. Renewable energy power generation

Our planet has a huge storage of ready-to-use natural sources of energy, which can be reproduced within a short time frame. Utilisations of such renewable energy storage would considerably inhibit the environmental problems related to the consumption of conventional fossil fuels, including global warming, air pollution, acid precipitation, etc. [14] Given the fact that currently 25% of world's population that live in the developed countries consume 75% of global energy production [15] and the prediction that the overall population will double by 2050 [16], enhancement of power generation techniques from renewable energy is imperative for sustainable development [17]. Renewable energy is normally in the form of either direct mechanical energy or thermal energy. Hence it is able to generate power via traditional electromagnetic induction processes. Electricity generation can be also realised not by alternatives to mechanical – electrical energy conversion using renewable energy. These concepts will be introduced later in this section.

1.1.3.1. Direct mechanical energy – hydro, tidal and wind power generation

A hydroelectric station uses the potential energy of water (converted to kinetic energy when water falls due to gravity) to transform mechanical energy to electricity by the electromagnetic induction effect. Hydroelectricity contributed to 16.6% of overall global power generation and 70% of renewable energy power generation in 2015 [18]. A upstream reservoir is necessary for hydroelectricity and thus whether it is environmentally friendly is in doubt. [19] Irreversible ecological damage has been observed within 10 years since the final completion of the Three Gorges Dam [20], a well-known tidal power system in China. A direct ecological issue related to dammed

ivers is the altered distribution of both river basin and habitat structure [21-24]. Most witnessed problems of damming are due to operations of the water on the upstream, comprising discharge, sedimentation and thickening of hazardous constituents [25-27]. As a result, the discussion about the validity of renewable or clean energy by dammed water continues.

Similarly, tidal and wind power generation take the advantage of kinetic energy of the tidal sea water or wind, to create induced electricity [28]. They cause little environmental damage compared to hydroelectricity. The disadvantages for both techniques are high construction costs and uncontrollable time/location variables [29].

1.1.3.2. Direct thermal energy – geothermal and solar power generation

The traditional geothermal electricity generation technique collects thermal energy from underground high-temperature bedrock [30], which is then used to heat underground water and hot steam is formed to drive the turbine. There is a stupendous geothermal reserve under the surface of Earth, which is in sufficient excess to resolve the current energy crisis [31, 32], if the necessary technologies were mature enough.

Enhanced Geothermal System (EGS) has been intensively developed in the 21st century [33] to slow down the tendency of climate change. To distinguish it from previous geothermal technologies, EGS obtains geothermal energy by first applying physical interaction, instead of collection of ready-to-use heat. A typical representative of EGS is hot dry rock (HDR) technology [34]. As shown in Figure 3,

high-pressurised water is injected into hot rock (usually above 200 °C) deep underground and thermal energy is generated in the form of direct heat or hot steam [35]. A minimum number of two drilled wells are necessary for HDR power generation, one of which is for cold water injection while the other is for heat collection.

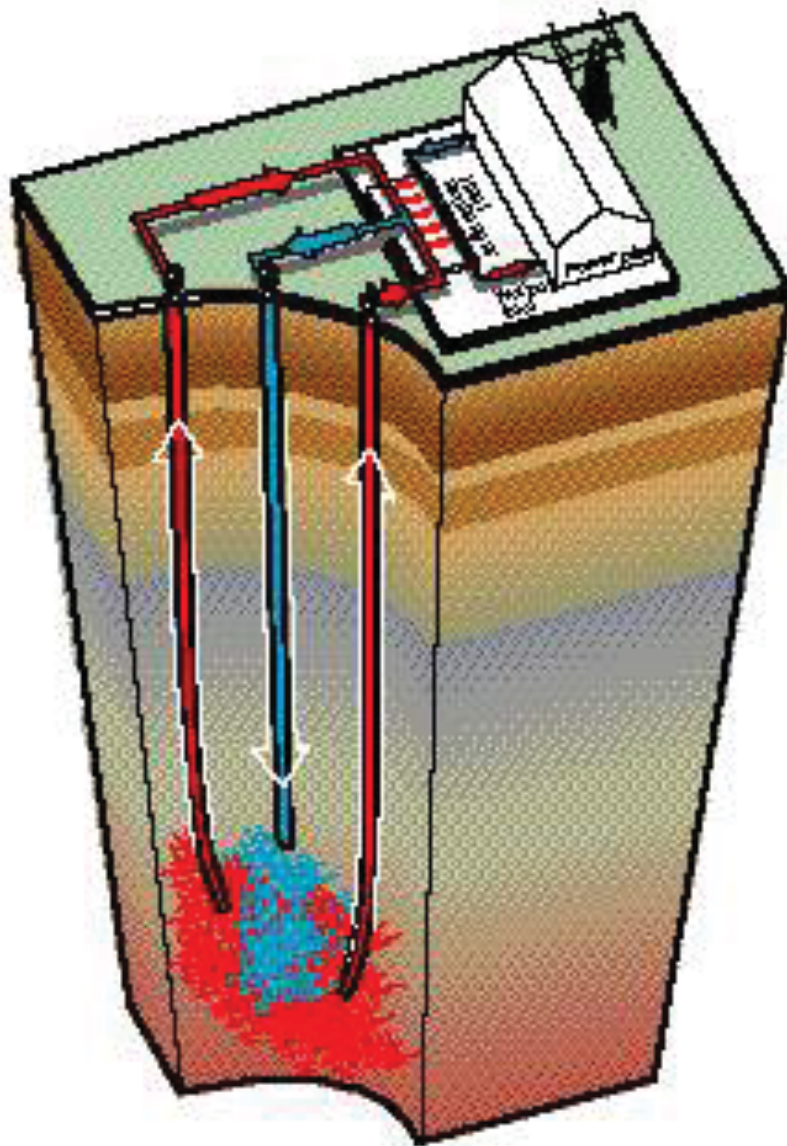


Figure 3 Schematic of HDR heat mining system [35]

Two types of techniques are related to solar power generation: concentrated solar power and photovoltaics, the latter of which will be introduced in the next section.

The concentrated solar power technique gathers solar power by mirrors and lenses (e.g. parabolic troughs) in the form of thermal energy within a concentrated small region, before conventional heat turbines are activated for power generation [36].

1.1.3.3. Chemical energy - biomass

Biomass refers to the live or just-dead organic material, which could be treated as fuels or industrial raw materials. The organic matter could be lignocellulose or converted biofuels (e.g. ethanol, methane, etc.) [37]. Burning of biomass is similar to that of fossil fuel, but the carbon cycle of the former is much shorter. Thus, biomass is regarded as a renewable energy. It could generate electricity in the same way as fossil fuel power stations or by electrochemical transformation during fuel cell operation, as discussed in Section 1.1.3.7.

1.1.3.4. Non-electromagnetic power generation technique

Power generation techniques introduced above all rely on the electromagnetic effect and hence alternating current (AC) [38, 39] would be created due to the configuration characteristics of conventional generators. However, in some special cases, electricity could be transformed directly from a range of energy types without the conversion to mechanical energy as an intermediate product. Power generated by these methods meet the demands for distributed generation (i.e. electricity generation in the neighbourhood of residence) [40], as it is usually on a small scale

[41] and in the form of direct current (DC). The rest of this chapter presents this type of power generation technique.

1.1.3.5. Photovoltaics

The photovoltaic (PV) effect is observed with some semiconductor materials, which could be applied to convert light energy directly into electricity [42]. Solar panels, an assembly of single power cells, are the core components of a photovoltaics system that can be installed either on the ground or top of roofs.

The mechanism of PV is given in Figure 4. By photovoltaic effect, electrons (negative charge) and holes (positive charge) are separated in pairs then transferred via n-type (n denotes negative) and p-type (p denotes positive) semiconductors respectively, in opposite directions within the circuit, where current flow is generated as a result [42]. Typical materials used for photovoltaic cells are monocrystalline silicon, polycrystalline silicon, amorphous silicon, cadmium telluride (CdTe) or copper indium gallium selenide (CIGS) [43].

Between 2000 and 2015, the global power capacity of PV was raised by a factor of 57, from 4 to 227 gigawatts (GW), with the capacity of total renewable energy growing more gradually by a factor of 9.2, from 85 to 785 GW [44].

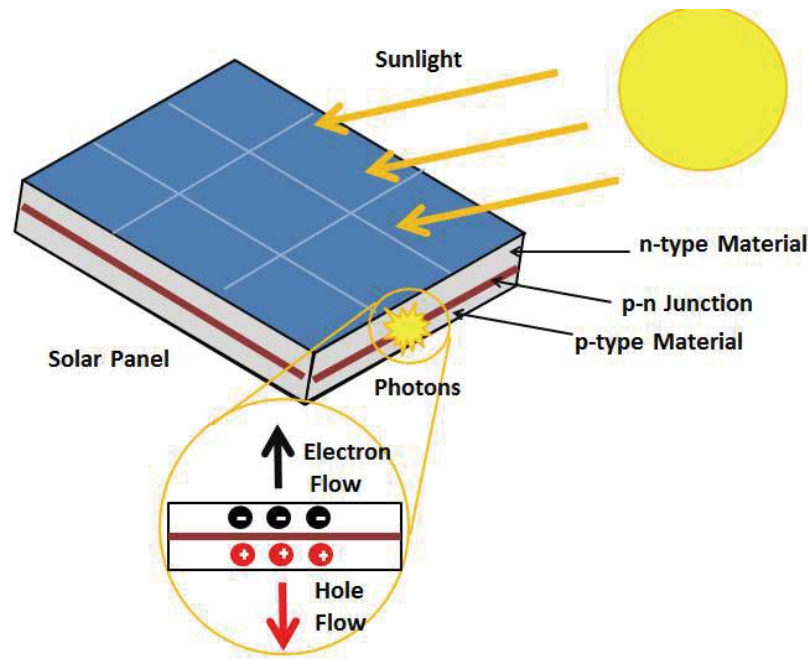


Figure 4 Mechanism of PV effect showing the direction of electron flows [45]

1.1.3.6 Thermoelectric power generation

Electric power could be alternatively produced if a temperature gradient exists between two terminals of a thermoelectric device [46]. The thermoelectric effect is a reversible phenomenon that was discovered independently by Seebeck in 1821 and Peltier in 1834 [47].

Figure 5 shows a schematic diagram of a small thermoelectric device. Thermal couple units are positioned on the top of the device, while being electrically connected to n-type and p-type thermoelectric semiconductors. Free electrons (e^-) and holes (h^+) are forced to move via separate types of semiconductors and a current path is formed. All the basic power generating units are electrically linked in series and thermally configured in parallel [48]. Thermoelectric materials that are able to create an adequate electrical potential include, for example, bismuth chalcogenides [49], lead telluride [50] and half Heusler alloys [51].

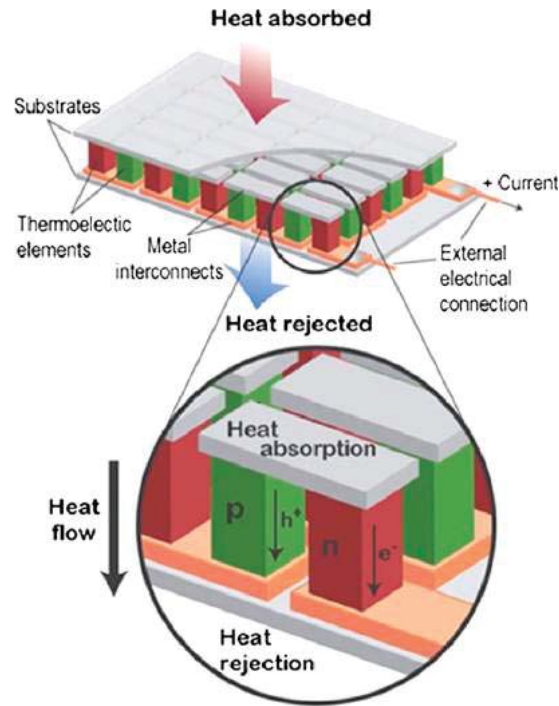


Figure 5 Schematic of a small thermoelectric device [52]

1.1.3.7. Electrochemical power generation – fuel cell

A fuel cell is a power generation device that converts chemical energy directly to electricity [53, 54]. The major difference between fuel cells and conventional batteries is the dependency on an external fuel supply, thus the working characteristics for the former are also similar to those of an engine [55]. Running on a continuous supply of fuels including hydrogen, methane and hydrocarbons, fuel cells should be able to output a constant current via electrochemical reactions. William Groove invented the world's first fuel cell in 1839 using an acidic electrolyte, together with two platinum (Pt) bar electrodes, to electrochemically transform hydrogen and oxygen to water while simultaneously generating external current flow [56].

	Anode	Electrolyte	Cathode
Internal Reformation Possible	$\xrightarrow{\text{H}_2, \text{CO}}$ $\xleftarrow{\text{H}_2\text{O}, \text{CO}_2}$	SOFC, 500 – 1000 °C $\xleftarrow{\text{O}^{2-}}$	$\xleftarrow{\text{O}_2}$
	$\xrightarrow{\text{H}_2}$ $\xleftarrow{\text{H}_2\text{O}, \text{CO}_2}$	MCFC, ~ 650 °C $\xleftarrow{\text{CO}_3^{2-}}$	$\xleftarrow{\text{O}_2, \text{CO}_2}$
Only External Reformation Possible	$\xrightarrow{\text{H}_2}$ $\xleftarrow{\text{H}_2\text{O}}$	AFC, ~70 °C $\xleftarrow{\text{OH}^-} \text{OH}^-$	$\xleftarrow{\text{O}_2}$
	$\xrightarrow{\text{H}_2}$	PAFC, 200°C $\xrightarrow{\text{H}^+}$	$\xleftarrow{\text{O}_2}$ $\xrightarrow{\text{H}_2\text{O}}$
	$\xrightarrow{\text{H}_2}$	PEMFC, ~70°C $\xrightarrow{\text{H}^+}$	$\xleftarrow{\text{O}_2}$ $\xrightarrow{\text{H}_2\text{O}}$

Figure 6 Summary of the most common types of fuel cell, the fuel and oxidising agents required, typical operating temperatures and the electrolyte ion transfer type and direction [57]

1.2. Types of fuel cells

A few representatives of the major fuel cell types are briefly introduced here, beginning with an informative diagram stating the distinctive features of them, Figure 6.

1.2.1. Phosphoric Acid Fuel Cell (PAFC)

The PAFCs were the first generation fuel cells for commercial use whose large-scale production can be traced back to the 1960s. The ion transfer media within the PAFC

electrolyte is in liquid form, which is always high-purity phosphoric acid (H_3PO_4) dispersed in a solid matrix (e.g. SiC). The electrodes for both air and fuel are made of porous carbon black, with a platinum coating as a catalyst [58].

As can be seen in Figure 7, a schematic diagram of a PAFC, the electrochemical reaction on the anode side is the oxidation of hydrogen, with the reduction of oxygen occurring on the cathode side. The charge carrier in the electrolyte region is hydrogen ions (H^+), coming from the hydrolysis of phosphoric acid.

PAFCs are more tolerant to carbon monoxide (CO) impurities than PEMFCs, therefore the required purity level of hydrogen within the reformed anode gas is more moderate, yet avoiding poisoning problems caused by carbon dioxide (CO_2).

Phosphoric acid is chemically stable at the cell working temperature (i.e. 150–210 °C), but solidifies at room temperature. Thus a maintained operation temperature is always applied on PAFCs to save the set-up cost and to meet non-stop working situations. PAFCs are also efficient at co-generation of electricity and heat, with the magnitude of both products comparable. Consequently, the low generation efficiency of pure electricity is one of the disadvantages of PAFC, plus its large space occupation. Another drawback is the relatively high production/maintenance cost, as a result of the precious metal catalyst and chemically aggressive electrolyte materials. Typical applications for PAFCs are stationary generators and vehicles (e.g. city buses) [58, 59].

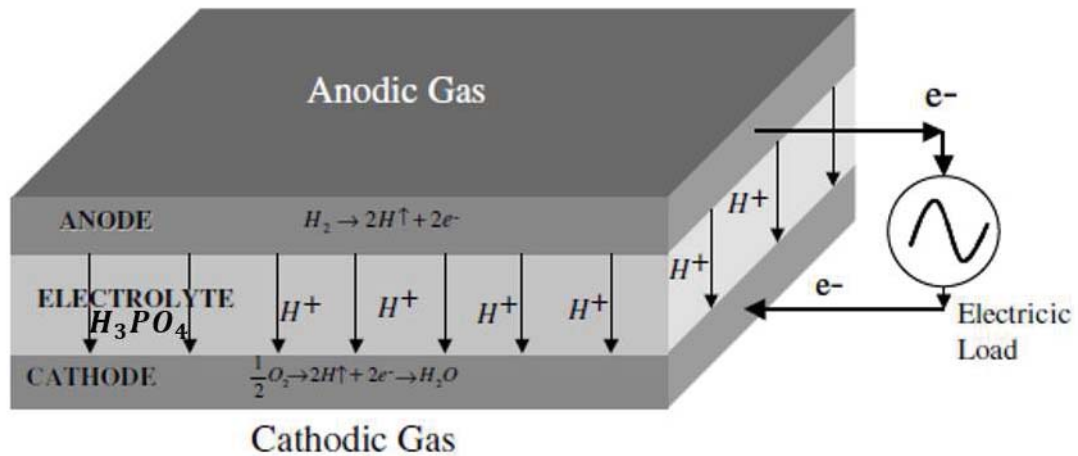


Figure 7 Schematic sketch of a phosphoric acid fuel cell [60]

1.2.2. Molten Carbonate Fuel Cell (MCFC)

The working temperature for MCFCs falls in the intermediate temperature range of 500-800 °C, where low-cost metallic catalysts become adequately active and production investment could be effectively reduced. Commercialised MCFCs were intensively developed chronologically after PAFCs, with the major technical leap for manufacture occurring in 1980s. The electrolyte of MCFCs consists of mixed molten carbonates, distributed uniformly through a solid ceramic base and providing carbonate ion (CO_3^{2-}) as the charge carrier during cell operation. The operation process of MCFCs can be found in Figure 8, indicating that although the overall cell reaction is still the combination of hydrogen and oxygen, with water generated, CO_2 and CO_3^{2-} participate in the separate electrode reactions with an entire cycle between them.

As the role of charge conductor is played by CO_3^{2-} , carbon-containing fuels are beneficial for the supplementation of CO_2 , as a thorough recycle of exhaust gas is

unrealistic. C-containing fuels such as carbon monoxide and hydrocarbons that may be poisonous to other types of fuel cells may be used and MCFCs also had the benefit that hydrocarbons could be pre-reformed internally to CO and H₂ before electrochemical reaction.

The disadvantages of MCFCs are mainly related to their high operation temperature. Life limiting examples are the poor long-term durability due to violent chemical activity and slow set-up process to reach the required temperature. Additionally, the electrolyte materials are also harmful for the environment.

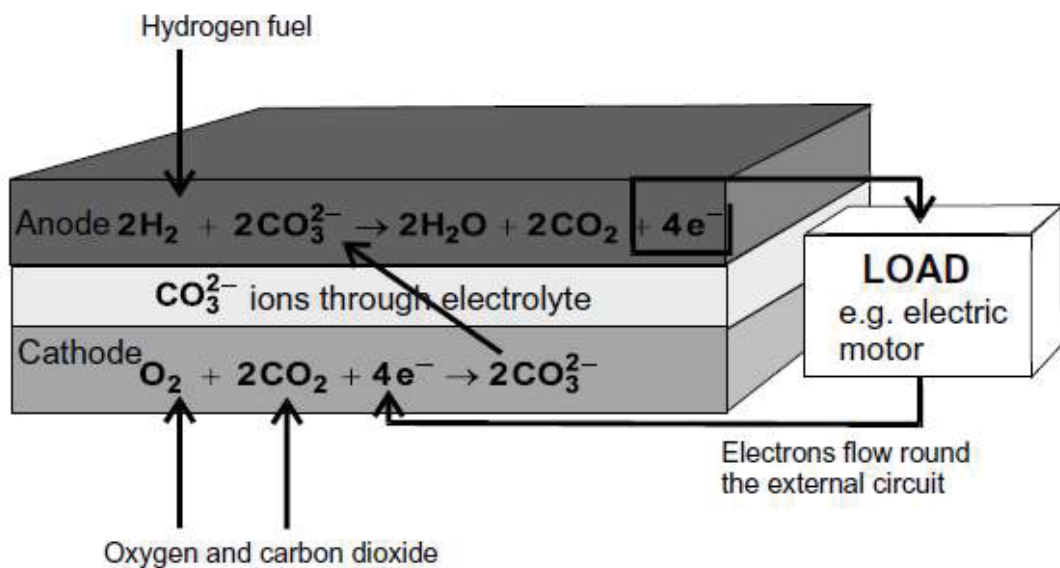


Figure 8 Operating process of a molten carbon fuel cell [61]

1.2.3. Proton Exchange Membrane Fuel Cell (PEMFC)

Initially designed by William T. Grubb in 1959 [62], PEMFCs operate in the temperature range of 50-150 °C. Both anode and cathode are formed of fibrous carbon, with noble metallic catalysts dispersed at the boundary between each

electrode and the electrolyte. The choice of electrolyte material could be a variety of proton-conducting membrane polymers, among which the most widely used one for current PEMFC production is Nafion, a sulfonic Teflon-based material manufactured by E.I. Du Pont in the middle of 1960s for use in the aviation field [63]. A hydrophobic treatment, normally a waterproof coating, is necessary at the end of both electrodes to guarantee efficient transfer of reactant to the catalytic region. A schematic diagram of a PEMFC can be seen in Figure 9.

Owing to their low operation temperature, PEMFCs have short setting up times and are easy to be integrated into multi-cell compacts. However, PEMFCs are also susceptible to the poisoning effect of CO, because the adhesion of CO on the surface of the catalyst would reduce the available reaction sites for hydrogen oxidation [64]. This cell type again requires a high purity of hydrogen supply and this increases the operation cost. Another problem to solve is the management of water, in order to reduce the resistance of fuel loading and to avoid flooding/freezing issues [65].

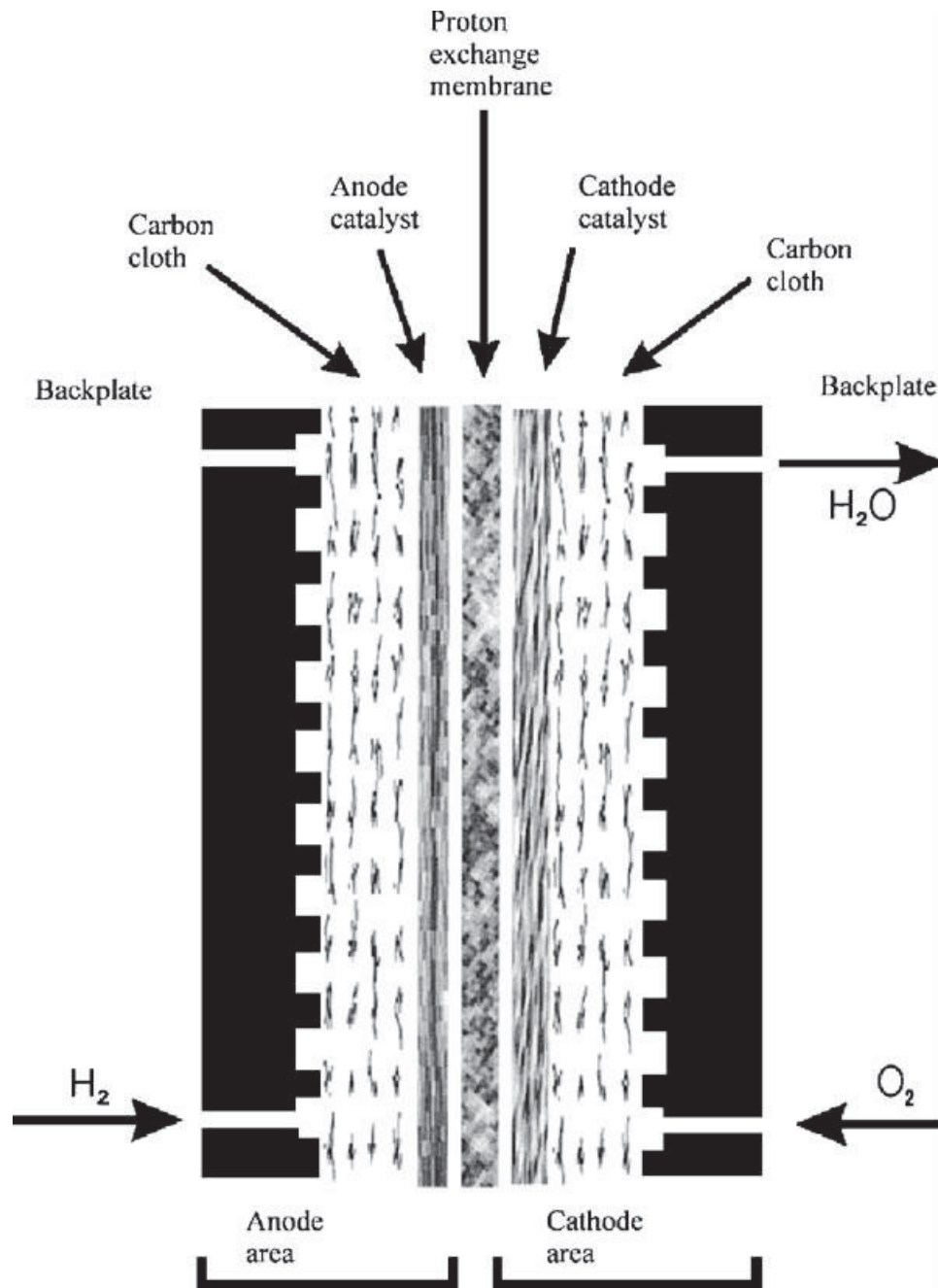


Figure 9 Essential components of a proton exchange membrane fuel cell [64]

1.2.4. Alkaline Fuel Cell (AFC) and Alkaline Exchange Membrane Fuel Cell (AEMFC)

The AFC was described by Reid [66, 67] in 1902 and Noel [68] in 1904. In the 1960s, AFCs were applied by NASA in its Project Apollo spaceflight missions. The most

recent AFC fabrication technology could lower the cell operating temperature down to the range of 25-75 °C.

The electrolyte of AFCs is usually a porous matrix saturated with aqueous potassium hydroxide (KOH) [69], as shown in Figure 10. During operations, AFCs can be poisoned by CO₂ if the anode gas (direct fuel or reformed organic fuels) contains a certain level of CO, as KOH is prone to be transformed to potassium carbonate (K₂CO₃), which blocks the ion transfer path [70, 71]. Thus the requirements for highly pure hydrogen and oxygen raise the operation cost of AFCs.

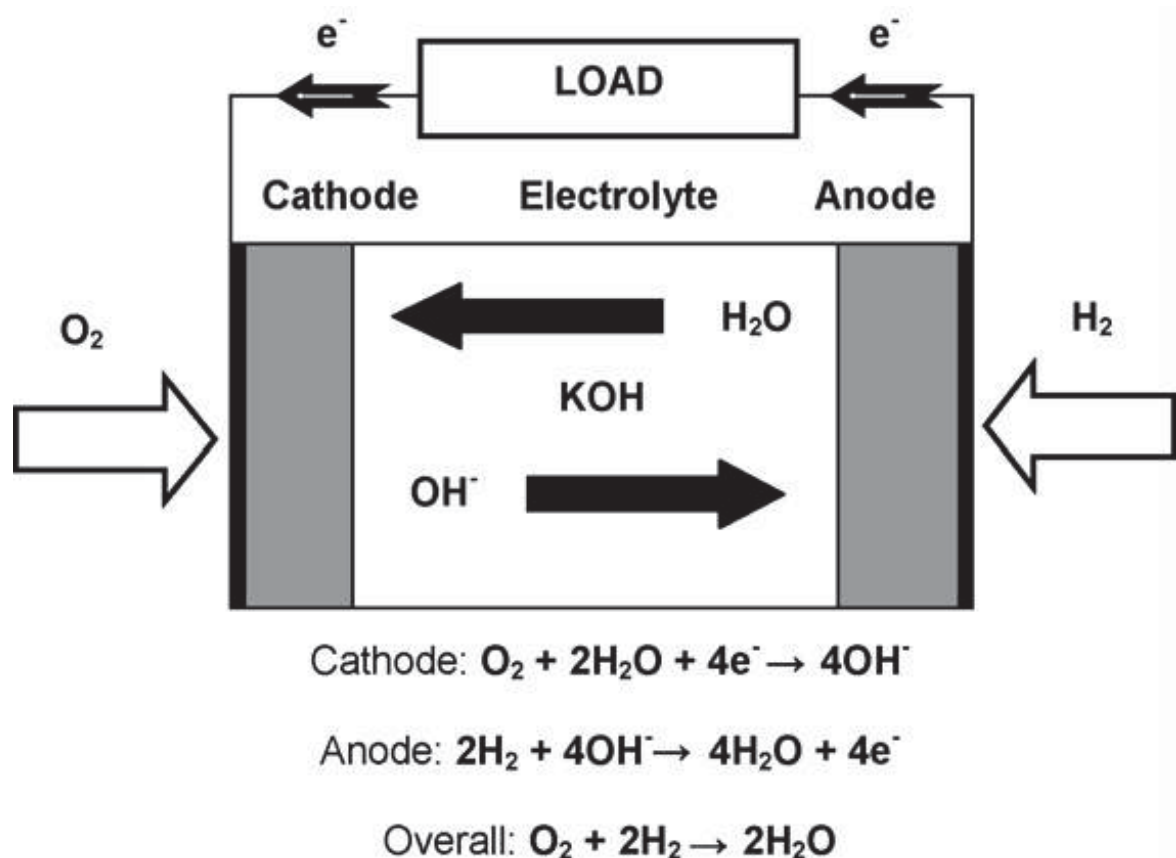


Figure 10 Fundamental layout of an alkaline fuel cell [72]

Although the power transformation efficiency of AFCs is the highest (~70%) among all fuel cell types, research work was gradually suspended worldwide due to some inevitable drawbacks. Besides the sensitivity to CO₂, the fabrication cost for AFCs could not be effectively controlled as they require electrodes and catalyst made of precious metals. Moreover, the lifetime for cell operation is only a few thousand hours, considering the current required lifetime for commercial fuel cells (i.e. 4,000 h for mobile application and 40,000 h for large stationary application) [69].

The concept of the AEMFC was proposed in 2005 to overcome the drawbacks of AFC mentioned above [73]. With the existence of an anion-exchange electrolyte membrane (Figure 11), which is made of a polymeric alkaline material, AEMFCs could be fuelled by carbon-containing organics, as the entry of CO₂ into the electrolyte is constrained. Researchers have investigated methods to reduce the electrode/catalyst cost. The major technical issue of AEMFCs is the effective ionic contact between the membrane and electrodes [74].

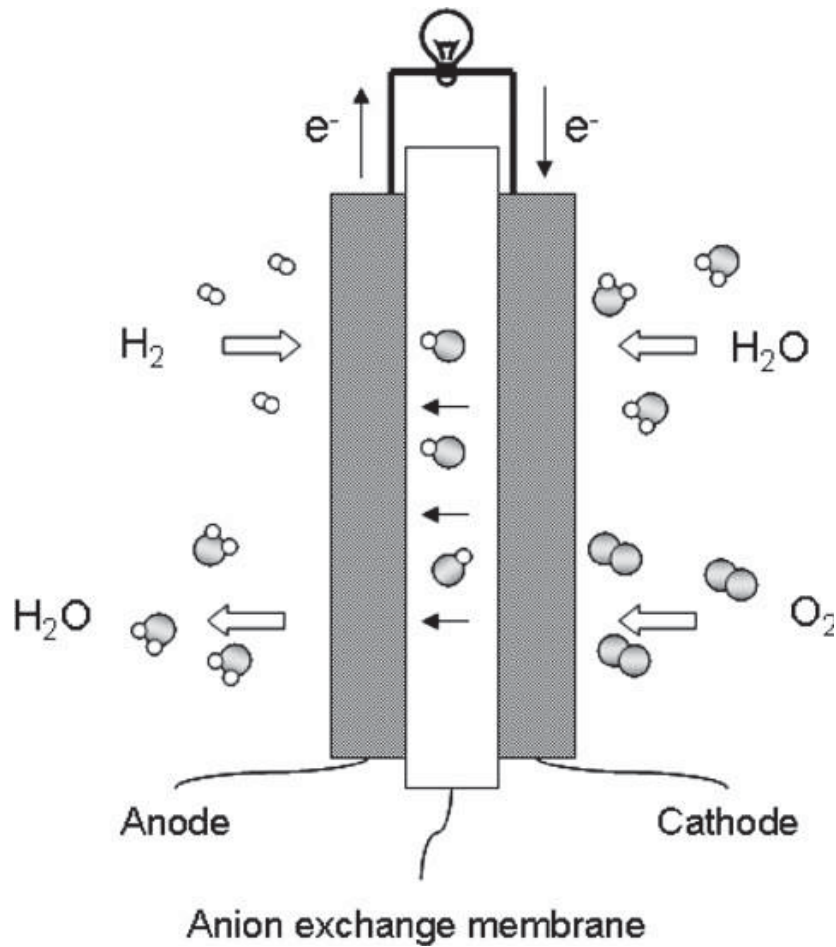


Figure 11 Schematic of an alkaline fuel cell with an anion-exchange membrane electrolyte [74]

1.2.5. Solid Oxide Fuel Cell (SOFC)

Solid oxide fuel cells (SOFC), which were first investigated intensively in 1960s, could be regarded as the third generation of commercialised fuel cells. Fuelled by hydrogen or reformed hydrocarbons, they work efficiently at high temperature range (700-1000 °C) to generate electricity at sub kilowatt level while providing heat energy for system heating and external application [75]. Compared to low temperature (100-200 °C) fuel cells (AFC, PEMFC and PAFC) and intermediate temperature (500-800 °C) MCFC,

SOFCs have higher power generating efficiency as a result of high temperature reactivity. Additionally, the flexibility of SOFC is a significant advantage for both stationary and mobile use [76], because all the components of the single cell are solid and can be installed easily. The description above also reveals the clean and noiseless nature of SOFCs, which is also a feature of all the types of fuel cells, as no ignition progress is required during the cell operation. Owing to the features of SOFC layout, the heat waste could be recaptured for a second cycle of power generation [77]. SOFCs are described in further detail in Section 1.4, 1.5 and Chapter 2.

1.3. Fuel types

1.3.1. Direct hydrogen

The most obvious advantage of applying hydrogen directly as a fuel is its non-hazardous by-products, as the only resultant of electrochemical reaction gives water. Compared to fuels that contain carbon (C) or sulphur (S), hydrogen could effectively avoid the emission of its combustion or electrochemical waste that may cause environmental problems such as the greenhouse effect gases or acid rain [78]. Nonetheless, the inconvenience of direct acquirement from natural energy reserves makes the fuel supply of pure hydrogen for fuel cell operations a high-cost activity. Traditional electrolysis of water would involve consumption of electricity [79], which contributes to the total cost and a tough evaluation of the overall sustainability by the energy cycle.

Presently, the most commercialised method to produce hydrogen is the conversion from fossil fuels, contributing to 96% of global hydrogen production [80]. This means

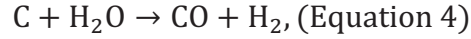
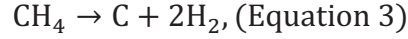
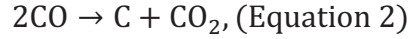
the current generation of hydrogen is still far from renewable and clean, resulting from the consumption of limited reserves of natural gas, oil and coal, plus the potential emission of CO₂ [81]. Several technologies could be developed to assist the hydrogen production to become more environmentally protective, such as the use of renewable hydrocarbons as hydrogen sources and the supplementary process of carbon capture and sequestration. Likewise, a viable hydrogen storage technique is also imperative [82] to eliminate the necessity of local hydrogen production.

1.3.2. Methane and hydrocarbons

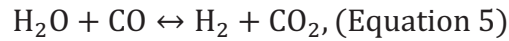
As methane (CH₄) is the major content of natural gas, the national gas network could be used for the immediate supply of fuels [83] for some types of fuel cells, such as SOFCs. The problems related to the utilisation of methane is similar to those of hydrogen production, namely the depletion of fossil fuel storage and the release of greenhouse gases. Renewable sources for CH₄ includes the decomposition of biomass [84] and direct collection from the natural resources such as marshes.

Hydrocarbons with multiple carbon atoms in their formula could be utilised as fuels too. An inevitable issue for direct fuelling with hydrocarbons is the carbon deposition onto the catalyst surface [85, 86], due to the incomplete oxidation of low-valence carbon into simple substances. Carbon deposition could be induced by the Boudouard reaction [87] or pyrolysis [88], as given in Equation 2 and 3 respectively, and removed by steam gasification (Equation 4). The existence of such deposition structures would inhibit the contact between anode gas and the active reaction areas. The hazard of carbon deposition is like that of the poisoning problem by CO₂, namely

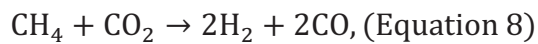
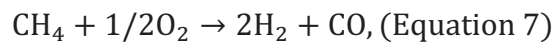
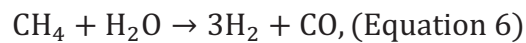
reduction of the electrochemical activity exhibited by the anode oxidising process, leading to poor long-term cell durability.



Methane and hydrocarbons, especially a liquid form for the latter, are hard to participate in the electrochemical oxidation directly at the boundary between anode and electrolyte. A pre-reforming process is necessary to convert the organic fuels into gaseous H_2 or CO , which would be converted again to H_2O and CO_2 later via electrochemical reactions. H_2 and CO could also be mutually converted via the water gas shift reaction [89], which is a competitive process against the anode electrochemical reaction (Equation 5).



When fuelling with methane, steam reforming is the most common process for the purpose of pre-oxidizing, which is shown in Equation 6. Other similar routes are partial oxidation and dry reforming [90], as shown in Equations 7 and 8 respectively.



Internal reforming is possible for fuel cells like SOFCs, as the high operation temperature is adequate for pre-reforming, while an additional external reforming

chamber is essential for fuel cells working at low temperatures, such as PEMFCs and AFCs. A coking issue is related to internal reforming, as carbon may be produced via Equation 4 on the anode to inhibit the gas transfer.

1.4. SOFC configurations

A single cell only generates limited electrical power and should be integrated into a multi-cell stack to output adequate electricity. The conventional layout of SOFC stacks are combinations of planar or tubular single cell units. The resulting cell stacks have a regular geometry (e.g. cubic) for the convenience of commercial and military installations.

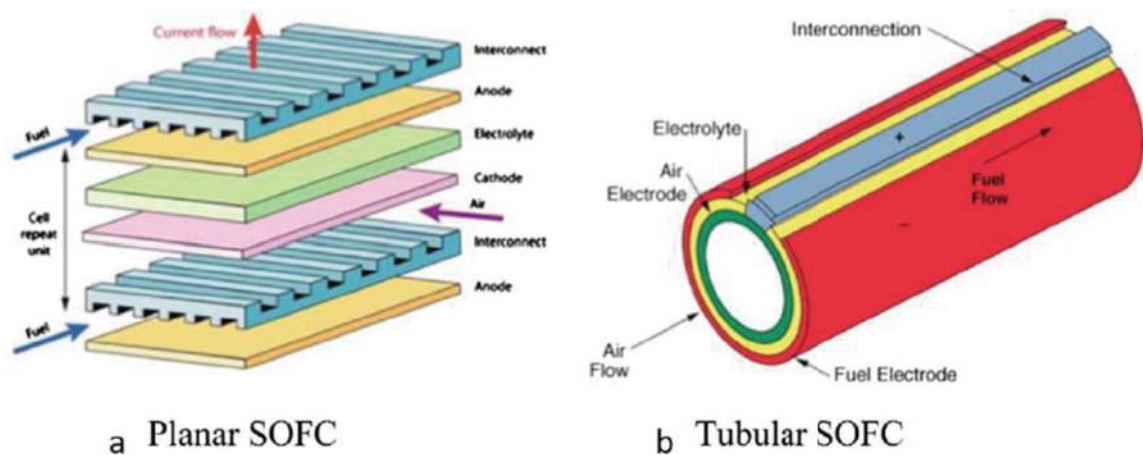


Figure 12 Typical designs for (a) planar and (b) tubular SOFCs [91, 92]

1.4.1. Planar Design

Figure 12a shows a representative layout of a planar SOFC design. In this type of cell configuration, all the cell components occupy a flat 2-dimensional shape.

Symmetrical and ordered fuel channels are designed to be near the anode and cathode surfaces. Due to its regular geometry of single units, few additional structural components are required to build up the whole SOFC stack. Fuel channels are even tactfully integrated into the conductive interconnection materials in Figure 12a.

The relatively lower cost of planar SOFC fabricated by tape casting and screen printing [93] makes this design the most commercialised one in the current market, but the sealing issue is a limitation as a result of the large area occupied by the fuel outlet.

1.4.2. Tubular Design

The tubular SOFC unit shown in Figure 12b, was first designed and manufactured in 1970s by Siemens Westinghouse [94]. The single units are separate from each other and additional structural components are required to construct a regularly shaped cell stack. In spite of this, the fabrication technique of the tubular design has become fairly mature [95]. Some tubular cells are created with the anode structure on the inside while others have a cathode structure inside.

The design shows better durability after thermal cycling than planar systems. The tubular shape also promotes easier sealing compared to that of the planar design [96], but it has a longer electron travel path from anode to cathode side, which

hinders the improvement of power density. Another challenge for tubular SOFCs is the current collection due to both inner and outer being curved surfaces.

1.4.3. Micro-tubular Design

To minimize the problems of tubular SOFCs, the concept of micro-tubular SOFC (mSOFC) was put forward in early 1990s by Kendall [93]. For micro-tubular design, the outer radius can be decreased to no more than a few millimetres and the wall thickness, less than 1 mm. This design can significantly increase the power density by shortening the length of the electron travel path. Smaller dimensions of the tubes are also beneficial for better thermal shock resistance and shorter set-up time [97]. Also, mobile applications of SOFC such as portable chargers become more feasible [98].

1.5. SOFC cell components

1.5.1 Components for the electrochemical reaction

The three main components for micro-tubular SOFCs are anode, electrolyte and cathode. Table 1 shows the basic requirements for each component. Materials selections for different cell components will be given in the next chapter.

1.5.2 Interconnects

Another important cell component is the interconnect material, which conducts electrons between single SOFC units. It has the same basic requirements as the 3 major cell components, as listed above. Popular interconnect materials are ceramic

and metallic materials [99]. Cheap metallic interconnects can save the fabrication cost but their high-temperature corrosion resistance is unfavourable. In comparison, precious metals and Cr-based ceramics are more widely studied for interconnect materials [100].

Table 1 SOFC main components and their capabilities

Cell components	Conductivity requirements	Porosity requirements	Stability requirements
Anode	High electronic conductivity	Porous structure for fuel permeability	Adequate chemical stability and
Electrolyte	High ionic conductivity	Dense structure to avoid gas transport [101]	thermal expansion
Cathode	High electronic conductivity	Porous structure for oxygen permeability	match at operation temperatures with other cell components
Interconnects	High electronic conductivity	Porous if any gas phase is supposed to reach the electrode through the structure	High melting point to retain physical integration at operation temperatures

Chapter 2 Literature review

2.1. mSOFC Materials

Generally, the materials used for mSOFC fabrication are also used for other types of SOFC. Among the possible mSOFC anode materials, nickel is the most frequently used due to its low cost and balanced performance [102]. Compounds of Ni, most frequently in the form of NiO are used before the cell reduction process. The NiO powders are always mixed with electrolyte powders [103] to produce anode layer (e.g. NiO mixed with yttria stabilized zirconia [104] or NiO mixed with gadolinia doped ceria), mainly for the purpose of thermal shrinkage match during heating process between anode and electrolyte, as well as preventing the sintering of nickel and consequent reduction in porosity. A reduction process is required after cell fabrication, where NiO would be reduced to Ni to guarantee sufficient electronic conductivity and create the required level of porosity.

There are a number of candidates for the electrolyte and cathode materials [105, 106]. Some commonly used mSOFC materials are shown in Table 2. Recently developed materials, for example lanthanum strontium cobalt ferrite (LSCF) [107-110], are favourable for cell operations at lower temperatures, as they can maintain adequate electrochemical activity [111] and conductivity when the working temperature range is down to 300-400 °C [112]. In order to solve the problems related to the application of these materials that performs well at intermediate temperatures, assistive manufacture processes, on the basis of those of the

electrodes and electrolyte, are sometimes applied. For instance, scandium stabilised zirconia (ScSZ) electron blocking layer has been inserted between electrolyte and electrodes [113] when gadolinium doped ceria (GDC) is chosen as electrolyte material, and GDC layer was sandwiched to avoid reaction of the LSCF in direct contact with YSZ electrolyte [114]. The most frequently used performance criteria for manufactured mSOFCs are Open Circuit Voltage (OCV) and surface power density, which will be detailed in Chapter 3.

Table 2 Most frequently used materials for mSOFC component manufacture [1]

Acronyms	Chemical formula	Function
YSZ	$(\text{ZrO}_2)_{1-x}(\text{Y}_2\text{O}_3)_x$, $0.08 < x < 0.1$	Electrolyte
ScSZ	$(\text{ZrO}_2)_{0.89}(\text{Sc}_2\text{O}_3)_{0.10}(\text{CeO}_2)_{0.01}$	Electrolyte
GDC, SDC	$\text{Ce}_{0.8}\text{Gd}_{0.2}\text{O}_{1.8}$, $\text{Ce}_{0.8}\text{Sm}_{0.2}\text{O}_{1.8}$	Electrolyte, barrier layer
LSGM	$\text{La}_{0.9}\text{Sr}_{0.1}\text{Ga}_{0.8}\text{Mg}_{0.2}\text{O}_3$	Electrolyte
LSO, LGO	$\text{La}_{10}\text{Si}_6\text{O}_{27}$, $\text{La}_{10}\text{Ge}_6\text{O}_{27}$	Electrolyte
LSM	$\text{La}_{0.8}\text{Sr}_{0.2}\text{MnO}_3$	Cathode
LSF	$\text{La}_{0.8}\text{Sr}_{0.2}\text{FeO}_3$	Cathode
LSC	$\text{La}_{0.8}\text{Sr}_{0.2}\text{CoO}_3$	Cathode
LSCF	$\text{La}_{0.6}\text{Sr}_{0.4}\text{Co}_{0.2}\text{Fe}_{0.8}\text{O}_{3-\delta}$	Cathode

Table 2 (Continued)

Acronyms	Chemical name	Function
PMMA	Poly methyl methacrylate	Pore former
—	Acrylic resin	Pore former
—	Graphite	Pore former
—	Starch	Pore former
PVC spheres	Polyvinyl chloride	Pore former
PAA	Polyacrylic acid	Dispersant
Beycostat	Phosphate ester	Dispersant
PVA	Polyvinyl alcohol	Binder
PVB	Polyvinyl butyral	Binder
DOP	Diethyl phthalate	Plasticizer
DBP	Dibutyl phthalate	Plasticizer
—	Ethanol	Solvent
—	Isopropanol	Solvent
—	Cyclohexanone	Solvent
—	α -Terpineol	Solvent
MEtK	Methyl ethyl ketone	Solvent

2.2. Fabrication techniques

Any of the three main functional layers (i.e. anode, electrolyte and cathode) of mSOFC can be manufactured as structural support [115], which then necessitates a greater thickness than the other two. Recent works are mainly focused on anode supported tubes, as they have better ionic conductivity and less electrolytic loss

owing to supporting a thinner electrolyte layer. As a result, anode supported mSOFCs can operate at relatively low temperatures [116].

2.2.1 Extrusion – support layer

The fabrication process of mSOFCs always starts with the shaping of the support part. Isostatic pressing (cold or hot) is a competitive technique to produce a uniform membrane tube for subsequent sintering (i.e. heat treatment for powder consolidation [117]) and deposition of additional cell components, compared with other powder pressing methods. However, production repeatability is usually poor when referring to pressing, as some characteristics of the green body such as shape and size, are not reproducible [1]. Thus production rate is low in this case, limiting the prospects of scaling up from laboratory work to factory fabrication. Although some other techniques such as gel casting and injection moulding are also practical for support fabrication, extrusion is considered the most commonly used method, because of its relatively high efficiency and low cost when generating homogeneous density and complex cross-sectional geometries [118].

2.2.1.1. Conventional extrusions

Thermoplastic extrusions, during which relatively rigid material compounds are heated to reach a softened plastic state for rapid shaping, are frequently used for mass production at an industry scale. However, for lab scale research, cold solvent based extrusions with a room-temperature plastic precursor are predominantly adopted for the controllability during systematic research. Ram extrusion is frequently applied for mSOFC fabrications, as it can provide an adequate product strength at a

high yield rate [119]. For all extrusion routes, powder mixtures (at least containing ceramics and polymer binder) have to be prepared first by high energy mixing processes and/or sufficiently long dispersion time with solvent. The homogeneous powder mixture will then be fed into an extrusion die, with a usual pre-formation into the viscous paste form [120]. Despite a low fraction in the powder formulation (typically 1 wt %), plasticizer is another important component with the function of forming a non-sticky compound and avoid any blocking or adhesion problems when passing through the die. Dispersant is occasionally added to the powder mixture to guarantee a well-distributed suspension and homogeneity of the green body. If the anode layer is designed to be the mechanical support, pore formers such as graphite or corn starch can be added at an appropriate concentration to enable high gas permeation around the fuel channel during operation. Typical organic polymer constituents involved in powder formulations are also listed in Table 2.

Sammes' group from the USA has developed plastic ram extrusion since 2004. They have already performed optimisation studies to develop the extrusion quality and realised ideal shaping of the tubes, i.e. constant annular cross section and straight in the longitudinal extrusion direction [116]. Under this premise, they state that extrusion die design is one of the important considerations of their work to unify the pressure distribution and force materials inside the extrusion die to the outlet as smoothly as possible [121]. In addition, they found that the drying process after extrusion is a crucial period for the shape retention and the prevention of microcrack formation, thus specially designed tube holders were used for drying, as shown in Figure 13. A power density of 1.31 W cm^{-2} at $550 \text{ }^{\circ}\text{C}$ [122] was realised in 2010, which is the maximum ever reported by the Sammes' group [123].

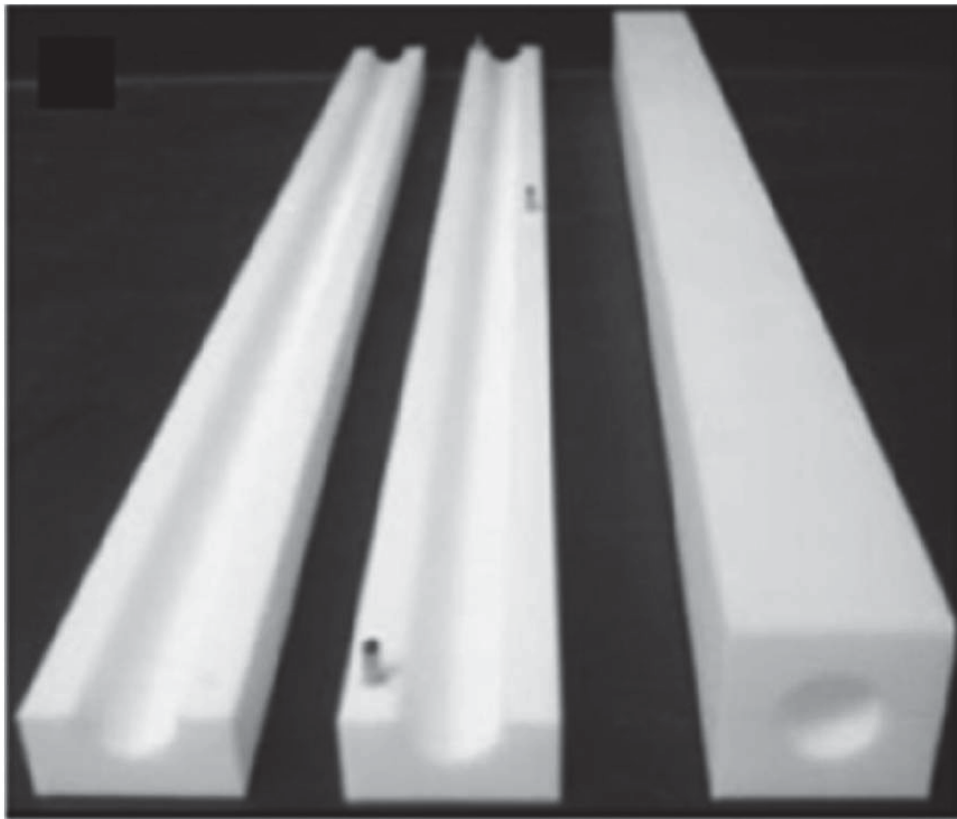


Figure 13 Picturing of C-shaped plastic tube holders [124]

Another group working in Japan and led by Suzuki has done considerable works on conventional ram extrusion. They mainly focused on lowering operation temperatures down to the intermediate range while maintaining sufficient cell performance. They managed to fulfil this purpose by alternating electrolyte material from YSZ to the better ionic conducting GDC [125], as well as promoting the connection between electrodes and current collectors [126]. Other routes to improve the cell performance developed by this group are the promotion of anode porosity [127], the reduction of electrolyte thickness [128] and the redesign of bundled cell stacks (i.e. a three-dimensional integration of a number of single cells to generate high electric power) [129]. An attempt to minimise the fabrication cost by performing anode-electrolyte co-

sintering was also made [130]. A reported power density of 1.29 W cm^{-2} at 600°C was the highest they achieved in all their published papers [131].

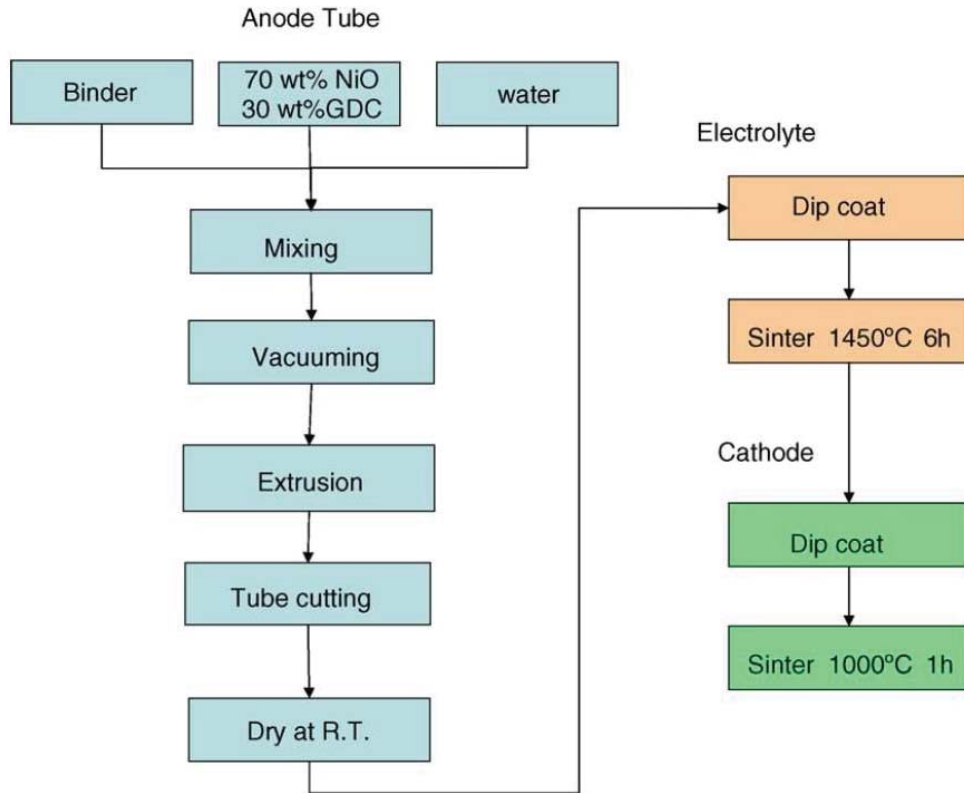


Figure 14 Single cell fabrication process by Suzuki et al.

According to the reports from the groups mentioned above, some conclusions can be drawn. For example, there is a positive correlation between gas permeability and anode porosity (by volume fraction) in the range 30-50% of the latter, with a saturation gas delivery efficiency at 50% porosity. Furthermore, a thickness of about $10 \mu\text{m}$ of the thin electrolyte layer is beneficial to both ionic conductivity and gas tightness. A temperature of 1450°C is shown to be most appropriate for anode-electrolyte co-sintering. The laboratory work carried out in this project will be based on these conclusions while seeking for further development of single cell fabrication.

2.2.1.2. Phase-inversion technique

The so-called phase inversion method is a newly initiated process for tubular support fabrication. This process can be regarded as a variation of conventional ram extrusion and is also called dry-jet wet extrusion [132]. Instead of a solid or quasi-solid extrusion compound being used, a liquid spinning suspension is utilised for wet extrusion, while phase-inversion (solidification) process occurs subsequently after the extrudate reaches an external coagulation bath, induced by a solvent-non-solvent exchange process, the mechanism of which is illustrated by a ternary phase diagram as shown in Figure 15 [133]. The terminology hollow fibre is used here to describe the green body produced by this type of phase-inversion method, as extremely thin annular structures ($OD < 1$ mm and wall thickness around $200\text{ }\mu\text{m}$) can be obtained, which should increase the power density through the mechanisms mentioned earlier. The particular advantage of hollow fibre over SOFC tubes fabricated by other techniques is the graded microstructure through the component thickness. By adjusting the fraction of the non-solvent component (i.e. ethanol) in the spinning suspension, fine graded anode layers with varied levels of porosity can be tailor-made for both good gas permeation and high electrochemical reactivity (i.e. high porosity anode layer in contact with the fuel channel, while a low porosity anode layer close to the electrolyte layer can be formed). The high porosity anode layer has a so-called finger-like porous structure, which is desired for gas delivery [134]. The low porosity sponge-like dense layer near the electrolyte provides longer and more active triple phase boundaries (i.e. the region between the electrode, the electrolyte and a gaseous fuel) (TPB) [135]. The performance of such tubes was significantly higher than that of conventionally solid extruded tubes when electrolyte thickness is

reduced, which will be described later in this chapter (Section 2.3). To sum up, the phase inversion technique is a promising fabrication process for mSOFC support and has potential of commercialisation from laboratory scale.

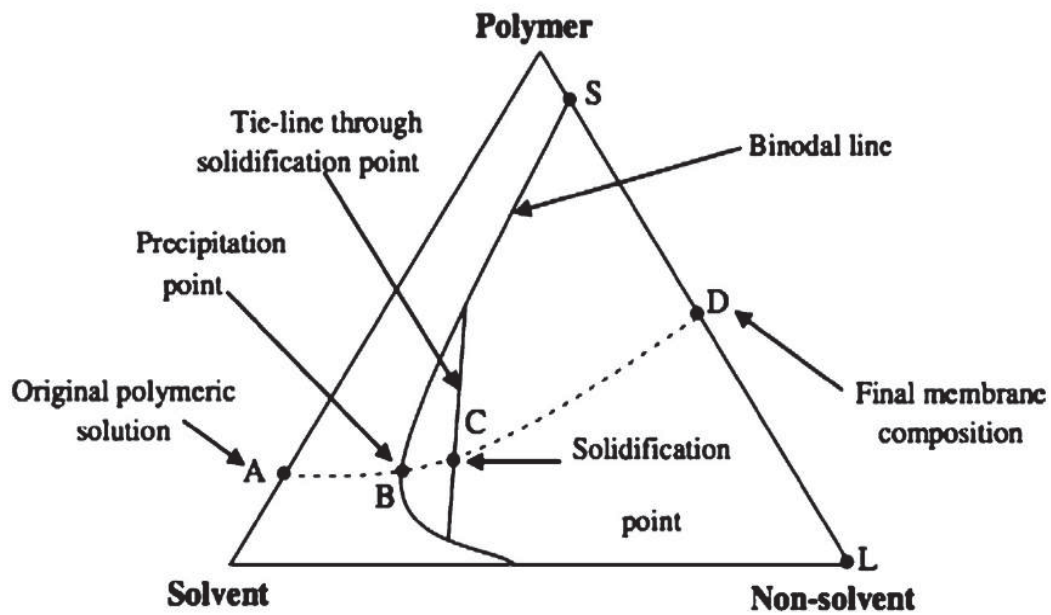


Figure 15 Schematic ternary phase diagram of polymer/solvent/non-solvent during polymeric membrane formation from Point A to Point D [133]

2.2.1.3. Co-extrusion

The conception of co-extrusion was brought forward at the beginning of this century to cut down the production cycle [136], although there was no performance shift in the cells and new technical obstacles were encountered by doing this. Researchers who had previously worked on conventional extrusion and hollow fibre techniques have developed co-extrusion experience for both routes for the purpose of more rapid production. During a co-extrusion process, at least two layers are extruded simultaneously to form a multi-layer membrane precursor functioning as the support

structure. Some of the problems related to co-extrusion are rheology mismatch of extrusion pastes between different layers, as well as delamination while co-sintering. To date, co-sintering is only a realistic proposition for anode-electrolyte co-production because good adhesion can be achieved between the two layers when the furnace temperature is as high as 1500 °C. However, its feasibility is underdeveloped for the cathode-electrolyte co-firing as a result of significant thermal expansion mismatch between the materials.

Based on the Benbow-Bridgwater six parameter model [137], the extrusion of ceramic pastes through dies with circular cross section and regular die entry at a certain velocity can be described by Equation 9.

$$P = P_1 + P_2 = 2(\sigma_0 + \alpha V^m) \ln\left(\frac{D_0}{D}\right) + \frac{4L}{D} (\tau_0 + \beta V^n), \text{ (Equation 9)}$$

where P is the total pressure drop and P_1 and P_2 are the pressure drop due to convergent flow and plug flow respectively. α is a velocity-dependent factor for the convergent flow, β is the velocity-dependent factor for parallel flow, n and m are exponents, σ_0 is the paste bulk yield value, τ_0 is the characteristic initial wall shear stress of the paste, D_0 and D are the diameters of the barrel and of the die, respectively, L is the die-land length and V is the extrudate velocity. According to pressures for different pastes derived from this model, the applicability of co-extrusion can be assessed.

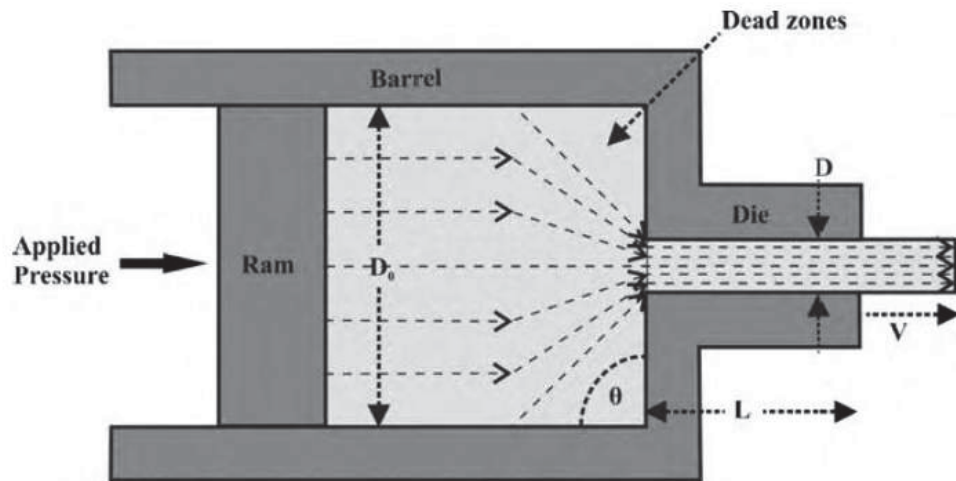


Figure 16 Schematic diagram of ram extrusion [138]

Powell at the University of Birmingham manufactured five-layer mSOFC half cells after adequate rheology analysis in 2010. The cell consisted of four layers of Ni-YSZ with reducing Ni volume ratios and an YSZ electrolyte layer. In this work, pressures required for different pastes were predicted and measured at different extrudate velocity with L/D ratios ranging from 1 to 8. Large pressure mismatch around 10% appeared with short die length ratio $L/D = 1$, indicating the rheology mismatch is more severe at the die entry than that occurs when the pastes flow through the die land. Such mismatch between pastes will cause delamination or other types of deformation, as it was shown that only pressure differences within 5% could be tolerated without formation of flow defects [139]. High L/D ratio and moderate extrudate speed (3 mm/s) were applied for multi-layer co-extrusion of fuel cell tubes, with good adhesion between adjacent layers being obtained [138].

One of the most successful research teams for phase-inversion co-extrusion is from Imperial College London, previously led by Li. They started from single layer electrolyte supported cell fabrication [140] and gradually their work expanded into

anode supported extrusion and multi-layer co-extrusion of NiO-GDC/GDC based half cells. Recently, the team successfully produced triple-layer (dual anode layers and an electrolyte layer) hollow fibres during single extrusion [141] by using a four-orifice spinneret, although problems were encountered for gas tightness due to the existence of finger-like microvoids in the electrolyte layer. The milestone of their previous work was the development of dual-layer hollow fibres with high anode porosity and superior cell performance [142]. The success based on the reduction of the electrolyte thickness [143]. Weight fractions ranging from 5% to 20% of ethanol were applied to spinning suspensions for pore forming in this work, and relatively thick electrolytes were produced to guarantee desirable ionic conductivity and sufficient gas tightness. The main characteristics of the best-performing tubes were long finger-like voids occupying 70% of the anode thickness (by adding 5% of ethanol) and 15 μm electrolyte thickness. These features gave the cell a power density of 2.32 W cm^{-2} at 600°C [144], which is the best cell performance ever reported in the literature.

Table 3 shows the structure information and major performances of mSOFCs mentioned in recent published papers, with the support layer fabricated by conventional or phase inversion based extrusions.

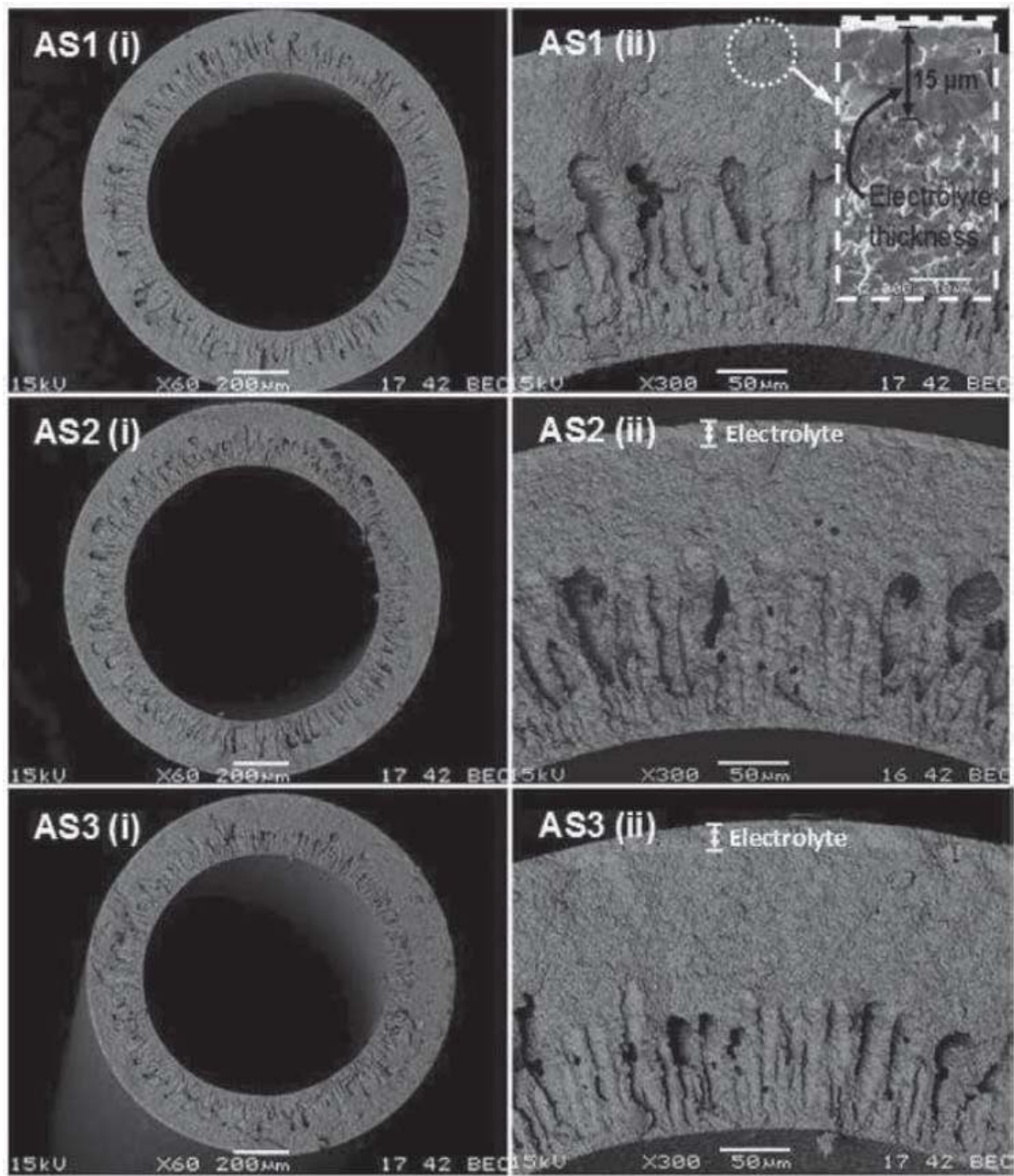


Figure 17 SEM images of the dual layer hollow fibres with increasing ethanol content from 5 wt. % to 20 wt. % [142]

Table 3 Single cell parameters for recently developed mSOFCs by conventional or phase-inversion extrusions

Fabrication method for support layer	Support component	Anode	Electrolyte	Cathode	Cell diameter (mm)	Fuel stream	Temp .(°C)	OCV (V)	Max. power density (W cm^{-2})	Ref.
Plastic mass ram extrusion	Anode	Ni-CGO	CGO	LSCF-CGO	1.60	Humidified $\text{H}_2\text{-N}_2$	570	0.84	0.35	[126]
Plastic mass ram extrusion	Anode	Ni-CGO	CGO	LSCF-CGO	0.80	Humidified $\text{H}_2\text{-N}_2$	550	0.85	0.35	[125]
Plastic mass ram extrusion	Anode	Ni-CGO	CGO	LSCF-CGO	1.48	Humidified $\text{H}_2\text{-N}_2$	550	0.78	0.4	[145]
Plastic mass ram extrusion	Anode	Ni-ScSZ	ScSZ	LSCF-CGO-Ag	1.80	Humidified $\text{H}_2\text{-Argon}$	650	1.06	1.06	[146]
Plastic mass ram extrusion	Cathode	Ni-CGO	CGO	LSCF-CGO	2.26	Humidified $\text{H}_2\text{-Argon}$	600	0.70	0.16	[147]
Plastic mass ram extrusion	Cathode	Ni-CGO	ScSZ	LSM	1.60	Humidified H_2	800	>1.0	0.31	[148]
Supplied by Adaptive Materials Inc. USA	Anode	Ni-YSZ	YSZ	LSM-YSZ	2.55	$\text{CH}_4\text{-air}$ (single chamber)	750	NA	0.6 (at 0.5 V)	[149]
Plastic mass ram extrusion	Cathode	Ni-CGO	ScSZ	LSM-CGO	1.63	Humidified H_2	750	1.06	0.45	[150]
Plastic mass ram extrusion	Anode	Ni-CGO	CGO	LSCF-CGO	0.40	Humidified H_2	550	0.76	0.3	[151]
Plastic mass ram extrusion	Anode	Ni-CGO	CGO	LSCF-CGO	0.80	Humidified H_2	600	0.80	1.29	[152, 153]
Supplied by Adaptive Materials Inc. USA	Anode	Ni-YSZ	YSZ	LSM	2.00	CH_4 (single chamber)	750	1.05	0.12	[154]
Plastic mass ram extrusion	Anode	Ni-CGO	CGO	LSCF-CGO	1.80	Humidified H_2	450	0.90	0.3	[155]
Cold isostatic pressing	Anode	Ni-YSZ	YSZ	LSM-YSZ	2.90	Humidified H_2	850	1.05	0.65	[156]
Plastic mass ram extrusion	Anode	Ni-CGO	CGO	LSCF-CGO	1.60	Humidified H_2	550	0.83	1.31	[122, 123]
Supplied by Adaptive Materials Inc. USA	Anode	Ni-YSZ	YSZ	LSM	2.00	CH_4 (single chamber)	750	0.92	0.036	[157]
Plastic mass ram extrusion	Anode	Ni-YSZ	YSZ	LSCF-CGO	1.70	Humidified H_2	600	1.00	0.39	[158]
Cold isostatic pressing	Anode	Ni-CGO	CGO	LSCF-CGO	3.00	Pure H_2	450	0.78	0.066	[159]
Plastic mass ram extrusion	Anode	Ni-CGO	CGO	LSCF-CGO	1.80	Humidified CO-H_2	550	0.76	0.63	[160]
Supplied by Adaptive Materials Inc. USA	Anode	Ni-YSZ	YSZ	LSCF-CGO	2.00	CH_4 (single chamber)	700	1.20	0.12	[161]
NA	Anode	Ni-CGO	CGO	LSCF-CGO	1.80	Humidified H_2	550	0.93	0.34 (at 0.7 V)	[162]
Plastic mass ram extrusion	Anode	Ni-YSZ	ScSZ-CGO	LSCF-CGO	NA	Pure H_2	700	1.08	0.57	[163]
Plastic mass ram extrusion	Anode	Ni-YSZ	CGO	LSCF	1.80	NA	NA	NA	NA	[164]

Plastic mass ram extrusion	Anode	Ni-YSZ	YSZ-CGO	LSCF-CGO	1.80	Humidified H ₂ -N ₂	650	0.4	0.73	[165]
Plastic mass ram extrusion	Anode	Ni-CGO	CGO	LSCF-CGO	2.00	Diluted H ₂	542	>0.9	0.6	[166]
Plastic mass ram extrusion	Anode	Ni-YSZ	YSZ-CGO	LSCF-CGO	1.8	Humidified H ₂ -N ₂	697	0.4	1.2	[167]
Phase inversion extrusion	Electrolyte	Ni	YSZ	LSCF-YSZ	1.58	Pure H ₂	800	1.20	0.018	[168]
Phase inversion extrusion	Electrolyte	Ni	YSZ	LSCF	>1.6	H ₂ -Argon	800	NA	0.005	[169]
Phase inversion extrusion	Anode	Ni-YSZ	YSZ	LSM-YSZ	6.04	Pure H ₂	800	1.03	0.85	[170]
Phase inversion extrusion	Anode	Ni-YSZ	YSZ	LSM-YSZ	1.70	Humidified H ₂	800	1.01	0.38	[171]
Phase inversion extrusion	Anode	Ni-YSZ-SDC	YSZ	LSM-YSZ-SDC	1.50	Humidified H ₂	800	1.03	0.78	[172]
Phase inversion extrusion	Anode	Ni-YSZ	YSZ	LSCM-SDC-YSZ	1.38	Humidified H ₂	850	1.03	0.51	[173]
Phase inversion extrusion	Electrolyte	Ni-YSZ	YSZ	LSM-YSZ	-2.00	H ₂ -Argon	800	0.93	0.018	[174]
Phase inversion extrusion	Anode	Ni-YSZ	YSZ	LSM-SDC-YSZ	1.50	Humidified H ₂	850	1.00	0.71	[175]
Phase inversion extrusion	Anode	Ni-BZCYYb	BZCYYb	LSCF-BZCYYb	1.65	Humidified H ₂	600	1.01	0.26	[176]
Phase inversion extrusion	Anode	Ni-BZCYYb	BZCYYb	SSC-BZCYYb	NA	Humidified H ₂	650	>1.0	0.25	[177]
Phase inversion extrusion	Anode	Ni-CGO	CGO	LSCF-CGO	1.4	H ₂	500	0.90	0.80	[178]
Phase inversion extrusion	Anode	Ni-CGO	CGO	LSCF-CGO	0.8	H ₂	570	0.89	0.58	[179]
Phase inversion extrusion	Anode	Ni-CGO	CGO	LSCF-CGO	1.4	H ₂	600	0.77	1.11	[180]
Phase inversion extrusion	Anode	Ni-CGO	CGO	LSCF-CGO	1.4	H ₂	580	0.80	1.00	[181]
Phase inversion extrusion	Anode	Ni-CGO	CGO	LSCF-CGO	1.4	H ₂	600	0.77	2.32	[144]
Phase inversion extrusion	Cathode	Ni-YSZ	YSZ	LSM-YSZ	NA	H ₂	850	0.98	0.29	[98]

2.2.2. Deposition techniques

Non-support thin layers can be deposited onto the inside/outside surface of substrate by wet power spray coating (WPS) or dip coating [1]. Suspensions are prepared again for deposition and polymer binders are also necessary in addition to the ceramic components to give the required rheology. During this process, dispersant is even more crucial than that in the fabrication of the support part, as no agglomeration is desired for well-distributed coating layers and the development of a non-porous sintered layer [182]. In the case of WPS, the coating slurry is sprayed over the substrate tube automatically by programmed apparatus, while for dip coating the tube will be immersed into the slurry and held for a while before pulling it up slowly from the suspension. Key parameters for coating thickness of these two methods are deposition rate and solid loading of the slurries. One thing should be mentioned is that, the deposition rate of dip coating refers to the speed of tube withdraw from the slurry suspension. Thick coated layers can be also achieved by deposition of a second layer after thorough drying (by solvent evaporation) of the previous one. In the case of electrolyte or cathode supported tubes, deposition on the inside surface of the tubes is required. Sometimes this is achieved by electroless plating technique, which can also be applied for the introduction of some catalyst particles to the porous electrode channels.

2.2.3. Impregnation technique

Metal catalysts are sometimes added to the anode layer in the form of nanoparticles [183]. This is done by impregnation or electroless plating techniques [184]. In the case of impregnation technique, metal nitrate solutions provide both fine particle size and great dispensability into the porous anode (sometimes also the cathode) being infiltrated. Later calcination processes are carried out to transfer nitrates to the expected oxide catalysts. Without co-sintering above 1000 °C, these processes avoid potential reactions between catalyst and other cell components and allow the application of materials which are unstable at high temperatures. One reason why anode nanopowder catalysts are desired for improving cell performance is that they form a path within the porous anode material (e.g. Ni) that enhances the anode conductivity [174].

2.3 Development of fuel cell performance

Recently, lowering operation temperature to the intermediate range (500-750 °C, ITSOFC) has attracted quite a lot attention in order to make a satisfactory thermal set-up and duration time of mSOFC. The only obstacle for ITSOFC is to maintain the cell performance at low temperatures.

An important parameter for cell performance is area-specific resistance (ASR), which is defined in Equation 10 [93].

$$ASR = \frac{Emf - U}{i}, (Equation 10)$$

where Emf is the electromotive force with the inlet fuel and air, and U is the point cell voltage at the current density i.

Here ASR is regarded as an index of total energy loss during the cell operation and should be controlled to a minimum level.

However for practical measurement, ASR is always divided into different sections as given in Equation 11 below:

$$ASR = R_s + R_p = R_{elect} + R_{connect} + R_{p,elchem} + R_{p,diff} + R_{p.conver}, (Equation 11)$$

where R_s is the Ohmic resistance, including electrolyte resistance (depends on thickness and geometric features) and connecting resistance (depends on contact between cell components and current collection), and R_p is the electrode polarisation resistance arising from electrochemical reaction, gas phase diffusion and gas conversion. Thus improvements of performance can be considered from the mentioned aspects above to minimize ASR.

Regardless of chosen techniques for the production of the support and other layers, further developments of cell performance can be realised by adjustments such as increasing anode porosity, reducing electrolyte thickness, tailoring cathode structure and redesigning current collector [179]. In some cases, an additional layer made of pure anode/cathode materials (e.g. Ni or LSCF) have been manufactured [185] to aid current collection instead of using precious interconnect material (e.g. silver), which saves the fabrication cost and enlarges the selection of materials for the current collector. Current collection should be performed to maximize the use of surface area of both electrodes if uniform current and minimum loss are required [186], so in many

cases, annular metallic meshes are inserted into the SOFC tubes and bundled wires are wound outside to approach the ideal situation as much as possible.

2.4. Aims of the project

The overall aim of this project was to explore and optimise the fabrication methods for mSOFC components. Ram extrusion was chosen for the anode tube fabrication as this method has the potential to be scaled to commercial manufacture, and most emphasis has been placed on the fabrication of the anode/electrolyte half cells. A number of separate objectives were defined in order to achieve this aim.

- Investigation and characterisation of solvent-based room temperature extrusion methods for the fabrication of porous anode support tubes. This includes the control of extrusion parameters, microstructure, porosity, and sintering processes.
- Development of a coating method for the application of thin, dense electrolyte layers onto the anode tubes. Control of electrolyte thickness, integrity and adhesion of the coating and suitable sintering/co-sintering regimes are all important factors to be considered.
- Demonstration of mSOFC performance using optimised fabrication procedures.

Chapter 3 Experimental techniques

3.1. As-received materials

Green nickel oxide (Grade F, mean particle size 1-2 μm) powders were purchased from Hart Materials Ltd. (UK) for mSOFC anode fabrication. Two types of yttria-stabilized zirconia (YSZ) powders were supplied by Imerys Fused Materials GmbH (Germany): YSZ powders with a mean particle size of 3-5 μm for the anode fabrication and 1.4-2 μm for the electrolyte, both contained 8-10 mol% Y_2O_3 as the dopant (Table 2). Corn starch (Product Number S4126) powders, used as the anode pore former, were supplied by Sigma-Aldrich Company Ltd. (UK). A solvent-based PVB binder system, developed by Functional Materials Group in University of Birmingham, was used for formulations of the paste/suspension system for anode/electrolyte processing. The processing method for anode paste is known as the viscous plastic processing (VPP), as detailed in Section 3.2. Menhaden fish oil (Product Number F8020) was purchased from Sigma-Aldrich Company Ltd. (UK), which was used as the dispersant for electrolyte manufacturing.

The manufacturing route for half cells employed in this project is given in Figure 18. On the basis of this, the addition of cathode and current collector, with heat treatment including sintering and reduction (where oxides in electrodes are reduced to pure conducting metal) was undertaken for electrochemical cell testing, which will be detailed in Chapter 9.

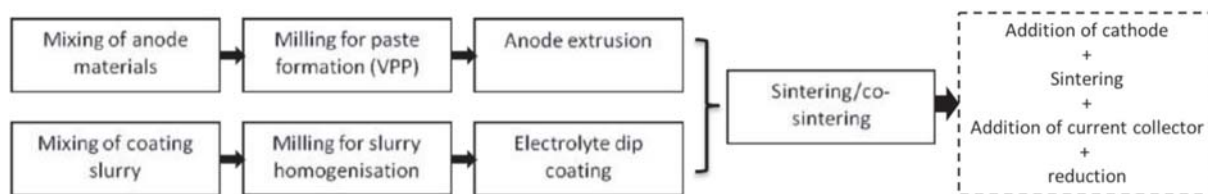


Figure 18 Manufacturing route for the structure of anode/electrolyte

3.2. Viscous plastic processing (VPP)

The Viscous plastic processing (VPP) technique is frequently used for fabrications involving non-metallic inorganic materials [187, 188]. First industrialised in 1983 for producing macro-defect-free cement [189], VPP has been developed into an effective method for the processing of functional materials related to the conversion of energy or electrical signals. During the processing, ceramic powders are forced to distribute homogeneously within an organic polymer phase to form a plastic paste under a high shear stress [190]. The developed paste system is shaped to the required geometry, i.e. via a net shape process such as extrusion, pressing or calendaring.

The characteristics of the viscous system are vital to the quality of the finished product. On the one hand, as the separate solid powder phase is surrounded by a continuous liquid phase, a powder packing study should be carried out to determine the optimum solid/liquid ratio when formulating the starting materials, on the premise that the minimum addition of liquid phase is required to fill the space between densely packed solid powders [191]. On the other hand, the rheological behaviour of the processed paste affects the final products, since an excessively stiff paste would cause potential processing defects and possible equipment damage while an over softened paste would not retain a fixed geometry after the net shaping step.

A developed powder packing study applies a discrete approach to predict the distribution of a second species, with a smaller particle size, in the interstices of the original coarse powders. The Westman model was the first successful formula using a non-continuous assumption [192], with a parabolic distribution of the packing density for a binary system, i.e. a peak packing density at a certain volume ratio between the two powder species. Similarly, Furnas proposed his expression for calculating packing density in the 1930s [193]. Compared to the Westman model, the Furnas model takes account of the mutual effect between the packing of the two types of powder. The limitation of both models is the deviation from actual packing density when applied to ternary or quaternary systems.

An extended expression for the Westman model is given in Equation 12 [194], which could be used for powder systems with more than two species.

$$\begin{aligned} & \phi_{m,i+1}^2 \left(\frac{1}{\phi_{\max,i+1}} - \frac{1 - x'_{i+1}}{\phi_{\max,i}} \right)^2 \\ & + 2G_i \frac{\phi_{\max,i} \phi_{m,i+1}}{1 - \phi_{\max,i}} \times \left(\frac{1}{\phi_{\max,i+1}} - \frac{1 - x'_{i+1}}{\phi_{\max,i}} \right) \\ & \times \left(\frac{1}{\phi_{\max,i+1}} - 1 + x'_{i+1} - \frac{x'_{i+1}}{\phi_{m,i+1}} \right) \\ & + \left(\frac{\phi_{\max,i}}{1 - \phi_{\max,i}} \right)^2 \times \left(\frac{1}{\phi_{\max,i+1}} - 1 + x'_{i+1} - \frac{x'_{i+1}}{\phi_{m,i+1}} \right)^2 = 1, \text{ (Equation 12)} \end{aligned}$$

$$\text{where: } G_i = \begin{cases} 0.738 \left(\frac{d_{i+1}}{\bar{d}_1} \right)^{-1.566}, & \frac{d_{i+1}}{\bar{d}_1} \leq 0.824 \\ 1, & \frac{d_{i+1}}{\bar{d}_1} > 0.824 \end{cases}$$

where $\phi_{m,i+1}$ is the packing density of the powder added at last (assuming it is packed alone), with the finest grain size of d_{i+1} and volume fraction of x'_{i+1} , $\phi_{\max,i+1}$ is the packing density of the eventual powder mixture. $\phi_{\max,i}$ is the packing density of the prior powder system before the addition of the finest material. G_i is a defined parameter specially for powder packing theory, which is a function of the particle size and geometry, whose determination requires the values of \bar{d}_i (i.e. the characteristic diameter of the prior powder system) and d_{i+1} .

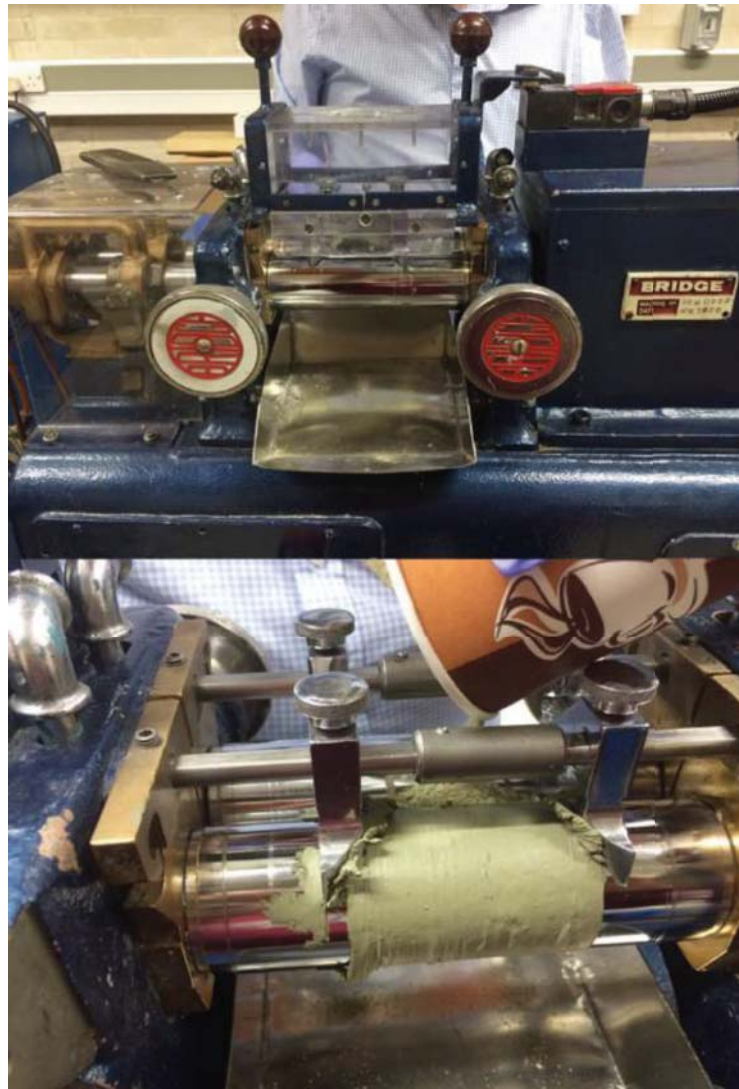


Figure 19 Twin roll Bridge milling machine with and without load of processed compound mixture

To mix the proposed paste formation, a Bridge twin roller miller (shown in Figure 19) was applied in this study. The roller is connected to a chiller that maintained the working temperature at 15 °C by running a water cooling system. The diameter of both rolls was 50 mm and the distance between them was adjustable. The rotational speeds of the rolls were fixed at 18 min⁻¹ and 16 min⁻¹, separately, hence the processed materials were always attached to the roll with a higher speed, as a result of a higher shear stress at that surface.

Prior to the milling of mixture of the starting materials, the dry powders are preliminarily mixed by hand with the polymer and liquid constituents. Then the distance between the mill rollers was set to 1 mm for the first milling, before further adjustment to 0.2 mm for three additional millings to break down any potential agglomerations within the processed paste. The formed thin film was cut off from the surface of the rolls after one milling and refed into the miller for the next cycle, with the total time spent for the whole milling process being roughly 10 minutes. The procedures described above were aimed at minimising the variation of solvent loss during the milling process, in order to guarantee the experimental repeatability.

The milled paste, in the form of a thin film, was then left in a freezer for 3 h before exposure back to the room temperature for 30 minutes, before subsequent extrusion being undertaken. This was also for the purpose of inhibiting solvent loss due to freezing and deforesting prior to extrusion and to reduce variation.

3.3. Extrusion die design

A three-dimensional schematic of the customised extrusion die set is given in Figure 20, together with its disassembled view. In order from the top to the bottom, the whole set includes a plunger to apply the extrusion pressure, a barrel to load the starting paste, a binary annular die set (comprising upstream a plate with six holes and supporting the central pin or mandrel to form the inner diameter of the extruded tube, and a downstream plate forming the outer diameter of the extrudate), a capping to fix the die parts and the necessary screws.

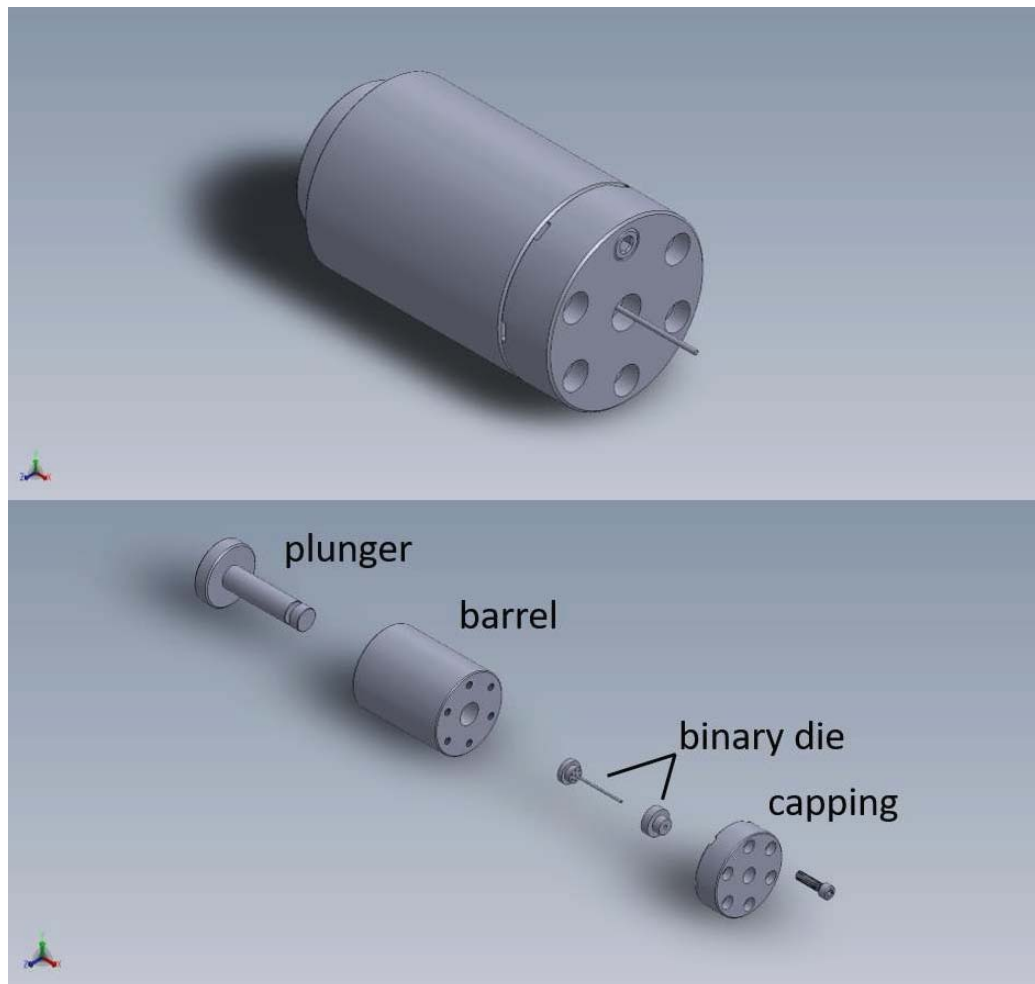


Figure 20 3-D schematic of assembling and disassembling views of the tailor made extrusion die set for this project

A simplified two-dimensional section diagram is also given in Figure 21 with necessary dimensional information. There are two convergent sections that would be experienced by the processed paste, which are labelled as section ① and ② respectively in Figure 21. In the first extrusion section, the processed material would be forced into six small holes before recombination at the outlet of these holes, while a tubular geometry would be generated after the paste passes through the second extrusion section. The die set was made of stainless steel.

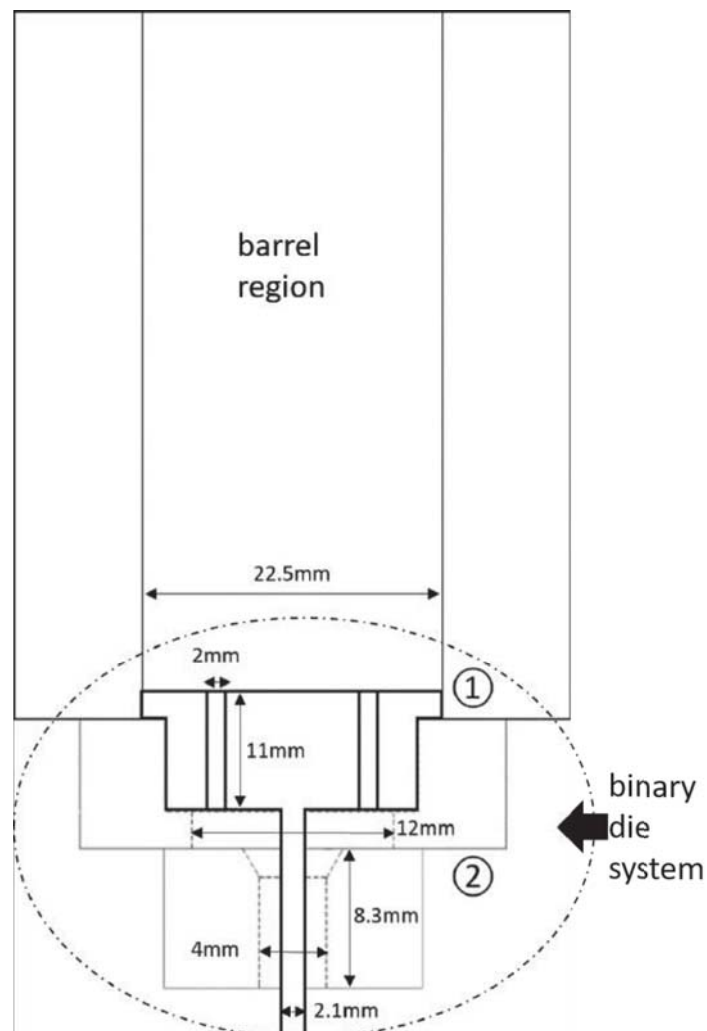


Figure 21 Simplified cross section view of core components for the die set with essential dimensional information and indications of two convergence regions (the plunger and the capping parts are not shown here)

3.4. The Instron load frame

A load frame (5507 Instron, UK) was applied for multiple purposes in this study, in addition to the extrusion of the anode tubes. The equipment could exert a programmed load or crosshead speed within a compression or tensile operation and has been widely applied for characterisation of mechanical and textural properties [195, 196]. For the extrusion processing (Figure 22) undertaken in this thesis, a fixed cross-head speed of 1 mm/min was selected for the tube extrusion. Other applications of the load frame will be detailed in the following sections.

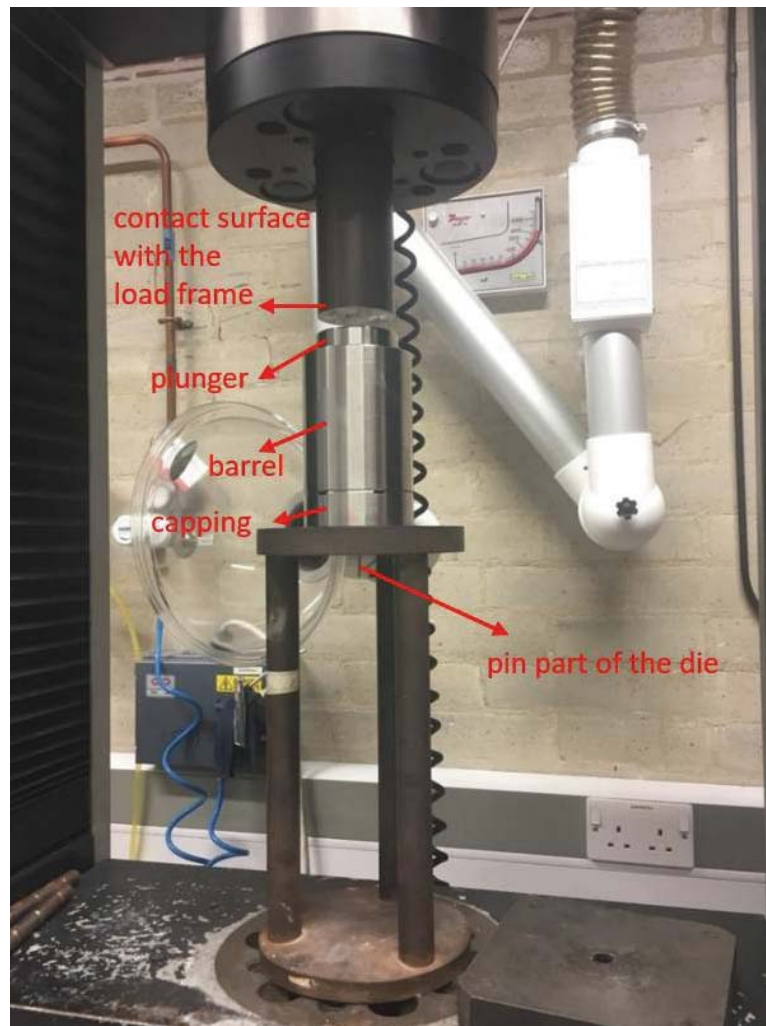


Figure 22 Extrusion process where a vertical load is exerted via an Instron load frame to force the extrudates out of the die

3.4.1. Powder packing behaviour

Cylindrical compacts consisting of dry solid powders (ceramics and the pore former) were formed by a uniaxial pressing process. A 13 mm-diameter die was used (Specac, UK) for this purpose, as shown in Figure 23. The height of the compacts could be directly read from the computer screen if the position for zero level was properly set where two metallic backup plates are just contact with each other. Then both the volume of the cylindrical sample and the space occupied therein by the solid powders could be computed before the packing density was determined. The packing density data were then used for the determination of liquid content required for the anode paste formulation prior to the VPP process.

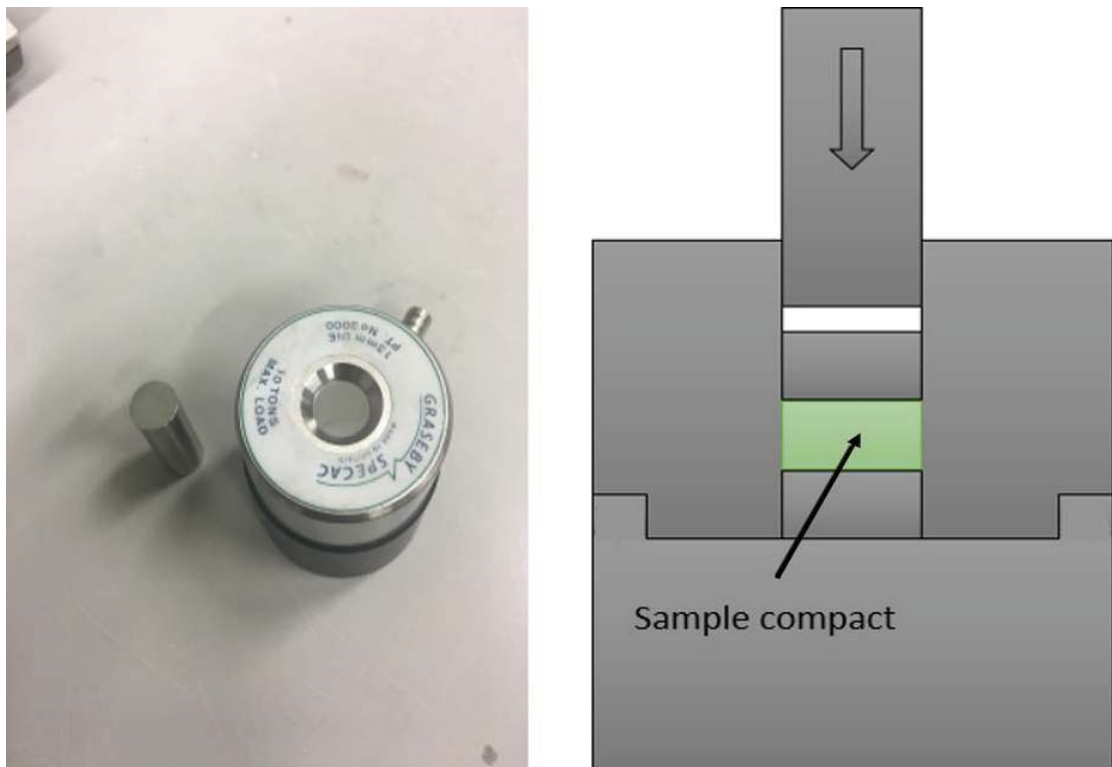


Figure 23 Photograph and schematic of the compaction die used for the powder packing study in this project

3.4.2 Paste rheology test

In order to determine the rheological behaviour of the dough-like paste after milling, a simply configured die set with a structure identical to that shown in Figure 16 was applied. This set has 3 interchangeable dies, which are shown in Figure 24. In order to gather the required data for rheological analysis a full barrel of material was run through each die. The ram velocity during this operation was varied between 1-50 mm/min in the initial tests and at other velocities for later tests as will be described in Chapter 5. The derived rheology data were applied to predict the pressure drop for the more complicated tube forming die set.

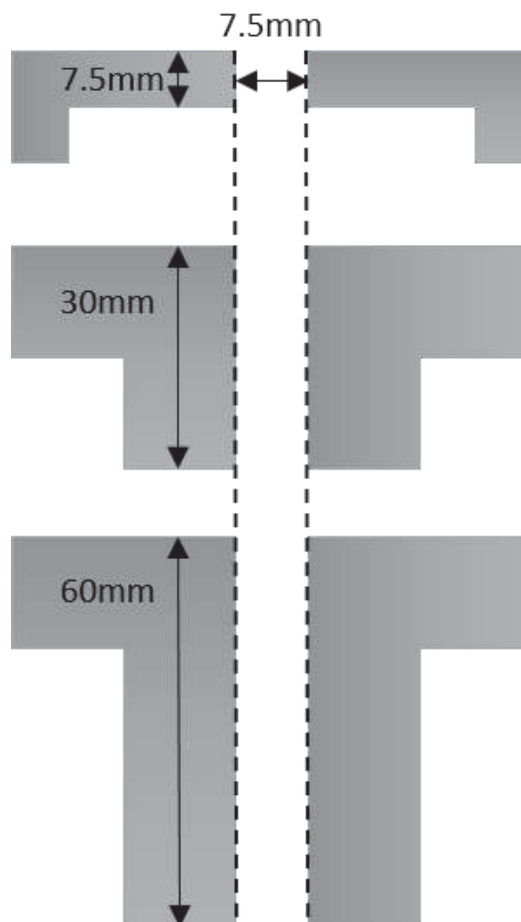


Figure 24 2-D drawing of the alternative dies with varying die lengths, used for paste rheology study

3.4.3 Dip coating

During the coating of the electrolyte layer, the anode tube was inserted into an elastic holder made of polydimethylsiloxane (PDMS). A thin magnetic disc was mounted in the same holder to achieve the attachment to the horizontal surface of the load frame (Figure 25). The pulling-up (withdrawal) speed could be programmed after the immersion of the tube into the electrolyte slurry, to obtain variation of coating thickness.

The dip coating slurry is prepared by adding the electrolyte material to the viscous liquid dispersing agent, made up of multiple organic compounds (the specified formulations can be found in Chapter 6). With the assistance of zirconia balls (at a slurry/ball ratio of 1:1) as a milling agent, the coating slurry was milled for 24 hours on a ball milling machine (Machine No. 21735, Pascall Engineering, UK) for 24 hours before being used.

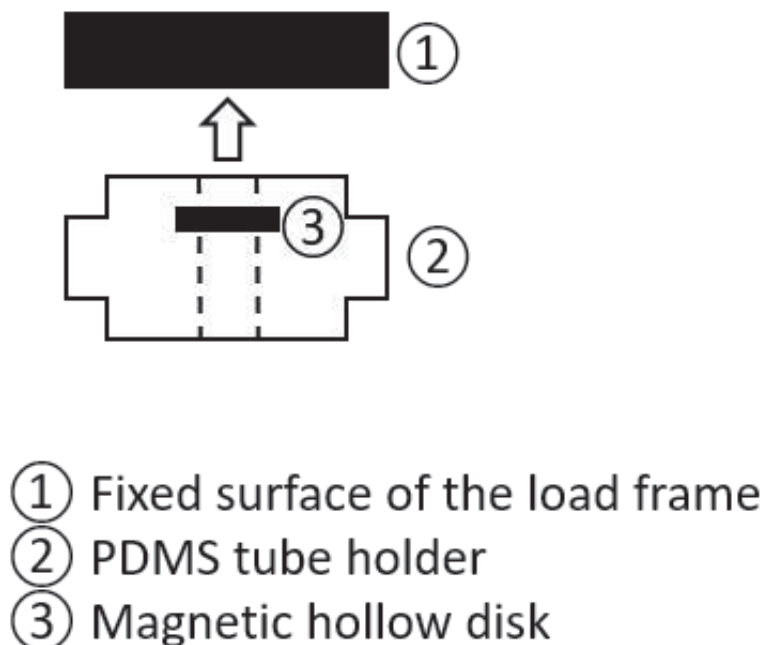


Figure 25 Layout of the dip coating holder installation

3.5. Sintering

A muffle furnace (Serial No. 5705, Lenton Furnaces, UK), in which the temperature ramp rate and dwell time could be set, was used to complete the heat treatment of the SOFC samples. This heating process includes the debinding stage and the sintering stage. The burnout of organic constituents (the binder system) usually finishes before the temperature reaches 600 °C and the densification of ceramic powders starts at ~1000 °C, with details of individual heating regimes being explained in separate chapters. Alumina crucibles were used to support the SOFC tubes with zirconia sand acting as a cushioning agent between them.

3.6. Particle size analysis

For the distribution and statistics of the particle size of the starting powders, namely NiO, YSZ and corn starch powders in this study, a particle size analyser (Gracell, Sympa Tec, Germany) was used. This machine utilises the laser diffractometry technique to detect the distribution of particle size [197]. For each test trial 0.5 g of the powder samples were dispersed in 3 g deionised water (ethanol in the case of corn starch that is soluble into water) with the assistance of 2 drops of a dispersant ($\text{Na}_4\text{P}_2\text{O}_7$, Sympa Tec, Germany), before adding to the testing tank, which was also filled with deionised water (again ethanol in the case of corn starch). The concentration was set to meet the observation requirements of the system and the appropriate optical model based on the refractive index of the powders developed. The particle size data were used to predict the powder packing densities described in Chapter 4.

3.7. Thermal gravity analysis (TGA)

TGA equipment (Netzsch, STA 449C, Germany) was used to characterise the mass change during heating with a specified temperature profile, in order to obtain the information at what temperature the removal of the binder and the pore former is completed. Within the equipment, a precise balance is mounted in a furnace to record the real-time sample mass at different temperatures [198]. The applied heating ramp was 10 °C/min and typically 2 g of sample was analysed.

The purpose of using TGA in this project was to determine the temperature that all components of the binder system were removed and to confirm that this is below the onset of sintering.

3.8. Dilatometry

The dimensional change (expansion or shrinkage) related to temperature change was characterised by a dilatometer (Netzsch, 402E, Germany) to judge the feasibility of co-sintering operations. The sample loaded into the dilatometer was in a rod form with both end surfaces flat and parallel to each other. A pushrod was set against one of the sample ends and could detect any tiny change in longitudinal sample dimension. In this project, dilatometry was performed to compute the difference in thermal expansion coefficient (TEC) between the anode and electrolyte samples in a compact form. The anode compact was cut from an extruded rod while the electrolyte compact was formed by using the same compaction die as shown in Figure 23. As the ceramic powders would experience neck growth and merging with each other during sintering, a negative dimensional change is expected (i.e. sample shrinkage).

A large mismatch of TEC is expected to cause defects such as cracking or delamination after the co-sintering of bi-layer structures. The definition of TEC is given in Equation 13.

$$TEC = \frac{L_f - L_i}{L_i(T_f - T_i)}, \text{ (Equation 13)}$$

where L_i is the initial length, L_f is the final length, T_i is the initial temperature and T_f is the final temperature

3.9. Viscosity test

A rheometer (TA Instruments, AR500, USA) was used in this project to optimise the dispersant fraction within the dip coating slurry, by obtaining the minimum viscosity. It is believed that there is a saturation condition for the adhesion of dispersant on the particle surface [199] and the slurry reaches an ultimately dispersed state as a result. During the test by the AR500 rheometer, the shear stress was programmed while the shear rate was characterised over a shear rate range 0-2500 s⁻¹. The apparent slurry viscosity (η) is determined by the ratio of instant shear stress (τ) and shear rate ($\dot{\gamma}$) as given in Equation 14 [200]. A plate geometry of 40 mm diameter was used with a solvent trap to avoid solvent loss during the test. The machine with the geometry used is shown in Figure 26.

$$\eta = \frac{\tau}{\dot{\gamma}}, \text{ (Equation 14)}$$

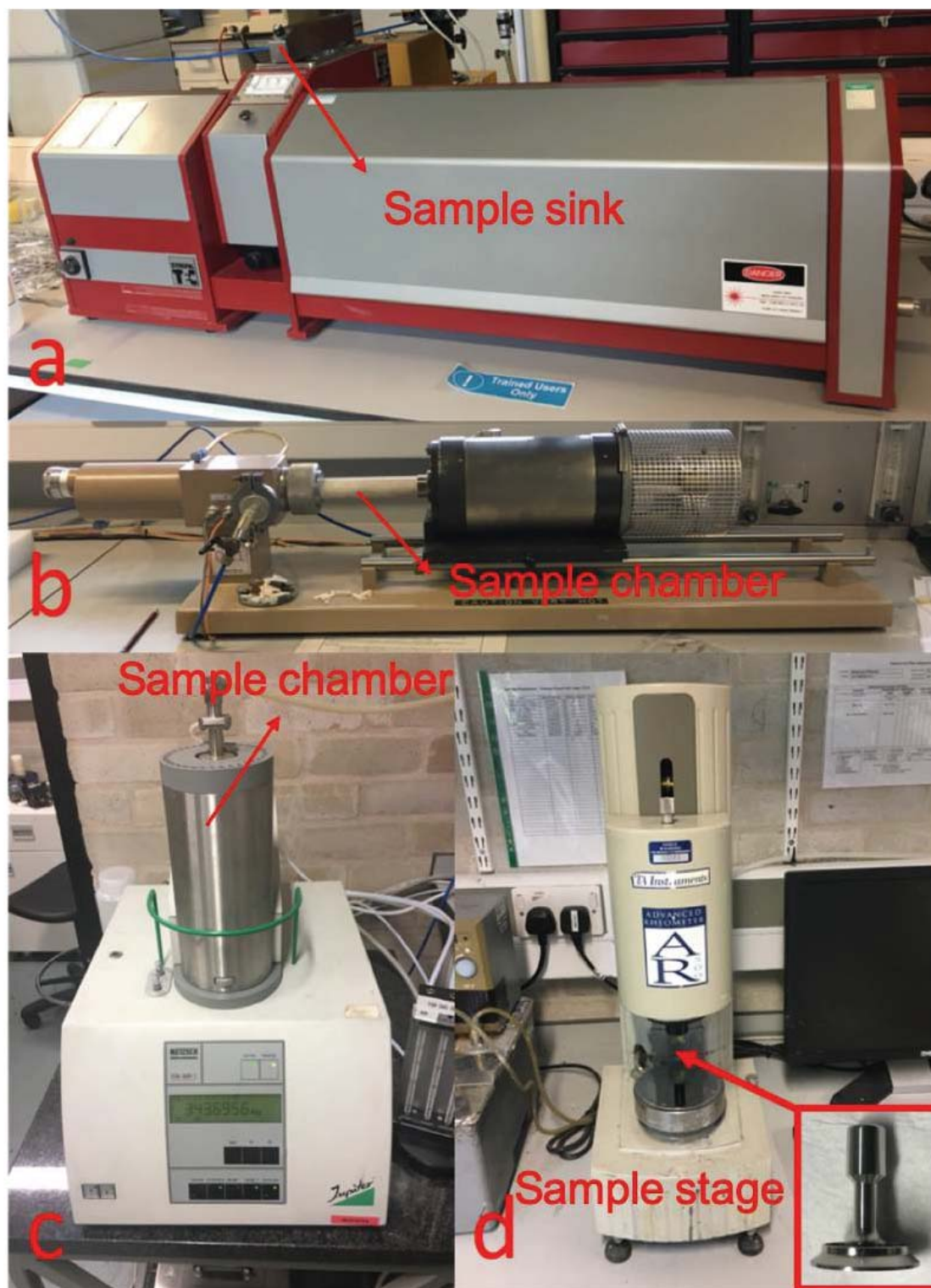


Figure 26 Photographs of some equipment used in the project, i.e. (a) particle size analyser, (b) dilatometer, (c) TGA and (d) rheometer

3.10. BET surface area characterisation

The Brunauer-Emmett-Teller (BET) method was used to determine the surface area, an assistant characteristic for packing density analysis of the powders, by gas adsorption at increasing pressures. A 3Flex instrument was used (Micromeritics Instruments Corporation, USA). The samples were precisely weighed after degassing and then evacuated with the vial submerged in liquid nitrogen. The pressure was increased and the adsorption isotherm was measured. From that isotherm the surface area was determined.

3.11. Scanning electron microscopy (SEM)

Two types of SEM (JEOL 6060 and XL30 ESEM) were used in this project. A JEOL 6060 SEM was used to characterise the fracture surfaces of the anode tubes and half cells, while an XL30 ESEM was used for the particle geometry of starting materials as it had a better resolution to distinguish microstructures under 1 μm . The characterised sample surface should be conductive. Thus a metal substrate, with the adhesion of a conductive film, or a plastic holder were selected here to mount the samples before surface coating with platinum or gold was undertaken, as shown in Figure 27. This is a destructive method for cells as they were necessarily broken into two parts to exhibit cross sections with a fracture surface. The cross section was then prepared without polishing in order to avoid unwanted scratches being introduced to the initial structures, and to obtain a more distinguishable boundary between the anode and the electrolyte. Sample surface morphology and thickness was detected afterwards in vacuum by electron beams released by heated tungsten filament. The

images were acquired in secondary electron mode normally at the 20 kV accelerating voltage.

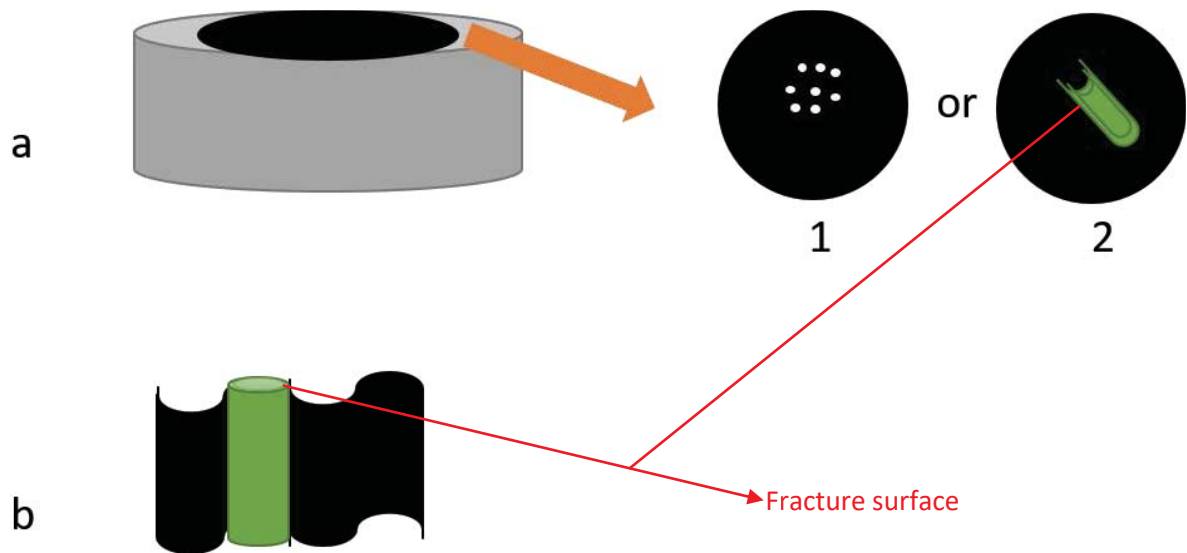


Figure 27 SEM samples for characterisations of (a1) as-received powders (a2) longitudinal cell fracture surface and (b) axial cell fracture surface

3.12. Cell testing

Cell tests of electrochemical performances were carried out in the School of Chemical Engineering, University of Birmingham. A schematic diagram of the fuel cell test rig is shown in Figure 28 and comprises MFC (Mass Flow Controllers), a heating furnace, a temperature controller and a cell test system. Insulating fire blocks (Thermal Ceramics) are the major structural components of the furnace, while Nichrome ribbon (Advent Ni80/Cr20 1.5 mm x 0.13 mm) acts as the heating element. A Eurotherm 2404 temperature controller was used, which could program the furnace heating or cooling regime for electrical testing at different temperatures. The cell test

system used for recording any cell performance was a Solartron™ 1400 that could also control the input electrical signal. The interactive operation with the test system was via Cell Test™ software, in order to adjust the input voltage or current.

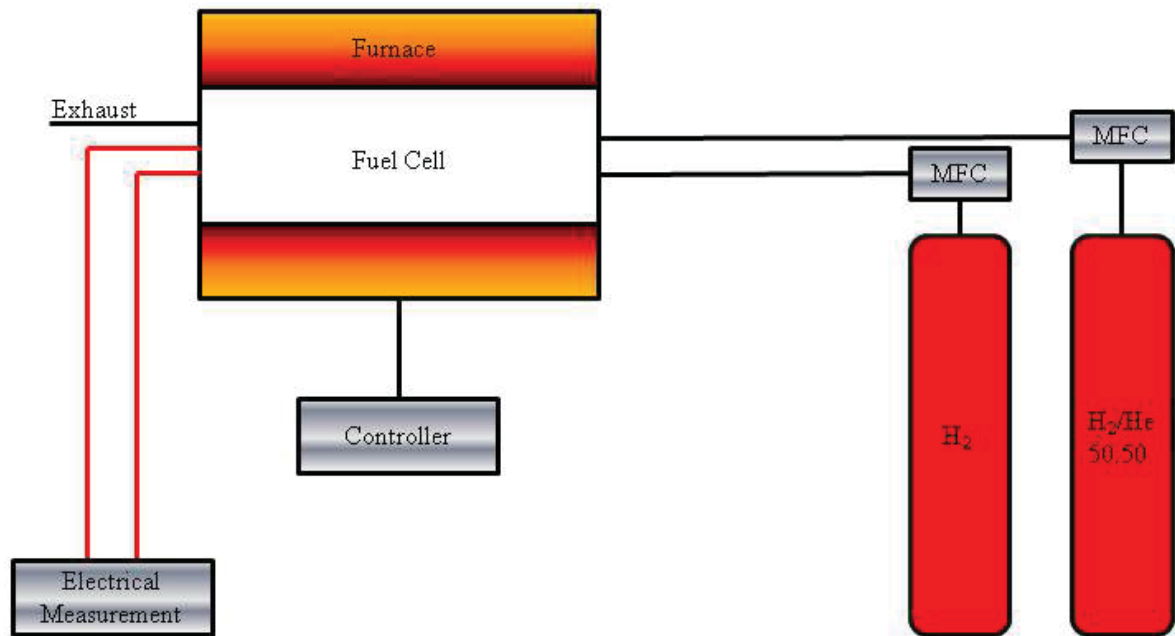


Figure 28 Schematic of the test rig for electrical cell performance [57]

3.12.1. Current-Voltage measurement

The manufactured mSOFCs were characterised in terms of output voltage at different input current densities. A typical I-V curve is given in Figure 29. A sharp drop would always occur at the beginning of the curve that is believed to arise from the activation energy required for the electrochemical reactions. This stage is followed by a linear correlation between the characterised voltage and increased current density, the reason for which is the Ohmic resistance loss, mainly resulting from the transfer of ions within the electrolyte [201]. At the final stage where the output voltage reduces significantly again, insufficient fuels or air at the Triple Phase Boundary (TPB) are

expected to cause the concentration loss that inhibits an adequate voltage output [202]. The extrapolation of the I-V curve to the vertical axis where current density is equal to zero would acquire the Open Circuit Voltage (OCV) of the cell, whose theoretical value is as explained below.

The calculations of total Gibbs free energy change and electromotive force, at standard temperature and pressure (STP, i.e. 298 K and 100 kPa), is given in Equation 15 and Equation 16, where n is the number of electrons transferred between reactants and products, while F is the Faraday constant (96485 C/mol).

$$\Delta G = G_{f,products}^{\phi} - G_{f,reactants}^{\phi}, \text{ (Equation 15)}$$

$$\Delta G = -nFE, \text{ (Equation 16)}$$

For the electrochemical reaction at STP between hydrogen and oxygen,

$$\Delta G = G_{f,H_2O}^{\phi} - G_{f,H_2}^{\phi} - G_{f,O_2}^{\phi} = -237.2 - 0 - 0 = -237.2 \text{ kJ/mol}, \text{ (Equation 17)}$$

Thus,

$$E^{\phi} = -\frac{\Delta G}{2F} = 1.23 \text{ V}, \text{ (Equation 18)}$$

When working at a given condition deviated from STP, a fuel cell would have an OCV less than 1.23 V (could be down to 0.9 V for SOFC operating at around 800 °C in hydrogen), which is able to be calculated by the Nernst equation [203] as given in Equation 19.

$$E = E^{\phi} + \frac{RT}{nF} \ln \left(\frac{p_{H_2} p_{O_2}^{\frac{1}{2}}}{p_{H_2O}} \right), \text{ (Equation 19)}$$

If an OCV less than 0.9 V is observed, the possible reason for it might be an insufficiently dense electrolyte, which could cause a short circuit between electrodes. Additionally, a slight excess of fuel supply is always used to avoid the concentration loss.

Figure 29 also shows the typical distribution of power density at different current densities. A peak power is characterised at an intermediate current density value.

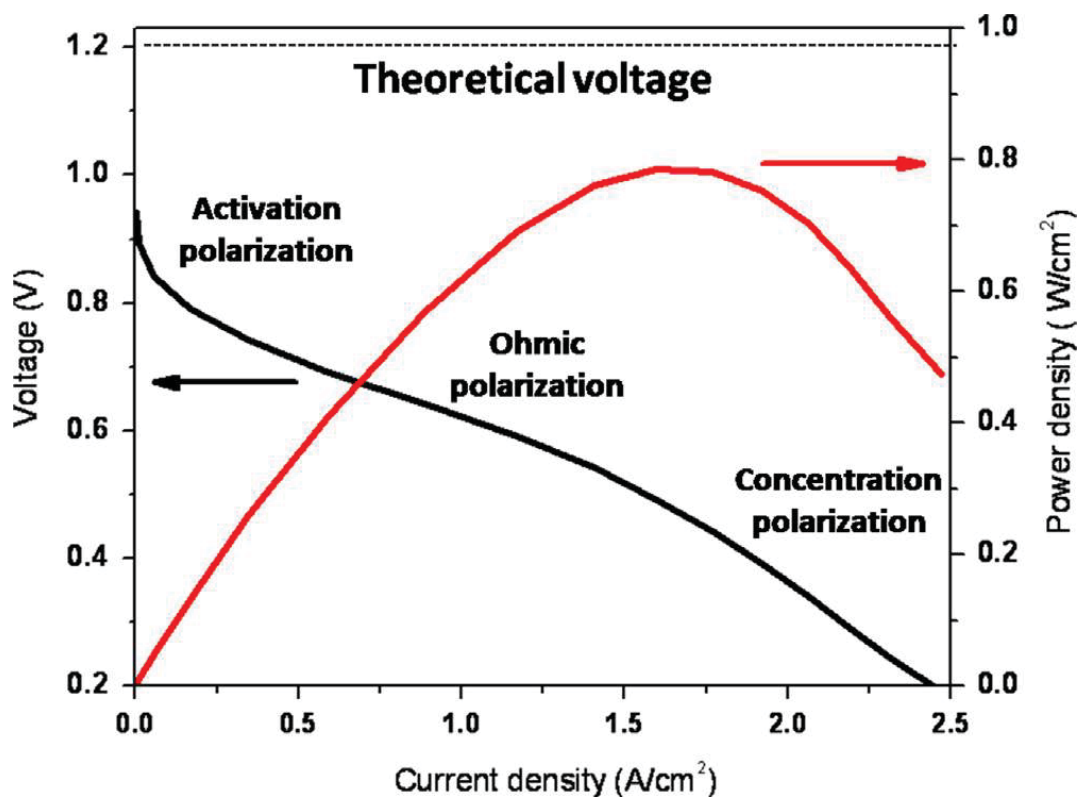


Figure 29 Typical polarisation plot of a fuel cell [204]

3.12.2. Electron Impedance Spectroscopy (EIS)

EIS is one of the most commonly used techniques for battery fuel cell studies [205, 206]. The technique involves loading a small amplitude AC voltage onto the cell and

receiving the response of current. The sinusoidal perturbation voltage and response current could be expressed in the forms shown in Equation 20 and Equation 21.

$$V(t) = V_0 \sin \omega t, \text{ (Equation 20)}$$

$$I(t) = I_0 \sin(\omega t + \theta), \text{ (Equation 21)}$$

$$Z = \frac{V(t)}{I(t)}, \text{ (Equation 22)}$$

The impedance is defined as Equation 22, similar in the form to the resistance in a DC circuit [207]. It has a real part and an imaginary part and could be interpreted as a vector in the complex plane (Figure 30). Two essential factors of the impedance Z are the magnitude ($|Z| = \frac{V_0}{I_0}$) and the phase (θ).

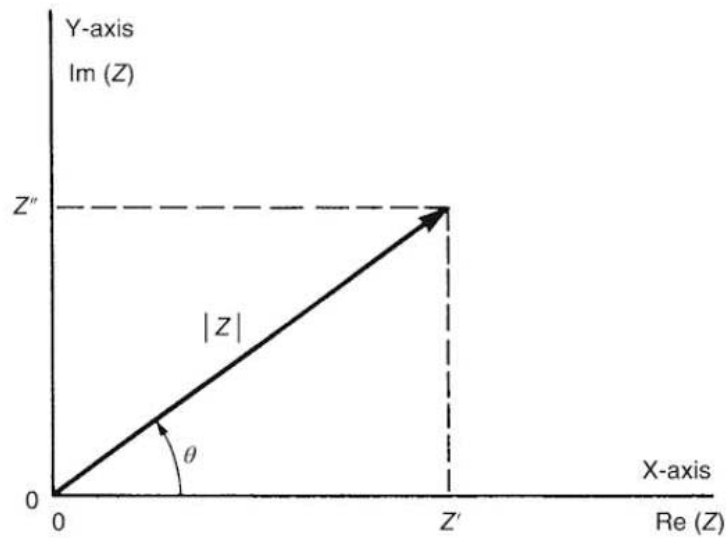


Figure 30 Impedance Z plotted in the complex plane [208]

Therefore, it could be noted by Equation 23.

$$Z = |Z| \cos \theta + j \sin \theta = Z' + jZ'' = |Z| e^{j\theta}, \text{ (Equation 23)}$$

Multiple impedance points could be plotted in a single complex plane, as a function of frequency. This type of impedance expression is called Nyquist plot, whose representative expressions for several simple circuits are shown in Figure 31.

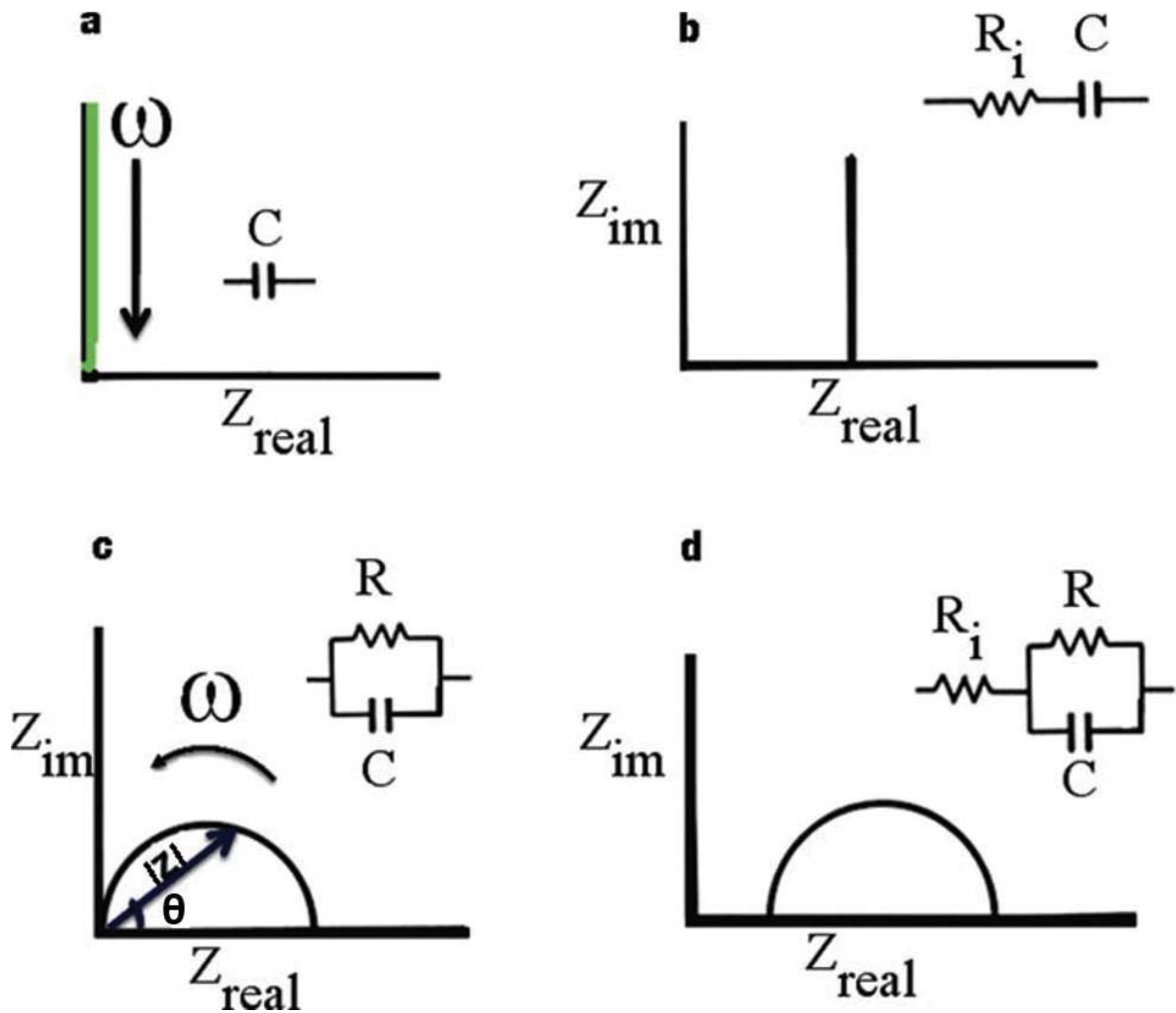


Figure 31 Nyquist plots for (a) a capacitor, (b) a capacitor in series with a resistor, (c) a capacitor in parallel with a resistor, and (d) a resistor in series with a parallel resistor-capacitor circuit [209]

The process of EIS analysis is like white-box testing, as the purpose of it is to understand the inside structure of a given fuel cell. Accordingly, an equivalent circuit

is necessary to reveal the cell configuration. The equivalent circuit usually contains a group of resistances and capacitances, arranged in a combination of series and parallel.

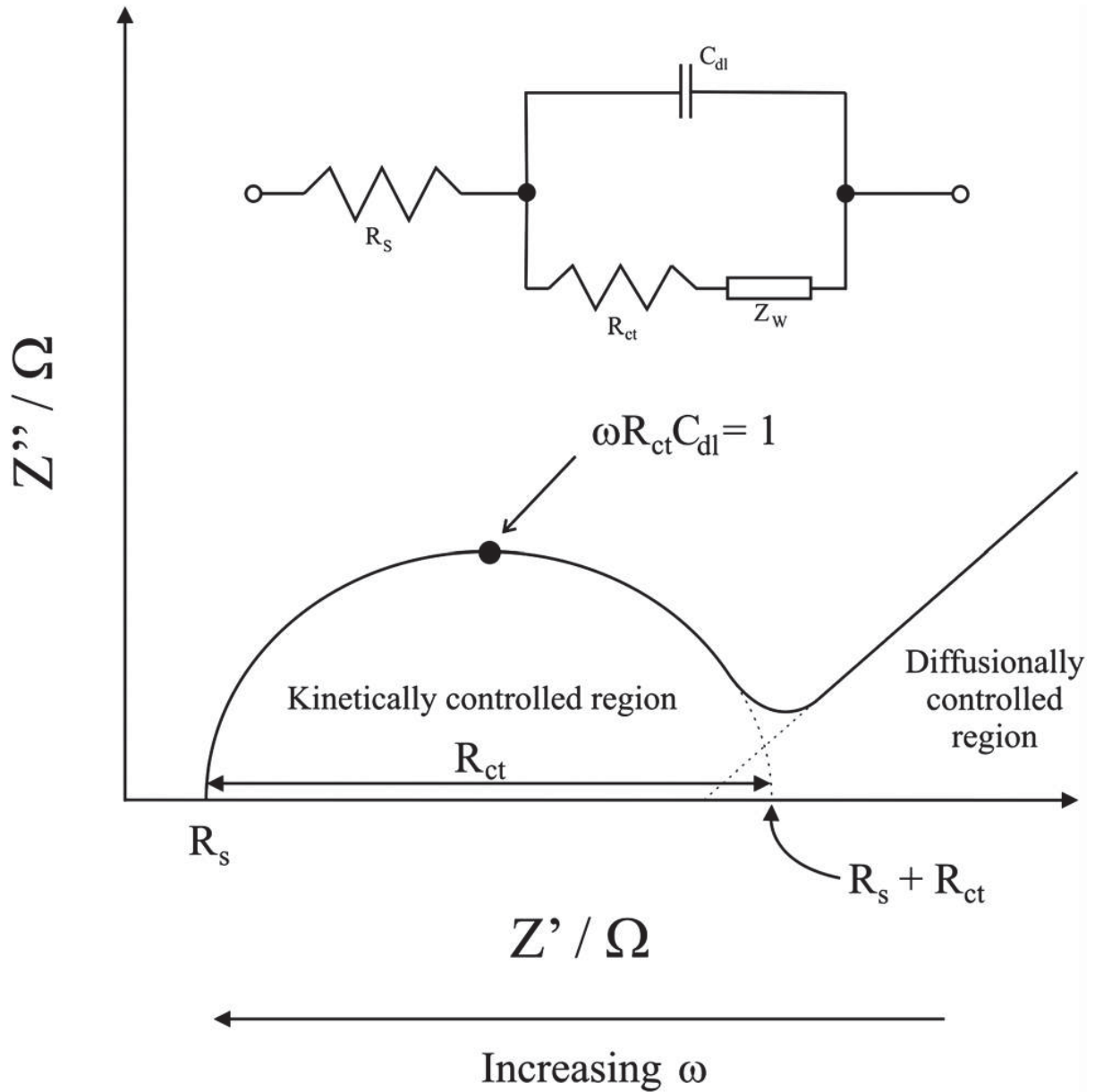


Figure 32 Equivalent circuit for a simple fuel cell [210]

A reasonable equivalent circuit for SOFC is shown in Figure 32, which is known as Randles circuit [211]. The circuit includes:

- (1) Resistance R_s , referring to the voltage loss predominantly within the range of electrolyte solution, described in the section of I-V testing, namely activation energy, Ohmic loss and concentration loss.
- (2) Capacitance C_{dl} , introduced to simulate the structure of double layer, formed of electrolyte ions along TPB, where electrostatic interactions occur.
- (3) Faradic impedance, consisting of the charge transfer resistance R_{ct} and the mass transfer impedance Z_w . The latter is also called the Warburg impedance [212], which is due to the diffusion of reactants and is negligible at high frequencies. It has the same numeric value for both imaginary and real parts, hence always has a phase angle of 45° in a Nyquist plot.

The descriptions lead to the ideal plot for a SOFC shown in Figure 32.

Chapter 4 Powder characterisation and anode processing

4.1. Introduction

In this chapter, the results of the characterisation of the purchased starting powders NiO (Hart Materials Ltd., UK), YSZ (Imerys Fused Materials GmbH, Germany) and corn starch (Sigma-Aldrich Company Ltd., UK) are presented and discussed in terms of particle size and microscopic morphology, in order to assist in the analysis of the powder packing behaviour that is essential to determine the solid/liquid ratio during the anode paste formulation. The chapter describes a powder packing study which includes the exploration of the powder compaction limit and the computation of packing density for a ternary system, using an extended binary model. The results of initial trials of anode extrusion based on the determination of solid/liquid volume ratio within the paste formulation are presented and discussed.

4.2. Results and discussion

4.2.1. As-received powder characterisation

The starting ceramic powders were characterised in terms of particle size, particle morphology and surface area. The YSZ powders used for anode fabrication were denoted as YSZ-A, while YSZ-E was used to denote the YSZ powders used in electrolyte layer. The characterisation results of initial powders provided the fundamental information to evaluate the feasibility of powder packing analysis carried out in Section 4.2.3.

Figure 33 and Figure 34 show the particle size distribution of NiO, YSZ-A and YSZ-E powders, the corresponding statistical data are given in Table 4 (see Section 3.6 for the methodology). In general, ceramic powders with a small mean particle size (D_{50}) show better densification behaviour during sintering processes, thus YSZ-E powder ($D_{50}=1.25\ \mu\text{m}$) was chosen for electrolyte fabrication to realise a dense structure. The size distribution of YSZ-A and YSZ-E powders can be regarded as a Gaussian mono-modal distribution, which is advantageous for subsequent packing analysis, except for a slight fraction of large-sized ($\sim 15\ \mu\text{m}$) particles or agglomerates within the YSZ-E powder. However, for the NiO powders, two peaks are observed at $D\sim 1\ \mu\text{m}$ and $D\sim 4\ \mu\text{m}$. As NiO and YSZ-A are used in combination in the anode formulation and powder packing behaviour of binary powder system will be studied later in this chapter, the bimodal distribution of NiO particles may increase the complexity of the packing model. In addition, the relatively wide size distributions of the two ceramic particles added uncertainty to the prediction of particle packing. This is because the majority of packing models assume mono-modal and narrow size distributions in the calculation.

Table 4 Statistical particle size data for as-received ceramic powders

Powder	D_{10}	D_{50}	D_{90}
Description			
NiO	0.38 μm	1.19 μm	5.11 μm
YSZ-A	0.64 μm	3.35 μm	8.40 μm
YSZ-E	0.42 μm	1.25 μm	3.34 μm

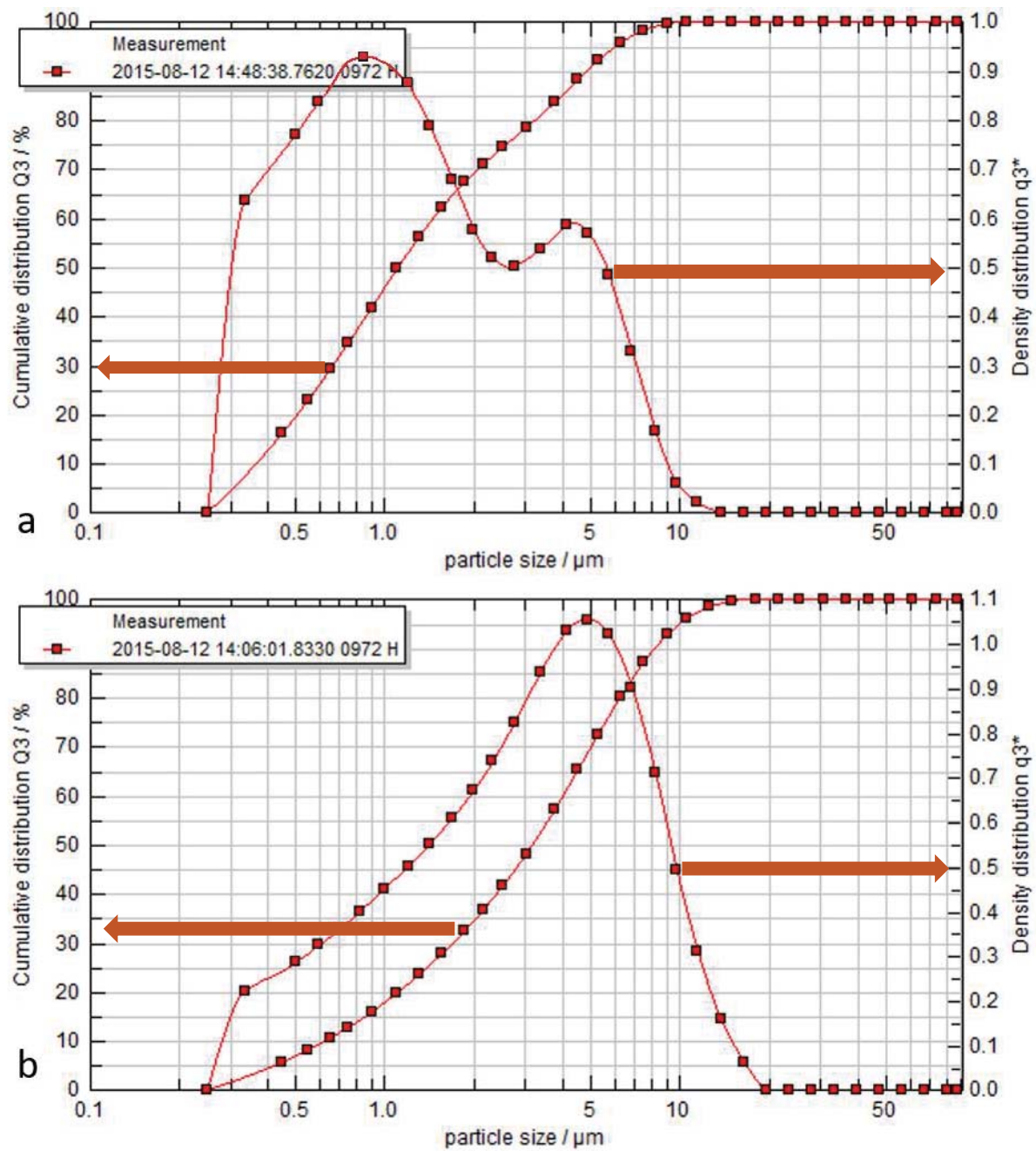


Figure 33 Particle size distribution for (a) NiO and (b) YSZ-A powders

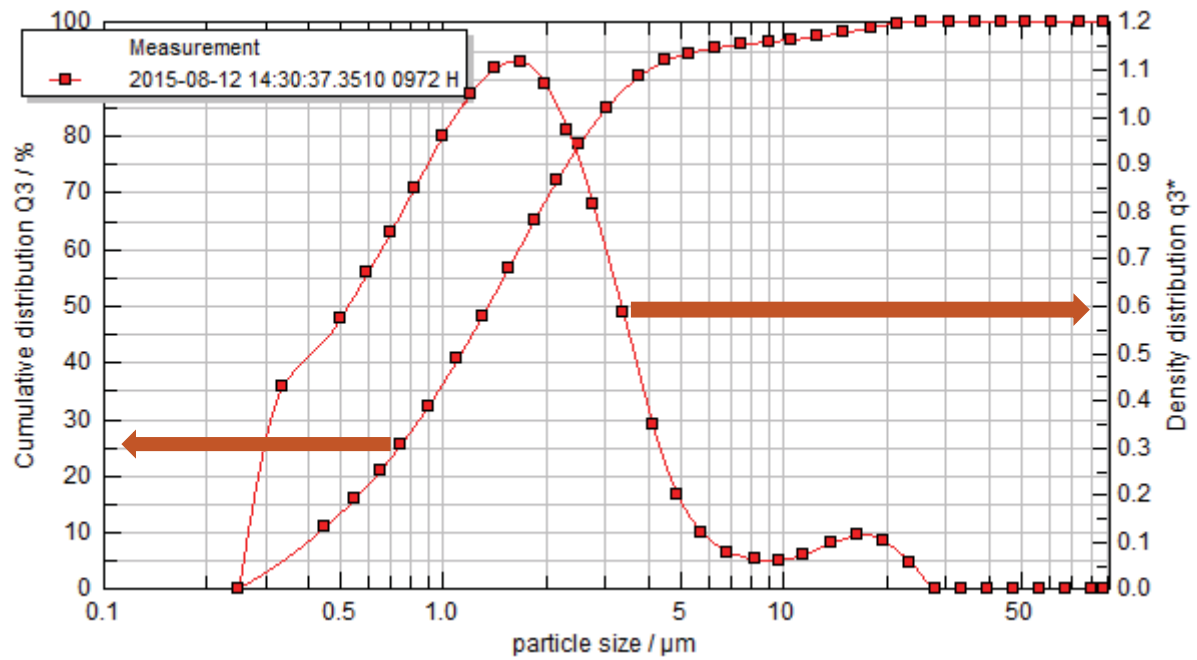


Figure 34 Particle size distribution for YSZ-E powders

SEM images of the three ceramic powders are shown in Figure 35 and Figure 36. In terms of the particle shape, it is believed that a regular geometry is desired for optimal powder packing, powder packing behaviour will be detailed in the later sections of this chapter. The microscopic geometry of the particles confirms the characteristic results of the particle size analysis. It is worth noting that all three types of powders are in the form of flake or lump, which means the irregularity of the particle shape cannot be neglected when powder packing or any other resultant analysis is being carried out. In modelling powder packing it is generally accepted that the particles are assumed to be spherical. Distributions are considered possible but generally narrow particle sizes are assumed in the simpler models. In the formulation of pastes, it has been said that irregular shaped particles can promote

phase migration [213] but unfortunately, the feed ceramic powders are rarely spherical as is the case here.

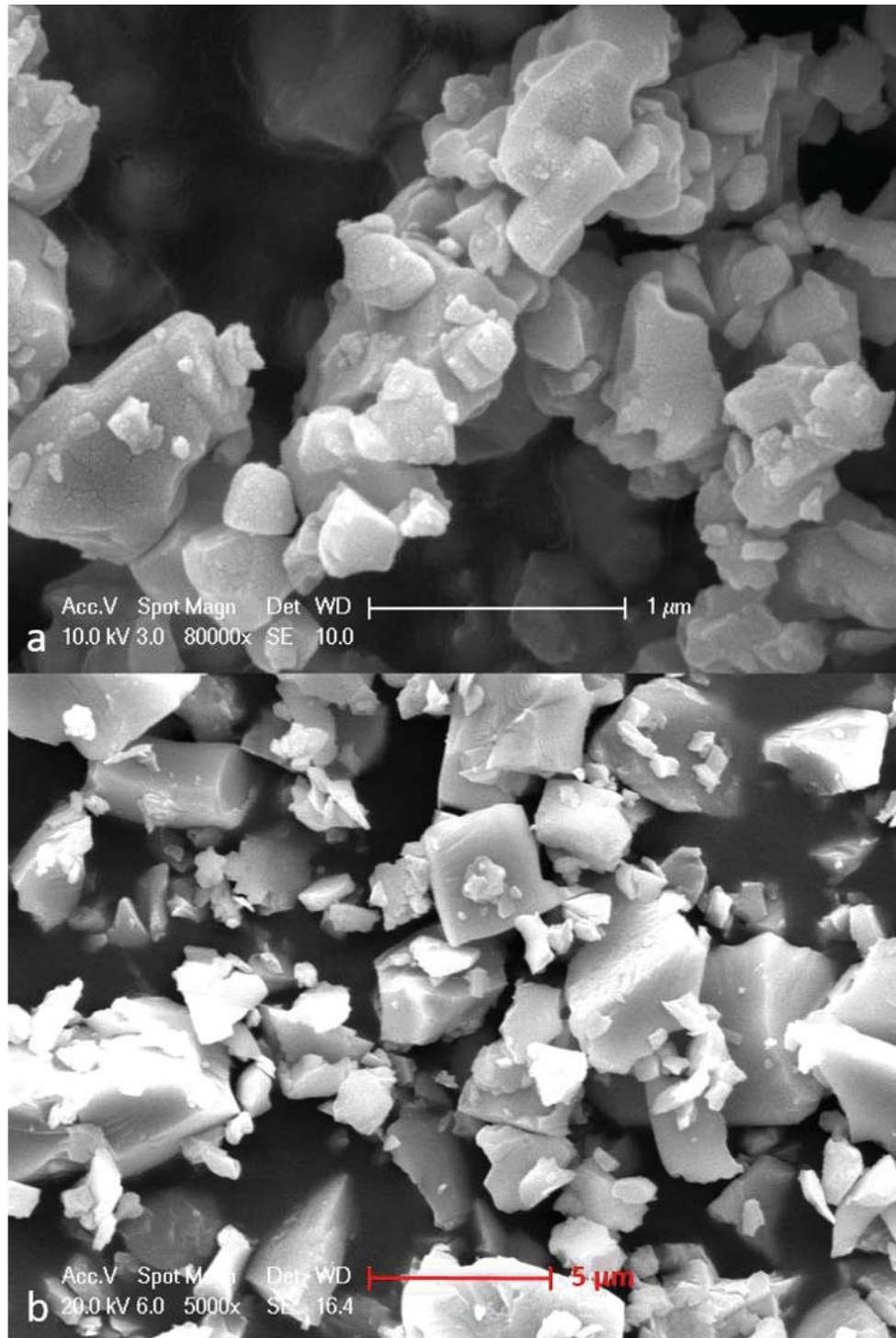


Figure 35 SEM imaging for (a) NiO and (b) YSZ-A powders

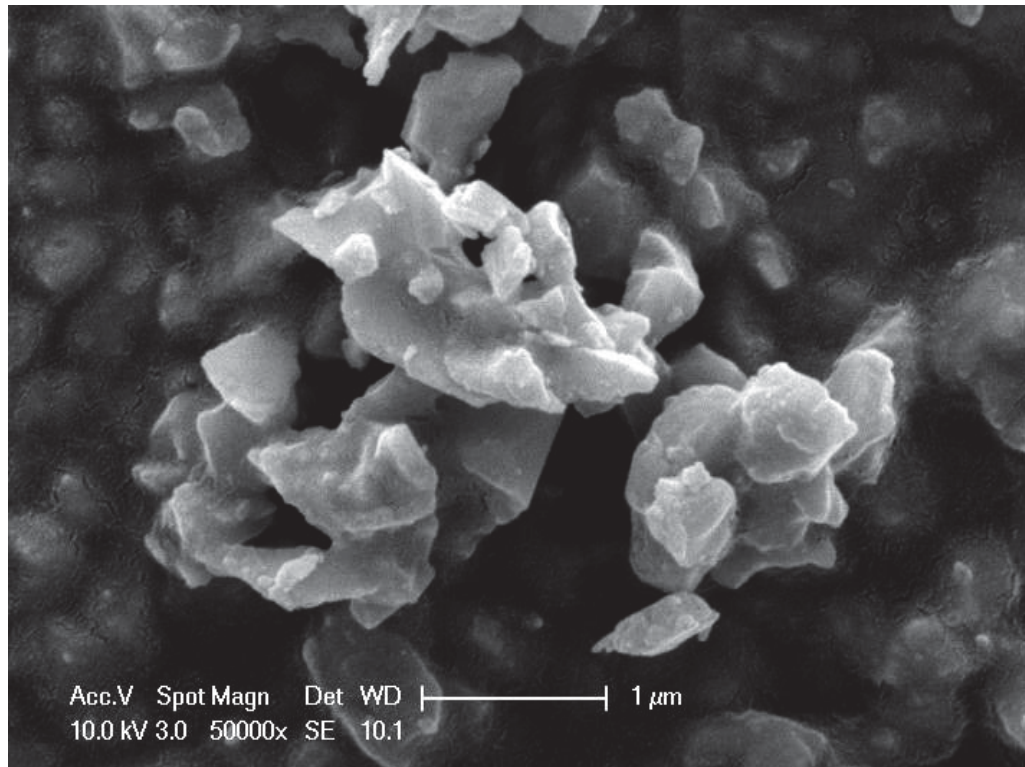


Figure 36 SEM imaging for YSZ-E powders

BET results are listed in Table 5. It would generally be expected that finer powders would have higher surface area but in the selected powders this is not strictly followed. Although the mean particle of NiO powder is comparable with that of the YSZ-E powder, the bimodal size distribution contributes to a surface area value that falls between the two zirconia powders. The finer zirconia powder is seen to contain discrete fine particles, which are assumed to contribute strongly to the powders' higher surface area.

Table 5 BET surface area data for basic ceramic powders

Powder Description	BET surface area
NiO	3.28±0.007 m ² /g
YSZ-A	1.26±0.004 m ² /g
YSZ-E	6.14±0.008 m ² /g

4.2.2 The introduction of pore former

Although initially only the ceramic powders were considered in the formulation of the extrudates, 5 g of corn starch (i.e. 46.16 vol% of the solid phases) was introduced to produce sufficient porosity within the anode layer, for the purpose of efficient gas transfer, after sintering. This was the primary reason for the corn starch addition but it was also shown that the distribution of corn starch in the extrudates could be related to phase maldistribution and this aspect is considered in Chapter 5. The characterisation results for particle size and shape for corn starch are shown in Figures 36, Figure 38 and Table 6, indicating a reasonably spherical particle morphology and a mean particle size of ~17 µm.

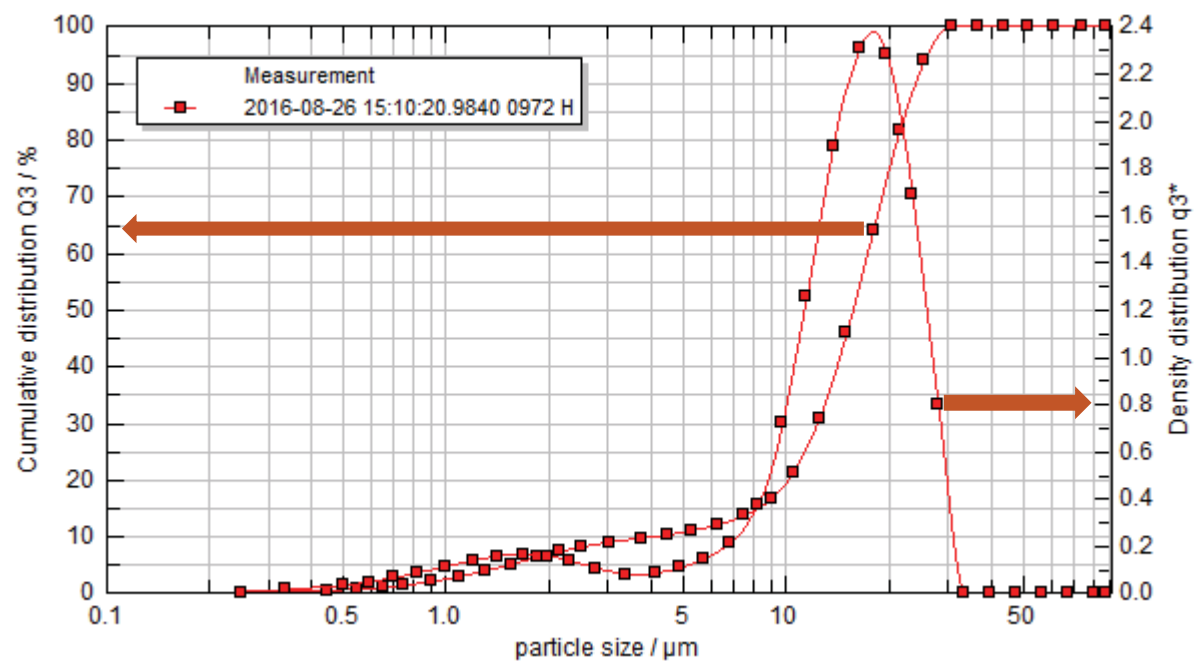


Figure 37 Particle size distribution for corn starch powders

Table 6 Statistical particle size data for the as-received corn starch powders

Powder	D_{10}	D_{50}	D_{90}
Description			
Corn Starch	5.68 μm	17.23 μm	29.88 μm

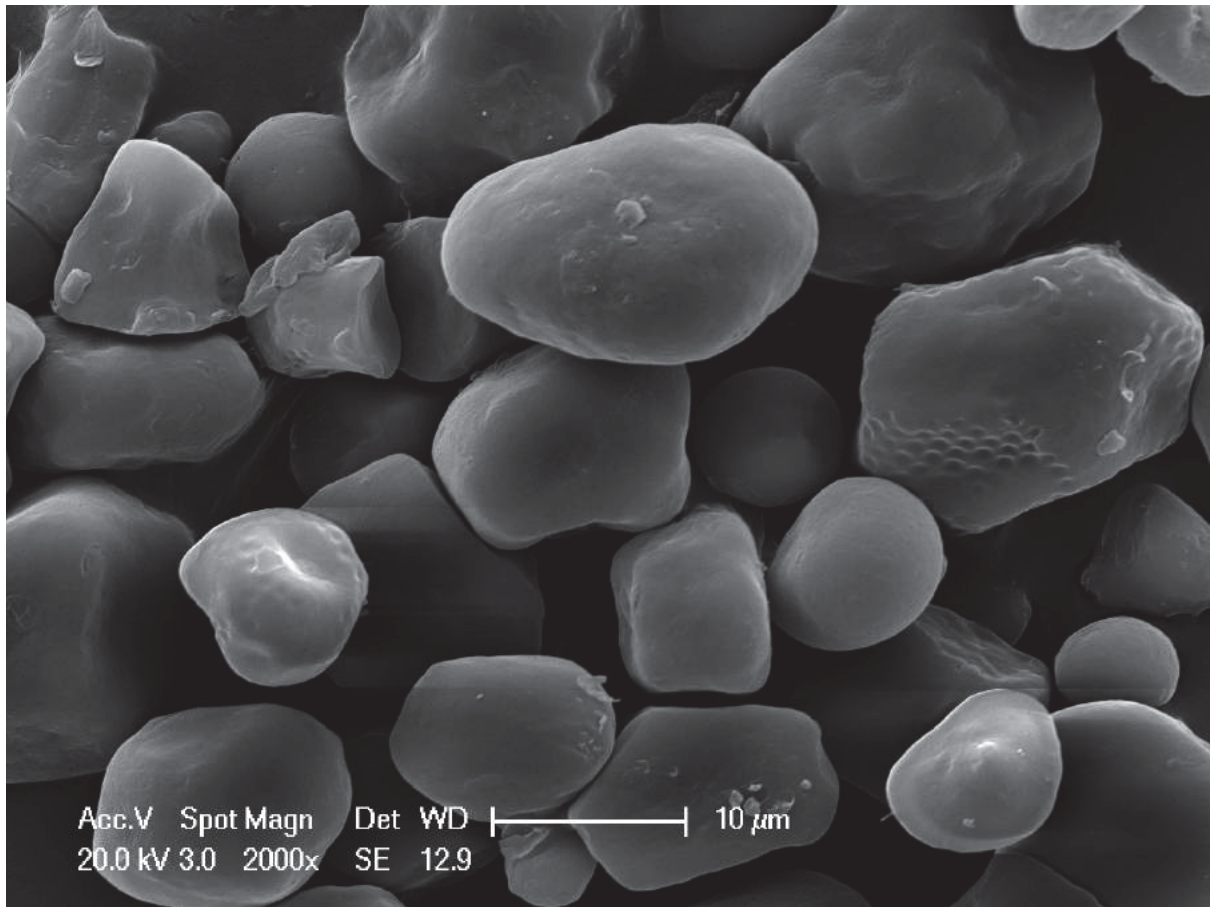


Figure 38 SEM image of the corn starch powders

4.2.3 Powder packing study and initial extrusion trials

4.2.3.1. Powder compaction behaviour

As the maximum volume fraction achievable for the random packing of the separate NiO and YSZ-A powders is an essential parameters for the prediction of minimum liquid fraction into a binary/ternary solid powder system during the paste formulation, a compaction die with a diameter of 13 mm was used to study the corresponding powder behaviour. The load was applied until a maximum load (initially at 5 kN) was attained. That load was held for 5 min and then released. Height measurements of

the cylindrical compact and a volume calculation were carried out to determine the maximum packing density achieved.

Plots of compressive load against compressive displacement are shown in Figure 39 for NiO powders, where the x-coordinate indicates the negative value of the compact height, by convention. The compaction process for the YSZ-A powders was consistent with that of NiO powders and so is not shown.

The volume reduction of the powder compact has to overcome two barriers: friction due to relative motion between the particles and elasticity due to instantaneous shape deformation. When the number of contact points between powders is increased, both barriers will be shifted (i.e. maximum static friction and macroscopic elastic modulus). As a result, the compression curves exhibit an increasing gradient with increasing compaction load. At the beginning of the compaction process, relative motion between loose powders predominates, while particle shape change gradually become dominant during the later stages of the process, as a result of limited powder mobility. In the extreme no more powder flow or slip will be induced by raising the pressure, unless irreversible plastic shape deformation occurs (not likely for rigid ceramic powders).

Repeated loading to the same maximum load in principle generates only particle shape change. Figure 39a shows that when the compact is reloaded to the fixed load of 5 kN the displacement is small with no change in curve profile with each successive repeat. A subsequent compaction load over the previous maximum value will re-generate powder flow behaviour. In the NiO powder this is indicated by a reduced slope beyond 5 kN in Figure 39b when the force was driven to 15 kN.

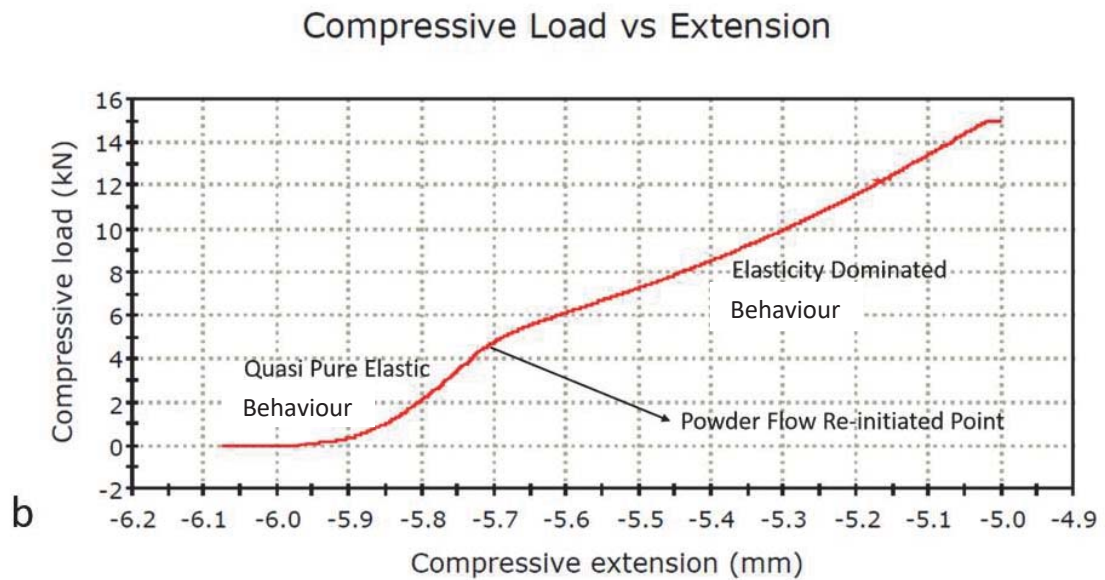
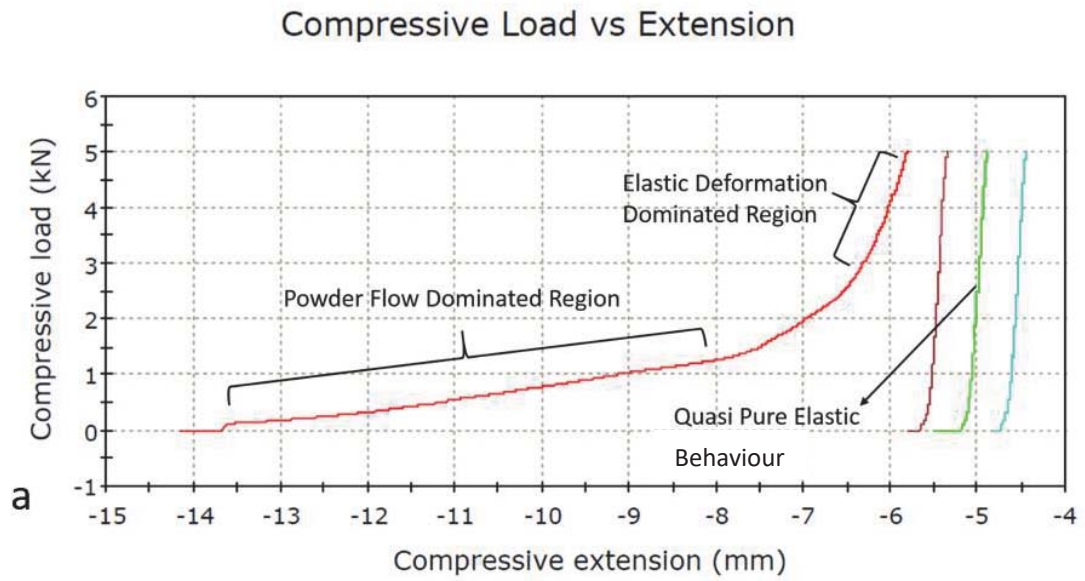
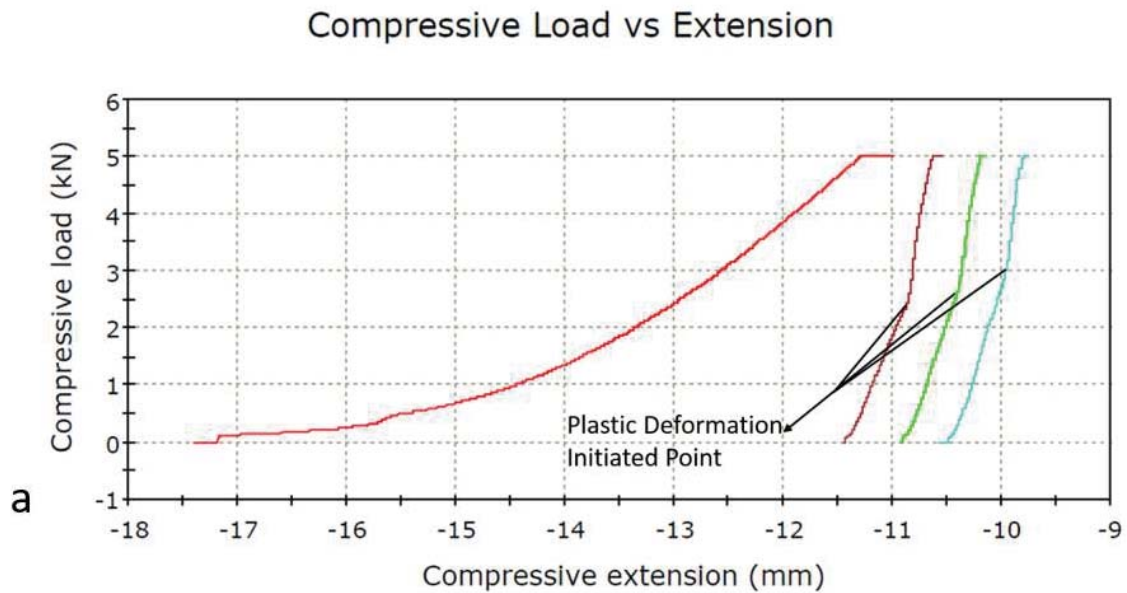


Figure 39 Continuous compaction curves for NiO powders (3 g) with (a) multiple reloads at fixed maximum load 5 kN and (b) single reload at raised maximum load from 5 kN to 15 kN

Figure 40 shows the compaction curves for corn starch powders using an identical test method.

For ceramic powders, the densest packing status is said to be reached before plastic deformation occurs. However, for corn starch, the plastic distortion of the particles within the bed was thought to be initiated well before the packing limit had been reached. This was thought to be indicated by the sudden gradient rise on the repeated load curves shown in Figure 40a, where plastic deformation or breakage of starch powders significantly increase the inter-particle contact points. Typically, for soft particle compaction such as in the case of starch the load-extension curve after a relatively low pre-load will show an initial gradient rise and followed by a fall, as shown in Figure 40b. This form of behaviour will continue if the compaction load at each repeat is increased, until no significant powder flow occurs (Figure 40c).



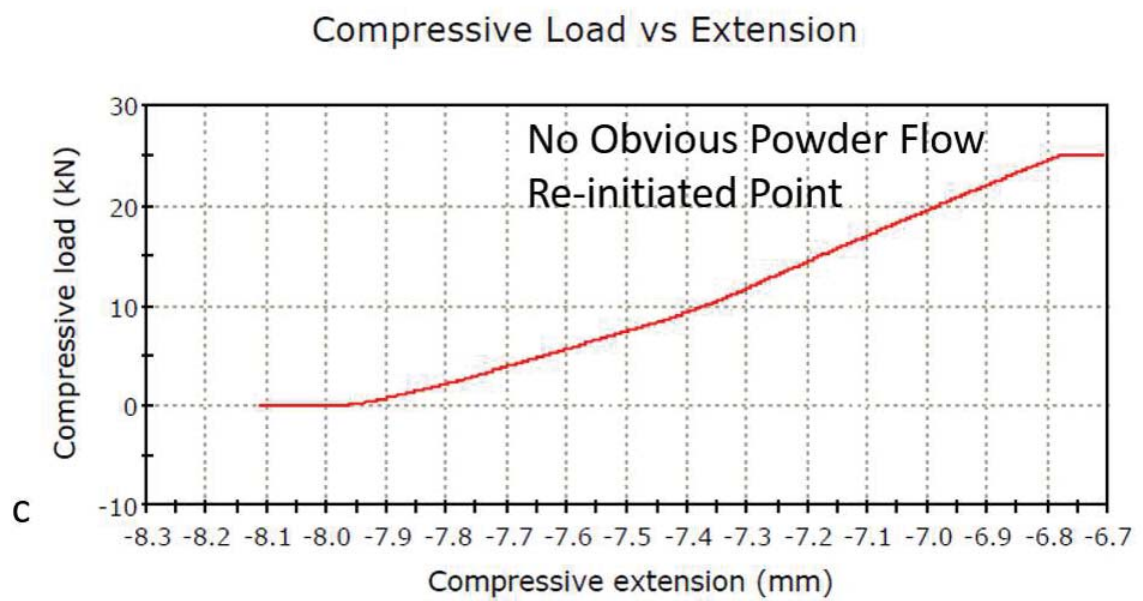
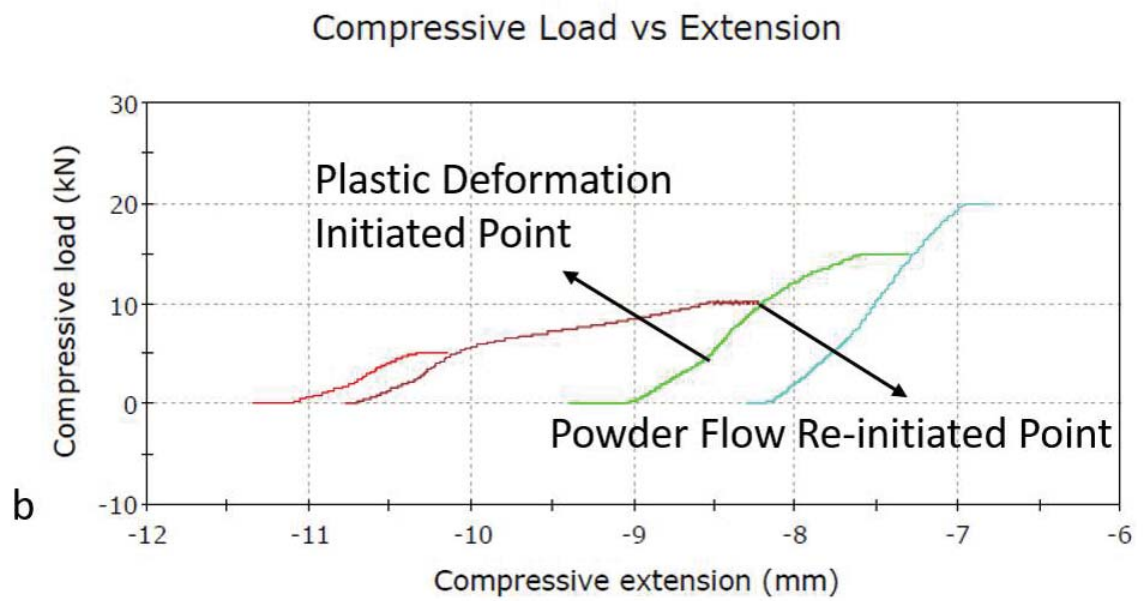


Figure 40 Continuous compaction curves for corn starch powders (1.5 g) with (a) multiple reloads at fixed maximum load, (b) multiple reloads with rising maximum loads and (c) single reload at the highest maximum load, 25 kN

Repeated pressing with rising load was stopped when no significant compact height change between adjacent reloads was observed. The compact volume and density were calculated and converted to packing density values, which are listed in Table 7 and Table 8. Note that for corn starch powders, further compact volume change is still feasible, but not necessary for this study.

Table 7 Processing parameters for powder compaction

Powder Type	Weight	Final Load	Final Height
NiO	3 g	44 kN	5.08 mm
YSZ-A	3 g	55 kN	5.58 mm
Corn Starch	1.5 g	15 kN	7.69 mm

Table 8 Calculated packing density results

Powder Type	Compact Density	Theoretical Density	Packing Density
NiO	4.45 g/cm ³	6.67 g/cm ³	66.72%
YSZ-A	4.05 g/cm ³	6.10 g/cm ³	66.40%
Corn Starch	1.47 g/cm ³	1.50 g/cm ³	98.00%

The maximum packing densities for both ceramic powders are around 2/3 of their theoretical densities, in agreement with literature reports [214, 215] of a random packing limit of ~0.64 (noting that this value is for monodispersed spherical powders).

The packing limit for corn starch is hard to obtain by this form of experiment, due to the large plastic deformation that occurs. If the transition between elastic and plastic deformation is considered then it is reasonable to assume a packing fraction of 0.64, especially as the particle shape of the starch is more spherical when compared to that of the other two powders with which it is being combined. In later analysis, the values of 66.72%, 66.40% and 64.00% will be used as the random packing limit volume fraction for NiO, YSZ-A, and corn starch powders, respectively. The determined values were used for the packing density predictions undertaken in Section 4.2.3.2 and 4.2.3.4, for the purpose of calculating the minimum liquid content necessary to form a homogeneous anode paste with a binary/ternary solid powder system.

4.2.3.2 Packing density prediction for binary powder mixture

The expression for extended Westman powder packing model (Equation 12) tailored for a binary system is shown in Equation 24.

$$\begin{aligned}
& \phi_{m,2}^2 \left(\frac{1}{\phi_{\max,2}} - \frac{1 - x'_2}{\phi_{\max,1}} \right)^2 \\
& + 2G_1 \frac{\phi_{\max,1} \phi_{m,2}}{1 - \phi_{\max,1}} \times \left(\frac{1}{\phi_{\max,2}} - \frac{1 - x'_2}{\phi_{\max,1}} \right) \times \left(\frac{1}{\phi_{\max,2}} - 1 + x'_2 - \frac{x'_2}{\phi_{m,2}} \right) \\
& + \left(\frac{\phi_{\max,1}}{1 - \phi_{\max,1}} \right)^2 \times \left(\frac{1}{\phi_{\max,2}} - 1 + x'_2 - \frac{x'_2}{\phi_{m,2}} \right)^2 \\
& = 1, \quad \text{(Equation 24)}
\end{aligned}$$

where G can be calculated by:

$$G_1 = 0.738 \left(\frac{d_2}{d_1} \right)^{-1.566}$$

where $\phi_{m,2}$ is the packing density of NiO with the grain size of d_2 and volume fraction of x'_2 , $\phi_{max,2}$ is the packing density of the binary powder mixture. $\phi_{max,1}$ is the packing density of the YSZ-A, with the grain size of d_1 .

The mean particle sizes of the NiO and YSZ-A powders are $d_2 = 1.19 \mu\text{m}$ and $d_1 = 3.35 \mu\text{m}$ respectively. Assuming both particles are spherical in form and their size distributions are sufficiently narrow, the packing density for any NiO/YSZ-A powder mixture can be predicted by applying corresponding characterised or calculated values of the parameters of the two powders.

The ratio of NiO to Y_2O_3 is fixed in the case of the anode structure by the requirements for optimal triple phase formation. Thus for the formulation under consideration a mixture of 15 g NiO and 10 g YSZ: $x'_2 = 0.58$, $G_1 = 3.73$, $\phi_{max,1} = 0.664$, $\phi_{m,2} = 0.6672$, is used and thus $\phi_{max,2} = 0.7218$. The required amount of liquid phase in paste formulation at this stage of development with a fixed solid dosage (i.e. 15 g NiO, 10 g YSZ) was calculated to be as 1.42 g cyclohexanone. Details of the calculation are:

$$(1) V = m / \rho;$$

$$(2) V_{\text{solid}} = V_{\text{NiO}} + V_{\text{YSZ}}; V_{\text{liquid}} \approx V_{\text{cyclo}} \text{ (No significant volume change after addition of other constituents into cyclohexanone);}$$

$$(3) V_{\text{solid}} / (V_{\text{solid}} + V_{\text{liquid}}) = \phi_{max,2}.$$

where $\rho_{\text{NiO}}=6.67 \text{ g/cm}^3$, $\rho_{\text{YSZ-A}}=6.1 \text{ g/cm}^3$, $\rho_{\text{cyclohexanone}}=0.95 \text{ g/cm}^3$

4.2.3.3 Paste formulations and anode fabrications for binary powder system

In the previous section it was predicted that the minimum weight of cyclohexanone for a binary powder system should be 1.42 g for the standard batch sizes used in this work. Using this as a starting point, a series of anode paste formulations with increasing liquid content were prepared, denoted as Paste 1, 2 and 3, which were subsequently extruded using the die set shown in Figure 21 (tube outside diameter (OD) 4 mm and inside diameter (ID) 2.1 mm) at a fixed plunger speed of 1 mm/min. Details of the material weights used in these paste formulations are listed in Table 9 and Table 10. The PVB binder system was developed by Functional Materials Group in University of Birmingham and proved capable of forming a homogeneous dough-like paste for subsequent extrusion trials [216]. The relative fractions of the separate constituents within the liquid binder phase have been modified by Powell especially for mSOFC anode extrusion [217], with a PVB/cyclohexanone weight ratio being roughly 0.9.

Table 9 Materials with fixed dosage for anode extrusion

Paste constituents	Weight	Weight fraction
NiO	15 g	59.64 wt%
YSZ-A	10 g	39.76 wt%
DBP	0.1 g	0.40 wt%
Steric acid	0.05 g	0.20 wt%

Table 10 Paste formulations with different liquid content

Paste No.	Cyclohexanone	PVB	Solid load vol%
1	1.5 g	1.4 g	71.12 vol%
2	2.0 g	1.8 g	64.87 vol%
3	2.6 g	2.4 g	58.69 vol%

Table 11 and Figure 41 indicate the milling (mixing) and extrusion characteristics of the paste formulations with varying liquid content. Paste 1 was unextrudable and this is thought to have a solids loading beyond the calculated critical value of 72.18%, due to the loss of liquid during paste processing (the theoretical solid loading of Paste 1 was 71.12 vol% from Table 10). Considering that the particle shape of ceramic powders is not spherical, which will generally be reducing the packing density and the relatively wide particle size distribution of these powders (which always increases the packing density) it is not surprising that the critical solids loading may not have been precisely predicted. Nevertheless, it proved worthwhile to use the calculated packing fraction as a reference threshold value when preparing workable ceramic pastes.

Table 11 Paste processing descriptions with different liquid content

Paste No.	Milling characteristics	Extrusion load at 1 mm/min
1	Paste slightly separate from the milling roll, and very easy to remove from the rollers at the end of the process	Unextrudable
2	Paste stuck to the milling roll, but was easily removed at the end of the process	Ranging from 7.5 kN to 8.8 kN
3	Paste had a gel-like form and was hard to remove from the milling roll at the end of the mixing process	Generally fixed at 4.0 kN

Paste 2 and Paste 3 exhibited good extrudability with no obvious surface or cross-sectional defects observed on or in the processed anode tubes, although extrudates manufactured from Paste 3 were relatively soft and could not hold their tubular shape well when lying horizontally during drying. An unexpected phenomenon was that the extrusion load for Paste 2 kept increasing (by 1.3 kN after the initial rapid increase in load and the emergence of the extrudate, i.e. 3.27 MPa) while being extruded, indicating that the paste consistency may rise during the process. According to Rough et al. [218], this phenomenon could be attributed to liquid phase migration,

which occurs when comparatively dry pastes are used. However, the solids loading of Paste 2 (64.87%) is far from the critical value solids loading of this system, and no significant phase migration was expected or observed. Gross phase migration can be detected by free liquid on the surface of the extrudate or at the joints of the extruder, but no such observations were made in the paste developed here. Therefore, further analysis was required to understand this phenomenon and is considered in detail in Chapter 5.

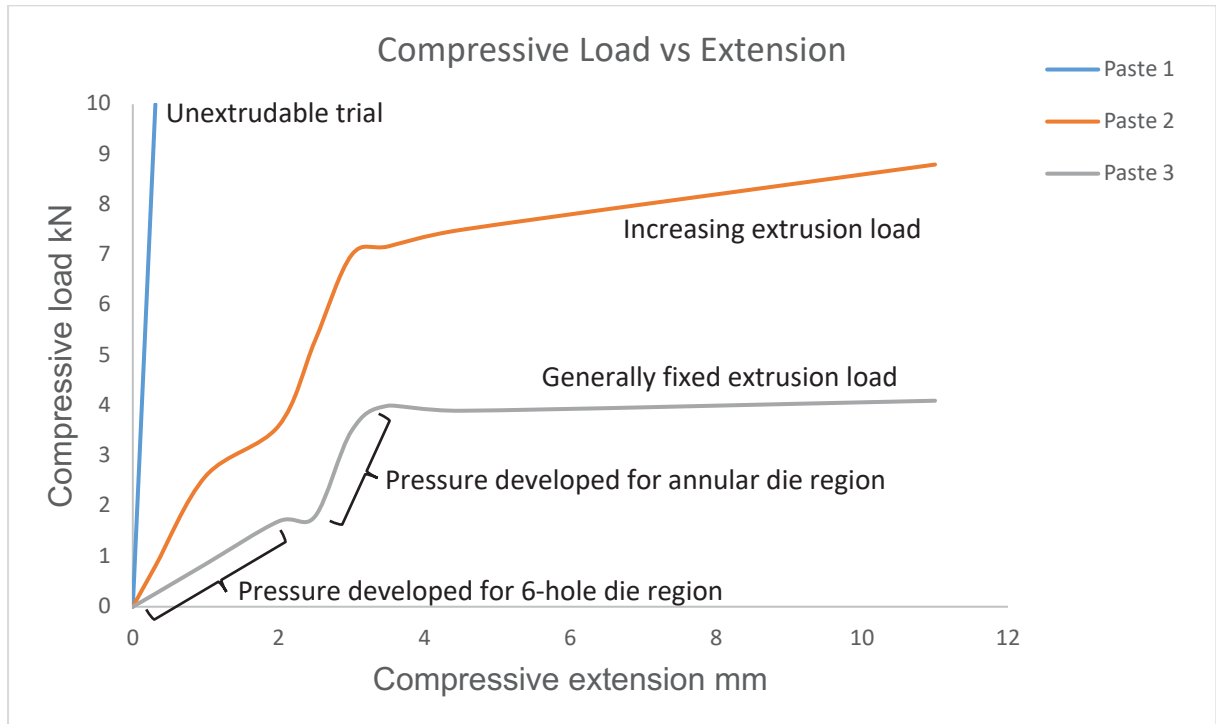


Figure 41 Compressive Load vs Extension curves for extrusions without pore former

To complete the whole fabrication route of anode tubes for further characterisation, the green extrudates were dried and furnace treated, based on the literature review in Section 2.2.1.1 and repeat laboratory experience, to acquire fully sintered

products. The drying and sintering process for the as-extruded anode tubes is detailed in Table 12 and Table 13. Careful drying and sintering processes were established, as it was observed that immediate drying in the oven would distort the tubular shape. Furthermore, hasty sintering before adequate drying would diminish the tube inside diameter (or even eliminate it) and leave considerable large pores within the ceramic body, as a result of violent solvent vaporisation.

Table 12 Drying process for anode tubes

Drying stage	Duration
Room temperature Drying	Overnight
Oven drying at 50°C	8 h
Oven drying at 90°C	Overnight

Table 13 Heating regime for anode tubes

Heating stage	Rate/Duration	Purpose
Ramp to 325 °C	1 °C/min	Drying
Dwell	1 h	
Ramp to 500 °C	1 °C/min	Debinding
Dwell	1 h	
Ramp to 1400 °C	5 °C/min	Sintering
Dwell	2 h	
Ramp to 40 °C	10 °C/min	Cooling

After heating, both the tubes extruded with Paste 2 and Paste 3 were characterised by SEM. A number of large pores (visible to naked eyes) were found which were non-uniformly distributed within some of the tube cross sections for Paste 2. These were found in the vicinity of both the inner and the outer tube surfaces (see Figure 42). These pores were normally concentrated in specific portions of the longitudinal sections and absent along others. The distribution of pores was linked to the regions where the anode paste recombined within the die before passing through the annular die entry (die region between ① and ② in Figure 21). The pores exhibited a tendency to move towards the tube surfaces through the subsequent extrusion in the tube forming die land (towards the die or pin wall) and occasionally forming a line of weakness for crack initiation. In some cases, cracking was observed in the location of this line of weakness after sintering. Additionally, there may have been some associate particle orientation issues where the six separate paste flows came together after the supporting pin plate, but this was not visible in the observed microstructure. Such alignment lamination has been described by Ribeiro et al [219].

In spite of the unwanted porosity formed within the green tubes due to processing features before heating, a dense bulk microstructure was achieved after sintering, as shown in Figure 42. Although it was expected that the debinding stage would generate a certain volume of capillary air channels, previously occupied by liquid and polymer phases, the sintering stage, which initiates merging and grain growth, eventually eliminated most of the inter-particle porosity (e.g. theoretically 35.1 vol% for Paste 2) and leaving a relatively dense compact.

With regard to the whole manufacturing path for SOFC (Figure 18), another origin of porosity is the downstream reduction process, where NiO is reduced to elemental Ni,

however the porosity generated by this is also limited. A dense anode structure is not desired for gas penetration when working as part of a fuel cell, hence the addition of a pore former is considered to be beneficial for enhancing cell performance. To overcome these issues a pore former was added to the formulation, and from the literature and general considerations corn starch was selected as the additive. It has a uniform particle size and burns cleanly leaving little ash in the product, an important feature for the performance of the cell.

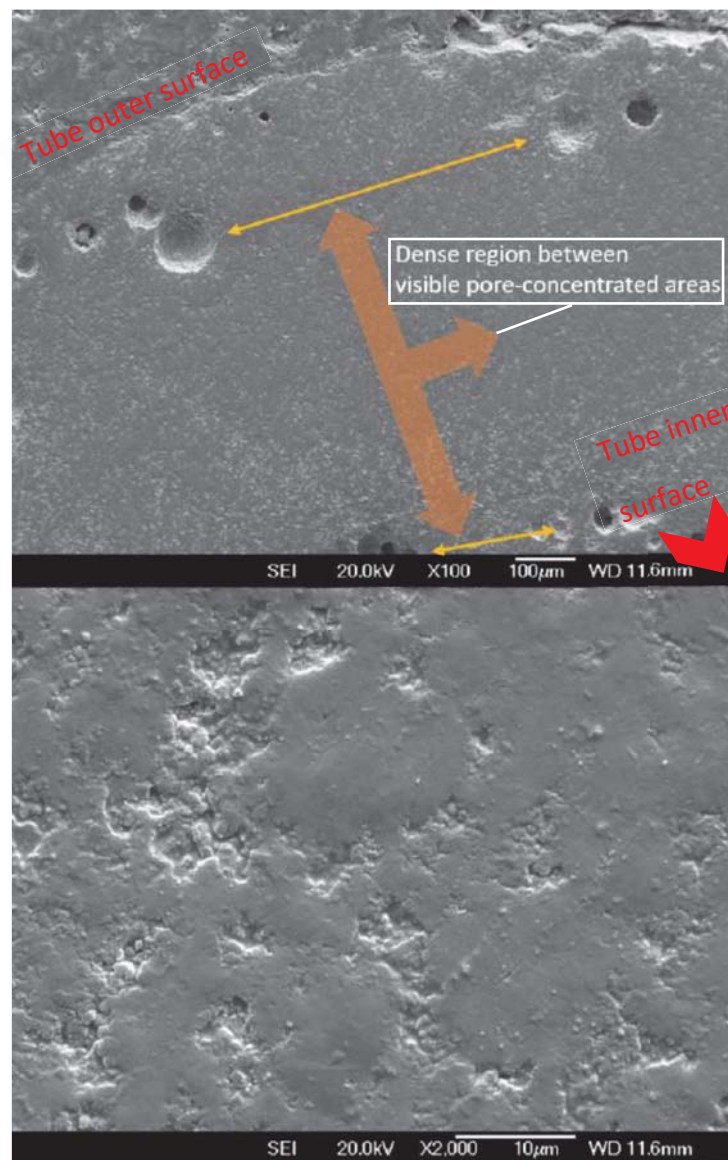


Figure 42 SEM imaging for sintered anode cross section without pore former

4.2.3.4. Packing density prediction for ternary powder mixture

The packing study of a ternary system (NiO, YSZ-A and starch powders) starts with the binary mixture of corn starch and YSZ-A, whose mean particle size is larger compared to NiO powders. Equation 24 was applied once more to work out the corresponding packing parameters. Then a tailored packing expression (Equation 25) for the ternary system was applied:

$$\begin{aligned} \phi_{m,3}^2 \left(\frac{1}{\phi_{\max,3}} - \frac{1 - x'_3}{\phi_{\max,2}} \right)^2 \\ + 2G_2 \frac{\phi_{\max,2}\phi_{m,3}}{1 - \phi_{\max,2}} \times \left(\frac{1}{\phi_{\max,3}} - \frac{1 - x'_3}{\phi_{\max,2}} \right) \times \left(\frac{1}{\phi_{\max,3}} - 1 + x'_3 - \frac{x'_3}{\phi_{m,3}} \right) \\ + \left(\frac{\phi_{\max,2}}{1 - \phi_{\max,2}} \right)^2 \times \left(\frac{1}{\phi_{\max,3}} - 1 + x'_3 - \frac{x'_3}{\phi_{m,3}} \right)^2 = 1, \text{ (Equation 25)} \end{aligned}$$

$$(G_2 = 0.738 \left(\frac{d_3}{\bar{d}_2} \right)^{-1.566})$$

where $\phi_{m,3}$ is the packing density of NiO with the grain size of d_3 and volume fraction of x'_3 , $\phi_{\max,3}$ is the packing density of the ternary powder mixture. $\phi_{\max,2}$ is the packing density of the binary powder system of corn starch and YSZ-A. $\phi_{m,2}$ is the packing density of YSZ-A with the grain size of d_2 and volume fraction of x'_2 , $\phi_{\max,2}$ is the packing density of the starch/YSZ-A powder mixture. $\phi_{\max,1}$ is the packing density of the corn starch, with the grain size of d_1 . \bar{d}_2 is the characterised mean particle size of the starch/YSZ-A powder mixture. For the mixture of 15 g NiO, 10 g YSZ and 5g corn starch: $d_1 = 17.23\mu\text{m}$, $d_2 = 3.35\mu\text{m}$, $d_3 = 1.19\mu\text{m}$, $\phi_{\max,1} = 0.64$, $\phi_{m,2} = 0.664$, $G_1 = 9.59$, $x'_2 = 0.33$, $x'_3 = 0.31$, $\phi_{\max,2} = 0.7583$, $\phi_{m,3} = 0.6672$, $\bar{d}_2 = 10.49\mu\text{m}$, $G_2 = 22.30$. Thus $\phi_{\max,3} = 0.84$.

Powell's [220] work developed an empirical method to determine the critical solids loading (or maximum packing density) for a given powder system, by extending the linear plot of the reciprocal of the Benbow-Bridgwater parameters versus paste liquid content to the horizontal axis. However, the determined solids loading values in that work were always below 60%, in terms of volume fraction, which is significantly lower than the predicted data for the materials and methods developed here. Paste formulations with a solids loading of more than 60 vol% proved extrudable and that work is discussed in section 4.2.3.5.

4.2.3.5 Paste formulations and anode fabrications for ternary powder systems

The minimum amount of solvent required to formulate the pastes was 1.38 g cyclohexanone. The determination of this value was undertaken in the same way as that of a binary system shown in Section 4.2.3.2. A single paste formulation (Table 14) was selected this time to guarantee sufficient extrudability. Repeated extrusions with this formulation were carried out and plots of the load vs extension curves analysed.

Table 14 Paste formulations for extrusions with pore former (72.6 vol% solid)

Paste constituents	Weight	Weight fraction
NiO	15 g	42.67 wt%
YSZ-A	10 g	28.45 wt%
Corn starch	5 g	14.22 wt%
DBP	0.1 g	0.28 wt%
Steric acid	0.05 g	0.14 wt%
Cyclohexanone	2.6 g	7.40 wt%
PVB	2.4 g	6.83 wt%

The extrusion pressure beyond the initial rise prior to extrudate emergence exhibits a similar tendency to that of Paste 2 with no pore former. The variation of plunger load generally falls in the range of 2-4 kN within a single extrusion. Interpretation of the extrusion curves was linked to the die configuration. A transitory slowdown of raising extrusion load was observed at $\sim 1/2$ of the force when the first formed extrudate was ejected from the die, corresponding to the paste recombination region between the 6-hole extrusion section and the annular extrusion section (die region between ① and ② in Figure 21). The profile of the load-extension curves presents a certain degree of variance in their profiles between the different extrusions from nominally identical paste formulations. Examination of the data forms lead to the curves being categorised as fitting one of two profiles, shown in Figure 43.

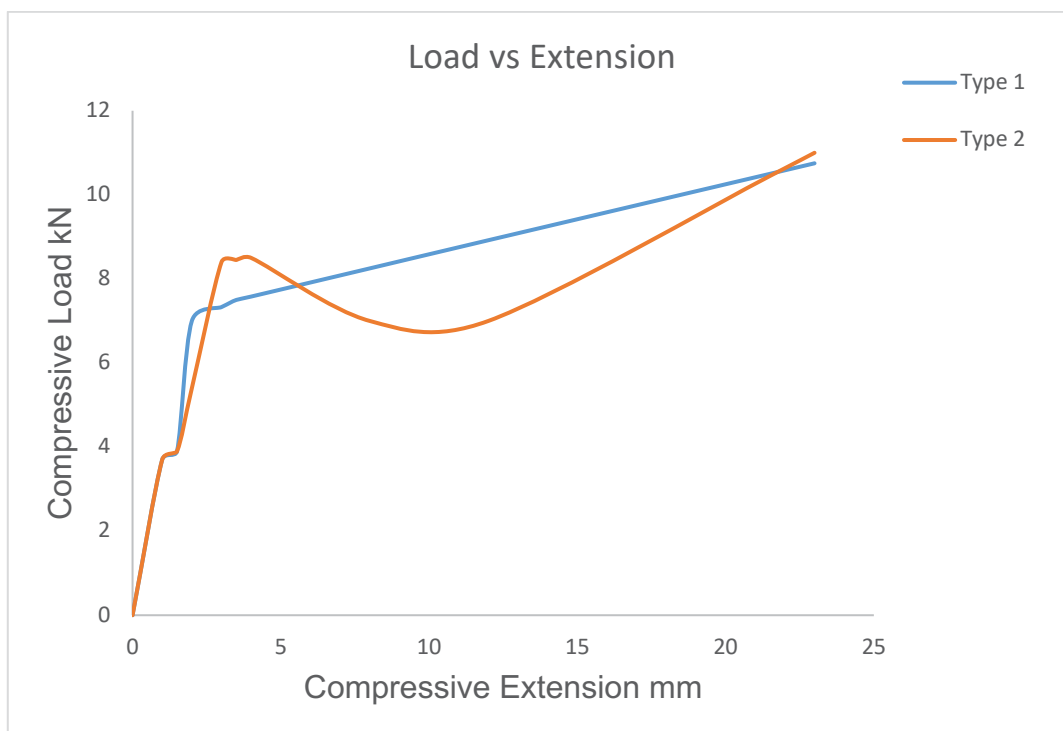


Figure 43 Typical load vs extension curve profiles for extrusions with 5 g pore former and 2.6 g solvent

Type 1 extrusions exhibit a load-extension relationship in which after the initial force rise and flow is initialised, the pressure rises linearly with time or displacement of the ram. Type 2 extrusions showed an interim reduction in load once flow was established before rising again. In the case shown in Figure 43, the rise starts after 10 mm of ram displacement and after about 5 mm of ram displacement after the start of flow. Mechanisms for these two extrusion types will be discussed in Chapter 5.

Another issue was that unwanted macro green body porosity was detected similar to that described for pastes with no pore former addition. This was thought to have been generated by the same mechanism as previously described for extrusions without pore former. This phenomenon, together with the unstable extrusion

pressure, suggested the necessity to increase the paste liquid content. After further extrusion trials a formulation using 3 g of cyclohexanone and 2.7g of PVB was developed with a solid loading 69.6 vol%. This formulation maintained the same fractions of the other constituents (Table 15). A stable extrusion load at 4.5 kN was achieved. Further increases of liquid content caused the paste to stick onto the extrusion pin and pucker up into a much thicker and uneven extrudate. This phenomenon was due to the lower stiffness of the system and there being free liquid at the surface (Figure 44c). If the extrusion was run with pastes of higher liquid content than shown in Table 15 post processing shape retention became an issue. Photographs of fabricated tubes and of them being dried can be seen in Figure 44.

Table 15 Paste formulations for extrusions with pore former (69.6 vol% solid)

Paste constituents	Weight	Weight fraction
NiO	15 g	41.84 wt%
YSZ-A	10 g	27.89 wt%
Corn starch	5 g	13.95 wt%
DBP	0.1 g	0.28 wt%
Steric acid	0.05 g	0.14 wt%
Cyclohexanone	3 g	8.37 wt%
PVB	2.7 g	7.53 wt%

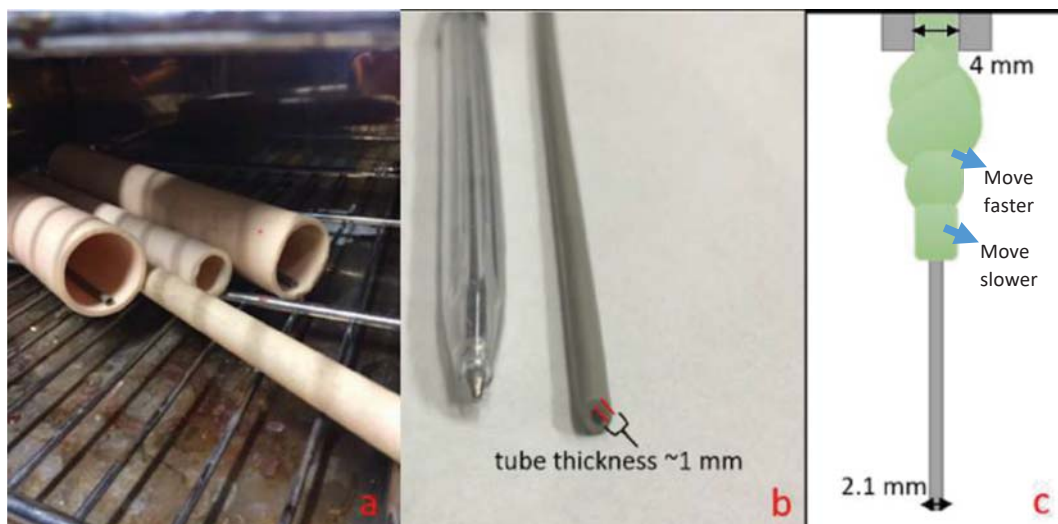


Figure 44 (a) Tube drying in the oven, (b) green anode tube and (c) schematic of anode paste sticking onto the extrusion pin and flowing slower than the paste being extruded behind it causing the paste to thicken and pucker up rather than forming a continuous tube.

4.3. Conclusions

The two ceramic powders and the pore forming agent used to manufacture the anode pastes had different particle sizes, with NiO being the finest and corn starch being the coarsest. Mixing these powders influenced the overall particle packing of the system. To evaluate this, the packing behaviour was modelled first for the required mixture of the two ceramic powders and then for the tri-powder mixture containing corn starch. It was concluded that potential cause of inaccuracy for powder packing prediction was the breadth of the particle size distributions, especially as a strong bimodal distribution was observed in NiO powder. The packing density of separate powder species was determined by compaction tests but the method was shown not to be valid for the plastically deformable corn starch powders.

As a compromise, the application of a theoretical random packing limit (i.e. 0.64 for spherical geometry) was taken for the critical packing fraction of corn starch, as the SEM images showed it to have a quasi-spherical particle shape. Initial extrusion trials were carried out with the paste solids loading determined on the basis of the powder packing predictions, and the extrusion quality was characterised. As a result, the formulations were adjusted to give the required tube structures. It was observed that the extrusion behaviour fell into two distinct types of pressure (load) variation, which will be discussed further in Chapter 5. Extrudates free of macro defects were prepared using the derived formulation and taken forward for further processing into SOFC tubes (Chapters 6, 7 and 8).

Chapter 5 Paste rheology analysis

5.1. Introduction

The mechanism that induced the varied plunger pressures at a given speed during anode paste extrusion required further explanation. In order to study the paste extrusion behaviour, it was important to study the rheological behaviour of the paste during extrusion using an appropriate model. For the rheological investigation, the Benbow-Bridgewater equation was used. This equation has been widely used in the literature [138, 221, 222]. It has found popularly due to its simplicity and because it is based on the concept of plug flow and slip at the wall, which has been demonstrated to dominate in highly solids loaded pastes such as have been developed in Chapter 4. The Benbow-Bridgewater equation was used in preference to the Herschel-Bulkley equation for these reasons. First the rheology parameters were investigated and calculated by capillary rheology applying the basic Benbow-Bridgewater equation (Equation 9). A model was developed for the micro tube extrusion die and the paste parameters derived from the characterisation were used to predict the pressure drop. The focus of this chapter is the interpretation of varying extrusion pressures, which are detailed in the following sections.

5.2. Results and discussion

5.2.1 Six-parameter Benbow-Bridgewater fit

The die set used for anode tube extrusion is complex and a simple ram extruder with interchangeable dies was used to acquire the rheological parameters. The simple die

configuration is given in Chapter 3. Even for this simplest die set, the Benbow-Bridgwater expression, with 2 terms and 6 parameters, still required curve fitting by software. Therefore, the derivation of rheological parameters is divided into two steps, with those for die entry flow acquired first followed by those for die land flow.

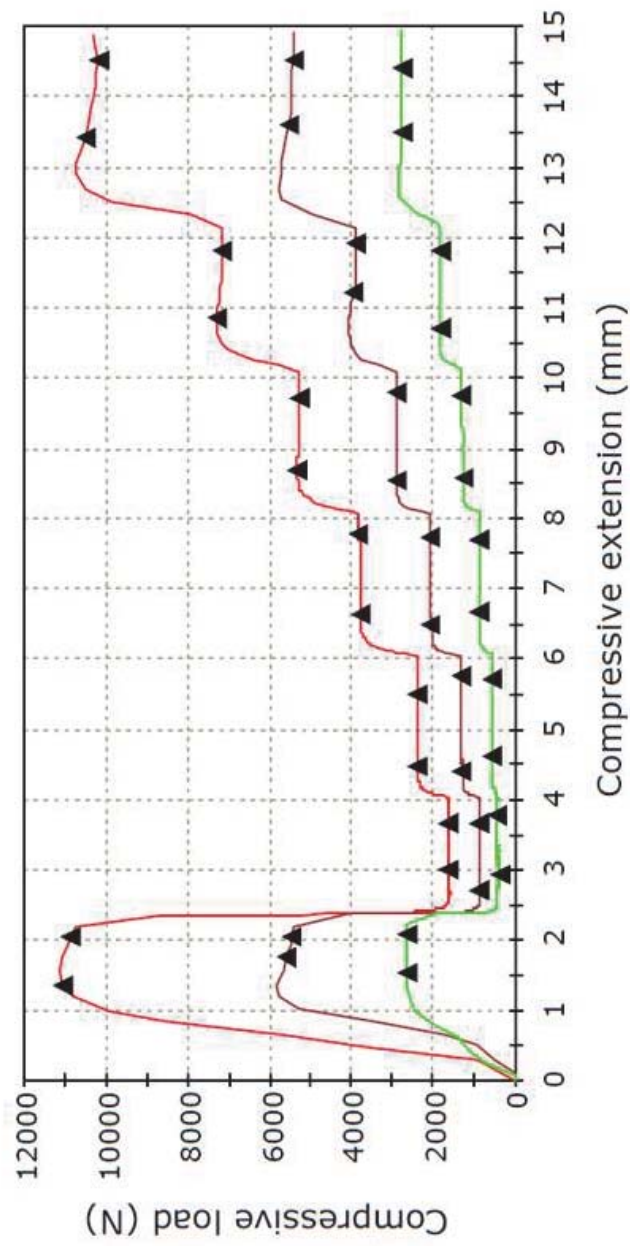
The paste with 5 g of pore former and 2.6 g of solvent (see the full paste formulation in Table 14) was used for the rheology characterisation. Pressure data collected at different extrusion velocities, with different die lengths were handled as follows:

- (1) Fit the pressure vs L/D plot at a fixed velocity (e.g. 1 mm/min) with a linear correlation;
- (2) Collect the intercept value with the vertical axis for each pressure vs L/D fit, to acquire the pressure data for $L/D=0$;
- (3) Fit the 3-parameter equation after eliminating the second term and derive the die entry flow parameters;
- (4) Put the derived parameters back into the equation and take the fitting results of the remaining unknowns.

For each die the paste was extruded at various speeds between 1 and 50 mm/min.

An example of the raw data is shown in Figure 45. The force for each speed is abstracted from the graph and converted to pressure. At any given speed the pressure is largely constant except perhaps at the longer die lengths. This indicates that the paste is reasonably homogeneous and stable in flow. It can be thereby reasonably deduced that, there must be some unrevealed issues existing in the process of anode fabrication with a more complex die layout, in terms of a varying extrusion pressure, as described in Chapter 4.

Benbow-Bridgwater - NiO/YSZ -7.5mm L/D1 - L/D4 - L/D8



	load 1 (50mm/ min) (N)	load 2 (50mm/ min) (N)	load 1 (1mm/ min) (N)	load 2 (1mm/ min) (N)	load 1 (2mm/ min) (N)	load 2 (2mm/ min) (N)	load 1 (5mm/ min) (N)	load 2 (5mm/ min) (N)	load 1 (10mm/ min) (N)	load 2 (10mm/ min) (N)	load 1 (20mm/ min) (N)	load 2 (20mm/ min) (N)	load 1 (50mm/ min) q(2) (N)	load 2 (50mm/ min) q(2) (N)	Average Load N (50mm)	Average Load N (20mm)	Average Load N (10mm)	Average Load N (5mm)	Average Load N (2mm)	Average Load N (1mm)	Average Load N (50mm)
1	11073	10048	1635.2	1635.6	2383.0	2383.0	3780	3780	5316.94	5316.11	7282.47	7179.72	10521.93	10207.640	2375.39	3796.43	5300.02	7236.09	10364.8	7236.09	10364.8
2	5573	5448.2	881.87	881.87	1290.1	1290.1	2043	2043	2891.22	2876.72	3933.34	3868.92	5508.610	5432.100	1309.91	2056.87	2883.97	3901.13	5470.35	2883.97	5470.35
3	2638	2658.4	405.90	410.73	564.56	573.4	890.7	905.2	1279.71	1295.01	1837.01	1948.29	2756.720	2766.390	568.990	897.970	1387.36	1842.65	2761.55	1387.36	2761.55

Figure 45 Extrusion load data for rheology test on the anode paste in relatively high-speed range

Unfortunately, the fitting results for the die entry term contained an exceedingly small value for the yield stress σ_0 (less than nano-magnitude), which was not thought reasonable. The reason for this was that the software starts its fitting with a power law correlation (i.e. without a constant term), and if the power-law-preferred fitting was undertaken then a negligible constant would be generated. To reject the false fitting, more extrusion trials in the plunger velocity range of 0-1 mm/min were designed. However, the extrusion load at extremely low speeds was very sensitive and gave inconsistent data with the model (an example is shown in Figure 46) and considerable repeat tests were carried out to minimise experimental inconsistencies.

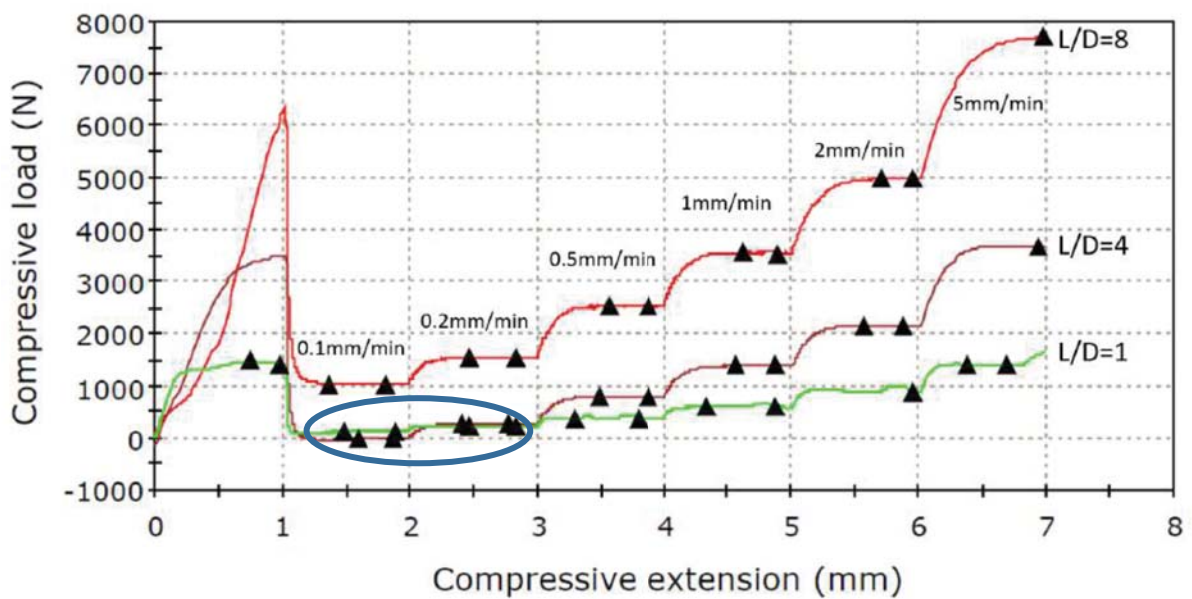


Figure 46 Unreliable extrusion trial with L/D=1 exhibiting a higher plunger load at 0.1 mm/min, compared to the one with L/D=4

Table 16 Pressure data taken for curve fitting with different velocity & L/D combinations

Pressure Plunger rate \ L/D	8	4	1	0
0.1 mm/min	0.88 MPa	0.43 MPa	0.34 MPa	0.21 MPa
0.2 mm/min	1.36 MPa	0.70 MPa	0.46 MPa	0.27 MPa
0.5 mm/min	2.23 MPa	1.21 MPa	0.64 MPa	0.37 MPa
1 mm/min	3.22 MPa	1.76 MPa	0.81 MPa	0.43 MPa
2 mm/min	4.69 MPa	2.59 MPa	1.12 MPa	0.59 MPa
5 mm/min	7.50 MPa	4.06 MPa	1.77 MPa	0.89 MPa
10 mm/min	10.47 MPa	5.69 MPa	2.54 MPa	1.31 MPa
20 mm/min	14.29 MPa	7.70 MPa	3.64 MPa	1.92 MPa
50 mm/min	20.47 MPa	10.80 MPa	5.45 MPa	2.88 MPa

Table 16 lists the pressure data used in the Benbow-Bridgwater fit, along with the fitted values at L/D=0 by linear extrapolation. It should be noted that the pressures at plunger velocities greater than 1 mm/min, for all L/D values, were better fitted by a straight line than at lower velocities, demonstrating again the difficulty of extrusion at low speeds. Curve fitting is executed on the L/D=0 data to fit the rheological paste parameters σ_0 , α and m for the die entry flow with typical R^2 values of 0.99, as given in Table 17.

When fitting for the remaining parameters τ_0 , β and n the same problem of the initial fitting was encountered, resulting in an infinitesimal die wall shear stress, τ_0 , despite the fact that significant work was undertaken attempting to exclude the fitting limitations. τ_0 was obtained by drawing a straight line connecting the adjacent pressure data points for plunger velocities at 0.1 mm/min and 0.2 mm/min and taking its intercept value with the vertical axis ($v=0$). Lastly, a 2-parameter power law fit is applied to determine β and n .

It can be seen from Table 17 that the paste evaluated in this thesis has much smaller bulk yield and die wall shear stresses (not of the same order of magnitude), compared to Powell's [138] results (e.g. $\sigma_0=0.74$ and $\tau_0=0.08$) of an extruded paste with equivalent α and β values.

Table 17 Determined paste parameters using Benbow-Bridgwater fit

Rheological parameter	Fitted value
σ_0	0.037 MPa
α	13.02 MPa·s/m
m	0.52
τ_0	0.009 MPa
β	9.64 MPa·s/m
n	0.57

5.2.2. Modifications to the Benbow-Bridgwater expression for the tubular anode extrusion die set

Aiming at customising the rheology expression for the die set applied for anode extrusion in this study, an attempt to analyse the pressure drop that develops within every step of the process was undertaken. The six-hole and the annular extrusion sections are handled separately, each of which can be subdivided into two adjacent regions with the die entry and the die land flow behaviour initiated successively in each case. The paste-recombination region between the two major extrusion sections is a standard cylindrical geometry (but with a mandrel through the middle), no pressure drop was considered for this region when the modified expression (Equation 26) was developed. As a result, 4 terms would be included in the equation, corresponding to pressure drops due to convergence flow and plug flow, for both main extrusion sections.

By referring to a similar die configuration in literature [223], a modified six parameter Benbow-Bridgwater equation (Equation 26), tailored for the anode extrusion die set and involving 4 terms as explained above, was derived and shown below:

$$P = 2(\sigma_0 + \alpha V_1^m) \ln \frac{D_1}{\sqrt{ND}} + (\tau_0 + \beta V_1^n) \frac{4L_1}{D} + (\sigma_0 + \alpha V_2^m) \ln \frac{D_2^2 - D_i^2}{D_o^2 - D_i^2} + (\tau_0 + \beta V_2^n) \frac{4L_2}{D_o - D_i}, \text{ (Equation 26)}$$

where D_1 is the diameter of the barrel, D is the diameter of the identical holes, N is the number of the holes, L_1 is the length of the holes, L_2 is the length of the annular die land, D_2 is the diameter of the paste recombination region, D_o is the outside

diameter of the annular outlet, D_i is the inside diameter of the annular outlet, V_1 is the paste velocity in the holes and V_2 is the extrudate velocity.

Then by substituting $D_1=22.5$ mm, $D=2$ mm, $N=6$, $L_1=11$ mm, $L_2=8.3$ mm, $D_2=12$ mm, $D_o=4$ mm, $D_i=2.1$ mm, $V_1=VD_1^2/(ND^2)$ and $V_2=VD_1^2/(D_o^2-D_i^2)$ into Equation 26, the predicted pressure for selected extrusion recipe (Table 17) at the plunger rate $V=1$ mm/min is: $P=0.7438$ MPa+ 2.4081 MPa+ 0.8554 MPa+ 2.8214 MPa= 6.8185 MPa, while the corresponding extrusion load is $F=P \cdot \pi D_1^2/4=2.72$ kN.

It was noted that for the die configuration designed for this project, the die land flow behaviour of the pastes dominates the anode extrusion process, compared to the contribution of the die entry flow. This is indicated by the larger numerical values for the 2 die land flows. Moreover, the predicted value for extrusion load is only $\sim 1/3$ of the observed experimental value (see Figure 43 in Section 4.2.3.5). Even when steady extrusion pressure was observed with a higher content of liquid binder system (i.e. 3 g of cyclohexanone with 15 g of NiO), where paste rheological characteristics were changed and a load lower than 2.72 kN should be expected, the experimentally characterised value (4.5 kN, see Section 4.2.3.5) was still significantly greater than the predicted load. The underprediction of the pressure can be attributed to a number of aspects. In Section 5.2.3 the paste behaviour is considered. However, we must consider the limitations of the model. First the parameters were difficult to fit but the final correlation coefficient was very good. However, the geometry of the micro-tubular forming die is far more complex and far finer than the geometry used to measure the data for parameter determination. In particular the velocity of the extrudate from the microtubular die is significantly greater than that used in the determination of the original parameters. Blackburn and Böhm have noted a similar

issue in the extrusion of honeycombs [224] for pastes which exhibit low values of m and n . This discrepancy between the two extrusion conditions and the pressure variations observed in preparing the tubes in Chapter 4, was studied further and the results are discussed in the following section.

5.2.3. Study of the extrusion pressure variations

As described in chapter 4, the suspected reason for varying extrusion pressures with an intermediate solids loading was liquid phase migration. To investigate its effect, the first barrier to overcome was the repeatability of extrusion pressure curves for nominally identical paste formulations. In addition to the two types of curvature profiles categorised in the previous chapter, there are still variations with the extrusion pressure under the same curvature type. This is probably due to the loss of liquid content during paste milling and defrosting, which is sensitive to the room temperature and humidity, and was relatively uncontrolled in these experiments.

Three load versus extension curves, for extrusions with 2.6 g of cyclohexanone and 5 g of corn starch (see the full paste formulation in Table 14), are shown in Figure 47. Curve 1-1 shows a curvature profile of Type 1, while Curve 2-1 and Curve 2-2 belong to Type 2. The difference between Curve 2-1 and Curve 2-2 is the extent of pressure drop from the initial peak before the pressure rises again, with only a slight pressure decrease for Curve 2-1 from the first peak to the trough. The observable extrusion load values for these three curves are listed in Table 18.

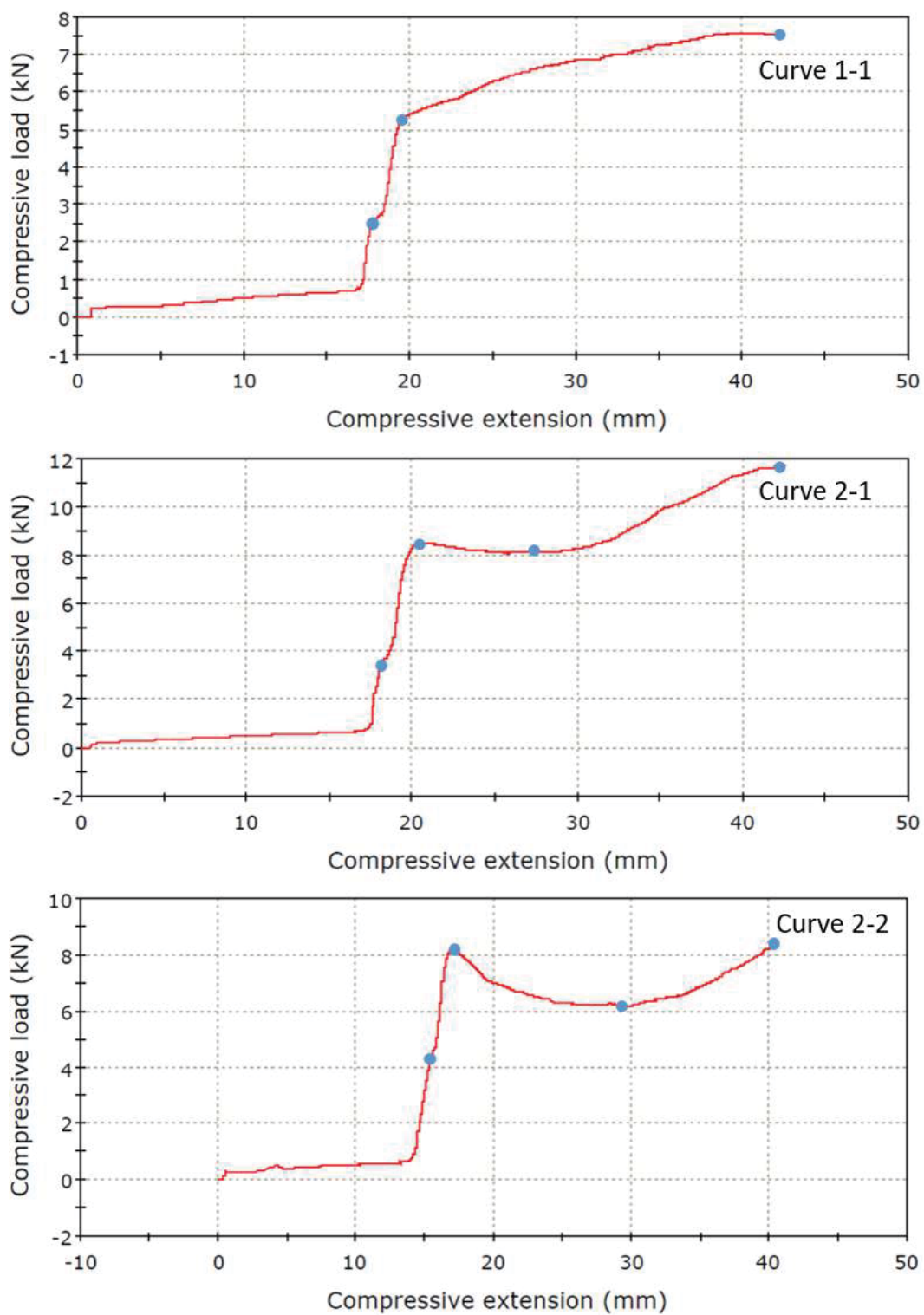


Figure 47 Original load vs extension curves for 3 separate extrusion trials with 2.6 g cyclohexanone and 5 g corn starch, with highlights of notable load points described in Table 18

Table 18 Characteristic extrusion load for 3 separate extrusion trails

Curve No.	1st inflection	2nd inflection	Minimum load after 2nd inflection	Maximum load after 2nd inflection
Curve 1-1	2.5 kN	5.4 kN	5.4 kN	7.6 kN
Curve 2-1	3.6 kN	8.5 kN	8.1 kN	11.5 kN
Curve 2-2	4.4 kN	8.2 kN	6.1 kN	8.4 kN

Compared to the die set used for paste rheology characterisation, the design of die layout for anode extrusion is much more complicated, thus the first inflection point of the curvature, after sufficient paste compaction has occurred, is said to be the pressure value least affected by the die configuration, where the extrusion in the 6-hole region is just initiated. Extrusion pressures at this point can be taken as a reference for liquid content in anode pastes, as extrudates with high liquid volume have higher flowability (i.e. lower viscosity) and require lower extrusion pressure. Accordingly, the liquid content for respective pastes being extruded in these 3 trails has an expected order of Curve 1-1 > Curve 2-1 > Curve 2-2.

The implication is that the pastes either do not have the same liquid content as a result of the inconsistencies of the mixing process or go through a process of phase separation during the extrusion process. It is possible for the liquid content to vary through a single extrusion and that will now be considered. On the one hand, the liquid phase, with higher flowability than the solid phases, migrates faster while the paste is being compacted, resulting in a higher liquid content on the bottom of the barrel. On the other hand, the same process would occur again when the extrusion

process is running, and the liquid phase begins to migrate into extrudates. Outwardly, these two processes would not interfere with each other as they both generate a reduced liquid content within the extruded tubes over the duration of the extrusion. However, as shown in Figure 48, convergent paste flow would create a radial velocity gradient at the base of the barrel, with paste in the central part transferred faster than other regions. Two static zones build up as a result. The static zones are initially composed of relatively high-liquid-containing paste from the bottom of the barrel, the liquid phase within which is thought to migrate into extrudates during subsequent extrusion, leaving a relatively dry solid zone. Simultaneously, a similar migration phenomenon is also occurring in the central flowing paste. Therefore, the resultant liquid phase content when the paste moves forward as a whole becomes complex, depending on the overall paste rheology. The two mechanisms of liquid content variations due to phase migration then have a superposition effect on the characterised pressure, which may lead to the different curve profiles obtained through anode extrusion. Initially there is a probability that the extrudate will be enriched in liquid phase and then progressively become drier as extrusion proceeds. This then would perhaps lead to the pressure initially falling if it is the case that the die land contribution is significant. Such migration could be more pronounced in an initially drier paste which appears to be the case here. At the later extrusion stage, no liquid content is available in the static zones for phase migration, and the extrusion pressure would rise again.

This interpretation is consistent with the observed pressure characteristics exhibited by the 3 chosen curves. Take Curve 2-1 as an example, the offset effect of liquid

phase migration by flowing paste nearly eliminates that by static paste, hence a slight pressure drop is observed before the significant increase occurs.

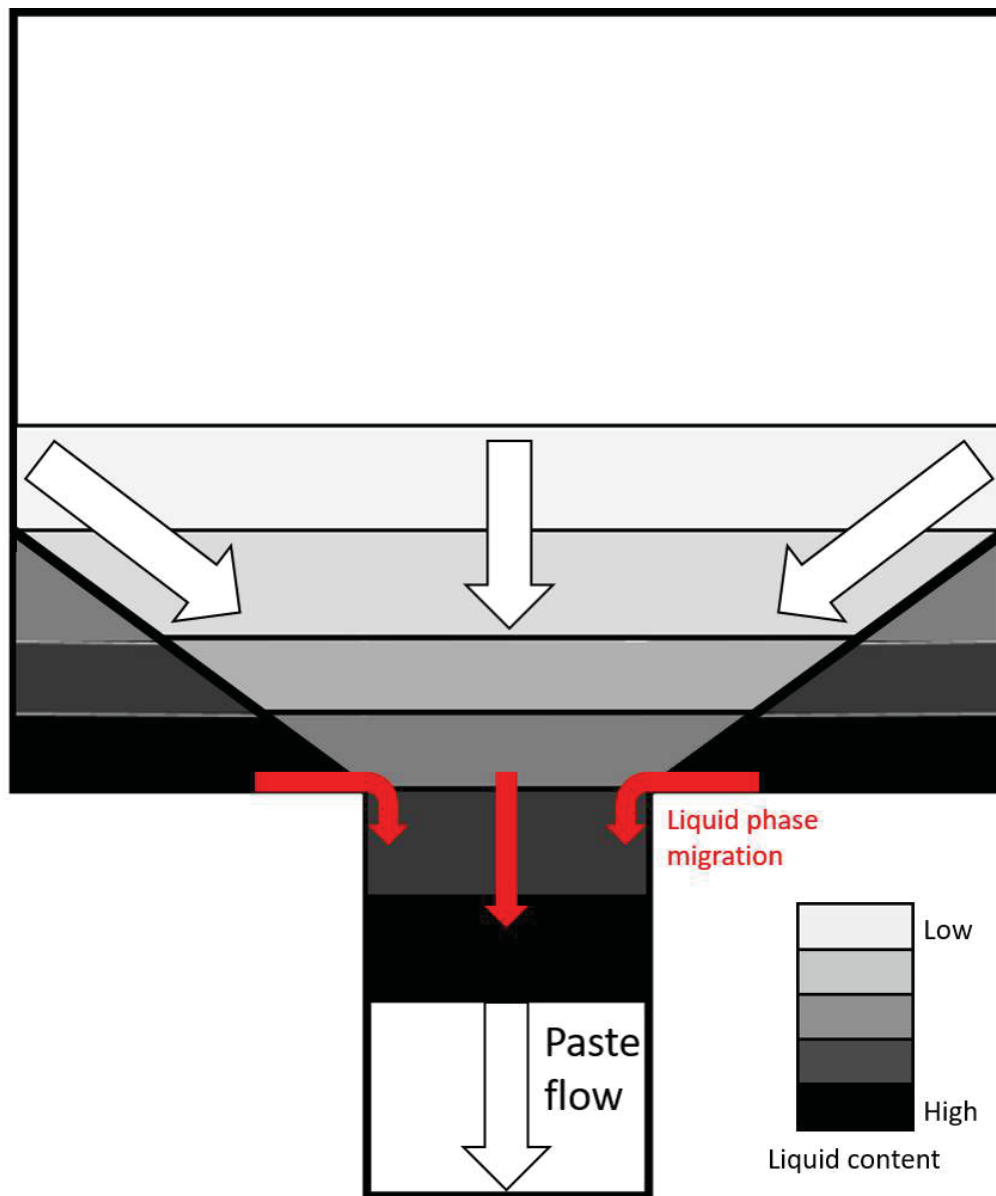


Figure 48 Assumed liquid phase distribution in the barrel during extrusion

More quantitative results are essential to validate or modify the interpretation of varying extrusion pressure. To quantify the liquid content of the extrudates it was first

essential to ensure that all the liquid phase was removed by pyrolysis. To check if the appropriate temperature was selected, thermal gravimetric analysis (TGA) and dilatometry tests were undertaken, and the results are given in Figures 49 and Figure 50. The green anode tube was heated at a rate of 10 °C/min until 1000 °C to characterise the weight change during TGA test, while the debound anode compact sample was heated to 1400 °C at a rate of 5 °C/min for the dilatometry test.

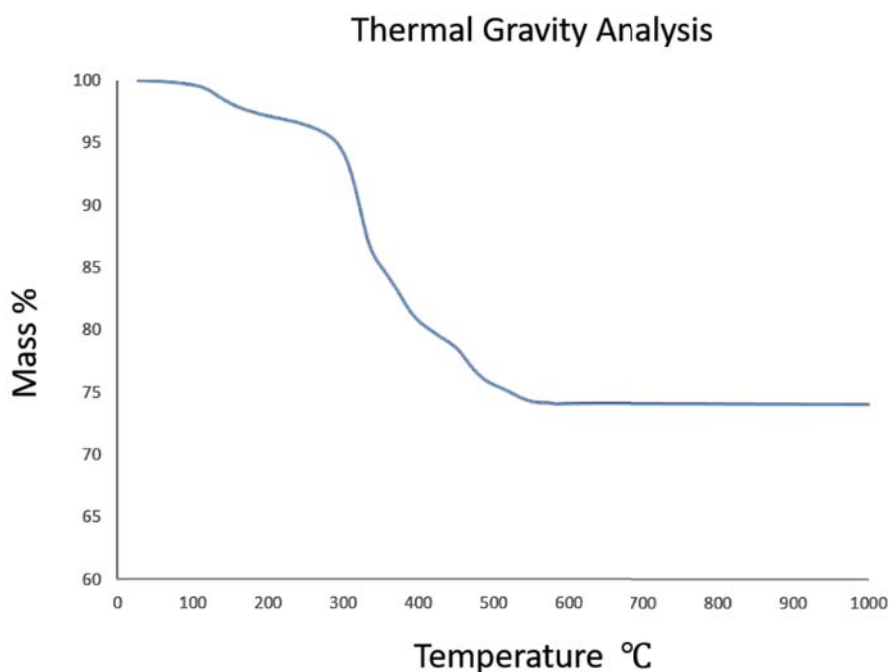


Figure 49 TGA of green anode sample

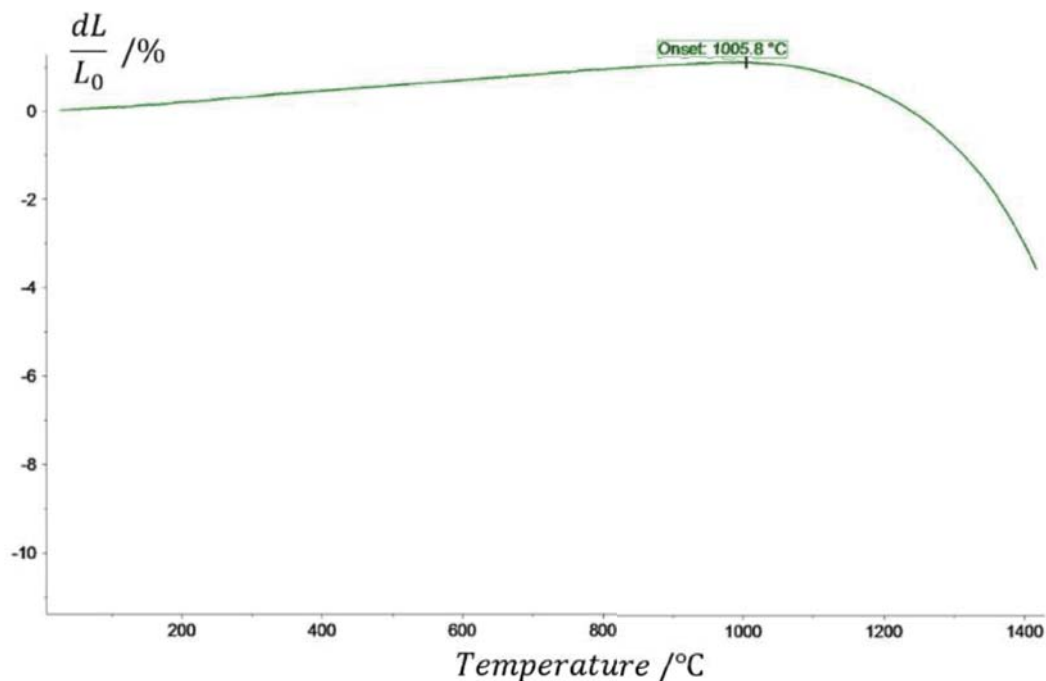


Figure 50 Dilatometry data showing dimensional change during heating of debound anode sample


The TGA result shows that all the organic constituents in the anode sample are thoroughly burnt off (weight loss of 25.9%) between 500 °C and 600 °C, which means the liquid binder phase and the pore former (theoretical weight fraction of 28.9% for the formulation given in Table 14), are totally removed above this temperature range. The dilatometry results indicate that the sintering (i.e. neck growth and grain growth) of anode layer has not been initiated at the temperature of 1000°C. Accordingly, subsequent analysis for phase location would use 1000°C as a heat treatment temperature.

Extrudates for Paste 2, discussed in the previous extrusion trails (Table 10) were used to characterise their liquid fraction as a function of time, as the weight of liquid phase in these extrudates without pore former can be measured with more accuracy.

Four samples of extrudate were collected from different sections of the same extrusion of Paste 2, at the start, approximately at 33% extruded, 66% extruded and at the end of the process. Tube samples were weighed immediately after extrusion and the instantaneous extrusion load recorded at the point of sampling. The samples were dried in an oven at 90 °C overnight before being weighed again. They were then furnace treated at 1000 °C with the end weight of the de-bound samples recorded. The weight change of the tubes can be found in Table 19.

The weight loss after heating is treated as the weight of liquid phase in the corresponding extrudate, while the weight change after overnight oven drying at 90°C is considered to be the solvent weight. However, the paste contained 2 g cyclohexanone in 3.95 g of total liquid phase (i.e. the mixture of cyclohexanone, PVB, steric acid and DBP) as formulated, but the derived liquid weight fraction from drying weight loss was between 10% and 11%, less than formulated for all of the 4 extrudates. The conclusion is that the solvent in extruded samples had not been totally removed after oven drying. Nonetheless, the overnight drying weight loss can still reveal relative liquid content differences between the extruded tubes.

Table 19 Weight change for extrudates of Paste 2 after drying and heating

	Extrudate 1	Extrudate 2	Extrudate 3	Extrudate 4
Increasing				
Extrusion				
time				
Instantaneous	7.5 kN	7.8 kN	8.2 kN	8.5 kN
extrusion				
load				
Initial weight	2.119 g	1.828 g	2.421 g	1.696 g
Weight	0.113 g	0.097 g	0.127 g	0.088 g
change after	(5.33 wt%)	(5.31 wt%)	(5.25 wt%)	(5.19 wt%)
drying (90°C				
overnight)				
Weight	0.261 g	0.225 g	0.297 g	0.207 g
change after	(12.32 wt%)	(12.31 wt%)	(12.27 wt%)	(12.21 wt%)
heating to				
1000 °C				

By comparison, the extrudates with a higher extrusion pressure do have a lower liquid content. However, the situation is not straight forward as the extrusion load rises by 1 kN (i.e. 2.5 MPa) with only a negligible liquid weight change of 0.11 wt%. From this study it is clear that there must be other mechanisms active in the process which lead to the variations in extrusion pressure as the bulk liquid variances cannot produce the observed magnitudes of pressure variation.

One hypothesis is that there is not only liquid phase separation, but also some form of the solid phase separation, which may lead to a higher flowability. These solid particles, together with the liquid phase, could be extruded with a low pressure. There are two types of solid phases that can be considered more likely to give preferential flow: particles with small dimensions and particles with smooth surfaces. To characterise these two features, heated samples of Paste 2, Extrudate 1 (short time) and Extrudate 4 (long time) were ground in a mortar and pestle, and their particle size and surface area measured.

Figure 51 shows the particle size distributions for both extrudates. Before doing the test, the powder samples were suspected to contain large agglomerates that may affect the results, but the data obtained shows that the solid particles in the ground extrudates were well separated. The figure shows the distribution of a NiO/YSZ-A to be a binary powder system, with no obvious differences developing through the duration of the extrusion process.

Table 20 Mean particle size and surface area data for extrudates exhibiting different instantaneous extrusion pressure

Extrudate No.	Instantaneous extrusion load	Mean particle size (D_{50})	BET surface area
Extrudate 1	7.5 kN	1.33 μm	1.401 \pm 0.021 m ² /g
Extrudate 4	8.5 kN	1.57 μm	1.303 \pm 0.036 m ² /g

The mean particle size values, plus characterised BET surface area values are listed in Table 20. Again, no significant difference is observed between the results of two powder samples, which suggests that they have similar particle size distribution and particle surface condition. It can be concluded therefore that there is no or very little bulk separation of the solid phases present in the pastes during the extrusion process. At most this mechanism can only account for minor changes in the extrusion pressure.

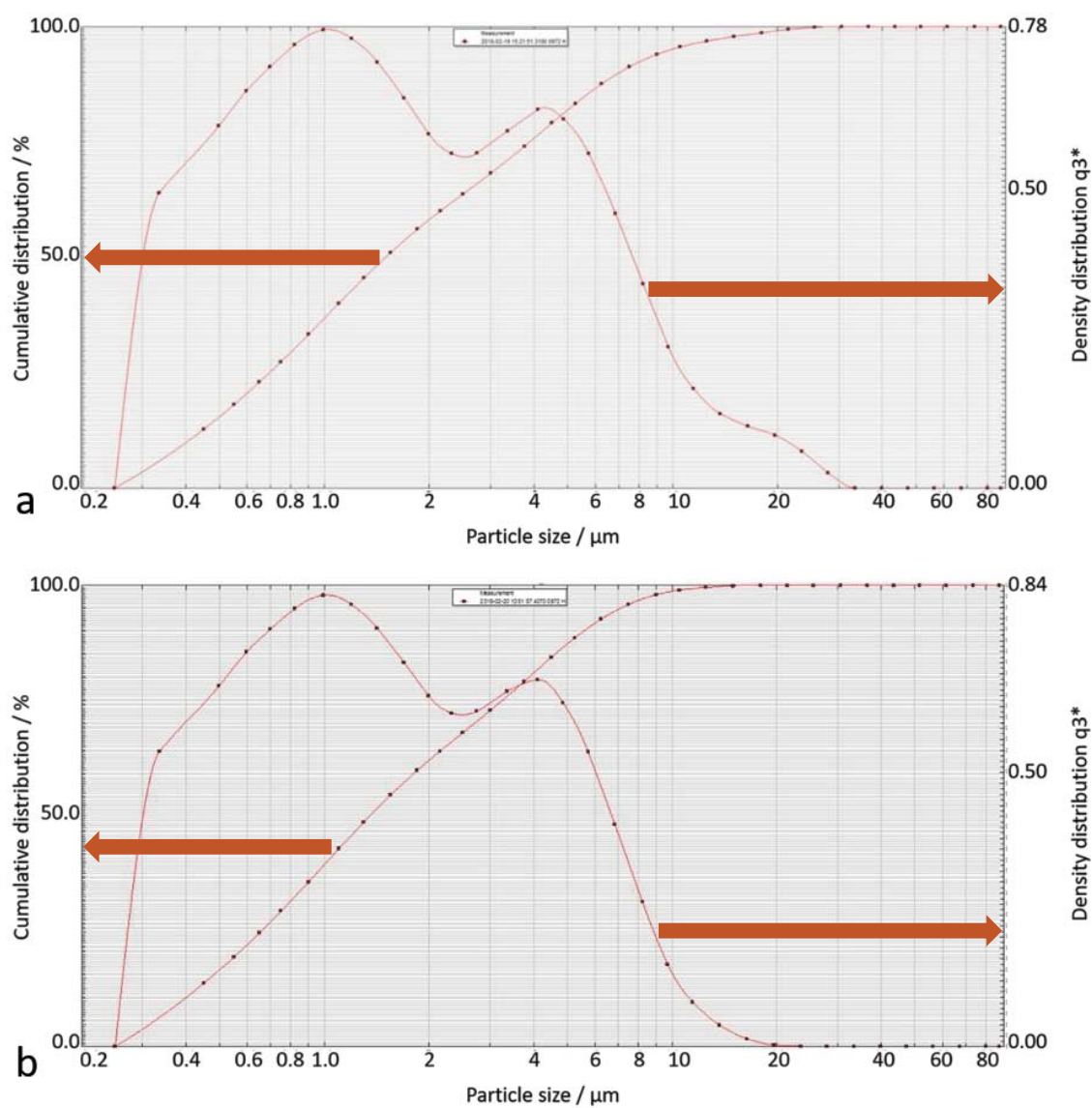


Figure 51 Particle size distribution for ground (a) Extrudate 1 and (b) Extrudate 4

5.2.4 Local phase redistribution analysis

From the discussions in the previous section, it is reasonable to exclude the possibility of the macroscopic constituent difference as a major origin of the varying extrusion pressure. The binder system used in this study is as a result believed to be effective at inhibiting phase migration for both liquid and solid phases, despite the fact that even a tiny drop of liquid content can signify a large change in extrusion load. Another hypothesis is brought into focus. Could the pressure variation be the result of local inhomogeneity within the total phase distribution. This concept gives rise to three aspects to consider:

- (1) A phase rearrangement is induced during the extrusion, which produces a transverse phase distribution, instead of the longitudinal variation which has been considered in the previous section;
- (2) The phase rearrangement is more significant within the die land flow and relatively moderate in the die entry flow;
- (3) Once the phase redistribution is built up, it will become very sensitive to relative local liquid content changes, regardless of the absolute liquid fraction in the paste.

Aspect (1) is based on the discussion of results shown in Table 19, Table 20 and Figure 51, where little longitudinal paste inhomogeneity was observed. Aspect (2) is considered plausible as the greatest contribution to pressure drop in the modified Benbow-Bridgwater equation are the two die land pressure terms (2.41 MPa and 2.82 MPa for paste 2) accounting for 77% of the total for the die land flow pressure

drop. Aspect (3) is considered plausible by the examination of Figure 47 where Curve 2.2, which is thought to have the lowest liquid content (section 5.2.3), has a lower extrusion force than paste curve 2.1, 6.1 kN and 8.1 kN respectively.

To validate these suggested mechanisms, SEM images for the heated extrudate fracture surfaces of Paste 2(Extrudate 1 - Extrudate 4) were examined. The extrudates were fractured and mounted in the microscope very carefully as the burnt-out tubes were effectively only assemblies of loose ceramic powders.

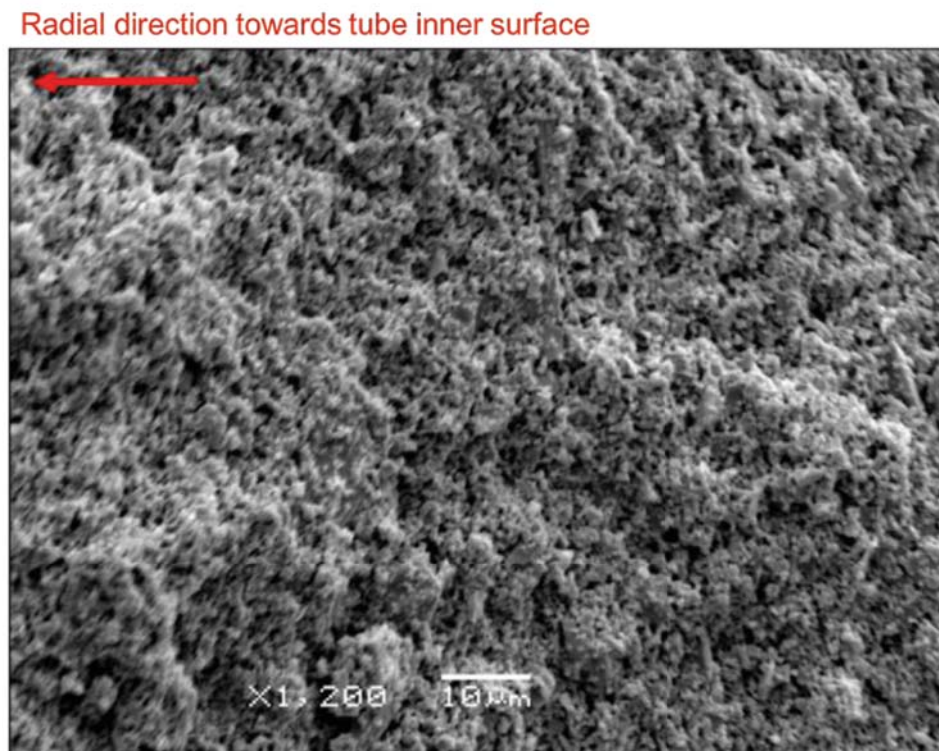


Figure 52 Fracture surface of an extrudate from Paste 2 heated at 1000 °C without pore former

Unfortunately, although the imaged microstructure is not as dense as the sintered fracture surfaces, no notable variation was observed across the tube in the radial direction. The typical homogeneous structure of extrudates heated at 1000 °C can be

seen in Figure 52, in which the original ceramic powder geometry, as well as large quantities of micro-pores can be observed. The micro-pores represent the channels previously occupied by the liquid binder phase and they are too many and varied to identify any variation in their distribution. From this image it is not possible to prove the hypothesis, and further experimental design was required.

The addition of a pore former was then reconsidered in order to evaluate the assumption of local phase redistribution, as it has a distinct particle size and morphology, which is advantageous in characterisation the porosity after heating of the extrudates to 1000 °C. However, there are additional barriers to overcome in the analysis once corn starch is added, over and above the difficulties already found in the analysis of extrudates without pore former. Generally, the additional 'barriers' to be overcome for the assumption validation are:

- (1) The introduction of corn starch would make the paste system a ternary-phase system, as it is soft and deformable, and cannot be treated as an identical solid phase to the ceramic particles;
- (2) The distribution of porosity after heating can only reflect the flow behaviour of corn starch, with no direct indication of the liquid phase distribution;
- (3) The liquid phase content can no longer be represented by the extrudate weight loss after heating, as a result of pore former removal;
- (4) The paste rheology is constrained to a small range, with a high liquid content exhibiting a stable extrusion, and a low liquid content (or high instantaneous pressure) resulting in entrapped air giving rise to large pores or deformed corn starch particles;
- (5) The large visible pores contained in the extrudates which can be regarded as a

fourth phase in the paste, add to the noise/error of the phase redistribution analysis and thus should be avoided as much as possible by selecting appropriate and highly developed paste formulations.

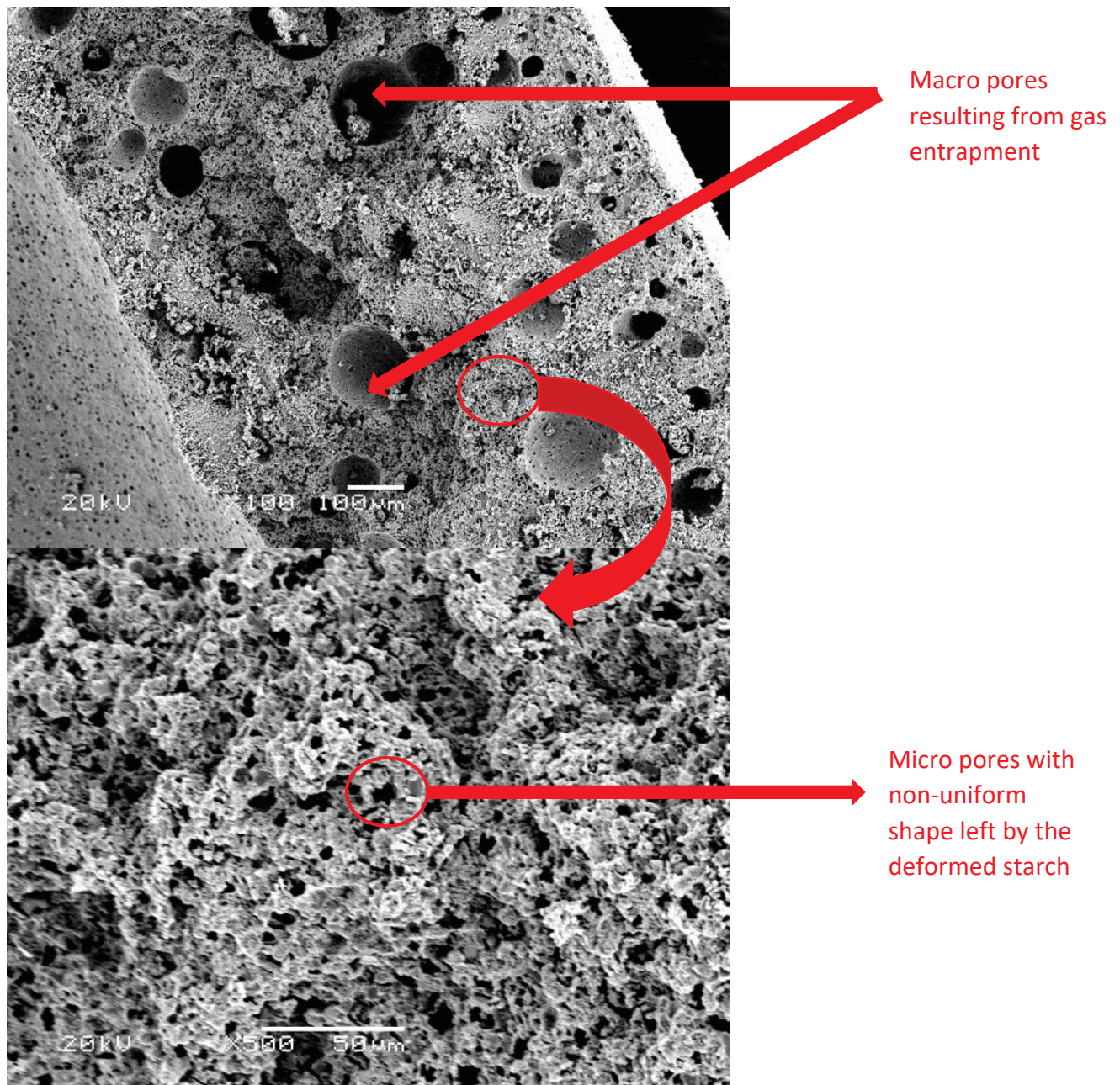


Figure 53 Fracture surface of an extrudate heated at 1000 °C, with an instantaneous extrusion load of 10.5 kN and 2.6 g usage of solvent

Figure 53 shows an example of heat treated extrudate failing to avoid Barrier (4) and Barrier (5). This paste contained 2.6 g solvent (see the full paste formulation in Table 14) and exhibited an instantaneous extrusion load of 10.5 kN. The consistency of the paste has caused gas entrapment which generated large spherical pores and pores formed from deformed corn starch particles visible on the fracture surface. Although quite a few dense regions with low porosity were observed, the image was not considered to be an adequate proof of local phase redistribution.

Table 21 lists the weight loss data for three extrudates formulated with 5 g pore former and 2.6 g solvent. While the similar weight loss fractions indicate the total content of pore former and liquid phase in these green extrudates are similar, the absolute composition of liquid content cannot be measured demonstrating the issue described in Barrier (3).

Table 21 Weight loss for extrudates at different instantaneous extrusion loads, with the usage of 2.6 g solvent and 5 g pore former

	Extrudate at 8.0	Extrudate at 8.8	Extrudate at 9.1
	kN	kN	kN
Weight loss %	28.58%	28.29%	28.16%
after heating at			
1000 °C			

Therefore, the additional 'points' to overcome Barriers (1) – (4) were developed and are listed below:

- (1) Assume that the order of flowability for three phase types are: liquid phase > corn starch (solid phase with regular geometry and adequate deformability) > ceramic powders;
- (2) Consider that the inhomogeneous distribution of corn starch is accompanied by a disorder of the liquid phase, but a homogenous distribution of the starch does not imply a similar arrangement of liquid phase;
- (3) Use the extrudate weight loss after overnight drying as an indicator of relative liquid content;
- (4) Take the SEM imaging as supporting results for the hypothesis, where sufficiently spherical pores created by the pore former are characterised;
- (5) Take the SEM images without observed large pores, which are shaped not by pore former, to aid in drawing a conclusion.

To investigate the validity of point (3), 8 extrudates were studied and their properties are listed in Table 22. These tubes were from 4 separate paste formulations (Batches 1-4), and the tubes within Batch 4 correspond to the extrusion shown in Curve 2-1 of Figure 47. The following analysis is based on the premise that the liquid loss during paste preparation is proportional to the initial liquid phases present during mixing, in terms of the component fractions. This implies the viscosity of the liquid phase within all the extrudates is consistent. Further if point (3) holds i.e. extrudate weight loss after overnight drying at 90 °C reflects the solvent content, and the first inflection load is taken to be indicative of the paste consistency, then the relative movement of fluid in the system can be monitored. The data relating to such an analysis is given in Table 22.

Table 22 Selected characterised results for different extrudates

Extrudate No.	Batch No.	Paste solvent content	First inflection extrusion load	Weight loss % after overnight drying	Instantaneous extrusion load
A	1	3 g	2.2 kN	7.70%	4.5 kN
B	2	2.9 g	2.5 kN	7.57%	4.7 kN
C	2	2.9 g	2.5 kN	7.50%	5.2 kN
D	3	3 g	2.7 kN	7.47%	5.3 kN
E	3	3 g	2.7 kN	7.38%	5.9 kN
F	4	2.6 g	3.6 kN	6.71%	8.1 kN
G	4	2.6 g	3.6 kN	6.64%	8.6 kN
H	4	2.6 g	3.6 kN	6.25%	11.0 kN

To interpret the data presented in Table 22 an empirical parameter, named the 'Load Growth Rate by Solvent Change' and given the symbol R, was developed. R is defined as the increase of extrusion load with a 1% of extrudate weight loss difference after overnight drying at 90 °C, which is given by Equation 27. For example, R_{AC} (where the subscript shows which extrudates of table 22 are being compared) is equal to $(5.2 \text{ kN} - 4.5 \text{ kN}) / (7.70 - 7.50) = 3.5 \text{ kN}$, reflecting the degree extrusion load rises with identical solvent content difference between two extrudates.

$$R = \frac{\text{instantaneous load difference}}{\text{weight loss \% difference}} \quad (\text{Equation 27})$$

Table 23 Calculated R values between different extrudates

R_{DE}	R_{FG}	R_{GH}	R_{AE}	R_{EF}
6.67 kN	7.14 kN	6.15 kN	4.38 kN	3.28 kN

Some representative R values are given in Table 23, in which R_{DE} , R_{FG} and R_{GH} indicate the load growth rate during the same extrusion trial (i.e. both extrudates have the same batch number), while R_{AE} and R_{EF} reveal the comparison between different extrusion formulations (batches). In order to avoid unnecessary variations, only Extrudates A, C, E and F were taken for load comparison between different tube batches, as they were all collected from extrudates at the beginning of an extrusion process (exemplified by the second point from left for any plot in Figure 47).

Generally higher R values are obtained when comparing extrudates from the same extrusion (batch), which indicates the pressure is more sensitive to the gradually varying liquid content while the extrusion is progressing. The high R value does not show any obvious dependency on the absolute liquid content. These observations can be regarded as a proof of point (3) being applicable within the study.

To validate points (1) and (2), a range of SEM images were gathered. Figure 54 shows the longitudinal fracture surface of a heat treated extrudate with an 8.5 kN instantaneous load and 2.6 g solvent formulation. Compared to Figure 53, the image has fewer examples the porosity generated by deformed corn starch, but still includes large pores formed during the paste preparation. It is possible to see for the first time a dense region next to the pin (mandrel) which has developed during the extrusion process.

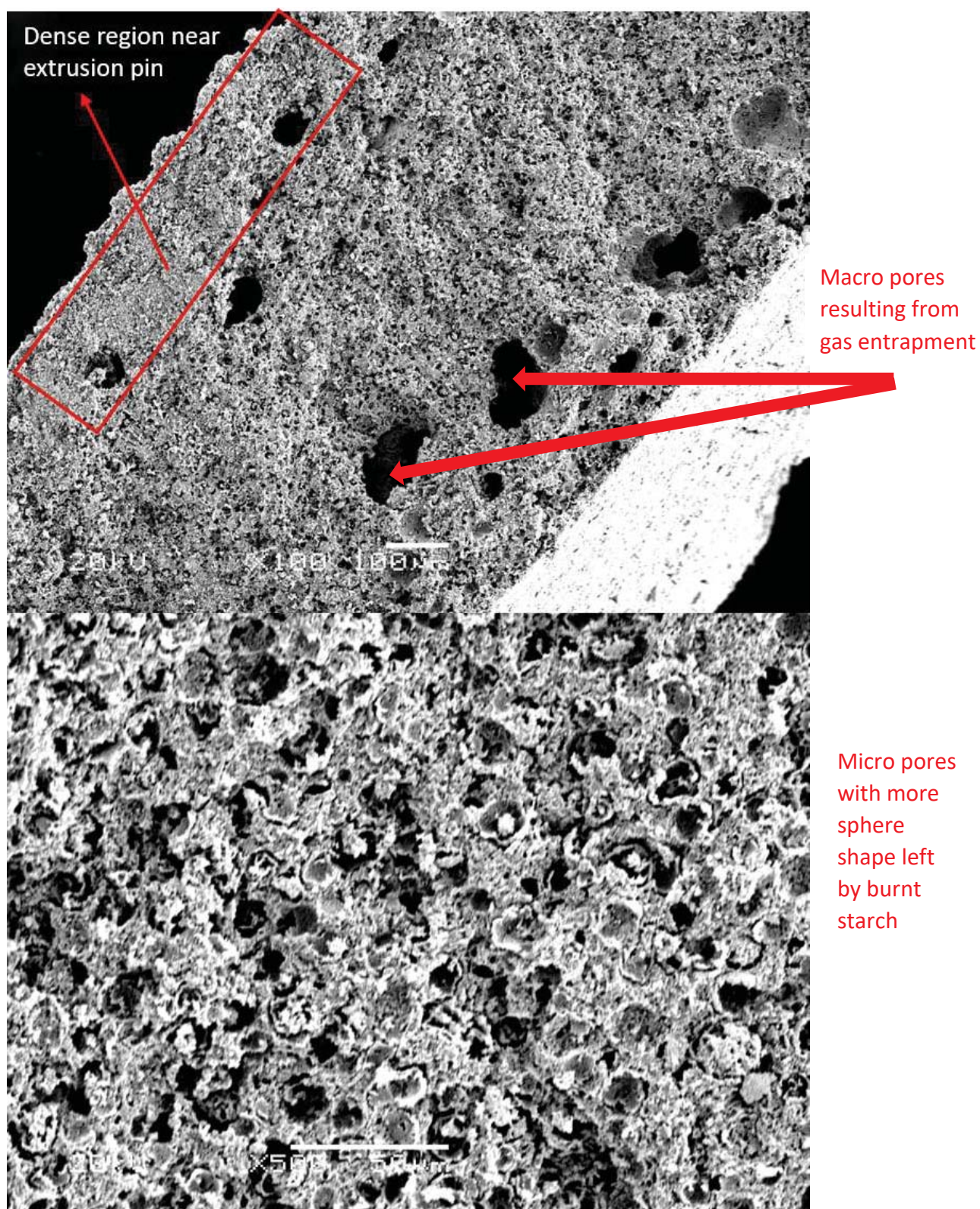


Figure 54 Fracture surface of an extrudate heated at 1000 °C, with an instantaneous extrusion load of 8.5 kN and 2.6 g usage of solvent

According to the derived pressure drop terms in the Benbow-Bridgwater equation for the tube forming die, die land flow behaviour dominates the overall extrusion pressure. Given that the pressure drop due to die land flow is caused by friction at the die wall, and the experimentally determined extrusion pressure is much greater than the predicted (calculated) value, the observation of ceramic-concentrated or dense region near the extrusion pin suggests that such a feature could be responsible for considerably increasing the capillary friction without significantly changing of overall liquid content. However, the statistical validity of this suggested mechanism needs to be considered. Thus, to improve the statistics, characterisation continued on pastes with more homogeneous structures to confirm the presence of such dense regions (reduced or absent pore forming starch) next to the pin. There proved to be a limited range of formulations over which the entrapped bubbles from processing were removed and the paste rheology allowed the formation of the integral micro tubes. It was found that tubes B-E of table 22 could be studied and used to draw further conclusions about the phenomena observed first in Figure 54. Pastes F, G and H had large bubbles while paste A was too soft to handle.

Figure 55 shows that the large pores, not generated by pore former, were successfully avoided in Extrudate E (instantaneous load 5.9 kN) and Extrudate D (instantaneous load 5.3 kN) (data from Table 22). It is also noted that no dense structure in the vicinity of extrusion pin is observed for Extrudate D where it was observed in Extrudate E, which means a homogeneous phase distribution during extrusion, at least for the pore former. A probable explanation for the loss of the dense region as extrusion progresses can be found by considering the plotted load vs extension curve shown in Figure 56, where the end of the curve does not rise as

the extrusion progresses beyond the point of sampling Extrudate D. It is suggested that the initial dense layer found in Extrudate E is sluffed off by the continued flow process. This is thought to be the local reduction of liquid phase eventually eliminating the dense ceramic structure at the die wall which initially formed as flow was initiated and pressure was high. The relative uniform structure once formed appears insensitive to liquid content change as extrusion continues. The paste rheology is then self-accommodated, and no upward extrusion load tend is developed.

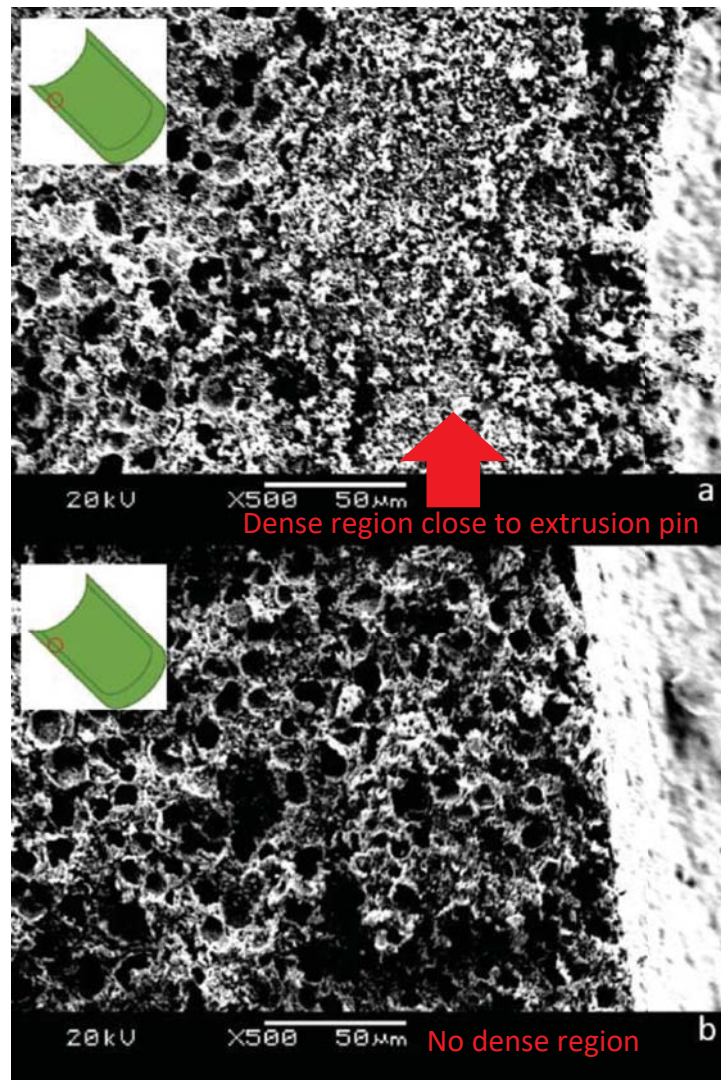


Figure 55 Fracture surface for (a) Extrudate E and (b) Extrudate D heated at 1000 °C

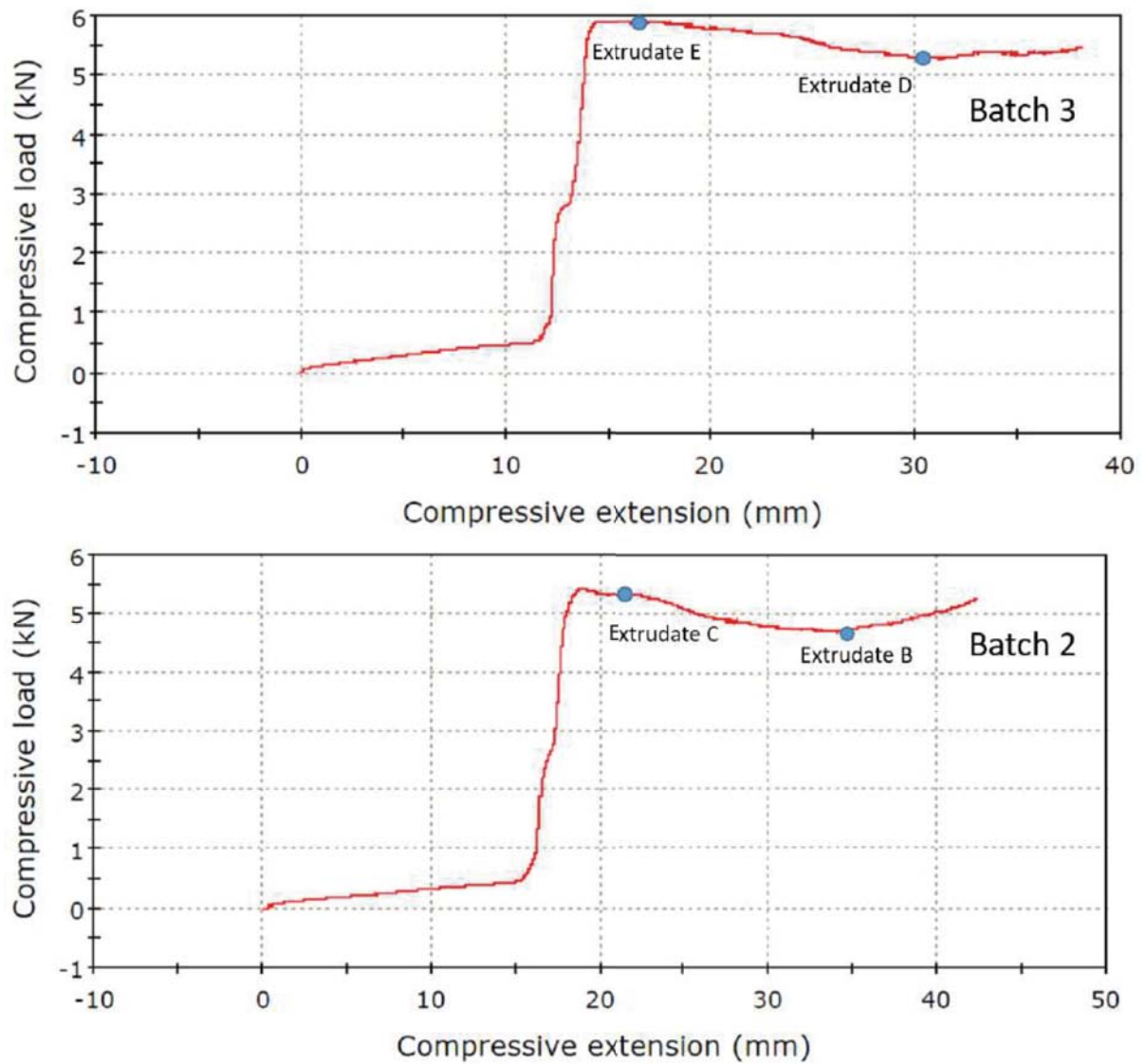


Figure 56 Plotted load vs extension curves for tubes made with Batch 3 and Batch 2

The load vs extension curves of Extrudate C (instantaneous load 5.2 kN) and Extrudate B (instantaneous load 4.7 kN) are also given in Figure 56, and the SEM images for their heat-treated fracture surface are shown in Figure 57. Both images in Figure 57 show a continuous dense zone on the tube inner surface, suggesting the lasting existence of local phase redistribution. This is consistent with the rising curve beyond the sampling point of Extrudate B in Figure 56 where the system is

increasingly depleted in liquid phase. This suggests that it is local redistribution of phases which cause the observed differences in pressure drop. It also shows the transient nature of the process and its sensitivity to small variations in formulation and flow. It is interesting to note that the dense region (depleted in starch) was only observed against the pin. The exact mechanism for its formation remains unknown but it is possible that due to the longer length of the pin the shear at the wall promotes movement of the larger starch particles from the wall.

Benbow and Bridgwater in their book [137] suggest that in the shear region at the wall the paste is only moving in a layer half the thickness of the largest particle. In this study the large particles are the starch and so the formation of the dense layer could be attributed to the migration of those large particles away from the region of high shear, which is next to the wall, and the extended length of the pin relative to any other feature in the die.

One thing to consider is the worn conditions of the extrusion die, as the small cross-sectional areas of the die land would result in significant friction and potential wear by the abrasive ceramic particles contained in the paste. Friction itself, together with the potential damage to the die surface during removal of sticky paste in the cleaning process, may potentially increase or decrease the wall shear stress in subsequent extrusions. It is suggested that in this study there was a rise in the extrusion pressure drop and a reduction in the maximum permissible solid loading, after one year of operation. This aspect could be taken forward for further study.

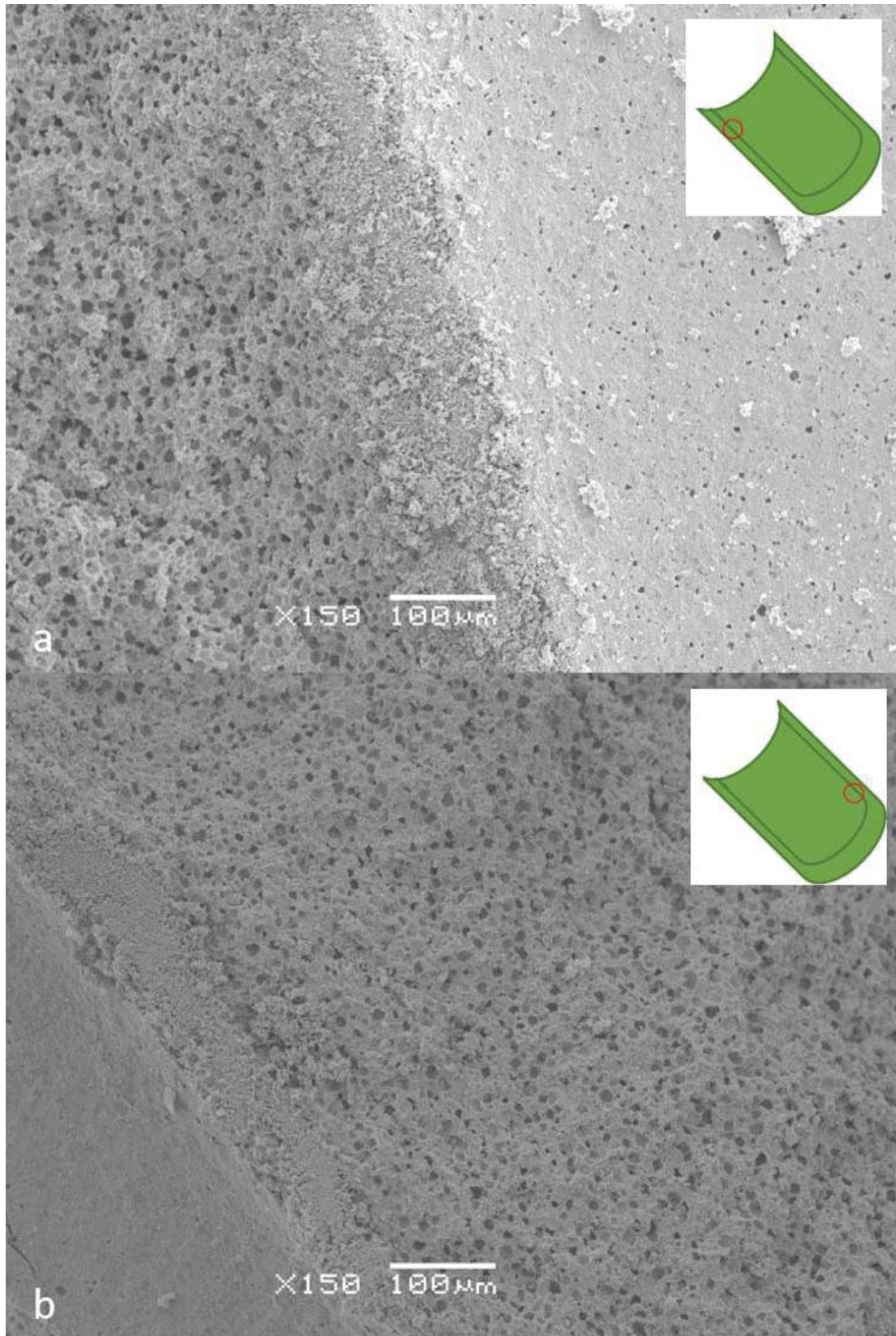


Figure 57 Fracture surface for (a) Extrudate C and (b) Extrudate B heated at 1000 °C

5.3. Conclusions and future work

In summary, the phenomenon of local phase redistribution is believed to be the mechanism behind abnormal extrusion pressure variation during the extrusion process examined here. It can significantly increase the friction between the die components and the paste (particularly the long central pin or mandrel), without a notable reduction of liquid content. Once built up, the dense ceramic region, accumulated in the vicinity of die components due to a low flowability, it drives the extrusion pressure and is sensitive to small liquid content changes, and such sensitivity is relatively unaffected by the absolute liquid content within the paste. The superposition of liquid phase migration in both barrel and extrudate would cause slight longitudinal liquid content difference in processed tubes, resulting in different forms of pressure variation.

The transvers phase redistribution is believed to occur in both the 6-hole die region and the annular die region. However, because the central extrusion pin is the last die component that contacts the paste and also the longest in contact, the dense ceramic regions are consequently observed only in the inner tube surface. Due to the high mobility of the liquid phase as well as the pore former, they always incline to move toward the region of low shear and low pressure respectively, as shown in the schematic in Figure 58.

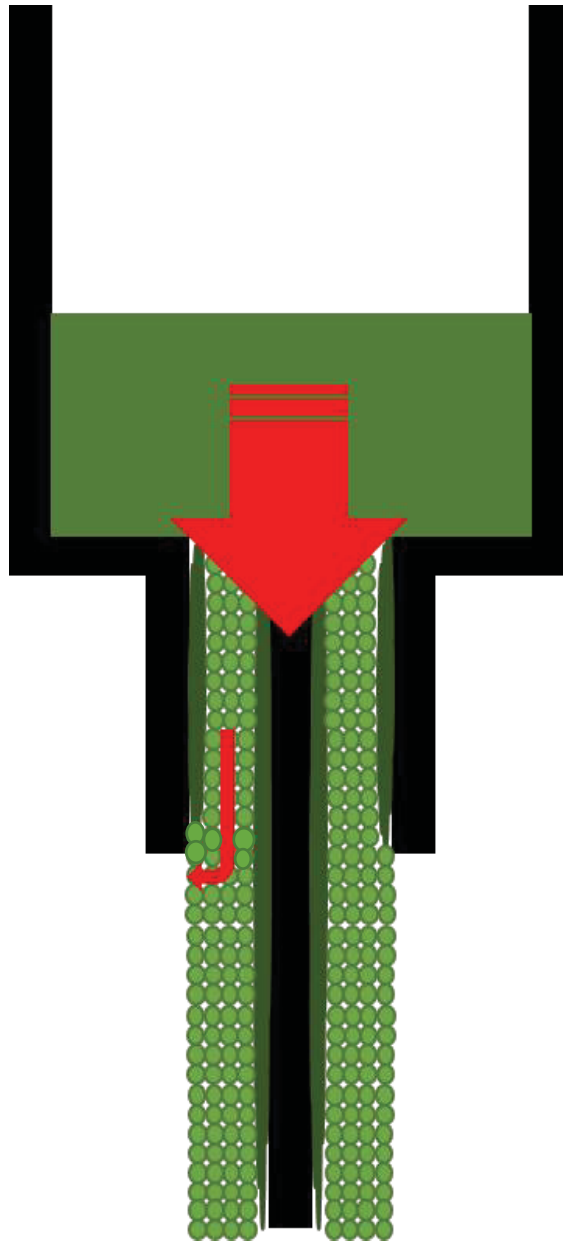


Figure 58 Schematic of dense ceramic regions formed during extrusion

It is also concluded that for extrusion dies with a small cross section area, an abnormal pressure rise cannot be simply attributed to liquid phase migration within the bulk material. Such a phase migration only determines the observed variation trend but is not considered to give rise to the magnitude of the pressure variations.

The Benbow-Bridgwater equations are generally fitted to a specific and simple die geometry before then going on to extend them to an unknown more complex geometry. It is possible that if the two geometries are considerably different in construction and particularly in terms of their flow distributions, then the model is not accounting for all the mechanisms operative in the new more complex die in which the pressure is being developed. This is the case in this study. In the simple dies used for generating the data for the parameter fitting the constrictions and flow may not lead to the development of the observed dense regions found in the more complex tube die.

If the system (paste formulation and die design) is only to be used for anode tube fabrication, a paste formulation with an appropriate liquid binder phase is achievable and able to give steady extrusion pressures through the extrusion of a complete barrel of material. In this case, a careful drying process is required to hold the as-extruded tubular shape especially for the softer pastes, which appear to perform better in terms of defect reduction.

Later work could focus on the assumptions made in this chapter, on liquid phase distribution in the barrel and die at different extrusion stages. This would require suspension of repeated extrusions through the extrusion process and detailed compositional analysis. As for the demonstration of local phase redistribution, processes that are more analytical could be considered such as positron emission particle tracking to look at the movement of the starch particle at the wall or NMR imaging to look at the fluid distribution at the wall. Lastly, it is also suggested by the author that all studies of paste rheology behaviour should be undertaken over a relatively short time period to avoid the issue of die wear.

Chapter 6 Dip coating of YSZ electrolyte

6.1. Introduction

In this chapter, the preparation of electrolyte slurries with different binder and dispersant fractions are reported, followed by their characterisation in terms of adhesion strength and viscosity. The slurries are based on an azeotropic solvent system, namely a mixture of toluene and ethanol, which has been widely used for dip coating processes [225-227]. An optimised slurry formulation is developed for coatings at different withdrawal speeds and solid loadings, in order to determine the range of electrolyte thicknesses that can be achieved.

6.2. Results and discussion

6.2.1 Coating slurry adjustment

The coating slurry was prepared by the methods described in Section 3.4.3. The first issue to be determined when adjusting the coating slurry formulation was the sequence of adjusting the binder and dispersant fractions. In the work of Alireza et al. [228], the dispersant fraction was determined first. However in this study, considering that the dispersant is an additive (not a necessary component) with a lower proportion, compared to that of the PVB binder, it was believed that a change of dispersant percentage without a known essential binder fraction was not the preferred approach. Thus the binder fraction was determined first, without the addition of the dispersant.

6.2.1.1 Binder fraction determination

Table 24 shows the results of the measurement of adhesion strength by tape testing with different binder concentrations at a fixed usage of 5 g YSZ-E (i.e. 50 wt% of solids fraction) and a withdraw rate of 80 mm/min. The testing standard for adhesion strength (ASTM D3359-08) was developed by ASTM International, with a strength of 5 A (A is the unit defined in this standard whose numerical value is to describe the adhesion strength) being considered as the highest level of adhesion. As the extruded anode tubes were too narrow to carry out the tape testing, the testing was carried out on sintered tubes with larger dimensions (ID 6 mm, OD 8 mm), which were extruded using an alternative annular die manufactured together with the original die set. This die has the same basic structural elements of the original tube forming die (Figure 21), but with larger dimensions.

Table 24 Adhesion strength at different binder fractions

Toluene	Ethanol	PVB	DBP	Binder Weight	Adhesion Strength
(g)	(g)	(g)	(g)	Fraction	after 1h
2.375	2.375	0.125	0.125	2.5%	0 A
2.25	2.25	0.25	0.25	5%	4 A
2.125	2.125	0.375	0.375	7.5%	5 A
2	2	0.5	0.5	10%	5 A

The drying of the electrolyte layer was found to be rapid after a single coating, implying that the vertical thickness variation due to gravity was well controlled. This is

because of the fast evaporation of the binary solvent system. The disadvantage of rapid solvent evaporation is that the slurry itself lost solvent and changed the consistency very quickly between coats so the coating thickness between successive coats increased. As a result, the prepared coating slurry was divided into small sealed glass tubes (ID 10.8 mm) immediately after ball milling. Each of the tubular containers was only opened once and the slurry within it was only used for one coating. Moreover, all of the prepared slurries were consumed within 30 minutes after milling.

A 7.5% weight fraction of binder was determined to be sufficient for adequate adhesion strength, with no recognisable removal of the coating layer observed on the sticky tape surface. By taking the subsequent addition of dispersant into account, which would increase the liquid content in the slurry, the chosen weight fraction of binder for the coating slurry formulation was 10%.

6.2.1.2 Dispersant fraction determination

As a first step to characterise the viscosity, the shear rate during coating was first derived, as shown in Figure 59. Assuming that the anode tube is immersed in the centre of the tubular container, the distance between the outer tube surface and the container wall, h , is 3.4 mm, hence the fluid shear rate, $\dot{\gamma}$, at a coating speed, v , of 80 mm/min is given by:

$$\dot{\gamma} = \frac{v}{h} = 0.392 \text{ s}^{-1}, \text{ (Equation 28)}$$

The assumption is made that the fluid is essentially Newtonian and that the shear profile is uniform across the annulus.

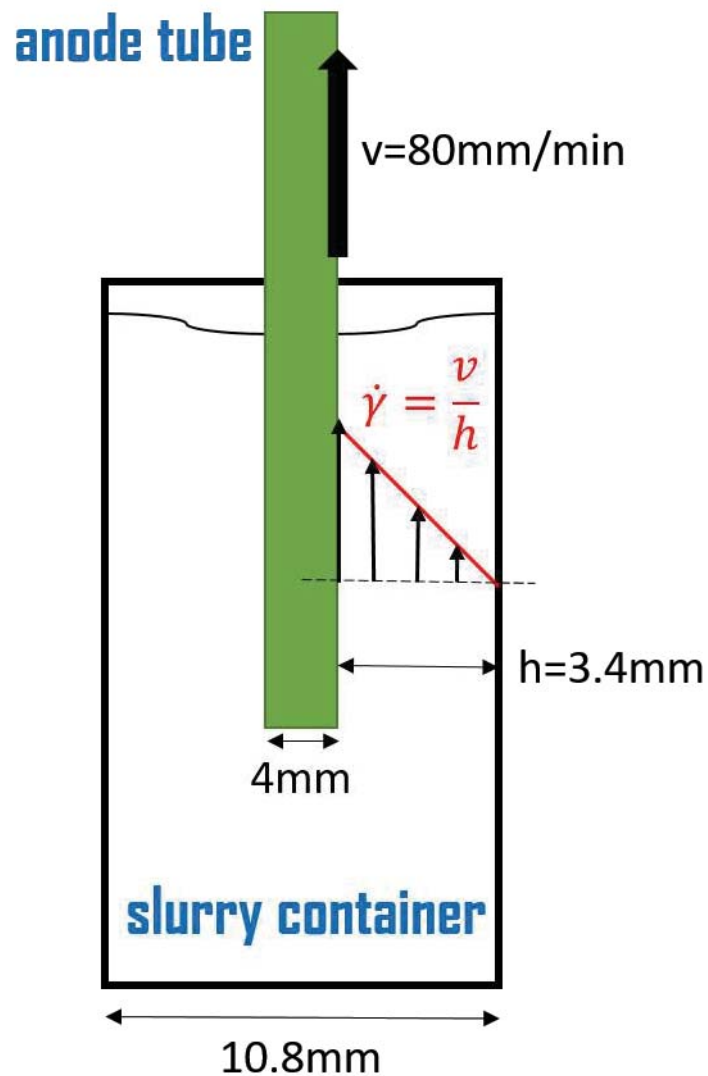


Figure 59 Schematic of fluid shear rate during dip coating

Therefore, the handling of characterised viscosity results was mainly focused on the viscosity at a low shear rate. In order to characterise the shear behaviour of the coating slurry, a shear stress range up to 50 Pa was then applied in a rotational

rheometer described in Section 3.9. This was done to determine more precisely how much dispersant was required to optimise the suspension stability.

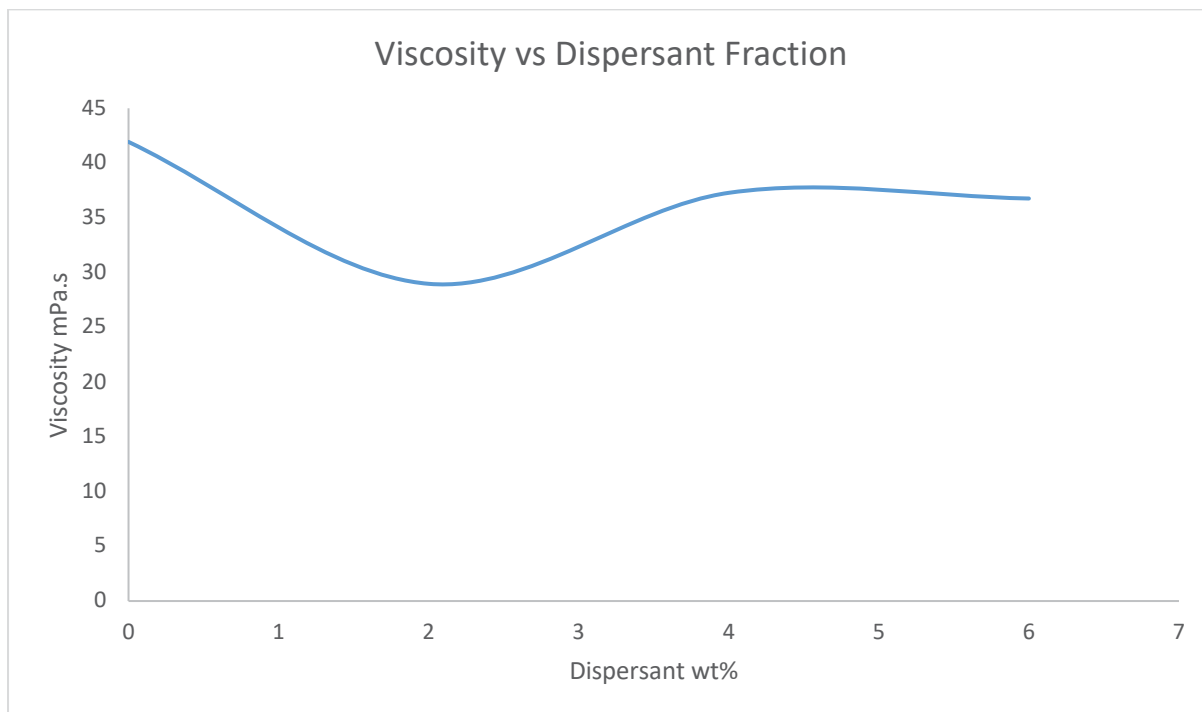


Figure 60 Viscosity for different dispersant contents at a shear stress of ~ 0.4 Pa

Another problem encountered was how to balance the solvent fraction and the solids loading. If the addition of dispersant was on the basis of a fixed amount of other constituents, the solids loading would change with different volumes of dispersant. However, if the solids amount was fixed, the other components in the liquid phase would be reduced to a certain extent in order to achieve the same solids loading. The continuous reduction of solvent, due to the addition of dispersant, would increase the slurry viscosity, which is indicated by the experimental results. Eventually, menhaden fish oil (Sigma-Aldrich Company Ltd., UK) was added at different weight percentages to an identical formulation of other constituents (i.e. 5 g YSZ-E, 0.5 g PVB, 0.5 g DBP, 2 g toluene and 2 g ethanol) and the change of solids loading was neglected.

Little difference in terms of slurry viscosity was found as the dispersant weight fraction was increased, as indicated by Figure 60, although a slight reduction was found at a 2 wt% addition. This is still possibly due to the reduction of solvent fraction, as addressed above. It is considered that although the addition of fish oil would increase the liquid content in the slurry, the dispersant itself is a viscous fluid and the solvent fraction in the liquid phase is correspondingly reduced. Thus, the dispersant which is meant to adhere to the particle surfaces up to a saturation condition, to generate a less viscous suspension, is countered by an increase of the overall slurry viscosity at the same time.

Another issue that should be noted is that an extremely low shear rate is hard to achieve in the rheometer geometry as a result of the low slurry viscosity. Since the rheometer introduced in Section 3.9 is stress controlled, the shear rate of 0.392 s^{-1} means a shear stress around 0.01 Pa, which is impossible for the machine to run steadily and generate a result that represents the true macroscopic viscosity (the minimum shear stress for the rheometer was 0.08 Pa that is normally used for pre-shear). Thus the slurry viscosities at a shear stress of $\sim 0.4 \text{ Pa}$ are reported where stable data was obtained. A relatively low viscosity (an average value of $28.97 \text{ mPa}\cdot\text{s}$) was characterised at the dispersant fraction of 2%, which would be used as a fixed dispersant portion in the later formulations.

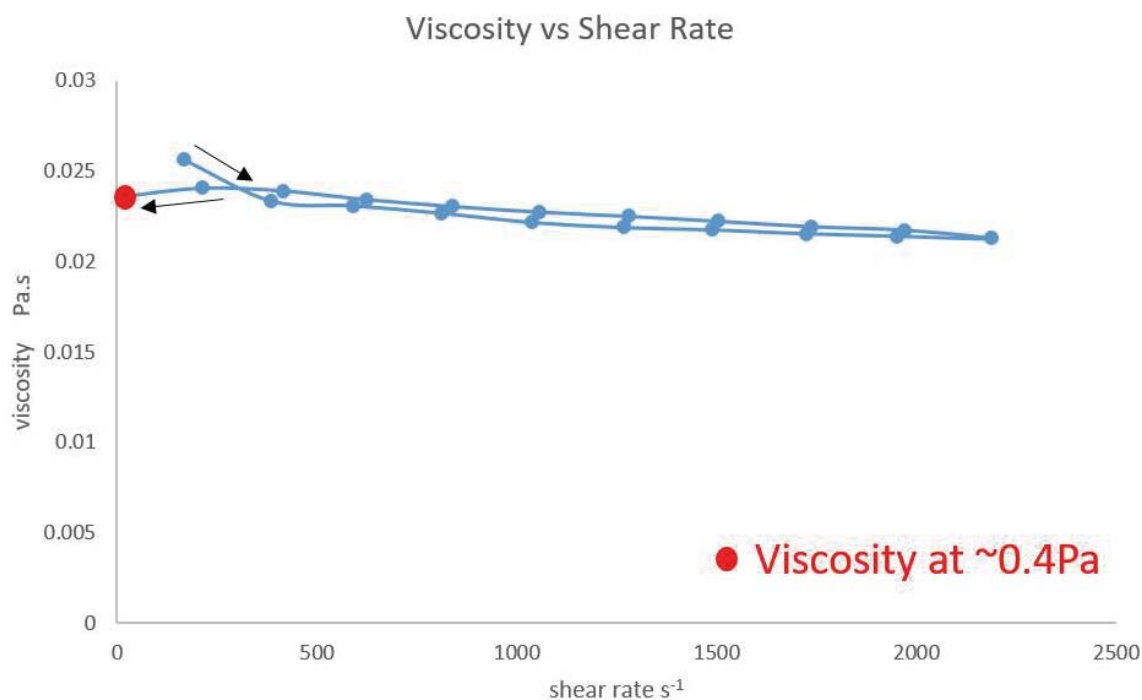


Figure 61 A viscosity test cycle for coating slurry with 2% dispersant and 50% solid weight fraction

Figure 61 shows a viscosity test cycle for the given coating slurry formulation. The viscosity data at the beginning of the test is thought to represent a slurry that has not reached a steady status, so the last point of the test cycle is selected for comparison between slurries with different dispersant fractions. The viscosity cycle indicates that over a relatively wide shear rate range, the slurry viscosity shows only a slight shear thinning behaviour, but for practical purposes it could be considered that the material is Newtonian.

6.2.2 Coating thickness control

6.2.2.1 Coating on green anode

Figure 62 - Figure 64 give the cross-sectional SEM imaging of coated green tubes with different withdraw speeds (the slurry formulation comprised 50 wt% of solid YSZ-E powders, as shown in Table 25). An issue related to the coating on green tubes is the identification of the coated YSZ layer, as both anode and electrolyte structures are non-porous before heating. Under SEM imaging, the coated layer exhibited serried porosity (a feature which was not obvious at the low dipping rate of 5 mm/min) with smaller dimensions, compared to the porosity of the anode substrate. This feature was used to assist in distinguishing the electrolyte/anode interface and the electrolyte thickness. The porous electrolyte is thought to arise from the fast evaporation of the toluene/ethanol solvent mixture.

Table 25 Coating slurry formulation for thickness characterisation at different withdrawal speeds

YSZ-E	PVB	DBP	Fish Oil	Toluene	Ethanol
10 g	1 g	1 g	0.4 g	4 g	4 g

An unexpected observation was that the imaged coating layer became thicker as the withdraw speed increased, as the viscosity test shows a quasi-Newtonian behaviour of the coating slurry. This indicates that at extremely low shear rate range (less than 1 s^{-1}), the fluid exhibits an apparent shear-thickening behaviour. The shear-thickening behaviour was generally overserved in the literature for dip coating processes and

the coating thickness (h) was concluded by the Landau-Levich equation [229, 230] (Equation 29). The equation assumes that if all things remain the same (i.e. no drainage occurs before the coating is completed) but the withdraw rate is increased the value of h will increase.

$$h = 0.945 \frac{(\eta v)^{\frac{2}{3}}}{\gamma^{\frac{1}{6}}(\rho g)^{\frac{1}{2}}}, \text{ (Equation 29)}$$

where η is the slurry viscosity, v is the withdrawal speed, γ is the surface tension, ρ is the slurry density and g is the gravitational acceleration

Plotted coating thickness vs speed curve is shown in Figure 64a. At a coating speed above 60 mm/min, it was found that the thickness growth of coating layer was no longer obvious with the increase of withdraw speed, which is either consistent with the Landau-Levich law (reduced growth rate for the coating thickness when the withdrawal speed is raised) or possibly evidence that the shear-thickening behaviour only exists within a low shear rate range, as indicated in Section 6.2.1.2. According to basic ceramic processing principals [231], the coating slurry flows easily at low withdrawal rates and behaves more like a lubricant, and both a more viscous suspension and a greater coating thickness are expected when the dip coating rate is increased.

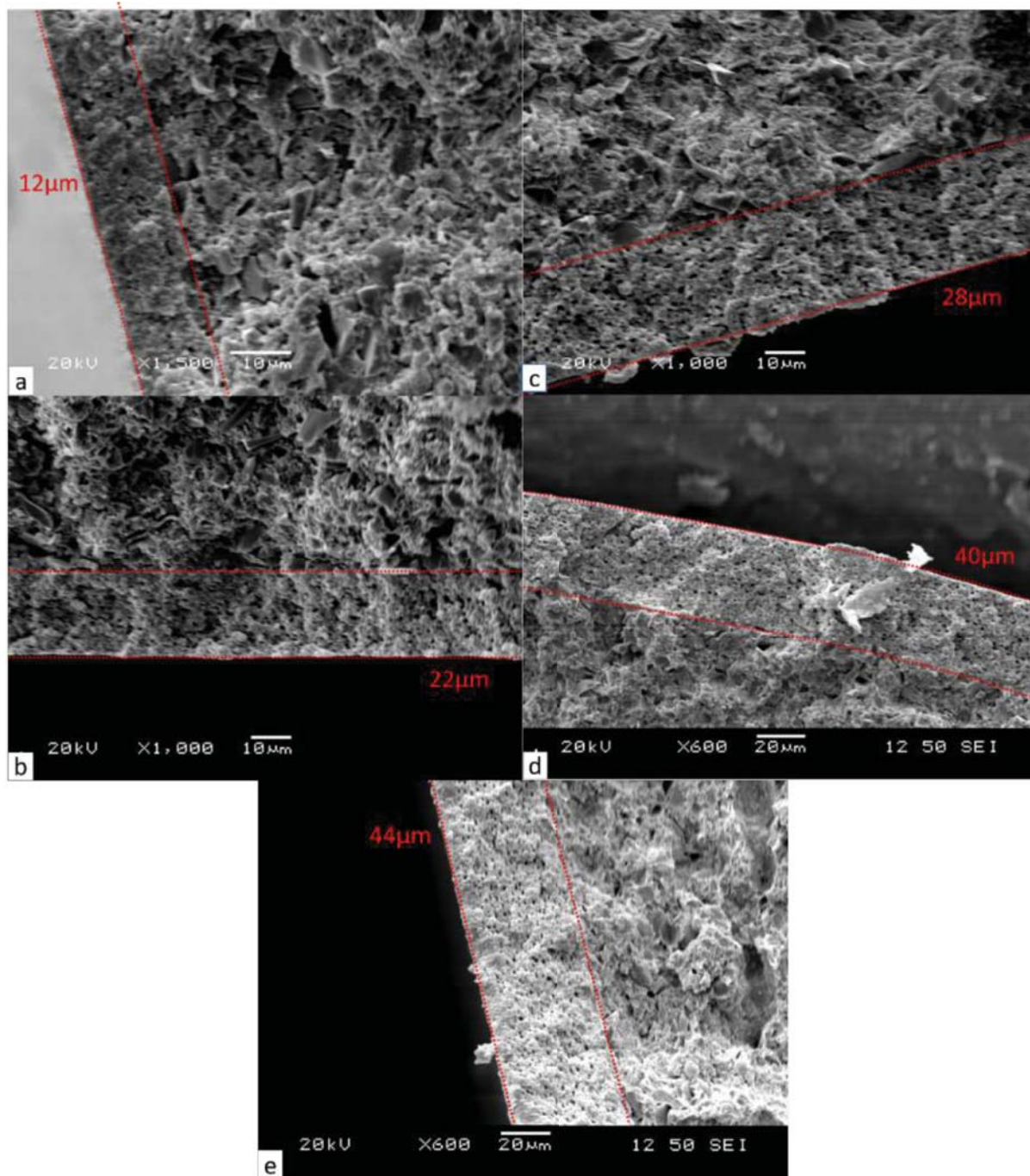


Figure 62 Cross section of coated green tubes at a withdraw speed of (a) 5 mm/min (b) 20 mm/min (c) 40 mm/min (d) 60 mm/min and (e) 100 mm/min

Figure 63 gives the coated layer thickness at different solids loading (by weight, as shown in Table 26) on green tubes, with a fixed withdraw speed of 100 mm/min, which is close to the upper limit of the machine capability. This was to avoid solvent evaporation as far as possible in a high-solids-loading suspension. The plotted coating thickness vs solids loading curve is shown in Figure 64b.

Table 26 Coating slurry formulations for thickness characterisation at different solids loadings

YSZ-E	PVB	DBP	Fish Oil	Toluene	Ethanol	Solids loading
4 g	0.6 g	0.6 g	0.2 g	2.4 g	2.4 g	40 wt%
5 g	0.5 g	0.5 g	0.2 g	2 g	2 g	50 wt%
6 g	0.4 g	0.4 g	0.2 g	1.6 g	1.6 g	60 wt%
7 g	0.3 g	0.3 g	0.2 g	1.2 g	1.2 g	70 wt%

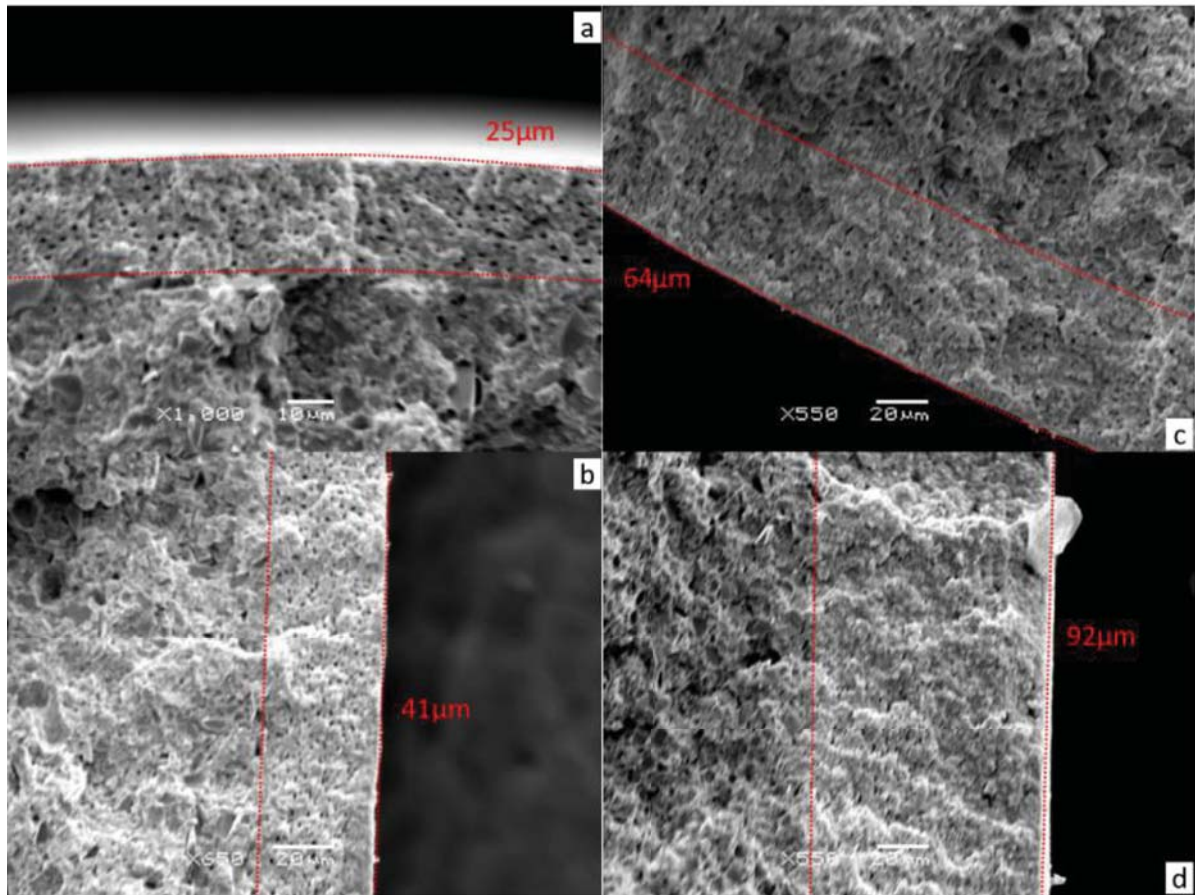


Figure 63 Cross section of coated green tubes at a solid weight fraction of (a) 40%, (b) 50%, (c) 60% and (d) 70%

As expected, there is a positive correlation between solids loading and coating thickness, with a 92-micron-thick electrolyte observed when the mass percentage of YSZ-E was 70%. Considering that the coating slurry is viscous at 70 wt% solids loading and the electrolyte layer is required not to be too thick, the solids loading was determined to remain at 50% for all subsequent trials. As a result, a coating thickness around 40 μm could be expected for the coatings on green anode tubes. For coatings on pre-sintered tubes, however, a much thinner layer should be supposed, due to the transformation of surface condition.

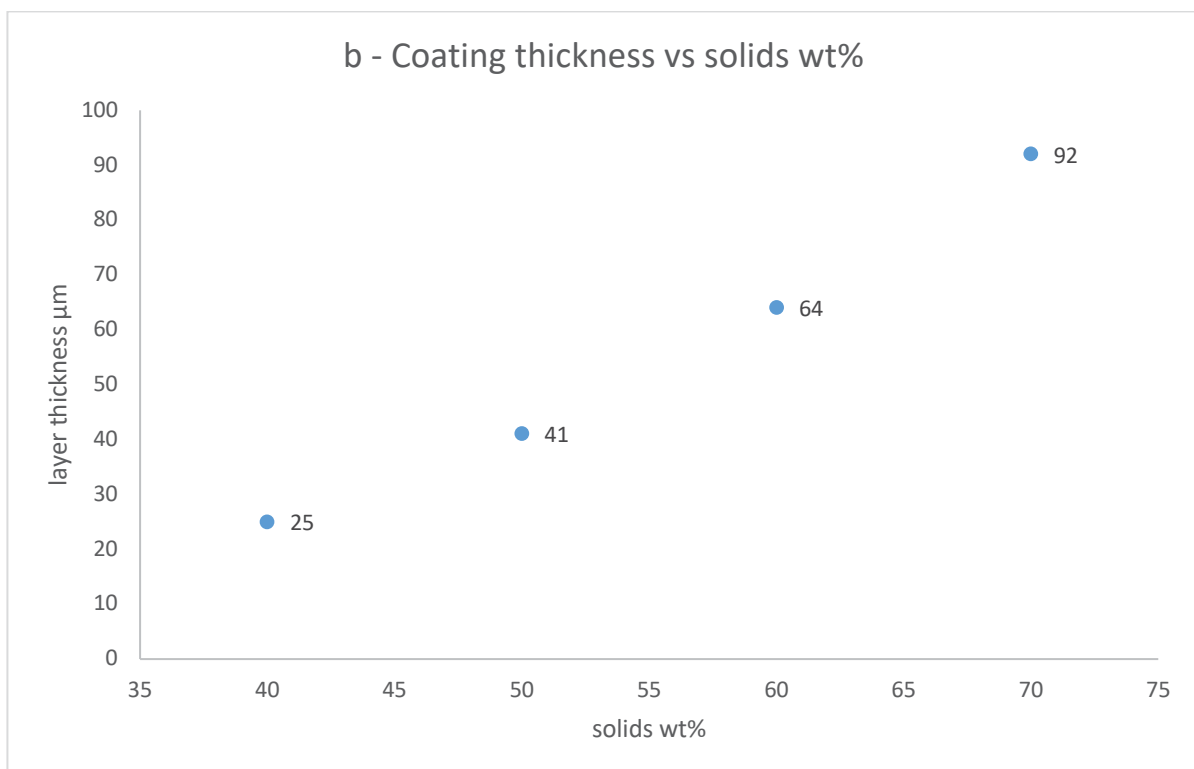
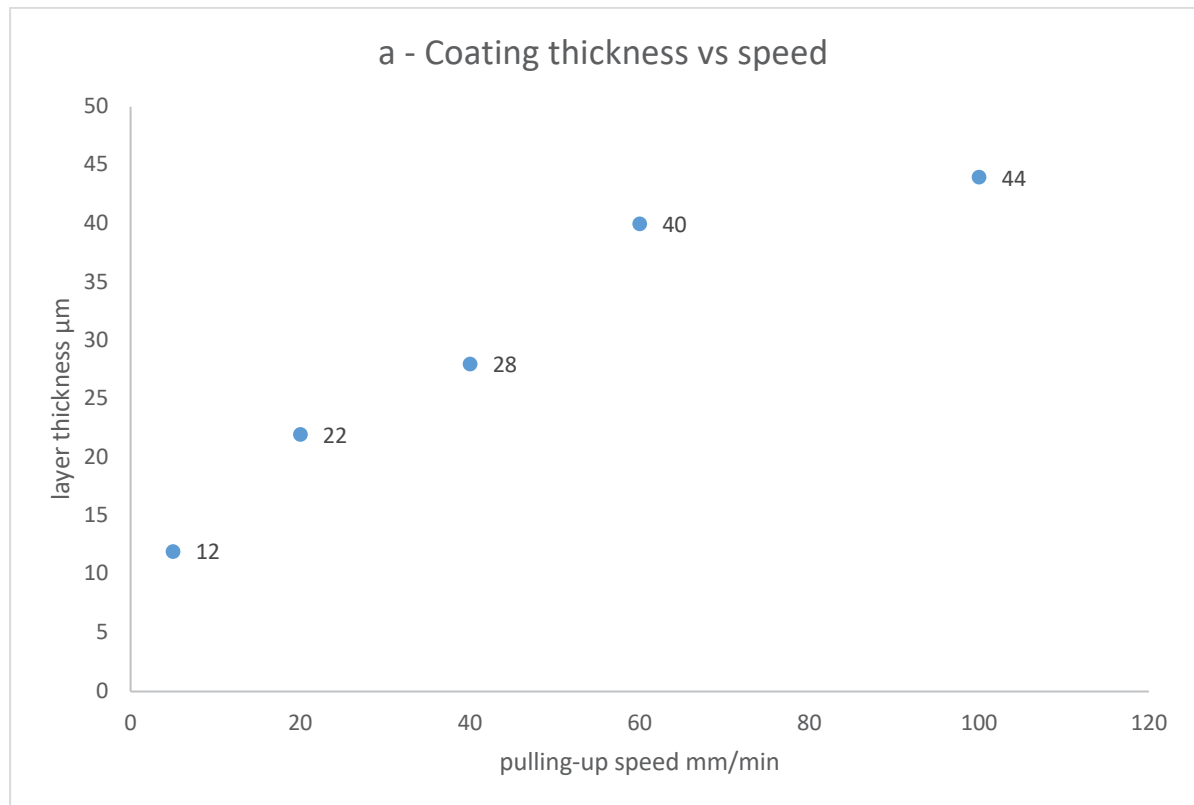


Figure 64 Plotted curves for coating thickness vs (a) speed and (b) solids weight fraction, with YSZ-E slurries

6.2.2.2 Coating on sintered anodes

Similar coating processes were carried out on the fully sintered anode tubes (see the heating regime in Table 13, Section 4.2.3.3). The surface condition of sintered tubes was significantly different from that of green tubes, as the latter were much rougher than the former and the shear thickening effect may be inhibited on a smooth surface. The SEM images are shown in Figure 65.

As expected, the thickness difference is less noteworthy between coated layers at varying withdraw speeds, although an identical shear thickening behaviour is observed. At a withdraw speed of 100 mm/min, an electrolyte thickness of only 20 μm is acquired, which would also be further reduced after electrolyte sintering.

Furthermore, a porous anode substrate may cause the discontinuity of a homogeneous electrolyte layer, a feature which can be observed in Figure 65a. If there is any section of anode surface not covered with electrolyte materials at all, a local short circuit would occur between anode and cathode during cell operation, leading to a decrease of output voltage.

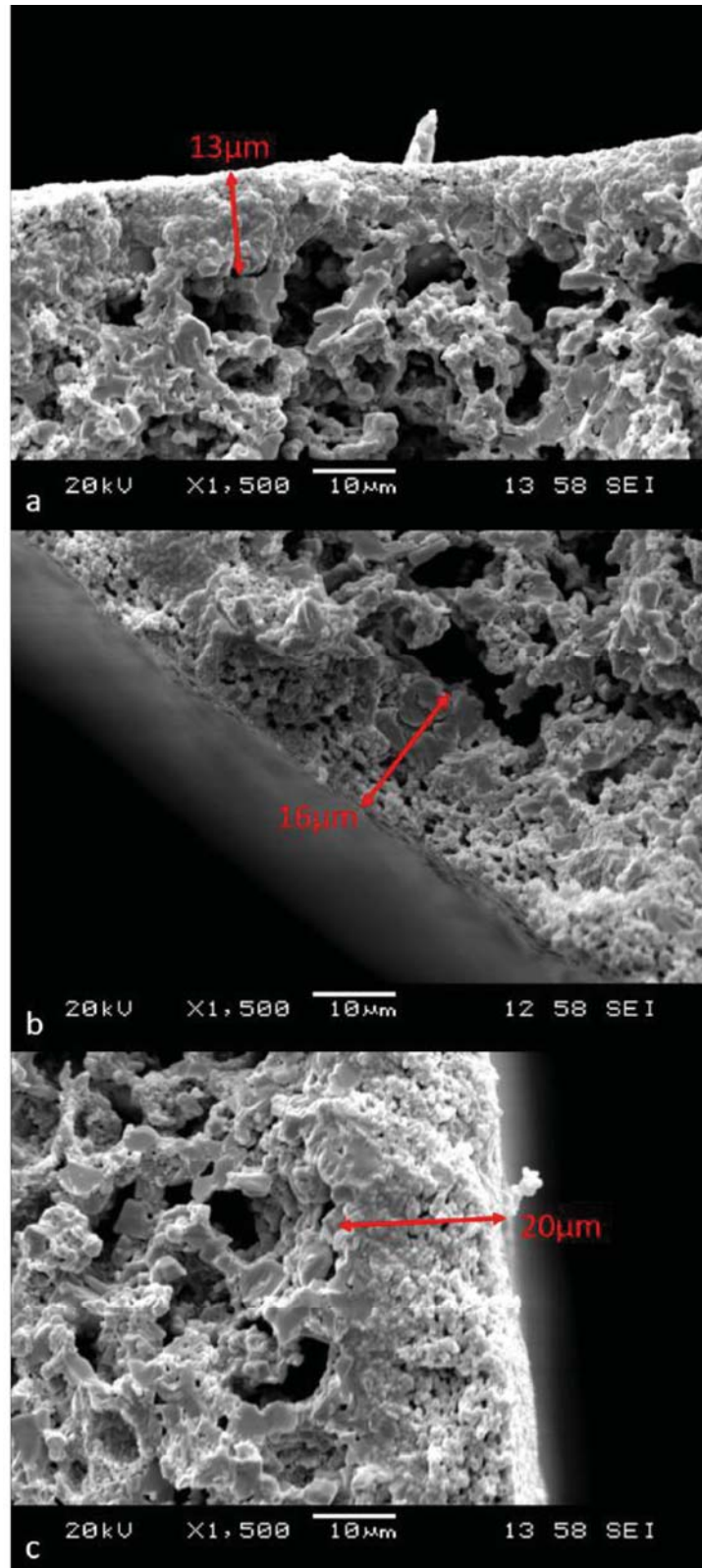


Figure 65 Cross section of coated pre-sintered tubes at a withdraw speed of (a) 20 mm/min, (b) 60 mm/min and (c) 100 mm/min

6.3. Conclusions and Future work

Optimised mass percentage of binder in the coating slurries was determined to be 10 wt% after testing the adhesion strength, while the viscosity test suggests a dispersant concentration of 2 wt%. The coating slurry was shown to be a shear-thickening fluid at a low shear rate range, for both coating experiences on green and sintered anode tubes. Finally the optimum processing parameters for electrolyte coating were determined to be a 50 wt% for solids loading and a 80 mm/min withdrawal speed.

The possible solutions to avoid coating on a porous substrate and the discontinuity of electrolyte were also described here. A dense anode functional layer, whose initial formulation excludes any pore forming material, could be added onto the green structural anode layer manufactured as described in Chapter 4 and Chapter 5. This additional dense structure could generate a smooth substrate surface for dip coating after pre-sintering, while simultaneously extending the length of TPB to enhance the efficiency of electrochemical transformation during the subsequent cell operations. The suggested assistant anode manufacturing process could be done by dip coating too. Moreover, a second electrolyte coating onto a dried pre-coated electrolyte layer is also feasible, if the eventual thickness of a dual-layer electrolyte configuration is acceptable.

The selected electrolyte processing parameters for later cell fabrication stages is as shown in Table 25 with a withdrawal speed of 80 mm/min.

Chapter 7 Sintering of dual-layer half cells

7.1. Introduction

In this chapter, the sintering and characterisation of electrolyte layers dip coated onto green/pre-heated anode tubes is described. The defects observed by SEM include cracking and porosity, both of which are due to thermal mismatch (i.e. different TEC, defined in Equation 13) between the anode and electrolyte layers. The next section of this chapter reports the dilatometry data for compacts made of the exact anode/electrolyte formulations, followed by systematic analysis of thermal mismatch between structures with different shrinkage levels.

7.2. Results and discussion

7.2.1. Co-sintering of dual-layer structure

With anode/electrolyte formulations given in Table 15 and Table 25, the heating process was first carried out on coated green anode tubes. Unfortunately, the sintered YSZ layer could not retain integrity after heating. Thus fully pre-sintered anode tubes were coated and co-sintered at 1300 °C. A continuous electrolyte layer was achieved after co-sintering.

The heating regime and the characteristics of co-sintered tubes are listed in Table 27. Note that both the pre-sintering and co-sintering processes are the same method as described in Chapter 3, except for the maximum dwell temperature.

For Tube A and Tube B, it is believed that the cracks (See Figure 67) were initiated at low temperatures within the electrolyte layer due to a larger shrinkage during co-sintering on a green anode layer. For Tube C (Figure 68), when co-sintered with coated electrolyte, the strong pre-sintered anode layer is able to maintain the structural integrity of the bi-layer configuration during the densification process, thus a higher thermal mismatch could be tolerated when 2-step sintering was carried out for the half cells. As the co-sintering trials with green anode failed to obtain an integrated bi-layer structure, one-step sintering proved not successful for half cells produced in this project.

Table 27 Heat treatments for the first-batch of tubular anode/electrolyte samples

Tube batch No.	Pre-sintering temperature	Co-sintering temperature	Characteristics after heating
A	Green	1300°C	Cracked and delaminated
B	Green	1400°C	
C	1400°C	1300°C	Continuous electrolyte layer with good adhesion

Dilatometry profiles for compacts made of anode and electrolyte formulations, using a method suggested in the literature [232], are shown in Figure 66 to assist in analysing the thermal shrinkage behaviour of the bi-layer structure. The compacts were debound (i.e. no liquid phase remaining in the samples) before testing in the dilatometer. It can be seen that both compacts start to shrink at $\sim 1000^{\circ}\text{C}$ and the dimension change becomes moderate when the furnace temperature is held at 1400°C for 30 minutes. The YSZ-E compact on sintering eventually acquires a thermal shrinkage of $\sim 16.5\%$ at the end of in-furnace treatment. On the other hand, the YSZ-A/NiO compact, with a different thermal expansion coefficient (TEC), reaches a corresponding shrinkage of $\sim 10.4\%$. This means a thermal mismatch of 6.1% , in terms of strain, which could not be tolerated by the co-sintered half cells, where the electrolyte is coated on a non-sintered anode substrate. It is also presumed that any pre-sintering of anode tubes would result in a thermal mismatch of $>6.1\%$ after subsequent co-sintering, since the anode shrinkage is expected not to reach 10.4% during co-sintering. More dilatometry tests were required to quantify the stress range of the 2-step sintering combinations.

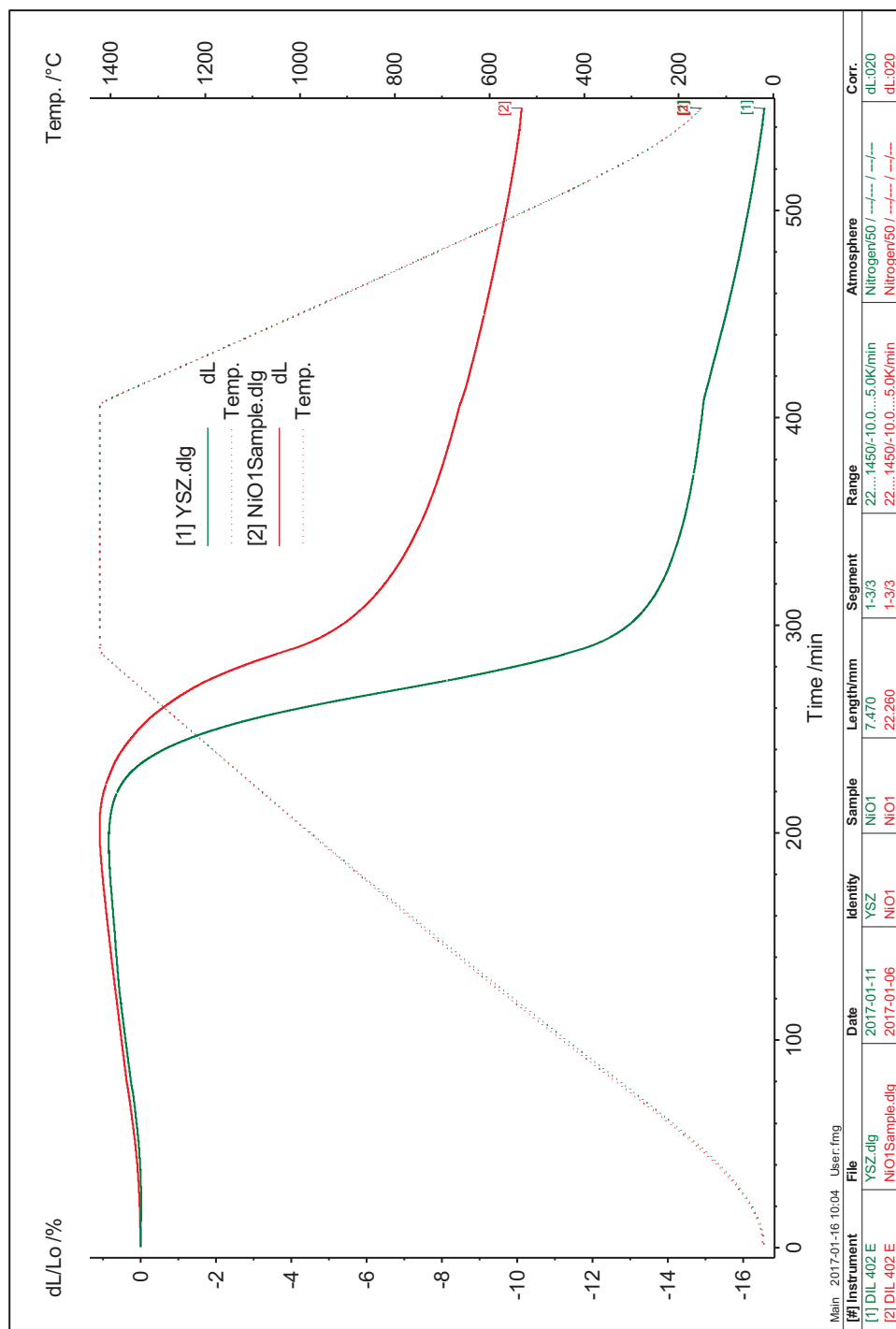


Figure 66 Dilatometry profiles for debound anode/electrolyte compacts

The cross-sectional imaging of 1-step co-sintered tubes is shown in Figure 67. It can be seen that there was a certain level of porosity within the cracked electrolyte layer when the electrolyte ink was on non-pre-sintered tubes. The anode tube that was pre-sintered at 1400 °C and then coated with electrolyte ink shows that porosity is also observed within the sintered electrolyte layer. The original porosity, generated shortly after dip coating process due to the rapid evaporation of solvent, is expected to be one of the causes of the characterised porosity after sintering. However, the porosity in electrolyte could inhibit the efficiency of ion exchange and should be ideally eliminated during densification process while heating. Literature [233] suggests that the reason why such porosity remains until the end of two-step sintering is the shrinkage of coated layer. As the pre-sintered anode would hardly change its dimensions during the co-sintering, the coated electrolyte layer, which is constrained by the substrate, could not shrink as an entity.

An explanation is provided here for the electrolyte porosity characterised in the 1-step sintered tubes and shown in Figure 67. When the cracked and delaminated electrolyte layer is not constrained by the anode layer, more degrees of freedom for dimension change would be generated and the existing porosity could not be effectively eliminated as a result.

Figure 68 shows only ~13 µm electrolyte layer develops when 2-step sintering was performed, while Figure 67 shows an electrolyte thickness of ~25 µm for 1-step sintered tubes. This indicates that the surface of fully sintered (at 1400 °C) anode tubes is too smooth to acquire a relatively thick electrolyte layer after coating and sintering. A rough anode surface or multiple coatings are necessary if a thicker YSZ layer is required. The additional shrinkage of the anode layer in the two-step process

is thought to arise because no cracking was observed and in order to accommodate the differential shrinkage of the two components, the mobile (through sintering plasticity) electrolyte layer shrinks in thickness.

The appearances of different combinations of anode/electrolyte conditions (green or sintered) are shown in Figure 69.

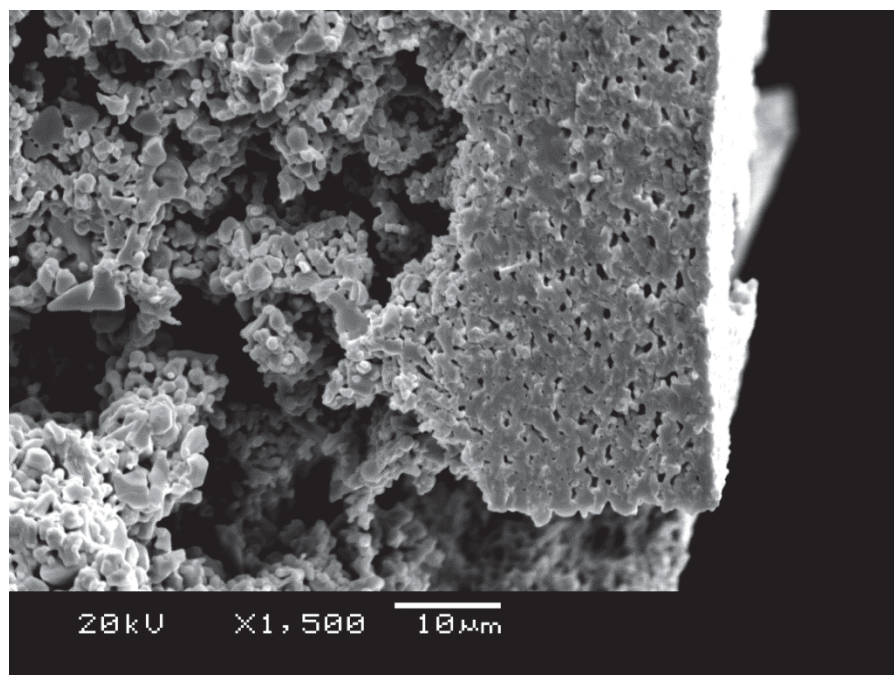


Figure 67 Cross section of co-sintered Tube B

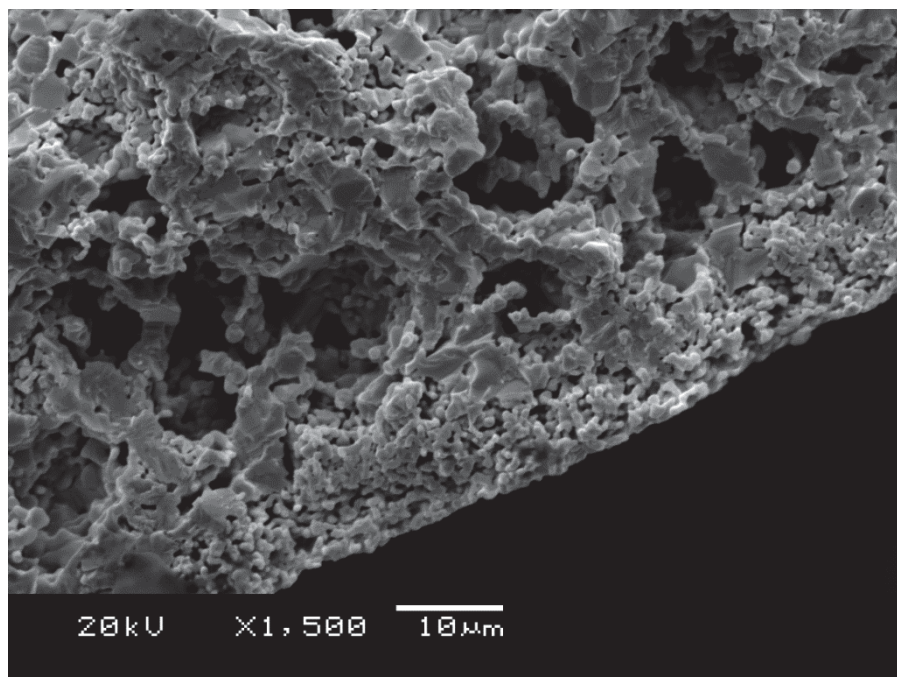


Figure 68 Cross section of co-sintered Tube C

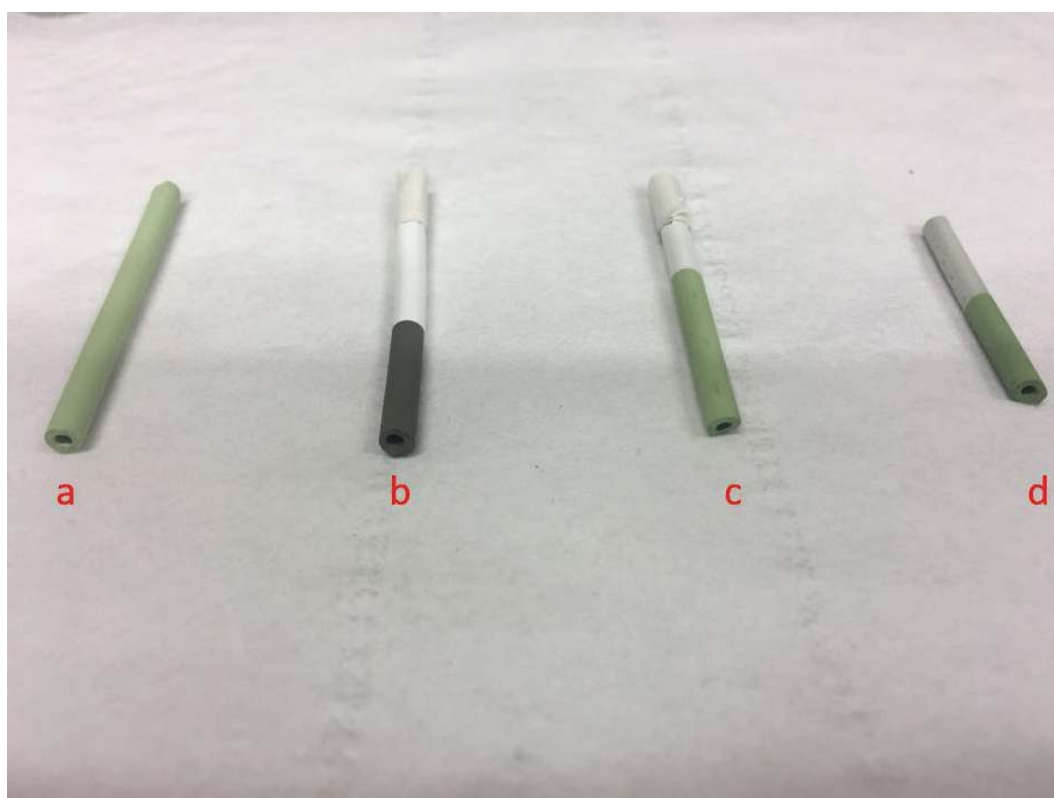


Figure 69 Apperances of (a) sintered anode tube, (b) non-sintered coating on green anode, (c) non-sintered coating on sintered anode and (d) co-sintered half cell

The porosity of the coated layer is thought to be controlled by adjusting the degree of the substrate shrinkage during the pre-heating process, which were proved valid for both anode supported [234] and electrolyte supported [235, 236] tubular cells. This means a fully sintered anode is not necessary for the cells manufactured in this thesis. Accordingly, two more heating combinations of 2-step sintering were then carried out, to explore the possibility of acquiring a dense and thick electrolyte layer. These are listed in Table 28. Both sintering trials eventually produce half cells with continuous and homogeneous electrolyte layers with a thickness between 20 and 30 μm .

Tube D shows a dense electrolyte layer (Figure 70), with no obvious porosity. Tube E exhibits similar characteristics, but a low level of porosity is observed within the electrolyte layer (Figure 71).

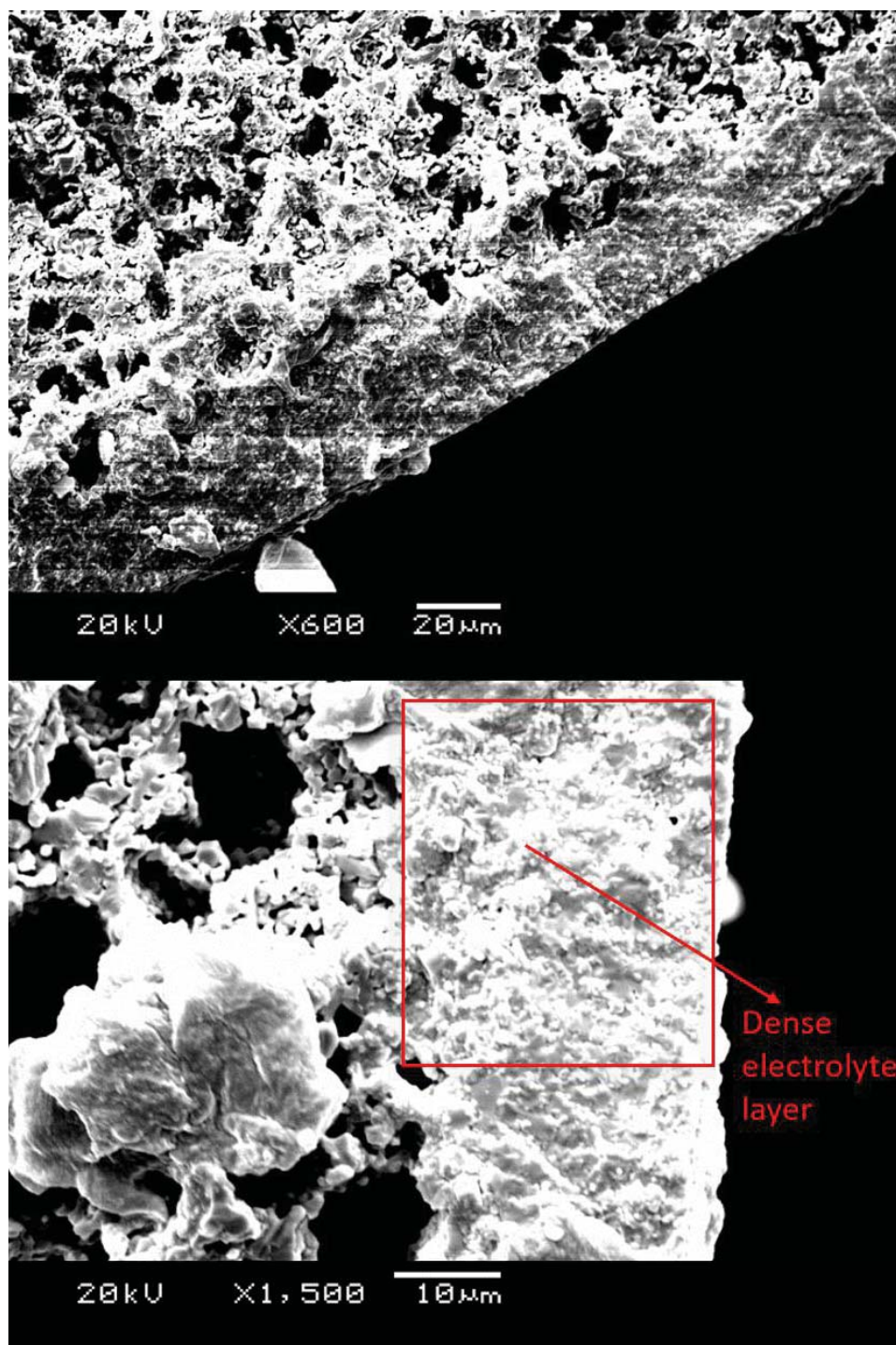


Figure 70 Cross section of co-sintered Tube D

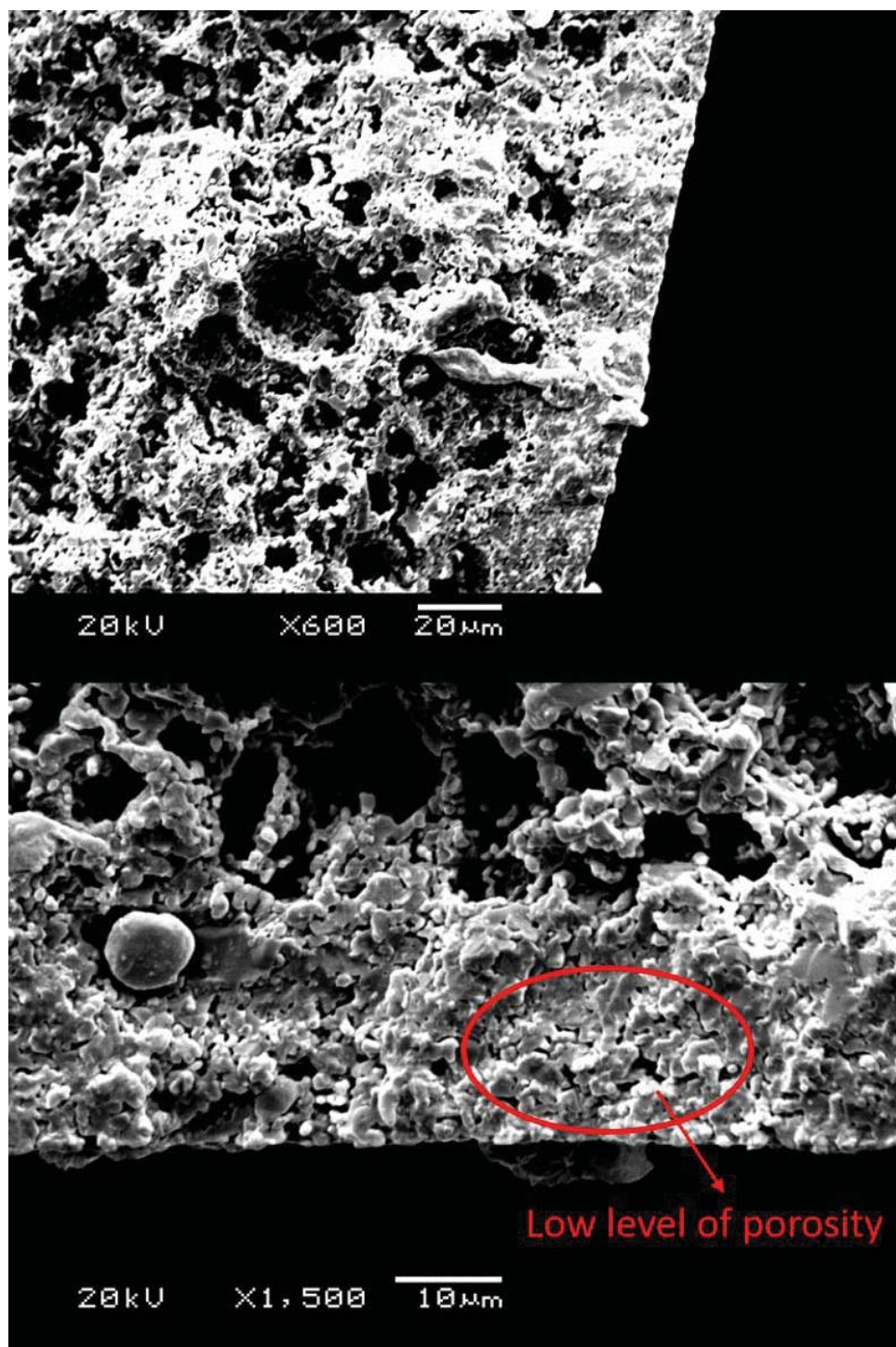


Figure 71 Cross section of co-sintered Tube E

Table 28 Heat treatments for second-batch tubular samples

Tube batch No.	Pre-sintering temperature	Co-sintering temperature	Electrolyte layer thickness
D	1100 °C	1350 °C	28 µm
E	1250 °C	1350 °C	25 µm

Thus, it can be concluded that a low thermal mismatch, in terms of strain, is necessary for the co-sintering step during 2-step sintering, to obtain a dense and thick electrolyte layer. In this case, the substrate anode layer would not apply a large drag force on the electrolyte layer, so both layers could shrink together to some extent. As a result, the porosity within the electrolyte layer could be eliminated.

7.2.2. Dilatometry analysis for anode/electrolyte compacts

Figure 72 shows dilatometry results for compacts made of identical anode and electrolyte formulations but with different pre-heating treatments. The four anode compacts denoted as Anode1100, Anode1250, Anode1400 and Anode were extruded into a rod form first, using the anode paste formulations. They were then pre-heated at temperatures of 1100, 1250, 1400 °C and room temperature (i.e. no pre-heating treatment) respectively, as the first heating step experienced by Tube A(B), C, D and E. The compact denoted as Electrolyte was prepared by collecting and pressing the solid content after drying the electrolyte slurry. All of the five compacts were tested to a maximum temperature of 1400 °C at a rate of 5 °C/min.

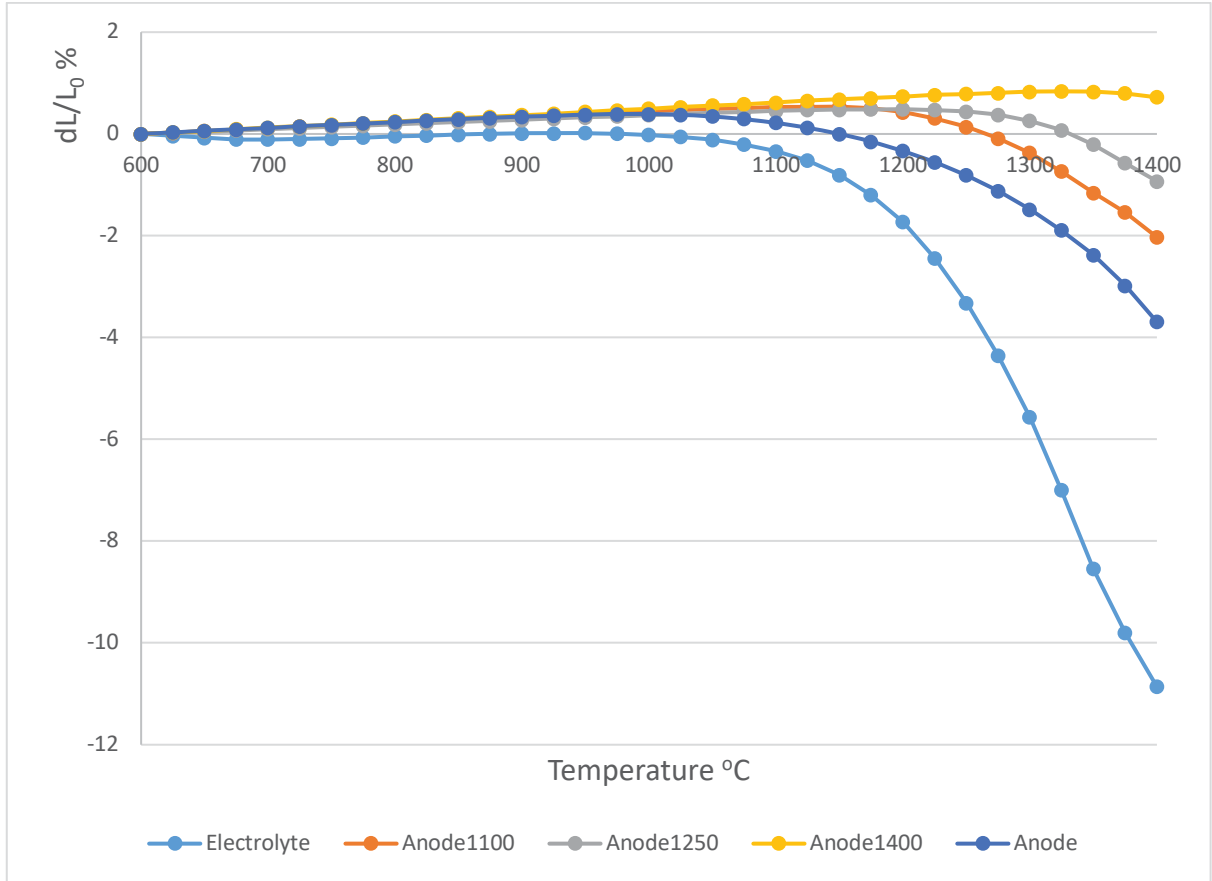


Figure 72 Dilatometry plots for anode/electrolyte compacts in the temperature range between 600 °C and 1400 °C

Here a term, mismatch strain, is introduced to assist the analysis, given in Equation 30 [237]. The mismatch strain describes the difference of sintering shrinkage between two co-sintering bodies, with a high numeric value indicating a high probability of sintering defects between half-cell layers.

$$\text{Mismatch Strain} = \left(\frac{\Delta L}{L_0} \right)_{\text{Electrolyte}} - \left(\frac{\Delta L}{L_0} \right)_{\text{Anode}}, \text{ (Equation 30)}$$

The mismatch strains for one-step sintering (denoted as Anode) at the temperature range between 600 and 1400 °C are given in Figure 73. A mismatch strain of 7.2% is known to be too high for the 1-step co-sintering to maintain the structural electrolyte integrity.

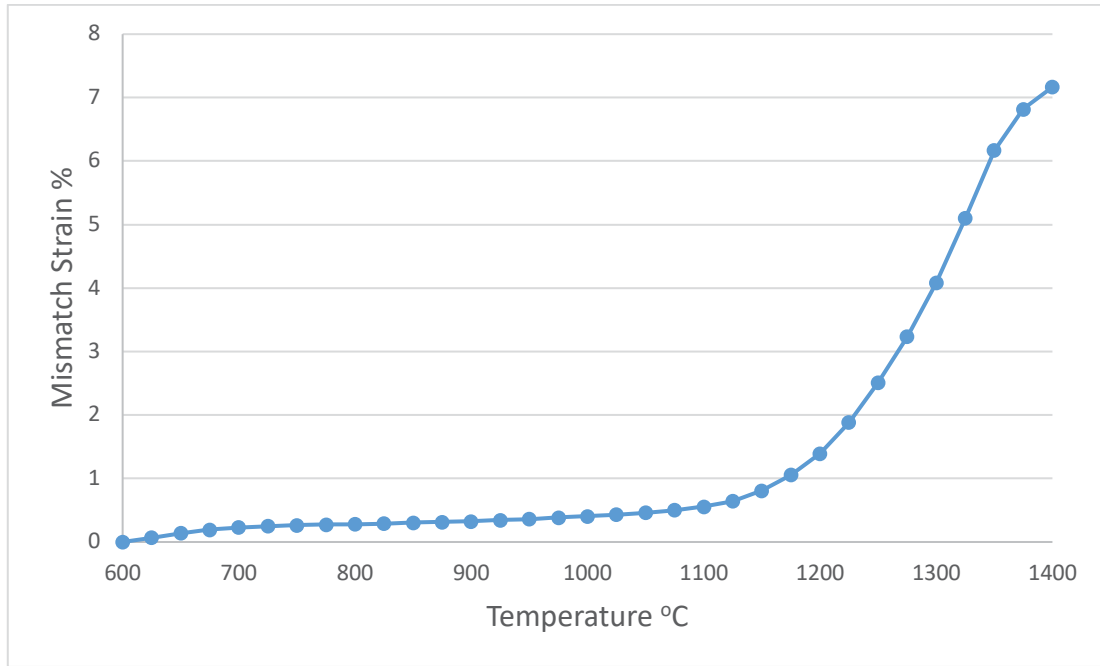


Figure 73 Mismatch strains between anode and electrolyte layers of Tube A-B

Figure 74 plots the mismatch strain for two-step sintering (Anode1100, Anode1250 and Anode1400). It indicates that the mismatch strain between Anode1100 and Electrolyte becomes 8.8% when temperature reaches 1400 °C. The mismatch strains are 9.9% and 11.6% for the combinations of Anode1250-Electrolyte and Adode1400-Electrolyte, respectively. This means a porous electrolyte is likely to form when the mismatch stain between the pre-sintered anode and the electrolyte extents to a level beyond ~10%. A persuasive assumption is that the further extension of mismatch

strain into a higher level may cause cracking for materials undergoing a 2-step sintering process.

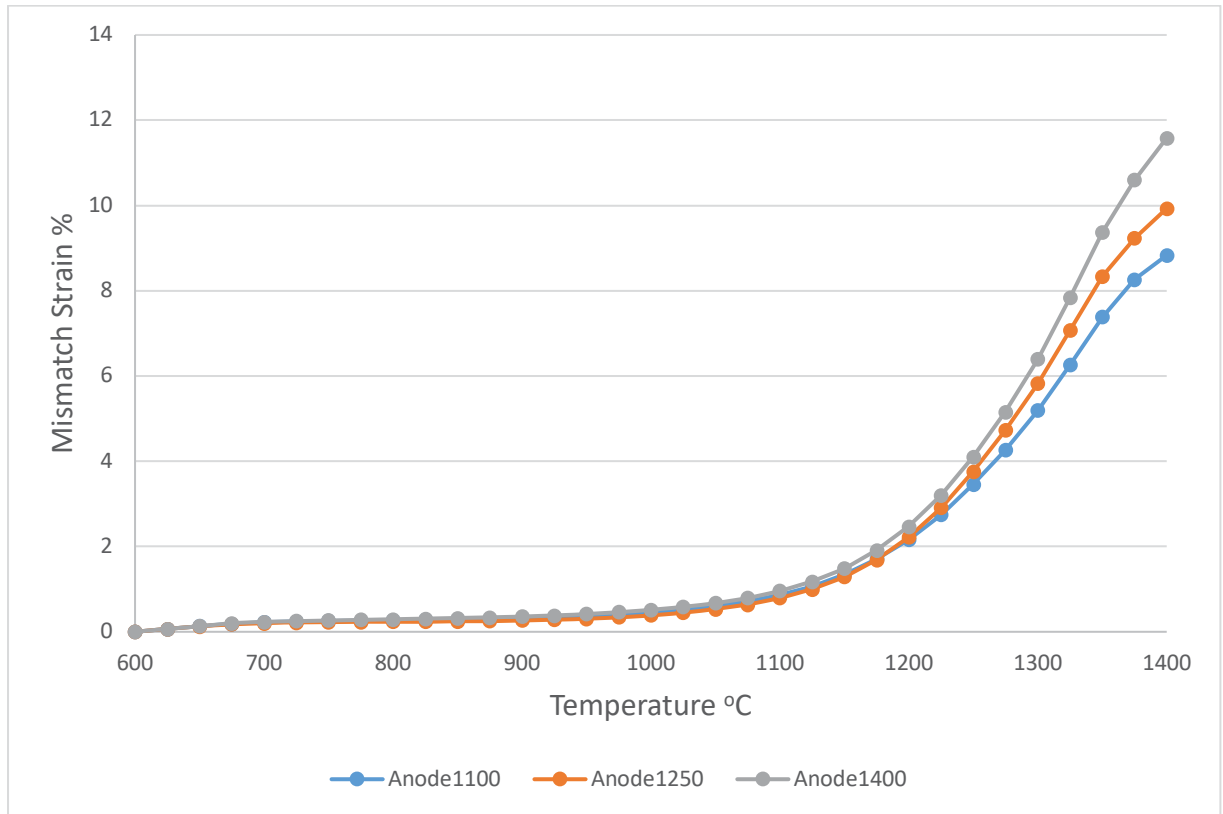


Figure 74 Mismatch strains between anode and electrolyte layers of Tube C-E

It should be noted that any plot of thermal strain shown before does not include the information of strain when dwelling at a fixed maximum temperature for a perceptible period. This means the data points shown in Figure 72 are all recorded during a ramp process where the furnace temperature is raised at a given rate (5 °C/min in this study). Both anode and electrolyte samples are expected to exhibit further shrinkage after the held in-furnace treatment with the heating regimes given in Table 13, 26 and 27. As a result, the mismatch strain should have a reasonable variation after the entire sintering practice, compared to the characterised values during a continuous

ramp process. On the one hand, the eventual thermal strain for the one-step sintered anode and electrolyte samples was seen in Figure 66, with a mismatch strain of 6.1%. On the other hand, the mismatch strain between these two samples is 7.2% in Figure 73 for a pure ramp heat treatment. The variation of mismatch strain after dwelling and cooling is considered to be acceptable for this simplified analysis.

According to Hsieh et al. [233], a mismatch strain of ~25% between pre-sintered ScSZ (Scandia Stabilized Zirconia) electrolyte support and coated anode layer (mixture of NiO, ScSZ and carbon) is still able to generate a porous sintered anode layer without cracking or delamination. However, they found severe sintering defects occurred when the mismatch strain reached ~30%. In this case, the anode layer would become porous, fragile and poorly attached to the electrolyte surface at that higher mismatch strain. Compared to the literature, the work reported here results in mismatch strains with much smaller numeric values hence no cracking is observed on the co-sintered electrolyte layer, which is coated onto the pre-heated anode tubes. Additionally, the electrolyte manufacturing process has been shown to be able to generate a dense structure on the anode extrudates.

7.2.3. Discussion of initiation of electrolyte cracking for one-step sintering

Figure 75 gives the entire dilatometry profile of the electrolyte compact, including the debinding process. It shows that before sintering shrinkage, a strain of ~20% has already been generated, mostly in the temperature range of 0-300 °C. A comparative shrinkage is also thought to occur for anode materials over this temperature range.

This is believed to result from the gasification of solvent in the liquid phase, namely cyclohexanone in the case of anode heating. More precisely, the constituents burnt off over this low temperature range are in liquid form and yet hard to evaporate at room temperature. Materials that comply with this characteristic include cyclohexanone and DBP for the anode formulation, and additionally DBP and fish oil for the electrolyte formulation. Burning of such constituents would definitely decrease both mass and volume of the liquid phase, triggering the observed dimension reduction. Nonetheless, the rest of materials within anode/electrolyte is still a continuous and stable entity, until the binder (PVB) is removed at a higher temperature ($\sim 500\text{ }^{\circ}\text{C}$). Accordingly, the dimension changes in this stage are not thought to cause any structural defects in the electrolyte layer.

No obvious dimension changes are characterised over the temperature range $400\text{ }^{\circ}\text{C}$ to $600\text{ }^{\circ}\text{C}$, which indicates that shrinkage defects due to mismatch of the TECs are also unlikely to initiate during this stage of the heat treatment, even if the binder system is thoroughly removed and the half cell becomes an assembly of loose ceramic powders. Combined with the TGA results shown in Figure 49, the burning out of PVB and corn starch will give rise to considerable mass loss, without significant volume loss being observed.

In the literature [233], the cracking observed in one-step sintering is considered to be initiated at low sintering temperatures and its magnitude intensified as the mismatch strain rises with temperature. The reason why no cracking is observed for 2-step sintering is the existence of a strong substrate on which the coated layer is placed. This interpretation is accepted by the author, but another possible origin of cracking defects is provided in this section.

At a temperature between 400 °C and 600 °C, the burning of binder (PVB) within the anode structure, as well as pore former (corn starch), might have a slight impact on the electrolyte layer, leading to a structural inhomogeneity for the half-cell surface. Such distortion could be considered as a potential source of cracking, although the coated layer is in a transitive form from viscous slurry to loose powder, at the temperature range being considered. Previously published papers also pointed out the problems associated with the binder removal procedure, such as tube warping and twisting [238], which could be regarded as supplementary support of the assumption.

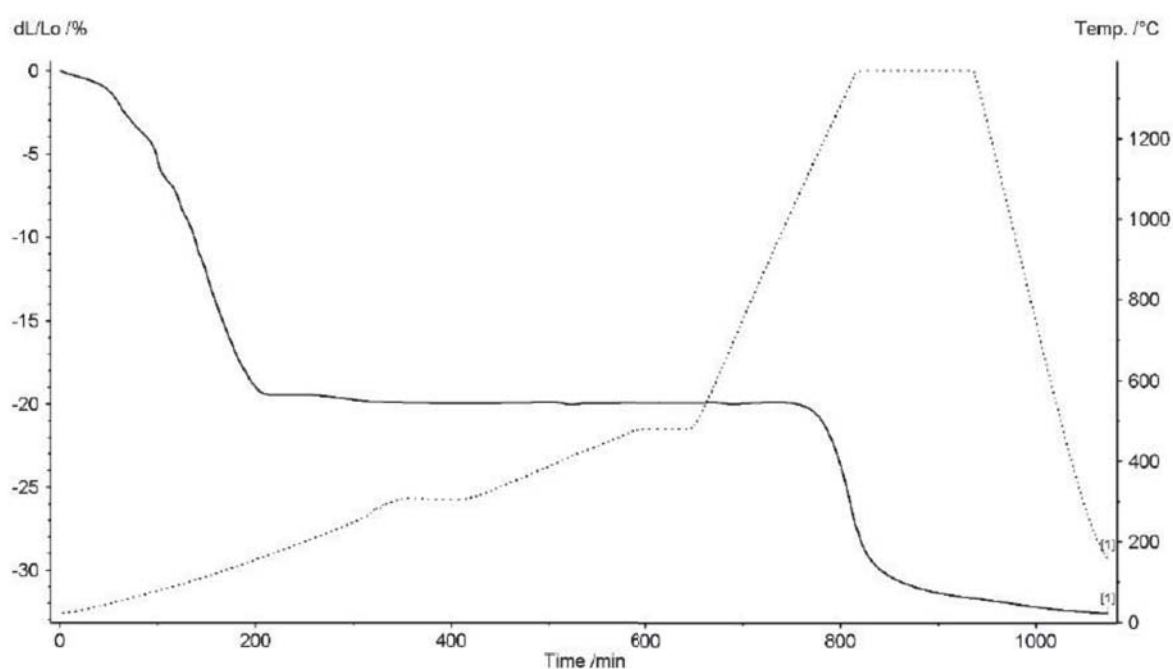


Figure 75 Dilatometry profile of electrolyte compact sintered at 1400 °C including debinding process

7.3. Conclusions and future work

One-step sintering is proved not valid for the half cells made in this project, as cracking develops due to mismatch of sintering behaviour. Pre-heating of the anode is believed to provide a robust substrate to constrain the sintering of the electrolyte and allow a higher thermal mismatch to be borne. The electrolyte shrinkage is desired to eliminate the initial porosity and not to generate additional porosity through stress. A dense electrolyte was acquired by using a 2-step heating combination of pre-sintering the anode at 1100 °C and co-sintering the pre-sintered anode together with the electrolyte at 1350 °C.

Dilatometry results for anode/electrolyte compacts indicate a mismatch strain above ~10% would no longer allow a dense electrolyte structure to develop in 2-step sintering. A mismatch strain of ~7% was sufficient to initiate cracks for 1-step sintering. The temperature where cracking originates during a 1-step sintering is believed to falls in the range between the starting point of sintering (~1000 °C) and the maximum temperature. However, the debinding process (occurring below 600 °C) is also thought to be a further source of cracking and delamination, as a result of structural impact on the electrolyte due to the burning off of organic components.

Future work should focus on the constrained sintering of a coated layer on a non-sintered debound support, in a loose powder form, followed by the characterisation of sintering defects. A well-controlled operation process is required for this purpose, as coating on an unstable substrate is quite intractable. If cracks are characterised at an equal level of mismatch strain to that of a 1-step sintering in this study, then the possibility that cracking is initiated during the debinding process could be excluded.

Chapter 8 Cell performance testing

8.1. Introduction

The structurally optimised mSOFCs were electrically tested in terms of Current-Voltage (I-V) and Electrochemical Impedance Spectroscopy (EIS) behaviour and the results are reported and discussed in this chapter. Half cells comprising extruded anode and dip coated electrolyte were fabricated and sintered using the methods discussed in Chapter 4-7 and after sintering, a cathode layer and current collecting components were added. The electrochemical performance of the cells are compared and discussed in the context of literature.

8.2. Preparation for cell testing

The half cells, with anode/electrolyte formulations given in Table 15 and Table 25, sintered using the heating regime identical to Tube D given in Table 28, were all coated with two LSM (Praxair Surface Technologies Ltd., UK, $D_{50} = 0.9 \mu\text{m}$) layers, to give a functional and a structural cathode layer. This produced a complete cell unit. The coating was applied by brush, and the coated cathode layer covered nearly the entire surface of the electrolyte, with only a tiny uncoated region at both ends of the electrolyte. Separate but identical sintering processes were carried out after each of the coating operations, as detailed in Table 29. The cathode slurries were developed by the Centre for Hydrogen and Fuel Cell Research, University of Birmingham.

Before being installed into the manifold, the completed cells were further coated with porous silver paste ink (SPI) on both the anode and electrolyte surfaces to allow current collection. Additionally, the two electrodes are wound with a bundle of silver

wire (99.98%, Silver Wire Co) to allow connection to the electrical analysis equipment. The drying of SPI was undertaken in the oven for 4 h at 120 °C. The prepared cell units ready for testing are shown in Figure 76.

Table 29 Heating regime for the functional/structural cathode layer

Heating stage	Rate/Duration	Purpose
Ramp to 350 °C	1 °C/min	Drying
Dwell	1 h	
Ramp to 550 °C	1 °C/min	Debinding
Dwell	1 h	
Ramp to 1100 °C	5 °C/min	Sintering
Dwell	4 h	
Ramp to 40 °C	5 °C/min	Cooling

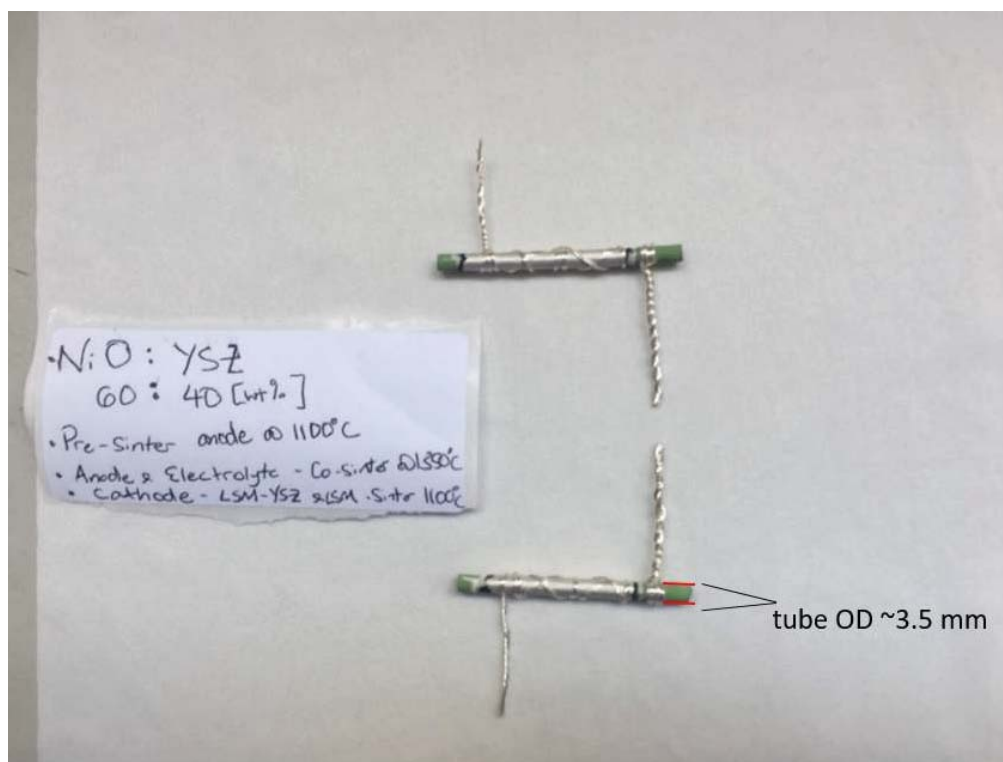


Figure 76 Imaging of prepared cells ready for testing

8.3. Handling of gas tightness issue

A ceramic manifold was used to hold the tested cell, as shown in Figure 77a.

Ceramabond (Aremco) was applied to form the seal in place between the cell and the ceramic manifold. The drying of Ceramabond was carried out in the oven for 6 h at 120 °C.

Multiple cell samples were tested using this manifold, with no recognisable open circuit voltages (OCVs) characterised in most cases. The furnace was reopened after testing and a damaged cell is shown in Figure 77b, with the current collection units (i.e. the SPI and silver wire) melted and separated from the cell. A reasonable cause for this failure is a hydrogen leak from the inside of the cell during testing, creating a flame that melts the silver components.

Leakage tests showed a number of gas leakage points located between the ceramabond and the manifold surface, even when careful sealing was applied repeatedly in this area. This was probably due to the thermal shrinkage mismatch between two types of materials which the bond failed to overcome.

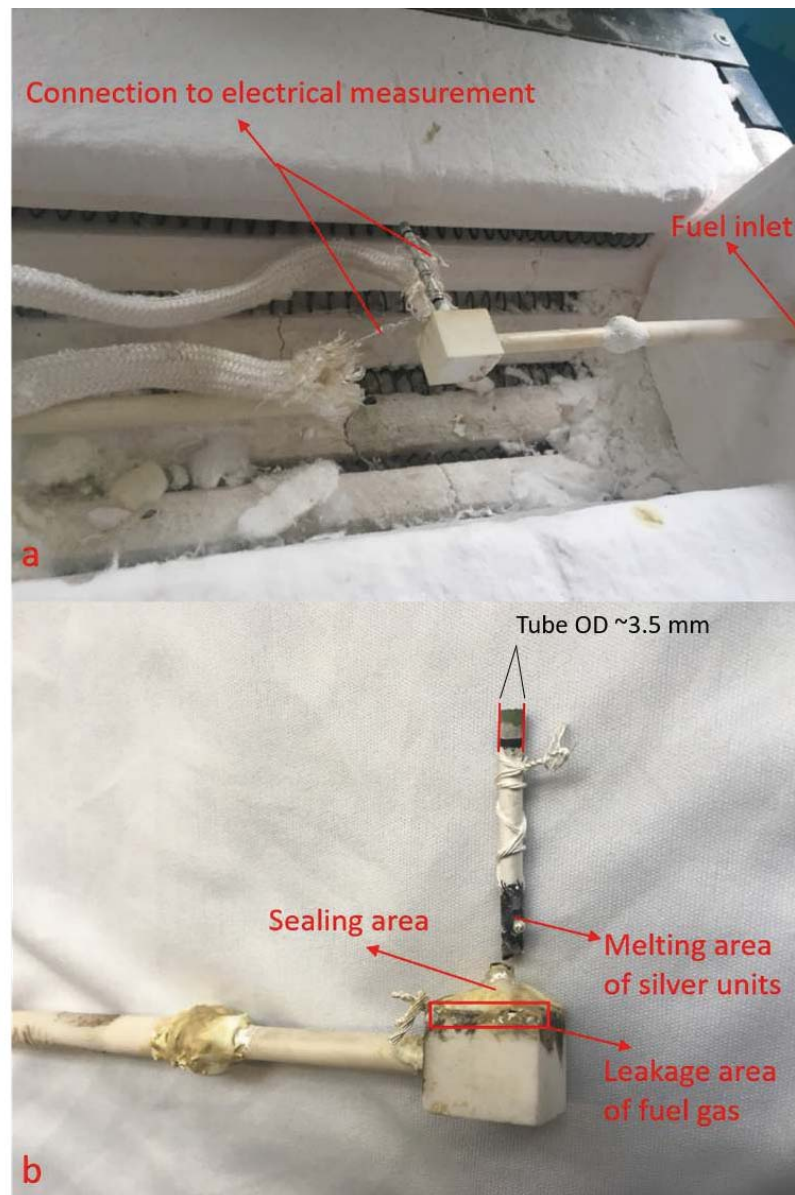


Figure 77 Ceramic manifold used (a) before and (b) after the initial tests

The melting of the current collectors would give rise to two effects that might cause the failure of OCV characterisation:

- (1) Breaking of the silver wire on the anode surface, leading to disconnection between the anode and the electrical measurement unit.
- (2) Direct conductive connection between the anode and the cathode layer, causing a short circuit and the extremely low OCV.

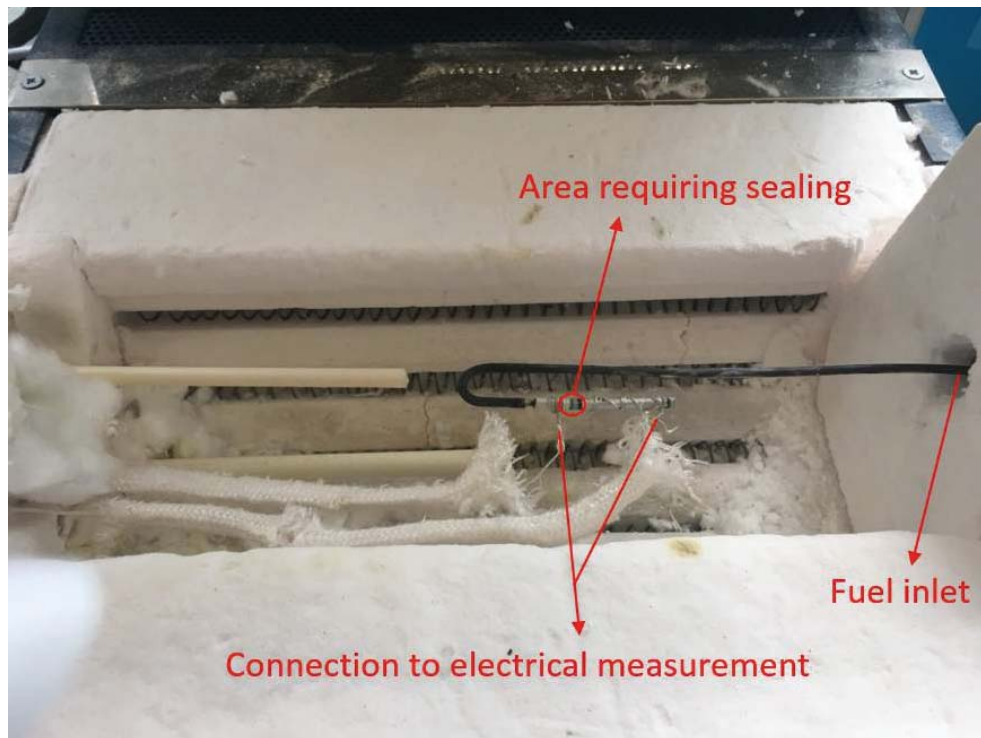


Figure 78 Metallic manifold used for later tests

In order to develop a better seal, a metallic manifold was designed and applied to the electrical testing of the mSOFC samples. This arrangement can be seen in Figure 78. This manifold was oxidized before any testing operations were undertaken to avoid

electrical conduction from the mounted cell. To achieve an easy connection, the end of the manifold was made from a length of tube which had a smaller diameter than the cell and could be inserted into the cell inlet without damage. The only region requiring sealing was then a small portion of exposed porous anode on the outer surface of SOFC tubes. Another benefit of this manifold design was its non-destructive nature so that the cells could be unloaded and tested again after the first run if required.

8.3. Results and discussion

As can be seen in Figure 79, the Current-Voltage (I-V) curve exhibits an Open Circuit Voltage (OCV) of 0.82 V, which is considered to be slightly lower than would be expected from the normal OCV range below the theoretical value. The cell voltage drops rapidly while current density is raised, with the peak power (0.11 W/cm²) being reached at a current density of ~0.25 A/cm². Although the electrical data for mSOFCs manufactured in this thesis are not ideal, they are quite normal for lab-made fuel cells when referring to Table 3. Laboratory made cells with equivalent power densities to those tested in this thesis can be found in References[147, 154, 161].

Electrolyte (formed from ScSZ) supported mSOFCs manufactured by Hsieh et al. [233] showed a peak power density of 0.14 W/cm² at 800 °C, indicating an equivalent power output level to the laboratory-made cells, though the OCV of their products could reach 1.1 V. There are several suggested mechanisms for the low characterised OCV within this study:

- 1) Thick electrolyte between 20 and 30 μm would increase the resistance for the transfer of anions;
- 2) Lack of a dense anode functional layer would shorten the length of TPB and inhibit the electrochemical process;
- 3) Potential discontinuities in the electrolyte would cause exchange of fuel and airgases across the electrolyte which could change the partial pressure distribution on both sides of the SOFC.

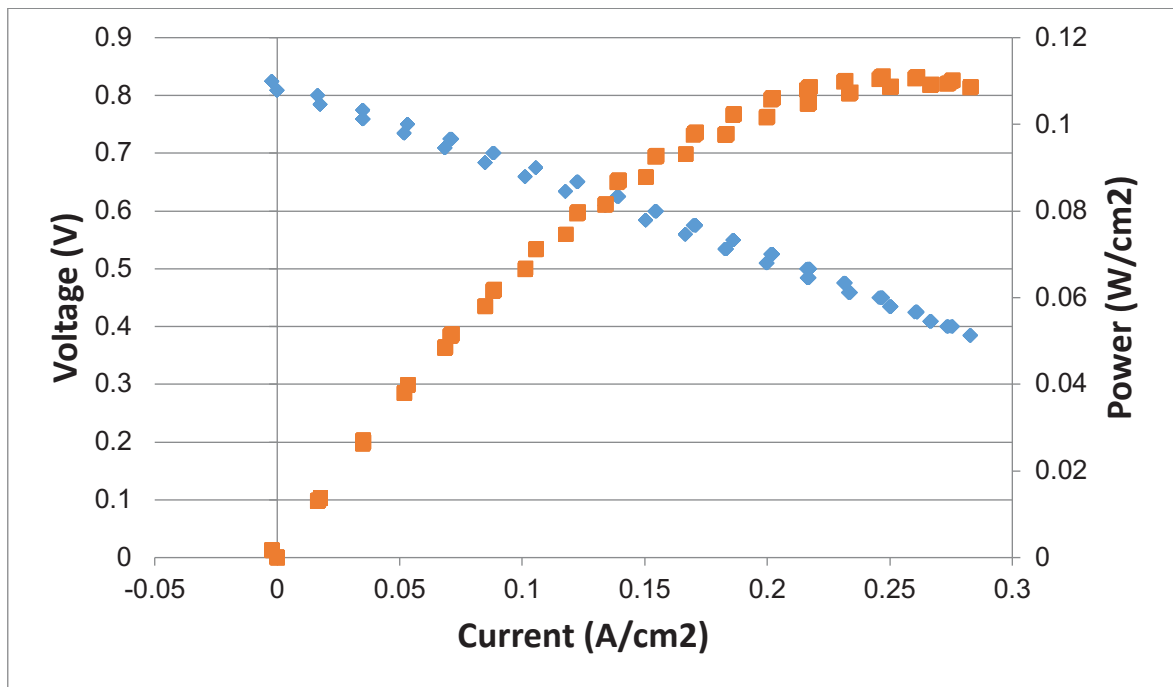


Figure 79 Current-Voltage curve at 750 °C with 50 ml/min H₂ and 50 ml/min N₂

Table 30 shows the comparison of electrolyte characteristics between commercial mSOFCs (Adaptive Materials Inc., USA, denoted as Cell AMI) and laboratory manufactured cells developed in this project (denoted as Cell FMG). The SEM

images of both cell structures are given in Figure 80. Accordingly, Mechanism 2 is thought to be the major origin of low OCV value, as the minor differences in layer thickness and density is not thought to significantly impact the electrochemical performance, in the way suggested by Mechanism 1. A high OCV has been reported by Hsieh et al. [233], as mentioned above and in SEM imaging of post-test cells. It was difficult to characterise directly the contact between anode and cathode. However, due to the large anode pore size, an exceedingly shortened TPB was observed in the laboratory made cells, which was expected to inhibit the activity of electrochemical conversion.

Table 30 Comparisons between commercial cells [2] and lab made cells using the identical electrical test rig

	Cell AMI	Cell FMG
Electrolyte thickness	~16 μm	~28 μm
Electrolyte tightness	Fully dense	Negligible porosity
Electrolyte resistance (acquired from EIS characterisation)	0.11 Ω (650 $^{\circ}\text{C}$)	0.33 Ω (750 $^{\circ}\text{C}$)
OCV	1.13 V	0.82 V

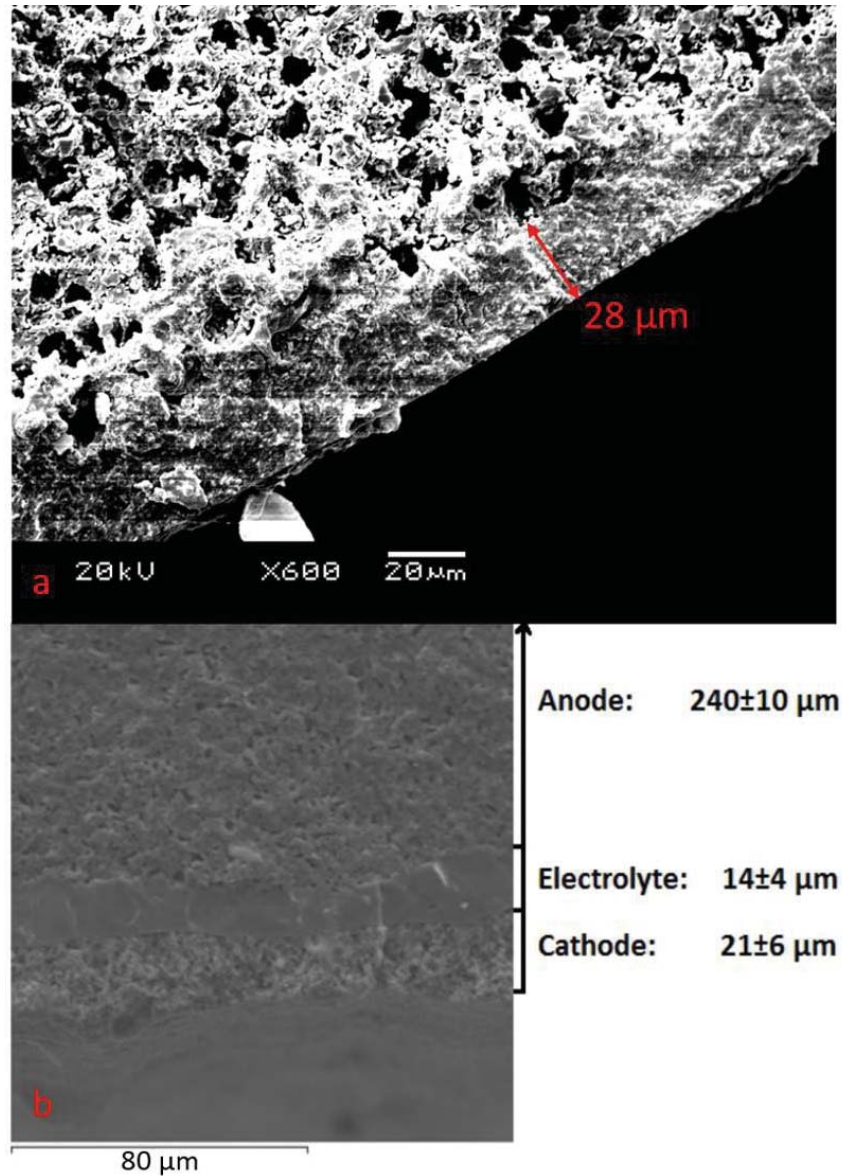


Figure 80 Electrolyte characteristics of (a) Cell FMG and (b) Cell AMI [2]

Figure 81 gives the Nyquist plot of the EIS responses. The lower intercept at Z' axis corresponds to a value of 0.33Ω , indicating that the inherent resistance of the electrolyte at 750°C is high, compared to the literature [2]. Although this ohmic value also involves the connection and circuit resistance, the relative magnitude between different electrolytes could be compared, given that the electrolyte resistance

contributes mostly to this resistance and the same test rig is used for both types of cells (Cell FMG and Cell AMI in Table 30). Moreover, temperature is the only factor that would relocate the lower intercept value as a result of limited ion conductivity at relatively low temperatures, but its effect is constrained at the operating temperature range. The high electrolyte resistance of laboratory made cells is consistent with the characterised low OCV value that is thought to arise predominantly from limited active reaction sites along TPB.

The higher intercept of the arc is strongly affected by fuel characteristics (fuel type, flow rate, etc.) and input current, as it reflects the resistance built kinetically through the electrochemical reactions. This value is also raised when the sample is cycled repeatedly as a result of cell degradation. Thus only impedance data for the sample being tested for the first time, at an input voltage 0.1 V below OCV were taken. This high voltage value corresponds to a low input current, thus the kinetic resistance (R_{ct} in Figure 32) could be greater than that obtained at lower voltages (e.g. at the peak power density), as a higher activation barrier is expected for lower currents.

Typically the arc region shows two semi-circles overlapping each other, corresponding to the processes at both interfaces between the electrolyte and one of the electrodes. McIntosh et al. [239] suggested that the right partial arc (i.e. plot at low frequencies) represents the impedance contributed by the anode. However, the overlapping phenomenon is not obvious for the tested cells manufactured in this project, making it hard to distinguish the individual resistance contributions of anode and cathode, respectively. Nonetheless a total kinetic resistance of $\sim 0.23 \Omega$ is characterised for the overall reaction.

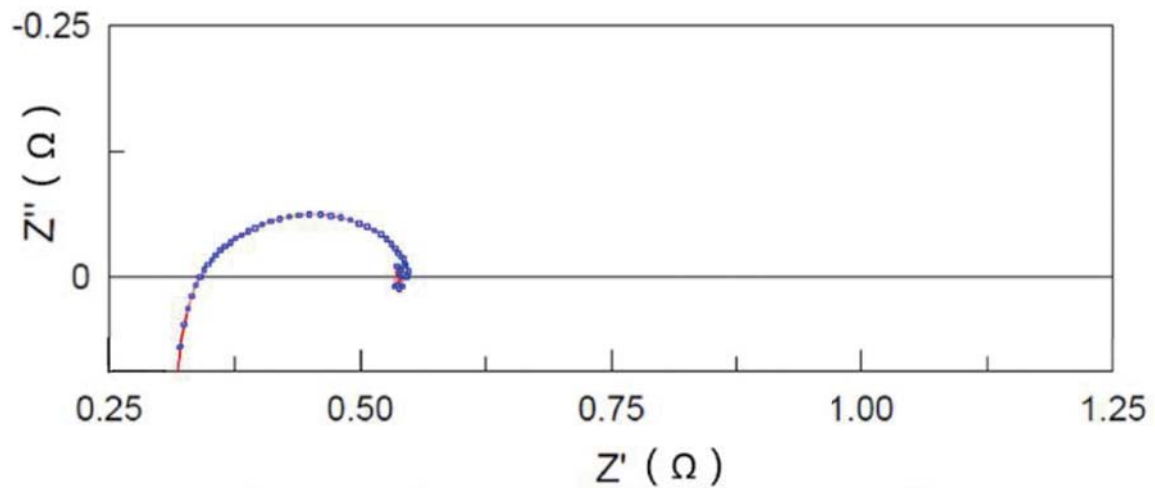


Figure 81 Nyquist plot of EIS at 750 °C and 0.1 V below OCV, with 50 ml/min H₂ and 50 ml/min N₂

8.4. Conclusions

I-V curve and EIS plots of lab made mSOFCs in this thesis indicates high electrolyte resistance and low OCV values. The most likely mechanism for this is that the limited contact points between anode and electrolyte due to large anodic pore size generates shortened TPB for adequate electrochemical reaction to take place. Consequently, the efficiency of ion transfer within electrolyte is inhibited and a degraded electrical performance is characterised. The phenomenon is believed to be promoted by adding a dense functional anode layer between the porous anode structure and the electrolyte, to extend the length of TPB.

Chapter 9 Conclusions and future work

Ram extrusion technology has been developed as a conventional fabrication method for the support tube of a mSOFC. Combined with viscous plastic processing (VPP), anode supported tubes have been manufactured with no intractable problems.

A powder packing study suggested a threshold for the volume fraction of solid phase within the viscous paste prepared for extrusion. The predicted packing of the powder mixture comprising the ceramic constituents (NiO/YSZ-A) and the pore former (corn starch) was 0.84. However, due to the processing characteristics of VPP (i.e. twin roll milling) and extrusion, an excess of liquid phase (i.e. organic binder system) was necessary for the paste formulation. Thus in the optimised formulation liquid phase was added above that required to just fill the voidage estimated by calculation. The upper limit of the solids loading computed in this thesis is high compared to that of an empirical method in the literature, but is proved to be a reasonably valid prediction for the methodology adopted in the study. A compromise should be made for the liquid content between the paste extrudability and the intractable issues related to high liquid fraction, i.e. paste stickiness and maintenance of the geometry of the tubes.

Rheology studies indicate that the formulated paste was homogeneous and that both die land regions for the six-hole and the annular extrusion sections of the die generate the majority of the pressure drop during the extrusion process. These two die land regions are considered as the origin of the pressure variations, when relatively dry pastes are being extruded, after several assumptions were explored. A variant of phase migration phenomenon, i.e. local phase distribution, was believed to cause the observed unsteady trends in extrusion load. This type of redistribution is

thought to be transverse, instead of longitudinal, with a dense ceramic region accumulating in the vicinity of die components. The derivation of the conclusion used the pore former as a tracer agent to indicate the distribution of paste constituents during extrusion.

A dip coating process for the YSZ electrolyte layers was successfully developed to apply the coating to the anode tubes. The minimum portion of binder necessary for an adequate adhesion strength between the coating slurry and the anode surface was found to be 10 wt%, while an intermediate dispersant percentage of 2 wt% was identified to optimise the slurry condition and stability. The coating slurry was shown to be a shear-thickening fluid at low shear rates, then the electrolyte layer thickness could be controlled by adjusting the withdraw rate as well as the solids loading of the slurry. The slurry involved an azeotropic solvent mixture of toluene/ethanol that volatilizes rapidly even at room temperature. This characteristic inhibited the slurry flowability after coating, driven by gravity, which was desired to acquire a homogenous electrolyte, but at the same time a porous structure was generated. This porous structure densified to closed porosity after sintering. Moreover, anode surface conditions were shown to have a notable effect on the coating quality, as any irregularity potentially caused a discontinuity in the electrolyte layer. The surface irregularities could originate from extrusion or drying process, while becoming more recognisable after sintering.

Different heating regimes for the dual-layer structure were studied and from there a two-step sintering combination was chosen for the fabrication of a continuously dense electrolyte layer. A one-step sintering process was shown to be not feasible as cracking and delamination were induced as a result of thermal shrinkage mismatch.

Additionally, the fully sintered anode tube exhibited high mismatch strains with the green electrolyte that was not sufficient to create cracking but was sufficient to prevent undesired porosity. A dilatometry study suggested a range of mismatch strains that were beneficial for the elimination of electrolyte porosity, when the electrolyte was coated on a pre-fired anode substrate.

The test of electrical cell performance gave moderate results. The most problematic issue proved to be the gas sealing stage when the tested cell was inserted into the manifold. The measured OCV was 0.82 V, with the peak power density of 0.11 W/cm². The relatively low OCV value is believed to result from limited contact points between the anode and the electrolyte, which lead to a shortened TPB.

Later studies could investigate the liquid content distribution of the paste at the base of the barrel as extrusion progresses during the rheology investigation, to further validate the interpretation of the observed variations in extrusion pressure.

A further study of the dip coating of non-support layers is recommended. The addition of a dense anode function layer or a second electrolyte layer by coating is suggested, aiming to increase or give a sufficient length to the TPB and a robust electrolyte structure.

Further work at furnace treatment of mSOFCs could be tailored to coat an electrolyte layer onto an anode substrate that is preheated without any sintering initiated (i.e. below 1000 °C), before the following co-sintering stage showing any firing defects. If no cracking or delamination is observed after such a 2-step heating process, the necessity of a strong substrate for obtaining a continuous electrolyte might be questioned.

Additionally, the extrusion die set manufactured for this project uses a conventional design that proved to lead to some processing issues. A portion of die parts, including the six-hole and the annular die land regions, experience extremely high pressures during the processing and the wear rate appeared significant as extrusion continued. This is one of the major sources of the characterised phase redistribution in this thesis. A more developed die design is needed to meet the demand for scaling up of the manufacturing process.

Chapter 10 References

- [1] V.M. Orera, M.A. Laguna-Bercero, A. Larrea, Fabrication Methods and Performance in Fuel Cell and Steam Electrolysis Operation Modes of Small Tubular Solid Oxide Fuel Cells: A Review, *Frontiers in Energy Research* 2 (2014).
- [2] K.S. Howe, Design improvements of micro-tubular solid oxide fuel cells for unmanned aircraft applications, University of Birmingham, 2014 PhD Thesis.
- [3] T.L. Chow, *Electromagnetic theory*, Jones and Bartlett, Sudbury MA, 2006, p. 171 ff.
- [4] F.T. Ulaby, U. Ravaioli, E. Michielssen, *Fundamentals of applied electromagnetics*, Prentice Hall 2014.
- [5] BYU. <https://physics.byu.edu>. (Accessed May 2018).
- [6] J.G. Singer, *Combustion fossil power*, Combustion Engineering Inc., Windsor, CT (1991).
- [7] DBEIS. <https://www.gov.uk/government/organisations/departments-for-business-energy-and-industrial-strategy>. (Accessed May 2018).
- [8] Royal Commission on Environmental Pollution *Energy—the changing climate*, The Stationery Office, London, 2000.
- [9] M. Grubb, C. Vrolijk, D. Brack, *The Kyoto Protocol: a guide and assessment*, Royal Institute of International Affairs Energy and Environmental Programme. 1997.
- [10] R. Clift, Climate change and energy policy: The importance of sustainability arguments, *Energy* 32(4) (2007) 262-268.
- [11] W. Shepherd, D.W. Shepherd, *Problems and Solutions: Energy Studies*, Imperial College Press 2008.
- [12] W.R. Nelson, *REACTOR: An Expert System for Diagnosis and Treatment of Nuclear Reactor Accidents*, AAAI, Pittsburgh, PA, 1982, pp. 296-301.
- [13] U. DoE, *DOE Fundamentals Handbook-Nuclear Physics and Reactor Theory*, Technical Report, 1993.
- [14] I. Dincer, Renewable energy and sustainable development: a crucial review, *Renewable and sustainable energy reviews* 4(2) (2000) 157-175.
- [15] I. Fells, The problem. In: J. Dunderdale (Ed.) *Energy and the environment*, Royal Society of Chemistry, UK, 1990.
- [16] Anon., *Global energy perspectives to 2050 and beyond*, Technical report, World Energy Council, London, 1995a.
- [17] Anon., *Urban energy handbook*, Organisation for Economic Co-Operation and Development (OECD), Paris, 1995b.
- [18] REN21, *RENEWABLES 2016 GLOBAL STATUS REPORT*, 2016. http://www.ren21.net/wp-content/uploads/2016/06/GSR_2016_Full_Report_REN21.pdf.
- [19] S. Chen, B. Chen, B.D. Fath, Assessing the cumulative environmental impact of hydropower construction on river systems based on energy network model, *Renewable and Sustainable Energy Reviews* 42 (2015) 78-92.
- [20] *Three Gorges Dam Case Study*, American University, The School of International Service, 2008.
- [21] R. Sternberg, Damming the river: a changing perspective on altering nature, *Renewable and Sustainable Energy Reviews* 10(3) (2006) 165-197.
- [22] T. Hennig, W. Wang, Y. Feng, X. Ou, D. He, Review of Yunnan's hydropower development. Comparing small and large hydropower projects regarding their

- environmental implications and socio-economic consequences, *Renewable and Sustainable Energy Reviews* 27 (2013) 585-595.
- [23] A. Ansar, B. Flyvbjerg, A. Budzier, D. Lunn, Should we build more large dams? The actual costs of hydropower megaproject development, *Energy Policy* 69 (2014) 43-56.
- [24] D.M. Rosenberg, P. McCully, C.M. Pringle, Global-Scale Environmental Effects of Hydrological Alterations: Introduction, *BioScience* 50(9) (2000) 746-751.
- [25] D. He, W. Zhao, L. Chen, The ecological changes in Manwan reservoir area and its causes, Asian International Rivers Centre, Yunnan University, Kunming, Yunnan, China, Accessed through internet on May (2015).
- [26] H. Zhai, B. Cui, B. Hu, K. Zhang, Prediction of river ecological integrity after cascade hydropower dam construction on the mainstream of rivers in Longitudinal Range-Gorge Region (LRGR), China, *Ecological Engineering* 36(4) (2010) 361-372.
- [27] Y. Zhang, J. Liu, L. Wang, Changes in water quality in the downstream of Lancangjiang River after the construction of Manwan Hydropower Station, *Resources and Environment in the Yangtze Basin* 14(4) (2005) 500-506.
- [28] C. Garrett, P. Cummins, The power potential of tidal currents in channels, *Proceedings of the Royal Society of London A: Mathematical, Physical and Engineering Sciences*, The Royal Society, 2005, pp. 2563-2572.
- [29] M. Milligan, P. Donohoo, D. Lew, E. Ela, B. Kirby, H. Holttinen, E. Lannoye, D. Flynn, M. O'Malley, N. Miller, Operating reserves and wind power integration: An international comparison, *proc. 9th International Workshop on large-scale integration of wind power into power systems*, 2010, pp. 18-29.
- [30] H.K. Gupta, *Geothermal resources: an energy alternative*, Elsevier 2014.
- [31] R. DiPippo, *Geothermal power plants: principles, applications, case studies and environmental impact*, Butterworth-Heinemann 2012.
- [32] J.W. Tester, B.J. Anderson, A.S. Batchelor, D.D. Blackwell, R. DiPippo, E. Drake, J. Garnish, B. Livesay, M.C. Moore, K. Nichols, The future of geothermal energy: Impact of enhanced geothermal systems (EGS) on the United States in the 21st century, *Massachusetts Institute of Technology* 209 (2006).
- [33] G. Zimmermann, A. Reinicke, Hydraulic stimulation of a deep sandstone reservoir to develop an Enhanced Geothermal System: Laboratory and field experiments, *Geothermics* 39(1) (2010) 70-77.
- [34] D. Hartley, D. Schueler, *Perspectives on renewable energy and the environment*, MIT, Massachusetts, 1990.
- [35] D.D.a.D. Brown, *Hot Dry Rock Geothermal Energy Development in the USA*, (1995).
- [36] H. Price, E. Lufert, D. Kearney, E. Zarza, G. Cohen, R. Gee, R. Mahoney, Advances in parabolic trough solar power technology, *Journal of solar energy engineering* 124(2) (2002) 109-125.
- [37] S.K. Sharma, I.M. Mishra, M.P. Sharma, J.S. Saini, Effect of particle size on biogas generation from biomass residues, *Biomass* 17(4) (1988) 251-263.
- [38] N.E.L. Association, *Electrical Meterman's Handbook*, Trow Press 1915.
- [39] N. Bhargava, N.B.S.G.D. Kulshreshtha, *Basic Electronics and Linear Circuits*, Tata McGraw-Hill Education 1984.
- [40] A. Kirubakaran, S. Jain, R.K. Nema, A review on fuel cell technologies and power electronic interface, *Renewable and Sustainable Energy Reviews* 13(9) (2009) 2430-2440.

- [41] D.P. Arnold, Review of microscale magnetic power generation, *IEEE Transactions on Magnetics* 43(11) (2007) 3940-3951.
- [42] A. McEvoy, T. Markvart, L. Castañer, T. Markvart, L. Castaner, *Practical handbook of photovoltaics: fundamentals and applications*, Elsevier 2003.
- [43] M.A. Green, Y. Hishikawa, W. Warta, E.D. Dunlop, D.H. Levi, J. Hohl-Ebinger, A.W. Ho-Baillie, Solar cell efficiency tables (version 50), *Progress in Photovoltaics* 25(NREL/JA-5J00-68932) (2017).
- [44] N.M. Haegel, R. Margolis, T. Buonassisi, D. Feldman, A. Froitzheim, R. Garabedian, M. Green, S. Glunz, H.-M. Henning, B. Holder, I. Kaizuka, B. Kroposki, K. Matsubara, S. Niki, K. Sakurai, R.A. Schindler, W. Tumas, E.R. Weber, G. Wilson, M. Woodhouse, S. Kurtz, Terawatt-scale photovoltaics: Trajectories and challenges, *Science* 356(6334) (2017) 141-143.
- [45] Created internally by a member of the Energy Education team. Adapted from: Ecogreen Electrical. (August 14, 2015). Solar PV Systems.
<http://www.ecogreenelectrical.com/solar.htm>.
- [46] J. Blatt, *Thermoelectric power of metals*, Springer Science & Business Media 2012.
- [47] S.B. Riffat, X. Ma, *Thermoelectrics: a review of present and potential applications*, *Applied Thermal Engineering* 23(8) (2003) 913-935.
- [48] G.J. Snyder, E.S. Toberer, Complex thermoelectric materials, *Nature Materials* 7 (2008) 105.
- [49] D.Y. Chung, T. Hogan, J. Schindler, L. Iordarridis, P. Brazis, C.R. Kannewurf, B. Chen, C. Uher, M.G. Kanatzidis, Complex bismuth chalcogenides as thermoelectrics, *Thermoelectrics, 1997. Proceedings ICT'97. XVI International Conference on*, IEEE, 1997, pp. 459-462.
- [50] J.P. Heremans, V. Jovovic, E.S. Toberer, A. Saramat, K. Kurosaki, A. Charoenphakdee, S. Yamanaka, G.J. Snyder, Enhancement of Thermoelectric Efficiency in PbTe by Distortion of the Electronic Density of States, *Science* 321(5888) (2008) 554-557.
- [51] L. Huang, Q. Zhang, B. Yuan, X. Lai, X. Yan, Z. Ren, Recent progress in half-Heusler thermoelectric materials, *Materials Research Bulletin* 76 (2016) 107-112.
- [52] M. Hamid Elsheikh, D.A. Shnawah, M.F.M. Sabri, S.B.M. Said, M. Haji Hassan, M.B. Ali Bashir, M. Mohamad, A review on thermoelectric renewable energy: Principle parameters that affect their performance, *Renewable and Sustainable Energy Reviews* 30 (2014) 337-355.
- [53] C. Wang, M.H. Nehrir, Distributed generation applications of fuel cells, *Power Systems Conference: Advanced Metering, Protection, Control, Communication, and Distributed Resources, 2006. PS'06, IEEE, 2006*, pp. 244-248.
- [54] A. Boudghene Stambouli, E. Traversa, Fuel cells, an alternative to standard sources of energy, *Renewable and Sustainable Energy Reviews* 6(3) (2002) 295-304.
- [55] B. Cook, Introduction to fuel cells and hydrogen technology, *Engineering Science & Education Journal* 11(6) (2002) 205-216.
- [56] W.R. Grove, Gas Voltaic Battery, *Philos. Mag* 14 (1839) 127.
- [57] T.W. Pike, Development and processing of solid oxide fuel cell materials, University of Birmingham, 2015.
- [58] H. Sotouchi, A. Hagiwara, Phosphoric Acid Fuel Cells, *Energy Carriers And Conversion Systems With Emphasis On Hydrogen-Volume II* 8 (2009) 333.
- [59] S. Romano, J.T. Larkins, Georgetown University Fuel Cell Transit Bus Program, *Fuel Cells* 3(3) (2003) 128-132.

- [60] N. Sammes, R. Bove, K. Stahl, Phosphoric acid fuel cells: Fundamentals and applications, *Current Opinion in Solid State and Materials Science* 8(5) (2004) 372-378.
- [61] A.L. Dicks, Molten carbonate fuel cells, *Current Opinion in Solid State and Materials Science* 8(5) (2004) 379-383.
- [62] W.T. Grubb, Proceedings of the 11th annual battery research and development conference, PSC publications committee, Red bank, NJ, 5 P 1957, US Patent No 2913511, 1959.
- [63] K. Prater, The renaissance of the solid polymer fuel cell, *Journal of power sources* 29 (1990) 239-250.
- [64] V.M. Vishnyakov, Proton exchange membrane fuel cells, *Vacuum* 80(10) (2006) 1053-1065.
- [65] A.L.D. J. Laminie, *Fuel cell systems Explained*, Wiley, New York, 2000.
- [66] J.H. Reid, US Patent No. 736016017, 1902.
- [67] J.H. Reid, US Patent No. 757637, (1904).
- [68] P.C.L. Noel, Fr. Patent No. 350111, (1904).
- [69] E. Gülzow, Alkaline fuel cells, *Fuel cells* 4(4) (2004) 251-255.
- [70] *Fuel Cell Handbook* (7th Edition), Office of Fossil Fuel, National Energy Technology Laboratory, U. S. Department of Energy, West Virginia, 2000.
- [71] M. Farooque, H.C. Maru, Fuel cells-the clean and efficient power generators, *Proceedings of the IEEE* 89(12) (2001) 1819-1829.
- [72] F. Bidault, D.J.L. Brett, P.H. Middleton, N.P. Brandon, Review of gas diffusion cathodes for alkaline fuel cells, *Journal of Power Sources* 187(1) (2009) 39-48.
- [73] R.C.T.S. J. R. Varcoe, *Fuel Cells*, 5 (2005) 187-200.
- [74] G. Merle, M. Wessling, K. Nijmeijer, Anion exchange membranes for alkaline fuel cells: A review, *Journal of Membrane Science* 377(1) (2011) 1-35.
- [75] N. Cooley, NexTech materials demonstrates world's largest SOFC platform, *International Journal of Hydrogen Energy* 34(19) (2009) 8454-8454.
- [76] S.C. Singhal, Solid oxide fuel cells for stationary, mobile, and military applications, *Solid State Ionics* 152-153 (2002) 405-410.
- [77] K.E. Swider-Lyons, R.T. Carlin, R.L. Rosenfeld, R.J. Nowak, Technical issues and opportunities for fuel cell development for autonomous underwater vehicles, *Proceedings of the 2002 Workshop on Autonomous Underwater Vehicles*, 2002., 2002, pp. 61-64.
- [78] D. Das, T.N. Veziroğlu, Hydrogen production by biological processes: a survey of literature, *International Journal of Hydrogen Energy* 26(1) (2001) 13-28.
- [79] P. Hoffmann, *Forever fuel: the story of hydrogen*, (1981).
- [80] K.S.V. Santhanam, R.J. Press, M.J. Miri, A.V. Bailey, G.A. Takacs, *Introduction to Hydrogen Technology*, Wiley 2017.
- [81] J.A. Turner, Sustainable Hydrogen Production, *Science* 305(5686) (2004) 972.
- [82] L. Schlapbach, A. Züttel, Hydrogen-storage materials for mobile applications, *Materials for Sustainable Energy*, Co-Published with Macmillan Publishers Ltd, UK 2010, pp. 265-270.
- [83] B.C.H. Steele, Running on natural gas, *Nature* 400 (1999) 619.
- [84] V. Nallathambi Gunaseelan, Anaerobic digestion of biomass for methane production: A review, *Biomass and Bioenergy* 13(1) (1997) 83-114.
- [85] J.-H. Koh, Y.-S. Yoo, J.-W. Park, H.C. Lim, Carbon deposition and cell performance of Ni-YSZ anode support SOFC with methane fuel, *Solid State Ionics* 149(3) (2002) 157-166.

- [86] T. Chen, W.G. Wang, H. Miao, T. Li, C. Xu, Evaluation of carbon deposition behavior on the nickel/yttrium-stabilized zirconia anode-supported fuel cell fueled with simulated syngas, *Journal of Power Sources* 196(5) (2011) 2461-2468.
- [87] J.-W. Snoeck, G. Froment, M. Fowles, Steam/CO₂ reforming of methane. Carbon filament formation by the Boudouard reaction and gasification by CO₂, by H₂, and by steam: kinetic study, *Industrial & engineering chemistry research* 41(17) (2002) 4252-4265.
- [88] D.P. Serrano, J.A. Botas, R. Guil-Lopez, H₂ production from methane pyrolysis over commercial carbon catalysts: Kinetic and deactivation study, *International Journal of Hydrogen Energy* 34(10) (2009) 4488-4494.
- [89] J. Xu, G.F. Froment, Methane steam reforming, methanation and water-gas shift: I. Intrinsic kinetics, *AIChE journal* 35(1) (1989) 88-96.
- [90] C.N. Ávila-Neto, S.C. Dantas, F.A. Silva, T.V. Franco, L.L. Romanielo, C.E. Hori, A.J. Assis, Hydrogen production from methane reforming: Thermodynamic assessment and autothermal reactor design, *Journal of Natural Gas Science and Engineering* 1(6) (2009) 205-215.
- [91] M. Aparicio, A. Jitianu, L.C. Klein, Sol-gel processing for conventional and alternative energy, Springer Science & Business Media 2012.
- [92] M.C. Williams, J.P. Strakey, S.C. Singhal, U.S. distributed generation fuel cell program, *Journal of Power Sources* 131(1) (2004) 79-85.
- [93] S.C. Singhal, K. Kendall, High-temperature solid oxide fuel cells: fundamentals, design and applications: fundamentals, design and applications, Elsevier 2003.
- [94] R.A. George, Status of tubular SOFC field unit demonstrations, *Journal of Power Sources* 86(1) (2000) 134-139.
- [95] N.M. Sammes, Y. Du, R. Bove, Design and fabrication of a 100W anode supported micro-tubular SOFC stack, *Journal of Power Sources* 145(2) (2005) 428-434.
- [96] A.V. Akkaya, Electrochemical model for performance analysis of a tubular SOFC, *International Journal of Energy Research* 31(1) (2007) 79-98.
- [97] K. Kendall, G. Sales, A rapid heating ceramic fuel cell, Institute of Energy's Second International Conference on Ceramics in Energy Applications: proceedings of the Institute of Energy conference held in London, UK. on 20-21 April 1994, Institute of Energy, 1994, p. 55.
- [98] X. Meng, X. Gong, N. Yang, X. Tan, Y. Yin, Z.-F. Ma, Fabrication of Y₂O₃-stabilized-ZrO₂(YSZ)/La_{0.8}Sr_{0.2}MnO₃- α -YSZ dual-layer hollow fibers for the cathode-supported micro-tubular solid oxide fuel cells by a co-spinning/co-sintering technique, *Journal of Power Sources* 237 (2013) 277-284.
- [99] J. Wu, X. Liu, Recent Development of SOFC Metallic Interconnect, *Journal of Materials Science & Technology* 26(4) (2010) 293-305.
- [100] J.C.W. Mah, A. Muchtar, M.R. Somalu, M.J. Ghazali, Metallic interconnects for solid oxide fuel cell: A review on protective coating and deposition techniques, *International Journal of Hydrogen Energy* 42(14) (2017) 9219-9229.
- [101] N.Q. Minh, Solid oxide fuel cell technology—features and applications, *Solid State Ionics* 174(1) (2004) 271-277.
- [102] N. Mahato, A. Banerjee, A. Gupta, S. Omar, K. Balani, Progress in material selection for solid oxide fuel cell technology: A review, *Progress in Materials Science* 72 (2015) 141-337.
- [103] W.Z. Zhu, S.C. Deevi, A review on the status of anode materials for solid oxide fuel cells, *Materials Science and Engineering: A* 362(1) (2003) 228-239.

- [104] H. Spacil, Electrical device including nickel-containing stabilised zirconia electrode, US, 1970.
- [105] K.C. Wincewicz, J.S. Cooper, Taxonomies of SOFC material and manufacturing alternatives, *Journal of Power Sources* 140(2) (2005) 280-296.
- [106] N.H. Menzler, F. Tietz, S. Uhlenbruck, H.P. Buchkremer, D. Stöver, Materials and manufacturing technologies for solid oxide fuel cells, *Journal of Materials Science* 45(12) (2010) 3109-3135.
- [107] L.W. Tai, M.M. Nasrallah, H.U. Anderson, D.M. Sparlin, S.R. Sehlin, Structure and electrical properties of $\text{La}_{1-x}\text{Sr}_x\text{Co}_{1-y}\text{Fe}_y\text{O}_3$. Part 1. The system $\text{La}_{0.8}\text{Sr}_{0.2}\text{Co}_{1-y}\text{Fe}_y\text{O}_3$, *Solid State Ionics* 76(3) (1995) 259-271.
- [108] L.W. Tai, M.M. Nasrallah, H.U. Anderson, D.M. Sparlin, S.R. Sehlin, Structure and electrical properties of $\text{La}_{1-x}\text{Sr}_x\text{Co}_{1-y}\text{Fe}_y\text{O}_3$. Part 2. The system $\text{La}_{1-x}\text{Sr}_x\text{Co}_{0.2}\text{Fe}_{0.8}\text{O}_3$, *Solid State Ionics* 76(3) (1995) 273-283.
- [109] W.G. Wang, M. Mogensen, High-performance lanthanum-ferrite-based cathode for SOFC, *Solid State Ionics* 176(5) (2005) 457-462.
- [110] F. Tietz, V.A.C. Haanappel, A. Mai, J. Mertens, D. Stöver, Performance of LSCF cathodes in cell tests, *Journal of Power Sources* 156(1) (2006) 20-22.
- [111] Z. Shao, S.M. Haile, A high-performance cathode for the next generation of solid-oxide fuel cells, *Nature* 431 (2004) 170.
- [112] P. Lamp, J. Tachtler, O. Finkenwirth, S. Mukerjee, S. Shaffer, Development of an Auxiliary Power Unit with Solid Oxide Fuel Cells for Automotive Applications, *Fuel Cells* 3(3) (2003) 146-152.
- [113] W.-S. Hsieh, P. Lin, S.-F. Wang, Characteristics of electrolyte supported micro-tubular solid oxide fuel cells with GDC-ScSZ bilayer electrolyte, *International Journal of Hydrogen Energy* 39(30) (2014) 17267-17274.
- [114] L. Antoni, Materials for solid oxide fuel cells: the challenge of their stability, *Materials Science Forum*, Trans Tech Publ, 2004, pp. 1073-1090.
- [115] S.P.S. Badwal, K. Foger, Solid oxide electrolyte fuel cell review, *Ceramics International* 22(3) (1996) 257-265.
- [116] Y. Du, N.M. Sammes, Fabrication and properties of anode-supported tubular solid oxide fuel cells, *Journal of Power Sources* 136(1) (2004) 66-71.
- [117] K. Li, *Ceramic membranes for separation and reaction*, John Wiley & Sons 2007.
- [118] S.N. M., D. Yanhai, Fabrication and Characterization of Tubular Solid Oxide Fuel Cells, *International Journal of Applied Ceramic Technology* 4(2) (2007) 89-102.
- [119] R.D.I.T. García, *Production of micro-tubular solid oxide fuel cells*, University of Trento, 2011.
- [120] N.M. Sammes, Y. Du, Fabrication and Characterization of Tubular Solid Oxide Fuel Cells, *International Journal of Applied Ceramic Technology* 4(2) (2007) 89-102.
- [121] N. Sammes, Y. Du, Fabrication and characterization of tubular solid oxide fuel cells, *International journal of applied ceramic technology* 4(2) (2007) 89-102.
- [122] Y.-W. Sin, K. Galloway, B. Roy, N.M. Sammes, J.-H. Song, T. Suzuki, M. Awano, The properties and performance of micro-tubular (less than 2.0mm O.D.) anode supported solid oxide fuel cell (SOFC), *International Journal of Hydrogen Energy* 36(2) (2011) 1882-1889.
- [123] F. Calise, G. Restuccia, N. Sammes, Experimental analysis of micro-tubular solid oxide fuel cell fed by hydrogen, *Journal of Power Sources* 195(4) (2010) 1163-1170.

- [124] N.M.a.D. Sammes, Y., Fabrication and Characterization of Tubular Solid Oxide Fuel Cells, *International Journal of Applied Ceramic Technology* 4: 89–102 (2007).
- [125] T. Suzuki, T. Yamaguchi, Y. Fujishiro, M. Awano, Fabrication and characterization of micro tubular SOFCs for operation in the intermediate temperature, *Journal of Power Sources* 160(1) (2006) 73-77.
- [126] T. Suzuki, T. Yamaguchi, Y. Fujishiro, M. Awano, Improvement of SOFC performance using a microtubular, anode-supported SOFC, *Journal of the Electrochemical Society* 153(5) (2006) A925-A928.
- [127] T. Suzuki, Y. Funahashi, T. Yamaguchi, Y. Fujishiro, M. Awano, Effect of anode microstructure on the performance of micro tubular SOFCs, *Solid State Ionics* 180(6-8) (2009) 546-549.
- [128] T. Suzuki, Y. Funahashi, T. Yamaguchi, Y. Fujishiro, M. Awano, Design and fabrication of lightweight, submillimeter tubular solid oxide fuel cells, *Electrochemical and solid-state letters* 10(8) (2007) A177-A179.
- [129] Y. Funahashi, T. Shimamori, T. Suzuki, Y. Fujishiro, M. Awano, Fabrication and characterization of components for cube shaped micro tubular SOFC bundle, *Journal of Power Sources* 163(2) (2007) 731-736.
- [130] T. Yamaguchi, T. Suzuki, S. Shimizu, Y. Fujishiro, M. Awano, Examination of wet coating and co-sintering technologies for micro-SOFCs fabrication, *Journal of Membrane Science* 300(1-2) (2007) 45-50.
- [131] T. Suzuki, Y. Funahashi, T. Yamaguchi, Y. Fujishiro, M. Awano, Development of fabrication/integration technology for micro tubular SOFCs, *Micro Fuel Cells—Principles and Applications* (2009) 141-177.
- [132] S.M. Jamil, M.H.D. Othman, M.A. Rahman, J. Jaafar, A. Ismail, K. Li, Recent fabrication techniques for micro-tubular solid oxide fuel cell support: A review, *Journal of the European Ceramic Society* 35(1) (2015) 1-22.
- [133] K.K. Strathmann H, Amar P, Baker RW, The formation mechanism of asymmetric membranes, *Desalination* 16 (1975) 179-203.
- [134] M.H.D. Othman, Z. Wu, N. Droushiotis, G. Kelsall, K. Li, Morphological studies of macrostructure of Ni–CGO anode hollow fibres for intermediate temperature solid oxide fuel cells, *Journal of Membrane Science* 360(1-2) (2010) 410-417.
- [135] U. Doraswami, P. Shearing, N. Droushiotis, K. Li, N.P. Brandon, G.H. Kelsall, Modelling the effects of measured anode triple-phase boundary densities on the performance of micro-tubular hollow fiber SOFCs, *Solid State Ionics* 192(1) (2011) 494-500.
- [136] J.M. Crum AT, Halloran JW, Arbor A, Method for preparation of solid state electrochemical device, 2004.
- [137] B.J. Benbow JJ, Paste flow and extrusion, Clarendon Press, Oxford, 1993.
- [138] J. Powell, S. Blackburn, Co-extrusion of multilayered ceramic micro-tubes for use as solid oxide fuel cells, *Journal of the European Ceramic Society* 30(14) (2010) 2859-2870.
- [139] C.V. Hoy, A. Barda, M. Griffith, J.W. Halloran, Microfabrication of Ceramics by Co-extrusion, *Journal of the American Ceramic Society* 81(1) (1998) 152-158.
- [140] C.C. Wei, K. Li, Yttria-stabilized zirconia (YSZ)-based hollow fiber solid oxide fuel cells, *Industrial & Engineering Chemistry Research* 47(5) (2008) 1506-1512.

- [141] T. Li, Z. Wu, K. Li, Single-step fabrication and characterisations of triple-layer ceramic hollow fibres for micro-tubular solid oxide fuel cells (SOFCs), *Journal of Membrane Science* 449 (2014) 1-8.
- [142] M.H. Othman, N. Droushiotis, Z. Wu, G. Kelsall, K. Li, High-performance, anode-supported, microtubular SOFC prepared from single-step-fabricated, dual-layer hollow fibers, *Adv Mater* 23(21) (2011) 2480-3.
- [143] M.H.D. Othman, N. Droushiotis, Z. Wu, K. Kanawka, G. Kelsall, K. Li, Electrolyte thickness control and its effect on electrolyte/anode dual-layer hollow fibres for micro-tubular solid oxide fuel cells, *Journal of Membrane Science* 365(1-2) (2010) 382-388.
- [144] M.H.D. Othman, N. Droushiotis, Z. Wu, G. Kelsall, K. Li, Dual-layer hollow fibres with different anode structures for micro-tubular solid oxide fuel cells, *Journal of Power Sources* 205 (2012) 272-280.
- [145] T. Yamaguchi, T. Suzuki, S. Shimizu, Y. Fujishiro, M. Awano, Examination of wet coating and co-sintering technologies for micro-SOFCs fabrication, *Journal of Membrane Science* 300(1) (2007) 45-50.
- [146] Y. Liu, M. Mori, Y. Funahashi, Y. Fujishiro, A. Hirano, Development of micro-tubular SOFCs with an improved performance via nano-Ag impregnation for intermediate temperature operation, *Electrochemistry Communications* 9(8) (2007) 1918-1923.
- [147] Y. Liu, S.-I. Hashimoto, H. Nishino, K. Takei, M. Mori, T. Suzuki, Y. Funahashi, Fabrication and characterization of micro-tubular cathode-supported SOFC for intermediate temperature operation, *Journal of Power Sources* 174(1) (2007) 95-102.
- [148] T. Yamaguchi, S. Shimizu, T. Suzuki, Y. Fujishiro, M. Awano, Fabrication and evaluation of cathode-supported small scale SOFCs, *Materials Letters* 62(10) (2008) 1518-1520.
- [149] T.J. Lee, K. Kendall, Characterisation of electrical performance of anode supported micro-tubular solid oxide fuel cell with methane fuel, *Journal of Power Sources* 181(2) (2008) 195-198.
- [150] T. Yamaguchi, S. Shimizu, T. Suzuki, Y. Fujishiro, M. Awano, Fabrication and characterization of high performance cathode supported small-scale SOFC for intermediate temperature operation, *Electrochemistry Communications* 10(9) (2008) 1381-1383.
- [151] T. Suzuki, Y. Funahashi, Z. Hasan, T. Yamaguchi, Y. Fujishiro, M. Awano, Fabrication of needle-type micro SOFCs for micro power devices, *Electrochemistry Communications* 10(10) (2008) 1563-1566.
- [152] T. Suzuki, Y. Funahashi, T. Yamaguchi, Y. Fujishiro, M. Awano, Effect of anode microstructure on the performance of micro tubular SOFCs, *Solid State Ionics* 180(6) (2009) 546-549.
- [153] T. Suzuki, Y. Funahashi, T. Yamaguchi, Y. Fujishiro, M. Awano, Chapter 4 - Development of Fabrication/Integration Technology for Micro Tubular SOFCs, in: T.S. Zhao (Ed.), *Micro Fuel Cells*, Academic Press, Boston, 2009, pp. 141-177.
- [154] N. Akhtar, S.P. Decent, D. Loghin, K. Kendall, Mixed-reactant, micro-tubular solid oxide fuel cells: An experimental study, *Journal of Power Sources* 193(1) (2009) 39-48.
- [155] K.V. Galloway, N.M. Sammes, Performance degradation of microtubular SOFCs operating in the intermediate-temperature range, *Journal of the Electrochemical Society* 156(4) (2009) B526-B531.

- [156] R. Campana, R.I. Merino, A. Larrea, I. Villarreal, V.M. Orera, Fabrication, electrochemical characterization and thermal cycling of anode supported microtubular solid oxide fuel cells, *Journal of Power Sources* 192(1) (2009) 120-125.
- [157] N. Akhtar, S.P. Decent, K. Kendall, Cell temperature measurements in micro-tubular, single-chamber, solid oxide fuel cells (MT–SC–SOFCs), *Journal of Power Sources* 195(23) (2010) 7818-7824.
- [158] T. Suzuki, M.H. Zahir, T. Yamaguchi, Y. Fujishiro, M. Awano, N. Sammes, Fabrication of micro-tubular solid oxide fuel cells with a single-grain-thick yttria stabilized zirconia electrolyte, *Journal of Power Sources* 195(23) (2010) 7825-7828.
- [159] V. Gil, J. Gurauskis, R. Campana, R.I. Merino, A. Larrea, V.M. Orera, Anode-supported microtubular cells fabricated with gadolinia-doped ceria nanopowders, *Journal of Power Sources* 196(3) (2011) 1184-1190.
- [160] F. Calise, G. Restuccia, N. Sammes, Experimental analysis of performance degradation of micro-tubular solid oxide fuel cells fed by different fuel mixtures, *Journal of Power Sources* 196(1) (2011) 301-312.
- [161] N. Akhtar, K. Kendall, Silver modified cathode for a micro-tubular, single-chamber solid oxide fuel cell, *International Journal of Hydrogen Energy* 36(1) (2011) 773-778.
- [162] T. Yamaguchi, K.V. Galloway, J. Yoon, N.M. Sammes, Electrochemical characterizations of microtubular solid oxide fuel cells under a long-term testing at intermediate temperature operation, *Journal of Power Sources* 196(5) (2011) 2627-2630.
- [163] T. Suzuki, B. Liang, T. Yamaguchi, H. Sumi, K. Hamamoto, Y. Fujishiro, One-step sintering process of gadolinia-doped ceria interlayer–scandia-stabilized zirconia electrolyte for anode supported microtubular solid oxide fuel cells, *Journal of Power Sources* 199 (2012) 170-173.
- [164] H. Sumi, T. Yamaguchi, K. Hamamoto, T. Suzuki, Y. Fujishiro, T. Matsui, K. Eguchi, AC impedance characteristics for anode-supported microtubular solid oxide fuel cells, *Electrochimica Acta* 67 (2012) 159-165.
- [165] H. Sumi, T. Yamaguchi, K. Hamamoto, T. Suzuki, Y. Fujishiro, High performance of $\text{La}_{0.6}\text{Sr}_{0.4}\text{Co}_{0.2}\text{Fe}_{0.8}\text{O}_{3-\delta}\text{--Ce}_{0.9}\text{Gd}_{0.1}\text{O}_{1.95}$ nanoparticulate cathode for intermediate temperature microtubular solid oxide fuel cells, *Journal of Power Sources* 226 (2013) 354-358.
- [166] T. Suzuki, W.-D. Yao, Molecular and structural bases for postsynaptic signal processing: interaction between postsynaptic density and postsynaptic membrane rafts, *Journal of Neurorestoratology* 2 (2013) 1-14.
- [167] H. Sumi, T. Yamaguchi, K. Hamamoto, T. Suzuki, Y. Fujishiro, Effects of Anode Microstructure on Mechanical and Electrochemical Properties for Anode-Supported Microtubular Solid Oxide Fuel Cells, *Journal of the American Ceramic Society* 96(11) (2013) 3584-3588.
- [168] C.-C. Wei, Yttria stabilised zirconia (YSZ) membranes and their applications, (2009).
- [169] F.D. Grande, A. Thursfield, K. Kanawka, N. Droushiotis, U. Doraswami, K. Li, G. Kelsall, I.S. Metcalfe, Microstructure and performance of novel Ni anode for hollow fibre solid oxide fuel cells, *Solid State Ionics* 180(11) (2009) 800-804.
- [170] C. Jin, J. Liu, L. Li, Y. Bai, Electrochemical properties analysis of tubular NiO--YSZ anode-supported SOFCs fabricated by the phase-inversion method, *Journal of Membrane Science* 341(1) (2009) 233-237.

- [171] C. Yang, W. Li, S. Zhang, L. Bi, R. Peng, C. Chen, W. Liu, Fabrication and characterization of an anode-supported hollow fiber SOFC, *Journal of Power Sources* 187(1) (2009) 90-92.
- [172] C. Yang, C. Jin, F. Chen, Micro-tubular solid oxide fuel cells fabricated by phase-inversion method, *Electrochemistry Communications* 12(5) (2010) 657-660.
- [173] X. Zhang, B. Lin, Y. Ling, Y. Dong, G. Meng, X. Liu, An anode-supported micro-tubular solid oxide fuel cell with redox stable composite cathode, *International Journal of Hydrogen Energy* 35(16) (2010) 8654-8662.
- [174] K. Kanawka, F.D. Grande, Z. Wu, A. Thursfield, D. Ivey, I. Metcalfe, G. Kelsall, K. Li, Microstructure and performance investigation of a solid oxide fuel cells based on highly asymmetric YSZ microtubular electrolytes, *Industrial & Engineering Chemistry Research* 49(13) (2010) 6062-6068.
- [175] C. Yang, C. Jin, F. Chen, Performances of micro-tubular solid oxide cell with novel asymmetric porous hydrogen electrode, *Electrochimica Acta* 56(1) (2010) 80-84.
- [176] F. Zhao, C. Jin, C. Yang, S. Wang, F. Chen, Fabrication and characterization of anode-supported micro-tubular solid oxide fuel cell based on $\text{BaZr}_{0.1}\text{Ce}_{0.7}\text{Y}_{0.1}\text{Yb}_{0.1}\text{O}_{3-\delta}$ electrolyte, *Journal of Power Sources* 196(2) (2011) 688-691.
- [177] L. Zhao, X. Zhang, B. He, B. Liu, C. Xia, Micro-tubular solid oxide fuel cells with graded anodes fabricated with a phase inversion method, *Journal of Power Sources* 196(3) (2011) 962-967.
- [178] N. Droushiotis, M.H.D. Othman, U. Doraswami, Z. Wu, G. Kelsall, K. Li, Novel co-extruded electrolyte–anode hollow fibres for solid oxide fuel cells, *Electrochemistry Communications* 11(9) (2009) 1799-1802.
- [179] N. Droushiotis, U. Doraswami, D. Ivey, M.H.D. Othman, K. Li, G. Kelsall, Fabrication by Co-extrusion and electrochemical characterization of micro-tubular hollow fibre solid oxide fuel cells, *Electrochemistry Communications* 12(6) (2010) 792-795.
- [180] M.H.D. Othman, N. Droushiotis, Z. Wu, G. Kelsall, K. Li, Novel fabrication technique of hollow fibre support for micro-tubular solid oxide fuel cells, *Journal of Power Sources* 196(11) (2011) 5035-5044.
- [181] M.H.D. Othman, N. Droushiotis, Z. Wu, G. Kelsall, K. Li, High-Performance, Anode-Supported, Microtubular SOFC Prepared from Single-Step-Fabricated, Dual-Layer Hollow Fibers, *Advanced Materials* 23(21) (2011) 2480-2483.
- [182] M.J. López-Robledo, J. Silva-Treviño, T. Molina, R. Moreno, Colloidal stability of gadolinium-doped ceria powder in aqueous and non-aqueous media, *Journal of the European Ceramic Society* 33(2) (2013) 297-303.
- [183] J.M. Vohs, R.J. Gorte, High-Performance SOFC Cathodes Prepared by Infiltration, *Advanced Materials* 21(9) (2009) 943-956.
- [184] W. Yin, B. Meng, X. Meng, X. Tan, Highly asymmetric yttria stabilized zirconia hollow fibre membranes, *Journal of Alloys and Compounds* 476(1-2) (2009) 566-570.
- [185] K. Kanawka, M.H.D. Othman, N. Droushiotis, Z. Wu, G. Kelsall, K. Li, Ni/Ni-YSZ Current Collector/Anode Dual Layer Hollow Fibers for Micro-Tubular Solid Oxide Fuel Cells, *Fuel Cells* 11(5) (2011) 690-696.
- [186] U. Doraswami, N. Droushiotis, G.H. Kelsall, Modelling effects of current distributions on performance of micro-tubular hollow fibre solid oxide fuel cells, *Electrochimica Acta* 55(11) (2010) 3766-3778.
- [187] J.D.B. N. McN. ALFORD, K. KENDALL, *Nature* 330 (1987) 51.

- [188] p. ICI, European Patent Application no. 0348104, 1989 June.
- [189] J.D. Birchall, Howard, A.J., Kendall, K., Raistrick, J.H., Cement composition and product, US Patent 4410366, 1983.
- [190] J. Shaw, S. Best, W. Bonfield, A. Marsh, J. Cotton, Study of the application of viscous plastic processing to hydroxyapatite, *Journal of materials science letters* 14(15) (1995) 1055-1057.
- [191] S. Blackburn, D.I. Wilson, Shaping ceramics by plastic processing, *Journal of the European Ceramic Society* 28(7) (2008) 1341-1351.
- [192] A.E.R. Westman, The packing of particles: empirical equations for intermediate diameter ratios, *Journal of the American Ceramic Society* 19(1-12) (1936) 127-129.
- [193] C. Furnas, Grading aggregates-I.-Mathematical relations for beds of broken solids of maximum density, *Industrial & Engineering Chemistry* 23(9) (1931) 1052-1058.
- [194] S. Liu, Z. Ha, Prediction of random packing limit for multimodal particle mixtures, *Powder technology* 126(3) (2002) 283-296.
- [195] F. Shama, P. Sherman, Evaluation of some textural properties of foods with the Instron Universal Testing Machine, *Journal of Texture Studies* 4(3) (1973) 344-352.
- [196] A.K. Sood, R.K. Ohdar, S.S. Mahapatra, Parametric appraisal of mechanical property of fused deposition modelling processed parts, *Materials & Design* 31(1) (2010) 287-295.
- [197] L. Beuselinck, G. Govers, J. Poesen, G. Degraer, L. Froyen, Grain-size analysis by laser diffractometry: comparison with the sieve-pipette method, *CATENA* 32(3) (1998) 193-208.
- [198] D. Dean, Thermal Gravimetric Analysis, University of Alabama at Birmingham (2016).
- [199] J.S. Reed, Principles of ceramics processing, (1995).
- [200] R.W. Fox, P.J. Pritchard, A.T. McDonald, Fox and McDonald's introduction to fluid mechanics, John Wiley & Sons, Inc. ; John Wiley [distributor], Hoboken, NJ; Chichester, 2011.
- [201] A.V. Virkar, J. Chen, C.W. Tanner, J.-W. Kim, The role of electrode microstructure on activation and concentration polarizations in solid oxide fuel cells, *Solid State Ionics* 131(1) (2000) 189-198.
- [202] J. Laramie, A. Dicks, Fuel cell systems explained, John Wiley and Sons, New York (2003).
- [203] M. Ciobanu, J.P. Wilburn, M.L. Krim, D.E. Cliffel, 1 - Fundamentals, in: C.G. Zoski (Ed.), *Handbook of Electrochemistry*, Elsevier, Amsterdam, 2007, pp. 3-29.
- [204] B. Shri Prakash, S. Senthil Kumar, S.T. Aruna, Properties and development of Ni/YSZ as an anode material in solid oxide fuel cell: A review, *Renewable and Sustainable Energy Reviews* 36 (2014) 149-179.
- [205] G.P. M., W.J. W., Analysis of electrochemical impedance spectroscopy in proton exchange membrane fuel cells, *International Journal of Energy Research* 29(12) (2005) 1133-1151.
- [206] Z. He, F. Mansfeld, Exploring the use of electrochemical impedance spectroscopy (EIS) in microbial fuel cell studies, *Energy & Environmental Science* 2(2) (2009) 215-219.
- [207] C. Alexander, M. Sadiku, Fundamentals of Electric Circuit. 3, revised, McGraw-Hill, 2006.
- [208] E. Barsoukov, J.R. Macdonald, Impedance spectroscopy: theory, experiment, and applications, John Wiley & Sons 2018.
- [209] J.F. Robinson, Y.P. Kayinamura, Charge transport in conducting polymers: insights from impedance spectroscopy, *Chemical Society Reviews* 38(12) (2009) 3339-3347.

- [210] E.P. Randviir, C.E. Banks, Electrochemical impedance spectroscopy: an overview of bioanalytical applications, *Analytical Methods* 5(5) (2013) 1098-1115.
- [211] J.R. Macdonald, Impedance spectroscopy and its use in analyzing the steady-state AC response of solid and liquid electrolytes, *Journal of Electroanalytical Chemistry and Interfacial Electrochemistry* 223(1) (1987) 25-50.
- [212] E. Warburg, *Ann. Phys. Chem.* (67) (1899) 493.
- [213] M.J. Patel, S. Blackburn, D.I. Wilson, Modelling of paste flows subject to liquid phase migration, *International Journal for Numerical Methods in Engineering* 72(10) (2007) 1157-1180.
- [214] A. Anikeenko, N. Medvedev, T. Aste, Structural and entropic insights into the nature of the random-close-packing limit, *Physical Review E* 77(3) (2008) 031101.
- [215] S. Torquato, T.M. Truskett, P.G. Debenedetti, Is random close packing of spheres well defined?, *Physical review letters* 84(10) (2000) 2064.
- [216] B. Su, T. Button, A comparative study of viscous polymer processed ceramics based on aqueous and non-aqueous binder systems, *journal of materials processing technology* 209(1) (2009) 153-157.
- [217] J. Powell, S. Assabumrungrat, S. Blackburn, Design of ceramic paste formulations for co-extrusion, *Powder technology* 245 (2013) 21-27.
- [218] S. Rough, J. Bridgwater, D. Wilson, Effects of liquid phase migration on extrusion of microcrystalline cellulose pastes, *International journal of pharmaceuticals* 204(1-2) (2000) 117-126.
- [219] M.J. Ribeiro, J.M. Ferreira, J.A. Labrincha, Plastic behaviour of different ceramic pastes processed by extrusion, *Ceramics International* 31(4) (2005) 515-519.
- [220] J. Powell, S. Blackburn, The unification of paste rheologies for the co-extrusion of solid oxide fuel cells, *Journal of the European Ceramic Society* 29(5) (2009) 893-897.
- [221] K.G. Kuder, S.P. Shah, Processing of high-performance fiber-reinforced cement-based composites, *Construction and Building Materials* 24(2) (2010) 181-186.
- [222] H.A.T. Behtash Mani, R. Babaie Moghadam, A new design for co-extrusion dies: Fabrication of multi-layer tubes to be used as solid oxide fuel cell, *Journal of Science: Advanced Materials and Devices* 2(4) (2017) 425-431.
- [223] J.J. Benbow, S.H. Jazayeri, J. Bridgwater, The flow of pastes through dies of complicated geometry, *Powder Technology* 65(1) (1991) 393-401.
- [224] S. Blackburn, H. Böhm, **A method for calculating the pressure drop in honeycomb dies**, *Journal of the European Ceramic Society* 17(2-3) (1997) 183-189.
- [225] T. Suzuki, T. Yamaguchi, K. Hamamoto, H. Sumi, Y. Fujishiro, Low temperature densification process of solid-oxide fuel cell electrolyte controlled by anode support shrinkage, *Rsc Advances* 1(5) (2011) 911-916.
- [226] D. Panthi, A. Tsutsumi, A novel multistep dip-coating method for the fabrication of anode-supported microtubular solid oxide fuel cells, *Journal of Solid State Electrochemistry* 18(7) (2014) 1899-1905.
- [227] D. Panthi, A. Tsutsumi, Micro-tubular solid oxide fuel cell based on a porous yttria-stabilized zirconia support, *Scientific reports* 4 (2014) 5754.
- [228] A. Torabi, T.H. Etsell, P. Sarkar, Dip coating fabrication process for micro-tubular SOFCs, *Solid State Ionics* 192(1) (2011) 372-375.

- [229] H.C. Mayer, R.J.P.o.F. Krechetnikov, Landau-Levich flow visualization: Revealing the flow topology responsible for the film thickening phenomena, 24(5) (2012) 42-54.
- [230] R. Krechetnikov, G.M.J.P.o.F. Homsy, Experimental Study of Substrate Roughness and Surfactant Effects on the Landau–Levich Law, 17(10) (2005) 42-88.
- [231] J.S.J. Reed, Principles of Ceramics Processing, 2nd Edition, (1995).
- [232] H. Monzón, M.A. Laguna-Bercero, A. Larrea, B.I. Arias, A. Várez, B. Levenfeld, Design of industrially scalable microtubular solid oxide fuel cells based on an extruded support, International Journal of Hydrogen Energy 39(10) (2014) 5470-5476.
- [233] W.-S. Hsieh, P. Lin, S.-F. Wang, Fabrication of electrolyte supported micro-tubular SOFCs using extrusion and dip-coating, international journal of hydrogen energy 38(6) (2013) 2859-2867.
- [234] C. Fu, X. Ge, S.H. Chan, Q.J.F.C. Liu, Fabrication and Characterization of Anode-Supported Low-Temperature SOFC Based on Gd-Doped Ceria Electrolyte, 12(3) (2012) 450-456.
- [235] C.C. Wei, K.J.I. Li, E.C. Research, Yttria-Stabilized Zirconia (YSZ)-Based Hollow Fiber Solid Oxide Fuel Cells, 47(5) (2008) 1506-1512.
- [236] K. Kanawka, F.D. Grande, Z. Wu, A. Thursfield, D. Ivey, I. Metcalfe, G. Kelsall, L.J.I. Kang, E.C. Research, Microstructure and Performance Investigation of a Solid Oxide Fuel Cells Based on Highly Asymmetric YSZ Microtubular Electrolytes, 49(13) (2010) 6062-6068.
- [237] E. Olevsky, R. Bordia, Advances in sintering science and technology, John Wiley & Sons 2010.
- [238] V. Lawlor, Review of the micro-tubular solid oxide fuel cell (Part II: Cell design issues and research activities), Journal of Power Sources 240 (2013) 421-441.
- [239] S. McIntosh, J.M. Vohs, R.J. Gorte, Impedance Spectroscopy for the Characterization of Cu-Ceria-YSZ Anodes for SOFCs, Journal of the Electrochemical Society 150(10) (2003).